Plasma Physics Reports, Vol. 30, No. 7, 2004, pp. 549–567. Translated from Fizika Plazmy, Vol. 30, No. 7, 2004, pp. 595–614.

TOKAMAKS

Effect of the Magnetic Field Curvature on Magnetic Islands in Tokamaks

A. B. Mikhailovskii[1, 2], S. V. Konovalov[1, 3], M. S. Shirokov[1, 4], and V. S. Tsypin[5]

[1] *Russian Research Centre Kurchatov Institute, pl. Kurchatova 1, Moscow, 123182 Russia*
[2] *Moscow Institute of Physics and Technology, Institutskiĭ pr. 9, Dolgoprudnyĭ, Moscow oblast, 141700 Russia*
[3] *Naka Fusion Research Establishment, Japan Atomic Energy Research Institute, Ibaraki 3111-0193, Japan*
[4] *Plasma Physics Department, Moscow Engineering Physics Institute, Kashirskoe sh. 31, Moscow, 115409 Russia*
[5] *Physics Institute, University of São Paulo, Cidade Universitaria, 05508–900, Brazil*

Received July 12, 2003; in final form, December 14, 2003

Abstract—The effect of the magnetic field curvature on magnetic islands in a tokamak is analyzed. It is demonstrated that the original investigation of this effect by Kotschenreuther *et al.* (1985) is inconsistent: on the one hand, the authors made the correct assumption that this is an ideal effect and, on the other hand, they described it in terms of the parameters characteristic of the "resistive ordering" approach, which is incompatible with the ideal approximation. More recent studies of the magnetic curvature effect have produced further ambiguities; as a result, a branch of the theory of magnetic islands has arisen that is based on the supposition that the effect under discussion can be described in terms of the Glasser–Greene–Johnson parameter D_R. This branch is shown to be erroneous, because the parameter D_R describes the plasma response to magnetic field perturbations on spatial scales of about the dimension of the linear resistive layer, while the characteristic spatial scale of the magnetic islands is much longer. It is concluded that the correct theory developed here for the magnetic curvature effect makes more optimistic predictions about its stabilizing role. *© 2004 MAIK "Nauka/Interperiodica".*

1. INTRODUCTION

Magnetic islands are one of the main magnetohydrodynamic (MHD) phenomena that limit the maximum plasma pressure in high-performance tokamaks [1]. Among the several factors that govern the dynamics of the islands [2] is the *magnetic curvature effect*, which was investigated for the first time by Kotschenreuther *et al.* [3].

In order to interpret the results of their calculations, the authors of [3] appealed to the paper by Glasser *et al.* [4], who studied linear resistive MHD modes and, in particular, resistive interchange modes. In [4], it was shown that resistive interchange modes may be either stable or unstable, depending on the sign of the parameter D_R, defined as

$$D_R = E + F + H^2, \tag{1.1}$$

where E, F, and H are the parameters of the magnetic configuration that were introduced in [4] (the Glasser–Greene–Johnson (GGJ) parameters). However, the generalized Rutherford equation for the island width evolution that was derived in [3] (see Eq. (71) in that paper) does not include the parameter D_R; instead, it contains only the sum $E + F$ and does not involve the term H^2. In this connection, Kotschenreuther *et al.* [3] tried to answer the question of whether the absence of this term is intrinsic to the theory of magnetic islands or results from the fact that they used the so-called large-aspect-ratio approximation. They concluded that the former supposition seems more likely: the term H^2 does not arise in the theory because, according to [4], it appears only in the case of a thin linear tearing layer, for which resistive diffusion is important, whereas nonlinear theory deals with magnetic islands whose width considerably exceeds the characteristic spatial scale on which resistive diffusion occurs.

Our objective here is the same as in [3]: to analyze the effect of the magnetic field curvature on magnetic islands. In our analysis, we distinguish between the physical ideas of Kotschenreuther *et al.* [3] and the calculations carried out by them, on the one hand, and the form in which the results of these calculations are represented, on the other. We show that the ideas, as well as the calculations, are correct, whereas the representation of the main calculated result in the form of the sum $E + F$ is not. Such a representation conflicts with the concept of the ideal nature of the magnetic curvature effect, because the sum $E + F$, which was used in [3] in the same sense as in [4], is peculiar to the theory in which resistivity plays a central role and which is incompatible with the ideal MHD approach. The use of this sum in [3] gave rise to the erroneous alternative idea that the magnetic curvature effect is resistive in nature. In this context, the present paper can be viewed as substantiation of another concept of the magnetic curvature effect—the one based on ideal magnetohydrodynamics.

1063-780X/04/3007-0549$26.00 © 2004 MAIK "Nauka/Interperiodica"

The question of which of the concepts—ideal or resistive—is correct is important from the standpoint of fundamental plasma physics and also for applications of the theory of magnetic islands. It is well known that, in tokamaks, magnetic islands can manifest themselves as neoclassical tearing modes [1, 2]. These modes may limit the maximum plasma pressure in the devices being designed in connection with the development of the ITER project; it is therefore very important to predict what the role of the magnetic curvature effect would be—stabilizing or destabilizing. It should be noted, however, that the ideal and resistive approaches yield different predictions, which are even incompatible with one another in some important cases. That is why it is worth analyzing a large number of various erroneous views concerning the problem under discussion here. Such an analysis is not a simple matter, because, on the one hand, the erroneous concepts have become too deeply rooted and, on the other, the magnetic curvature effect occurs against the background of some simpler effects.

We begin our analysis by a general survey of the problem. This is the subject of Section 2. One of the most important results of this section is the introduction of the notion of *the magnetic well of the magnetic islands* (denoted by U_{MI}) and the interpretation of the magnetic curvature effect as *the magnetic well effect.*

In Section 3, we formulate the problem and present the basic equations. With the earlier theoretical research on magnetic islands in mind, we reduce the problem to that of determining the contribution of the magnetic well effect to the Rutherford equation for the island width evolution (see Eq. (3.4) below). In this formulation, the plasma resistivity enters only the coefficient D_{res}, which characterizes the evolution rate of the island width. Thereby, in the Rutherford equation, the contribution of the magnetic well effect, denoted by Δ_{mw}, is calculated without considering the resistivity.

As in [3], we determine the so-called magnetic-well-related current (denoted by J_{mw}) from the current continuity equation [see Eq. (3.6)] in which the transverse current is driven by the plasma pressure gradient [see Eq. (3.23)]. Since the toroidal effects are taken into account, we work with functions of three variables, two of which, x and ξ, are used to describe a chain of magnetic islands and the third—the poloidal angle θ—is used to describe the effects associated with the poloidal oscillations of the equilibrium functions. In Section 3 (as in [3]), we divide all the functions into two groups (those that depend on θ and those that do not) and work with the equations that relate these two groups of functions.

In Section 4, we calculate the magnetic-well-related current J_{mw} and determine the magnetic well contribution Δ_{mw}. The result of these calculations is Eq. (4.37).

Section 5 is devoted to the analysis of the general features of the magnetic well of the magnetic islands and its particular manifestations in a number of equilibrium plasma states. It is pointed out that the most important of these features is the stabilizing effect of the parameter Δ_{mw} at a positive magnetic shear and a negative plasma pressure gradient. Here lies the key difference between our results and the predictions of the resistive D_R trend, according to which the stabilizing magnetic well may either stabilize or destabilize magnetic islands, depending on the values of the equilibrium parameters.

We are interested in particular equilibrium states in a circular tokamak with a low (but finite) plasma pressure and in a slightly noncircular tokamak with moderate plasma pressure. Since such equilibrium states have already been discussed in the literature, the corresponding parts of Section 5 (Subsections 5.2 and 5.3) constitute a review of the earlier studies. We show that, in these two cases, the difference between the magnetic well of the magnetic islands and the resistive magnetic well is unimportant (see relationships (5.4)). At the same time, we show that, in the second stability region of the ideal ballooning modes, the magnetic well of the magnetic islands differs radically from the resistive magnetic well. Our analysis indicates that, in contrast to the resistive magnetic well, the magnetic well of the magnetic islands produces a stabilizing effect in this region.

Section 6 begins by discussing the problem of why the magnetic well of the magnetic islands differs from the ideal magnetic well of the linear modes (see Subsection 6.1). In Subsection 6.2, we consider the limiting transition to zero resistivity in the GGJ approach [4]. The difficulties arising in deriving the equation for the linear resistive magnetic well are elucidated in Subsection 6.3.

Final comments are given in Section 7. In addition, the results on the equilibrium parameters in the linear stability theory are summarized in Appendix A, and the contribution of the plasma compressibility to the equation for linear resistive modes is considered in Appendix B.

2. GENERAL REVIEW OF THE PROBLEM

2.1. Paradox of the Mutual Cancellation of the Resistive Parts of the Glasser–Greene–Johnson Parameters

Here, the problem is to find out whether or not the sum $E + F$ can be considered a basis for an adequate description of an ideal MHD phenomenon. As was noted above, the parameter D_R arises as a result of the essentially resistive ordering approach used in [4] and describes the very resistive magnetic field curvature effect. In this sense, the parameter D_R, as well as the parameters E, F, and H in the expression for D_R, can be called linear resistive parameters. These parameters can be used to describe an *ideal phenomenon* only if they appear in the description of *linear ideal modes*, i.e., when the sum $E + F$ turns out to be relevant to the problem of linear ideal modes. Meanwhile, in [4], the only

parameter that is definitely ideal is the parameter D_I, defined by the relationship

$$D_I = E + F + H - 1/4. \quad (2.1)$$

In this situation, there are two possibilities. First, all the parameters on the right-hand side of relationship (2.1) are intrinsic to ideal theory, so that the representation of the curvature effect in [3] is justified. Second, some of the parameters on the right-hand side of relationship (2.1) are not intrinsic to ideal theory; i.e., they are composed of ideal and resistive parts in such a way that the resistive parts *mutually cancel out.* In this case, the representation of the curvature effect in the form of the sum $E + F$ in [3] may turn out to be *inadequate* and may lead to a misunderstanding of the result obtained in [3].

The approach used in [4] does not provide information enabling one to decide which of the two possibilities will be realized. This is why we now turn to papers [5–7], the first of which was aimed at studying ideal modes (in particular, Mercier modes) in general toroidal geometry, the second dealt with the same modes in the axisymmetric geometry of a tokamak, and the third considered resistive modes in general toroidal geometry and in axisymmetric tokamak geometry. The main results of [5–7] were summarized in [8].

In [5–8], the linear ideal curvature effect was described not in terms of the parameter D_I, defined by relationship (2.1), but rather in terms of the parameter U_0, which characterizes the linear ideal magnetic well and is related to D_I by the expression

$$U_0 = -(D_I + 1/4). \quad (2.2)$$

Consequently, in terms of the parameters E, F, and H, we have

$$U_0 = -(E + F + H). \quad (2.3)$$

On the other hand, according to Eq. (7.60) from [8], the parameter U_0 is represented as

$$U_0 = \frac{q^4}{q'^2}\left(A_0 W^{(0)} + A_1 \frac{q'}{q^2} - A_0 A_2 + A_1^2\right), \quad (2.4)$$

where q is the safety factor, the prime denotes the derivative with respect to the "radial coordinate" that labels equilibrium magnetic surfaces, and A_0 is a geometric factor given by relationship (A.1) with $n = 0$. The parameter $W^{(0)}$ is defined by Eq. (A.4) from [8] and the parameters A_1 and A_2 are given by relationship (A.1) with $n = 1$ and 2. (For the simplest case of a circular tokamak or a slightly noncircular tokamak, the explicit expressions for the parameters A_0 and A_1 will be presented in Subsections 4.3 and 5.1, respectively.)

The parameters $W^{(0)}$, A_0, A_1, and A_2 characterize the linear ideal magnetic curvature effect. In order to determine how these parameters are related to the parameters E, F, and H, which were used in [4], we utilize Eqs. (4.18) and (4.19) from [7] to construct an auxiliary parameter U that generalizes the parameters U_0 to the case of arbitrary resistivity:

$$U = U_0 - H\frac{d}{dk_x}\left(\frac{k_x^3}{k_x^2 + k_R^2 A_0/C_0}\right) - \frac{H^2}{1 + k_R^2 A_0/(k_x^2 C_0)}. \quad (2.5)$$

Here, k_x is a radial wavenumber characterizing the reciprocal of the radial scale of the mode and k_R is a characteristic resistive radial wavenumber defined by the relationship

$$k_R^2 = \gamma/\eta, \quad (2.6)$$

where γ is the growth rate of the mode and η is the plasma resistivity. The parameter H is given by the equality

$$H = -\frac{q^2}{q'}\left(A_1 - \frac{A_0}{C_0}C_1\right), \quad (2.7)$$

and the parameters C_0 and C_1 are defined by relationships (A.2). It can be seen that the parameter H defined by equality (2.7) coincides with the parameter H used in [4]. It is also evident that, when the resistivity is ignored ($k_R/k_x \longrightarrow \infty$), relationship (2.5) reduces to relationship (2.3); as a result, we obtain

$$U = U_0. \quad (2.8)$$

On the other hand, in the limit of high resistivity ($k_R/k_x \longrightarrow \infty$), relationship (2.7) yields

$$U = U_R, \quad (2.9)$$

where U_R is the linear resistive magnetic well given by the relationship

$$U_R = U_0 + H - H^2. \quad (2.10)$$

We thus can see that

$$U_R = -D_R. \quad (2.11)$$

Relationships (2.4), (2.10), and (2.11) lead to

$$E + F = -(U_0 + H). \quad (2.12)$$

A comparison of relationship (2.7) with relationship (2.4) shows clearly that the parameter H is not intrinsic to linear ideal MHD theory. However, it contains a part that is associated with the parameter A_1 and thus is inherent to this theory. Therefore, equality (2.7) can be rewritten in the form

$$H = H_I + H_R, \quad (2.13)$$

where

$$H_I = -q^2 A_1/q', \quad (2.14)$$

$$H_R = q^2 A_0 C_1/(q' C_0). \quad (2.15)$$

The parameters H_I and H_R can be called the "ideal" and "resistive" parts of the parameter H. Since the parameter H is not an attribute of ideal theory, relationship (2.12) implies that the sum $E + F$, too, is not its attribute. This indicates that the main results of [3] should be explained in terms of the *second of the two possibilities under discussion*—the mutual cancellation of the resistive parts of different terms on the right-hand side of relationship (2.1).

It is now necessary to understand precisely what cancels the resistive part of the parameter H: Is it the resistive part of one of the parameters (E or F) or is it the sum of their resistive parts?

In order to answer this question, we express E and F in terms of the equilibrium parameters used in [7, 8]. According to Eq. (A11.6) from [8] (cf. relationship (2.1)), we have

$$F = \frac{q^4}{q'^2}\left[A_2A_1 - A_1^2 + A_0\left(\frac{2\pi p'}{\Phi'}\right)^2\left(\frac{\sqrt{g}}{\mathbf{B}^2}\right)^{(0)}\right], \quad (2.16)$$

where p is the equilibrium plasma pressure, Φ is the equilibrium toroidal magnetic flux, $\mathbf{B}$ is the equilibrium magnetic field, the superscript (0) stands for the θ-independent part of a function, and g is the determinant of the metric tensor. Analogously, we arrive at

$$E = -\frac{q^4}{q'^2}A_0\left[W^{(0)} + \left(\frac{2\pi p'}{\Phi'}\right)^2\left(\frac{\sqrt{g}}{\mathbf{B}^2}\right)^{(0)}\right] - q^2A_0C_1/(q'C_0). \quad (2.17)$$

We can see that the parameter F is a purely ideal parameter. In contrast to F, the parameter E is the sum of the ideal and resistive parts, so that we can write the following relationship (cf. relationship (2.13)):

$$E = E_I + E_R, \quad (2.18)$$

where

$$E_I = -\frac{q^4}{q'^2}A_0\left[W^{(0)} + \left(\frac{2\pi p'}{\Phi'}\right)^2\left(\frac{\sqrt{g}}{\mathbf{B}^2}\right)^{(0)}\right], \quad (2.19)$$

$$E_R = -q^2A_0C_1/(q'C_0). \quad (2.20)$$

Expressions (2.15) and (2.20) give

$$E_R + H_R = 0, \quad (2.21)$$

which shows that the resistive part of H is canceled by the resistive part of E. Then, with allowance for formulas (2.13)–(2.16) and (2.18)–(2.21), relationship (2.4) for U_0 can be represented in a purely resistive form:

$$U_0 = -(E_I + F + H_I). \quad (2.22)$$

Accordingly, relationship (2.1) for the parameter D_I can also be written in a purely resistive form:

$$D_I = E_I + F + H_I - 1/4. \quad (2.23)$$

The situation just considered can be referred to as the effect of mutual cancellation of the resistive parts of the parameters E and H—a possibility that was not anticipated in [3]. Note that the resistive parts E_R and H_R given by Eqs. (13) from [4] coincide in absolute value but have opposite signs. In our analysis, relationship (2.21) serves merely to provide a physical explanation of this circumstance.

2.2. Fine Details of the Ideal Limit of the Glasser–Greene–Johnson Equations

In order to better understand the difference between the linear ideal and resistive curvature effects, it is expedient to analyze the limiting transition to zero resistivity in the equations for linear resistive modes that were used in [7] and in [4]. For the equations of [7], the zero resistivity limit is easy to take, because, in [7], the ordering characteristic of the resistive modes was not used. In contrast, in [4], this ordering was utilized, so that the limiting transition to zero resistivity in the GGJ equations for the resistive modes is more complicated. In order to take the limit correctly, it is necessary to accurately resolve singularities of the 0/0 type in a number of formulas. Such a nontrivial procedure was applied in [9], devoted to the linear theory of ideal modes in a compressible plasma of arbitrary toroidal geometry. We will use the procedure from [9] in Subsection 6.2, in which we also give the necessary explanations of the physical effects described in the resistive and the ideal versions of the GGJ equations.

2.3. Plasma Compressibility Paradox

The equation used in [3] to describe the magnetic curvature effect (see Eq. (71) in that paper) does not contain the term H^2. This indicates that the sum $E + F$ differs from the parameter D_R. The authors of [3] interpreted this circumstance as a *plausible consequence* of the fact that the characteristic width of the island is much greater than the resistive scale length. If we, however, try to arrive at the parameter D_R by assuming that the ratio of the characteristic radial scale of the mode to the resistive scale length is arbitrary, we then find that, using the approach of [3] and under the assumption that the plasma is incompressible, this cannot be done without resolving the *plasma compressibility paradox.*

The essence of this paradox can hardly be understood exclusively in terms of the approach of [4], because basic equations (9)–(12) in that paper were derived not from the first principles but by appealing to the procedure described in [10]. At the same time, turning to [10], we can see that, in order to derive Eqs. (9)–(12) of [4], it is necessary to repeat the corresponding nontrivial calculations carried out in [10], in particular, those with Eq. (16), which contains the adiabatic index (denoted by γ in that paper). On the other hand, the parameter D_R does not involve the adiabatic index. To

explain this circumstance, it may be assumed that the adiabatic index is zero (the incompressible plasma approximation) or is infinity (the fully compressible plasma approximation). However, neither of these assumptions will produce the correct result because of the plasma compressibility paradox. It may be easier to resolve this paradox by reference to [7], in which the linear resistive modes were studied on the basis of the first principles (the results of [7] were presented in Section 11 of [8]). In Subsection 6.3, we will show how it is possible to derive an expression for the parameter D_R with allowance for plasma compressibility.

2.4. D_R Trend in the Theory of Magnetic Islands

The above analysis shows that the magnetic curvature has different effects on the magnetic islands and on the resistive and linear ideal modes. In principle, this conclusion follows from [3], where the effect of the curvature on the magnetic islands was studied for the first time. However, the fact that the authors of [3] frequently appealed to the results on linear resistive modes obtained in [4] and that they inadequately used the notation of [4] in describing the nonlinear curvature effect led to the erroneous view that the effect of the magnetic curvature on magnetic islands can be described in terms of the parameter D_R, which characterizes the linear effect of the curvature. As a result, an ambiguous trend—the D_R trend—arose in the theory of magnetic islands.

An attempt to justify this trend was made in [11], in which, however, the plasma compressibility was ignored. In Subsections 2.3 and 6.3 of the present paper, it is shown, however, that the magnetic curvature cannot, in principle, be described under the assumption that the plasma is incompressible.

2.5. Magnetic Well in the Linear and Nonlinear Modes

Since there is a precisely formulated rule [4] for calculating the parameter D_R for any particular equilibrium state, this parameter can be found by a routine computational procedure. However, since the parameter D_R does not characterize the effect of the curvature on magnetic islands, it is necessary to find out in which respects the predictions of the D_R trend differ from those of the correct theory. To understand this point, it is expedient to turn to the *notion of the magnetic well.* Above, we introduced the *linear ideal magnetic well* U_0 and *linear resistive magnetic well* U_R. We now introduce *the magnetic well of the magnetic islands* and denote it by U_{MI}.

From what has been said above, the *linear ideal magnetic curvature effect* can be described in terms of the *linear ideal magnetic well* U_0, while the *linear resistive curvature effect*, in terms of the *linear resistive magnetic well* U_R. Note that Glasser *et al.* [4] described these two effects by the parameter D_I, introduced by relationship (2.1), and the parameter D_R, introduced by relationship (1.1), respectively. According to relationship (2.11), the only difference between U_R and D_R is in their signs. The answer to the question of why we are characterizing the linear resistive curvature effect by the parameter $-D_R$ rather than by $+D_R$ is that we are interested here in the *suppression* of the modes, while the parameter D_R is more suitable for calculating the *growth rates of unstable modes.* As an example, the condition for the existence of unstable resistive interchange modes has the form $D_R > 0$ (see, e.g., Eq. (11.40) from [8]) while at the same time their growth rate is determined by the parameter $+D_R$, in accordance with Eq. (11.38) from [8].

The ideal parameter D_I is related to the parameter U_0 by expression (2.2). The physical meaning of the parameter U_0 can be understood in terms of the Mercier stability criterion, which arises in the problem of linear ideal modes and has the form (see relationship (2.1))

$$\frac{1}{4} + U_0 > 0, \tag{2.24}$$

where the terms 1/4 and U_0 describe the effect of stabilization by the magnetic shear and the magnetic curvature effect, respectively. Hence, unlike the parameter D_I, which describes the combined action of these two effects, the parameter U_0 describes the curvature effect alone.

However, the parameter U_0 actually describes several curvature effects that are different in nature. In the simplest case of cylindrical geometry, the only nonzero component of the magnetic curvature is that normal to the magnetic surface; i.e., the *geodesic curvature* is zero. In this case, the cylindrical magnetic well is expressed in terms of the *normal curvature* and is described by a fairly simple formula. In contrast, in toroidal geometry, the parameter U_0 describes, among other things, a number of effects associated with the geodesic curvature, or, in other terminology, *local ballooning effects*. Accordingly, the magnetic well in toroidal geometry has the fairly complicated structure described by relationship (2.3). One of the main parts of the linear ideal magnetic well U_0 is the parameter $W^{(0)}$, which enters relationship (2.4) and can be called a *modified magnetic well.* This parameter characterizes the plasma pressure response to the *strictly flute* component of the plasma displacement (see Eq. (7.49) from [8]). The parameters A_1 and A_2 in relationship (2.4) account, respectively, for the so-called *local linear* and *quadratic ballooning* effects, i.e., effects due to the ballooning component of the perturbed plasma displacement (see the terms with $X_k^{(1)}$ in Eqs. (7.49) and (7.50) from [8]). Both of these effects are associated with the *geodesic curvature.* Because of its complicated structure, the parameter U_0 can naturally be called the *gen-*

eralized ideal magnetic well. We will, however, omit the adjective "generalized" for brevity.

Using expression (2.14), we can rewrite relationship (2.4) as

$$U_0 = \frac{q^4 A_0}{q'^2}(W^{(0)} - A_2) - H_I + H_I^2. \quad (2.25)$$

Here, the term H_I^2, as well as the term A_2, accounts for the geodesic component of the perturbed poloidal magnetic field, whose strength is proportional to the flute component of the perturbed plasma pressure (see Eq. (6.8) for details). These two terms differ from one another: the term A_2 arises from the averaging of the squared geodesic curvature over θ, while the term H_I^2 is associated with the square of the θ-averaged geodesic curvature.

Using condition (2.24) makes it possible to normalize the ideal magnetic well (i.e., to choose the corresponding normalizing factor). At the same time, for *linear resistive modes*, for which the effect of stabilization by the magnetic shear is absent, it is unclear what factor is to be taken as a basis for normalizing the resistive magnetic well (i.e., for introducing the parameter U_R). This problem can be resolved by turning to cylindrical geometry, in which the geodesic effects are absent. Since the parameters U_R and U_0 differ only in the rules by which the geodesic curvature is averaged, they coincide with one another when the geodesic curvature is zero. In this case, the magnetic curvature effect in cylindrical geometry is insensitive to the plasma resistivity, so we can set

$$U_R^c = U_0^c, \quad (2.26)$$

where the superscript "c" stands for "cylindrical." We thus normalize the *cylindrical resistive magnetic well.* Taking into account formula (2.25) and using the stability criterion for the resistive modes in toroidal geometry, we then construct an expression for the toroidal resistive magnetic well. Further, using Eq. (5.2) from [7], we obtain the following expression for the resistive magnetic well:

$$U_R = U_0 - \frac{q^2}{q'}\left(A_1 - \frac{A_0}{C_0}C_1\right) - \frac{q^4}{q'^2}\left(A_1 - \frac{A_0}{C_0}C_1\right)^2. \quad (2.27)$$

As can be seen, this expression coincides with expression (2.9). Note also that, for $H < 1$, relationship (2.10) gives

$$U_R > U_0, \quad (2.28)$$

while in the opposite case, $H > 1$, it gives

$$U_R > U_0. \quad (2.29)$$

We now construct an expression for the magnetic well of the magnetic islands, which was denoted above as U_{MI}. We begin by normalizing this magnetic well in *cylindrical geometry*, in which the geodesic effects are absent and, as a result, the nonlinear plasma response to the magnetic curvature effect is the same as the linear response. Thus, we arrive at the normalization condition

$$U_{MI}^c = U_0^c = U_R^c. \quad (2.30)$$

This naturally raises the following questions: In what way can the cylindrical magnetic well U_{MI}^c be generalized to toroidal geometry? Will the magnetic well U_{MI} in toroidal geometry be the same as U_0 or U_R, or will it be different from U_0 and U_R? However, these questions have already been answered in the above discussion of the results obtained in [3]: in toroidal geometry, the magnetic well of the magnetic islands U_{MI} is given by the expression

$$U_{MI} = U_0 - \frac{q^2}{q'}A_1, \quad (2.31)$$

which can also be rewritten as

$$U_{MI} = U_0 + H_I, \quad (2.32)$$

where H_I is the ideal part of the GGJ parameter H, whose physical meaning was clarified in [7]. One more representation of U_{MI} is as follows:

$$U_{MI} = -(E_I + F), \quad (2.33)$$

where the ideal part E_I of the GGJ parameter E is given by relationship (2.19) and the GGJ parameter F is given by relationship (2.16).

Below, we will show that, for standard tokamak discharges with positive magnetic shear and with a radially decreasing plasma pressure profile, the parameter H_I is positive, $H_I > 0$. Consequently, relationship (2.32) contains the stabilizing effect of the magnetic well of the magnetic islands, $U_{MI} > 0$, provided that the effect of the linear ideal magnetic well is stabilizing, $U_0 > 0$.

Formulas (1.1), (2.18), (2.21), and (2.33) yield the following relationship between the linear resistive magnetic well U_R and the magnetic well of the magnetic islands U_{MI}:

$$U_R = U_{MI} - (H_R + H^2). \quad (2.34)$$

We can show that

$$H_R > 0. \quad (2.35)$$

In accordance with what was said above, the magnetic well of the magnetic islands has a favorable (i.e., stabilizing) effect when $U_{MI} > 0$. Hence, in working with U_R, it should be kept in mind that the resistive D_R trend leads to less favorable predictions than those obtained by using the correct theory.

The effect of the magnetic curvature on magnetic islands was commonly identified with the GGJ effect [4, 12]. As was explained above, however, a description

of the effect of the curvature on magnetic islands in terms of the parameter D_R can produce erroneous results. So, to avoid misunderstanding, we propose to follow [13] and to refer to the *effect of the magnetic curvature on magnetic islands* as the *effect of the magnetic well on magnetic islands.* Moreover, the above analysis shows that the linear resistive magnetic well effect (i.e., the so-called GGJ effect) and the effect of the magnetic well on magnetic islands are physically different.

2.6. When Is the Curvature Effect Important in the Theory of Magnetic Islands?

Let us consider large-aspect-ratio tokamaks. For such tokamaks with moderate magnetic shear, with magnetic surfaces of circular cross section, and with an electron temperature comparable to or higher than the bulk ion temperature, the curvature exerts a weaker effect on the neoclassical tearing modes than does the bootstrap current [2, 14, 15]. However, for tokamak discharges with optimized magnetic shear [16, 17], the magnetic curvature effect may exceed the bootstrap current effect [13]. As was explained in [13], it is this situation that occurs inside an internal transport barrier, in which the ions are hotter than the electrons and the relative ion temperature gradient is larger than the relative plasma density gradient [17].

Another possible way of enhancing the magnetic curvature effect is to shape the magnetic surfaces into a configuration with nonzero ellipticity and triangularity. In this case, the expression for the magnetic well contains a stabilizing term that is proportional to the product of the ellipticity and triangularity, multiplied by a large coefficient on the order of the aspect ratio (see Subsection 5.3 for details).

The relative role of the curvature effect becomes more important when the bootstrap current effect is weakened by intense transverse transport [18–20]. The fact that, in the presence of such transport, the role of the magnetic well increases was pointed out in [21, 22]. On the other hand, the magnetic well effect can be reduced because of the flattening of the equilibrium plasma pressure profile in the vicinity of a magnetic island [23].

The smaller the aspect ratio (which corresponds to a finite-aspect-ratio tokamak), the greater the relative role of the magnetic well effect. However, we restrict the analysis here to large-aspect-ratio tokamaks. Although our analysis is also useful for the development of the existing theory of finite-aspect-ratio tokamaks, their consideration lies outside the scope of the present paper.

2.7. Difficulty in Calculating the Matching Parameter in the Theory of Tearing Modes with Allowance for the Magnetic Curvature Effect

In the linear theory of tearing modes [24], the calculation of the matching parameter Δ' in the Rutherford equation for the island width evolution with allowance for the ideal magnetic well U_0 represents a difficulty because the so-called constant-ψ approximation, in which the expression for Δ' is derived, fails to hold for $U_0 \neq 0$. This difficulty was pointed out, in particular, in [23]. Above, we showed that $U_0 \neq U_{MI}$. So, assuming that $U_{MI} \neq 0$, we will treat U_0 as being sufficiently small, $U_0 \ll 1$, to overcome the difficulty in question.

3. FORMULATION OF THE PROBLEM AND BASIC EQUATIONS

3.1. Preliminary Remarks

In the terminology used in the current literature, the magnetic islands are characterized by the magnetic flux function ψ, defined as

$$\psi = \tilde{\psi}(t)\cos\xi - x^2 B_0/(2L_s). \tag{3.1}$$

Here, the cyclic variable of the islands, ξ, has the form

$$\xi = m\theta - n\zeta - \omega t, \tag{3.2}$$

where $\tilde{\psi}(t)$ is a positive constant that depends weakly on time and is related to the island half-width w by the relationship

$$w = 2(L_s\tilde{\psi}/B_0)^{1/2}, \tag{3.3}$$

$x = r - r_s$ is the radial deviation from a singular equilibrium magnetic surface $r = r_s$, in the vicinity of which the chain of magnetic islands is localized; r is the radial coordinate; B_0 is the equilibrium magnetic field; L_s is the shear length; m and n are the radial and toroidal mode numbers; ζ is a toroidal angle characterizing the equilibrium state; and ω is the rotation frequency of an island. The evolution of the island width is described by the generalized Rutherford equation [2], which can be represented as

$$G_1\frac{\partial w}{\partial t} = D_{res}\left(\frac{\Delta'}{4} + \Delta_{bs} + \Delta_{mw} + \Delta_{pol}\right). \tag{3.4}$$

Here, Δ' is the standard matching parameter in the theory of tearing modes [24]; Δ_{bs}, Δ_{mw}, and Δ_{pol} are, respectively, the contributions of the bootstrap current, magnetic well, and polarization current; $G_1 = 0.412$ [25]; and the magnetic resistive diffusion coefficient D_{res} is defined by the relationship $D_{res} = c^2/(4\pi\sigma)$, where σ is the plasma electric conductivity and c is the speed of light.

We assume that the constant $\tilde{\psi}$ in relationship (3.1) is independent of x (which corresponds to the so-called constant-$\tilde{\psi}$ approximation) and that the ideal magnetic

well U_0 is small, $U_0 \ll 1$. This latter assumption also concerns Eq. (3.4). The effect of the ideal magnetic well U_0 was discussed, in particular, in [3, 11] (see, e.g., Eqs. (67) and (69) in [3]).

In accordance with [13], the contribution of the magnetic well to the generalized Rutherford equation, i.e., the quantity Δ_{mw} in Eq. (3.4), is described by the expression

$$\Delta_{mw} = -\frac{2\sqrt{2}}{cs}\frac{Rq}{wB_0}\sum_{\sigma_x}^{\infty}\int_{-1}^{} d\Omega \int \frac{J_{mw}\cos\xi d\xi}{(\Omega + \cos\xi)^{1/2}}, \quad (3.5)$$

where R is the major radius of the torus, $s = qR/L_s \equiv (rq'/q)_{r = r_s}$ is the magnetic shear, $\Omega = -\psi/\tilde{\psi}$, $\sigma_x \equiv \operatorname{sgn} x$, and J_{mw} is the magnetic-well-related current. This current will be the subject of the next subsection.

3.2. Magnetic-Well-Related Current

According to the current continuity equation

$$\mathbf{B}\cdot\nabla\left(\frac{J_\parallel}{B}\right) + \nabla_\perp \cdot \mathbf{j}_\perp = 0, \quad (3.6)$$

the transverse current $\mathbf{j}_\perp$ generates a longitudinal current $J_\parallel$. The current J_{mw} is a component of this longitudinal current (see below for details). The peculiar feature of Eq. (3.6) is that the longitudinal gradient operator acts not only on $J_\parallel$ but also on the ratio $J_\parallel/B$ as a whole (see Eq. (7.5) in [8]).

In contrast to the problem treated in cylindrical geometry and, accordingly, formulated in two variables, (x, ξ) or (ψ, ξ), the problem at hand is formulated in three variables, e.g., in (x, ξ, θ), where the variable θ is introduced to describe toroidal plasma equilibrium. In terms of the variables (ξ, θ), we represent the perturbed functions in Eq. (3.6) as the sum of two parts, one that depends on the variable θ and another that is independent of it. Hence, the θ-independent functions depend on two variables, (x, ξ) or (ψ, ξ), whereas the θ-dependent functions depend on three variables, (x, ξ, θ) or (ψ, ξ, θ). Here, the functions that are independent of the variable θ and depend on it are distinguished by the superscripts (0) and (1), respectively (cf. Section 7 in [8]). We denote with B_0 the θ-averaged part of the equilibrium magnetic field $B_0^{(0)}$; it is assumed that the right-hand side of relationship (3.1) contains precisely the part $B_0^{(0)}$ in which the superscript (0) is dropped for simplicity. On the other hand, the functions that are independent of θ can also be divided into two groups: those that depend on ξ and those that do not. The ξ-dependent part of the θ-independent component of the longitudinal current $J_\parallel$ is denoted by J_{mw}, so that we have $J_\parallel^{(0)}(\xi) \equiv J_{mw}$.

Note that, in contrast to the bootstrap current, which determines the quantity Δ_{bs} in Eq. (3.4), the magnetic-well-related current is a ξ-dependent function (see Subsection 3.3 for details). Note also that the polarization current, which determines the quantity Δ_{pol} in Eq. (3.4), too, is a ξ-dependent function. However, unlike J_{mw}, this quantity also depends on the island rotation frequency ω, which is contained in expression (3.2), and vanishes as $\omega \longrightarrow 0$. Consequently, in the limit $\omega \longrightarrow 0$, the only component of the longitudinal current that depends on ξ is the magnetic-well-related current, which, in addition, is independent of θ.

3.3. Description of the θ-Dependent and θ-Independent Functions

In accordance with the aforesaid, we obtain the expression

$$J_\parallel = J_{\parallel 0}(r) + J_{\parallel 0}^{(1)}(r, \theta) + J_{mw}(x, \xi) + J_\parallel^{(1)}(x, \xi, \theta). \quad (3.7)$$

The operator $(\partial/\partial\theta)_{\xi, x}$, acting on the functions that are independent of the variable θ and on those that depend on it, reduces to the operators $m(\partial/\partial\xi)_{\theta, x}$ and $(\partial/\partial\theta)_{\xi, x} + m(\partial/\partial\xi)_{\theta, x}$, respectively. In contrast, the operator $(\partial/\partial\zeta)_{\theta, x}$ simplifies to $-n(\partial/\partial\xi)_{\theta, x}$ in both cases.

For toroidal geometry, the operator $\mathbf{B}\cdot\nabla$ acts on the functions that are independent of the variable θ and on those that depend on it in different ways. Assuming that, in the first case, the aspect ratio is large, we can use the approximate expression

$$(\mathbf{B}\cdot\nabla)(\ldots)^{(0)} = \frac{(\sqrt{g})^{(0)}B_0^{(0)}}{\sqrt{g}}\nabla_\parallel^{(0)}(\ldots)^{(0)}. \quad (3.8)$$

Here, the θ-independent part of the longitudinal gradient operator, $\nabla_\parallel^{(0)}$, is defined in cylindrical geometry by

$$\nabla_\parallel^{(0)} = k_\parallel\left(\frac{\partial}{\partial\xi}\right)_\psi \equiv k_\parallel\left[\left(\frac{\partial}{\partial\xi}\right)_x - \frac{w^2}{4x}\sin\xi\left(\frac{\partial}{\partial x}\right)_\xi\right], \quad (3.9)$$

and the longitudinal wave vector $k_\parallel$ is given by

$$k_\parallel = -xk_y/L_s, \quad (3.10)$$

where $k_y = m/r_s$. We are justified in ignoring toroidal effects in expression (3.9) because we are interested in magnetic islands whose width is considerably less than the characteristic equilibrium radial scale length.

In working with B_0 and $B_0^{(0)}$, we must also introduce the θ-dependent component of the equilibrium magnetic field, $\mathbf{B}_0^{(1)}$, through the representation

$$\mathbf{B}_0 = \mathbf{B}_0^{(0)} + \mathbf{B}_0^{(1)}. \quad (3.11)$$

Analogously, we must utilize the θ-dependent component of the equilibrium longitudinal current, $J_{\|0}^{(1)}$, which is given by the representation (cf. expression (3.7))

$$J_{\|}^{(1)} = J_{\|0}^{(1)} + \tilde{J}_{\|}^{(1)}, \quad (3.12)$$

where $\tilde{J}_{\|}^{(1)}$ is the θ-dependent component of the perturbed longitudinal current. The function $J_{\|0}^{(1)}$ also depends on the radial coordinate $r \equiv r_s + x$, so that we can write the following approximate relationship:

$$J_{\|0}^{(1)} = J_{\|0s}^{(1)} + (J_{\|0}^{(1)})'x. \quad (3.13)$$

Here, the subscript s indicates the value of the function at $r = r_s$ and the prime denotes the derivative of the function at $r = r_s$. It is clear that Eq. (3.6) should be split into two independent equations: the equilibrium equation at $r = r_s$,

$$\left[\mathbf{B}_0 \cdot \nabla\left(\frac{J_{\|0}^{(1)}}{B}\right) + (\nabla_\perp \cdot \mathbf{j}_\perp)_0\right]_s = 0, \quad (3.14)$$

and the equation in which all the terms are proportional to x. On the other hand, we can introduce the function

$$\hat{J}_{\|}^{(1)} = \tilde{J}_{\|}^{(1)} + (J_{\|0}^{(1)})'x, \quad (3.15)$$

which can be called the θ-dependent component of the *longitudinal island-related current.*

According to [26], the *perturbed poloidal magnetic field* $\sqrt{g}\tilde{B}^2$ (cf. Subsection 2.5), in which the superscript "2" indicates the contravariant θ-component of the vector, is an important perturbed function in linear theory. Linear theory also makes use of the equilibrium function $\sqrt{g}B_0^2$, which depends on the radial coordinate. Consequently, by analogy with formulas (3.13) and (3.15), we can use the representation

$$\sqrt{g}B_0^2 = (\sqrt{g}B_0^2)_s + (\sqrt{g}B_0^2)'x \quad (3.16)$$

and introduce the function

$$\sqrt{g}\hat{B}^2 = \sqrt{g}\tilde{B}^2 + (\sqrt{g}B_0^2)'x, \quad (3.17)$$

which characterizes the *contravariant* θ*-component (poloidal component) of the magnetic field of the island.* The θ-independent part of this function, $(\sqrt{g}\hat{B}^2)^{(0)}$, is determined by the equation

$$\hat{\mathbf{B}} = -\nabla\psi \times \mathbf{z}_s. \quad (3.18)$$

Here, ψ is given by relationship (3.1); $\mathbf{z}_s$ is a unit vector that points along the equilibrium magnetic field and, at $r = r_s$, is equal to

$$\mathbf{z}_s = (B_{0\zeta s}\boldsymbol{\zeta} + B_{0\theta s}\boldsymbol{\theta})/B_{0s}, \quad (3.19)$$

and $\boldsymbol{\theta}$ and $\boldsymbol{\zeta}$ are unit vectors in the direction of the gradients of θ and ζ, respectively. As a result, we obtain

$$(\sqrt{g}\hat{B}^2)^{(0)} = (\partial\psi/\partial x)_\xi = -xB_0/L_s. \quad (3.20)$$

Using the above formulas, we arrive at the following rule by which the operator $\mathbf{B} \cdot \nabla$ acts on the θ-dependent functions (cf. rule (3.8)):

$$(\mathbf{B} \cdot \nabla)(\ldots)^{(1)} = \frac{(\sqrt{g})^{(0)}}{r_s\sqrt{g}}\left(B_p + \frac{\sqrt{g}\hat{B}^2}{R}\right)\frac{\partial}{\partial\theta}(\ldots)^{(1)}, \quad (3.21)$$

where B_p is the θ-independent component of the equilibrium poloidal magnetic field at $r = r_s$.

In order to apply expression (3.8) to calculate the first term on the right-hand side of Eq. (3.16), it is necessary to take into account the following relationship, which is a consequence of formulas (3.12)–(3.15):

$$\left(\frac{J_\|}{B}\right)^{(0)} = \frac{J_{\rm mw}}{B_0^{(0)}} - \frac{1}{(B_0^{(0)})^2}[B_0^{(1)}(J_{\|0s}^{(1)} + \hat{J}_\|^{(1)})]^{(0)}. \quad (3.22)$$

From this relationship, it is clear that the expression for the θ-independent component of the poloidal magnetic field of the islands does not contain a perturbed poloidal magnetic field. As will be shown below (see Subsection 6.1), this is important in order to understand why the magnetic well of the magnetic islands differs from the linear ideal magnetic well.

3.4. Basic Equations

As usual (see, e.g., [3, 11]), in studying the magnetic well effect, the inertia of the plasma is ignored and its motion is described by the one-fluid equation

$$\frac{1}{c}[\mathbf{j} \times \mathbf{B}] = \nabla p, \quad (3.23)$$

where $\mathbf{B}$ is the total magnetic field, $\mathbf{j}$ is the net current density, and p is the plasma pressure. Equation (3.23) yields

$$\mathbf{j}_\perp = \frac{c}{\mathbf{B}^2}[\mathbf{B} \times \nabla p]. \quad (3.24)$$

Account is also taken of the following consequence of Eq. (3.23):

$$\mathbf{B} \cdot \nabla p = 0. \quad (3.25)$$

The above equations are supplemented with Ampère's law

$$\nabla \times \mathbf{B} = \frac{4\pi}{c}\mathbf{j} \quad (3.26)$$

and Maxwell's equation

$$\nabla \cdot \mathbf{B} = 0. \quad (3.27)$$

The equation of plasma motion in its simplest version (3.23) is sufficient to calculate the magnetic well of

the magnetic islands. On the other hand, to obtain an expression for a linear resistive magnetic well, it is necessary to use a more general equation of motion (see Subsection 6.3 for details).

4. CALCULATION OF THE MAGNETIC WELL EFFECT

4.1. Transformation of the Basic Equations

Equations (3.14) and (3.24) yield the following expression (cf., e.g., the corresponding expression in Section 3 of [26]):

$$J_{\parallel 0s}^{(1)} = cQ/(8\pi^2 r_s), \tag{4.1}$$

where the function Q is defined by the relationship

$$Q = -\frac{8\pi^2 p_0'}{RB_p}\sqrt{g}^{(1)}. \tag{4.2}$$

In expression (4.1), the function Q is assumed to be taken at $r = r_s$.

Using formulas (3.8), (3.20), (3.12)–(3.14), and (4.2), we obtain from Eq. (3.6) the equations

$$\nabla_\parallel J_{\mathrm{mw}} = -\frac{c}{8\pi^2 B_0 r^2 R}$$

$$\times\left\{m\left[\frac{\partial}{\partial\xi}(Q\sqrt{g}\hat{B}^2)^{(0)}\right]_x - \left[Q\frac{\partial}{\partial\theta}(\sqrt{g}\hat{B}^2)\right]^{(0)}\right\} \tag{4.3}$$

$$-c\left\langle \nabla p\cdot\left[\nabla\times\frac{\mathbf{B}}{\mathbf{B}^2}\right]\right\rangle_\theta,$$

$$\frac{1}{qR}\left(\frac{\partial\hat{J}_\parallel^{(1)}}{\partial\theta}\right)_\xi = -c\frac{\partial\hat{p}^{(0)}}{\partial x}\left(\left[\nabla\times\frac{\mathbf{B}}{\mathbf{B}^2}\right]^1\right)^{(1)}. \tag{4.4}$$

Here, the superscript "1" indicates the first contravariant component of the vector, the function $\hat{p}^{(0)}$ is introduced through the relationship (cf. relationship (3.17))

$$\hat{p}^{(0)}(x,\xi) = \tilde{p}^{(0)}(x,\xi) + xp_0', \tag{4.5}$$

and the symbol $\langle\ldots\rangle_\theta$ denotes averaging over the variable θ at a fixed value of the variable ξ.

In order to understand the physical meaning of the first term on the right-hand side of Eq. (4.3), it is expedient to turn to Eqs. (17) and (19) from [26]. Taking into account the relationship

$$\left(\left[\nabla\times\frac{\mathbf{B}_0}{\mathbf{B}_0^2}\right]^1\right)^{(1)} = \frac{1}{Rr^2B_T}\frac{\partial\sqrt{g}^{(1)}}{\partial\theta}, \tag{4.6}$$

we can reduce Eq. (4.4) to

$$\tilde{J}_\parallel^{(1)} = -\frac{c}{rRB_p}\frac{\partial\hat{p}^{(0)}}{\partial x}\sqrt{g}^{(1)}. \tag{4.7}$$

In the large-aspect-ratio approximation, Ampère's law gives

$$\hat{J}_\parallel^{(1)} = \frac{c}{4\pi r}\left(N\sqrt{g}\frac{\partial\hat{B}^2}{\partial x}\right)^{(1)}, \tag{4.8}$$

where $N \equiv g_{22}/\sqrt{g}$, with g_{22} the corresponding element of the metric tensor. We integrate Eq. (4.7) over x to obtain the equation (cf. Eq. (18) in [26])

$$(N\sqrt{g}\hat{B}^2)^{(1)} + \frac{4\pi}{RB_p}\hat{p}^{(0)}\sqrt{g}^{(1)} = 0, \tag{4.9}$$

in which the constant of integration is set equal to zero.

Note that the θ-dependence of the determinant of the metric tensor, $\sqrt{g}$, on the right-hand side of Eq. (4.6) is a consequence of the *geodesic curvature*. Accordingly, the current $\hat{J}_\parallel^{(1)}$, defined by Eq. (4.7), can be interpreted as the *geodesic component* of the island-related current.

Using Eq. (4.6), we convert the second term on the right-hand side of Eq. (4.3) into the form (see Eqs. (7.7) and (7.14) in [8])

$$\left\langle \nabla p\cdot\left[\nabla\times\frac{\mathbf{B}}{\mathbf{B}^2}\right]\right\rangle_\theta = m\left(\frac{\partial\hat{p}^{(0)}}{\partial\xi}\right)_x\left\langle\left[\nabla\times\frac{\mathbf{B}_0}{\mathbf{B}_0^2}\right]^2\right\rangle_\theta$$

$$+ p_0'\left\langle\left[\nabla\times\left(\frac{\tilde{\mathbf{B}}}{\mathbf{B}_0^2} - \frac{2\mathbf{B}_0\cdot\tilde{\mathbf{B}}}{\mathbf{B}_0^4}\mathbf{B}_0\right)\right]^1\right\rangle_\theta \tag{4.10}$$

$$+ \frac{1}{Rr^2B_T}\left\langle\frac{\partial\tilde{p}^{(1)}}{\partial x}\frac{\partial\sqrt{g}}{\partial\theta}\right\rangle_\theta.$$

The first term on the right-hand side of this equation describes the vacuum magnetic well and its deepening due to the plasma diamagnetism (cf. Eq. (7.41) in [8]). The second term accounts for the effect that competes with the effect responsible for this deepening in a plane geometry approximation, i.e., one that is described by the last term on the right-hand side of Eq. (7.41) in [8]. This competing effect is associated with the *poloidal magnetic field perturbation* by virtue of the balance equation for the perturbed pressures (see Eq. (7.19) in [8]). Finally, the last term on the right-hand side of Eq. (4.10) is the contribution of the geodesic curvature.

The second term on the right-hand side of Eq. (4.10) is transformed in the same manner as in Subsection 7.1 of [8]. Equation (4.3) then reduces to the following (cf. Eq. (12) in [13]):

$$k_\parallel\left(\frac{\partial J_{\mathrm{mw}}}{\partial\xi}\right)_\psi = -\frac{cw'}{B_0^3 r}m\left(\frac{\partial\hat{p}^{(0)}}{\partial\xi}\right)_\theta - \frac{c}{8\pi^2 B_0 r^2 R}$$

$$\times\left\{m\left[\frac{\partial}{\partial\xi}(Q\sqrt{g}\hat{B}^2)^{(0)}\right]_x - \left[Q\frac{\partial}{\partial\theta}(\sqrt{g}\hat{B}^2)\right]^{(0)}\right\} \tag{4.11}$$

$$-\frac{c}{Rr^2B_T}\left\langle\frac{\partial\hat{p}^{(1)}}{\partial x}\frac{\partial\sqrt{g}}{\partial\theta}\right\rangle_\theta,$$

where the function w' is defined by the relationship

$$w' \equiv \frac{d}{dr}\langle \mathbf{B}_0^2 + 8\pi p_0 \rangle_\theta. \tag{4.12}$$

In the large-aspect-ratio approximation, Eqs. (7.65)–(7.70) in [8] yield the following relationship between the function w' and the function $W^{(0)}$ in formula (2.25):

$$w' = -\frac{r_s B_0^4}{p_0' R} W^{(0)}. \tag{4.13}$$

Equation (4.11) is similar in structure to Eq. (65) from [26].

We now turn to expression (4.8). The θ-independent component of this expression gives

$$\left(\frac{\partial \hat{p}^{(1)}}{\partial \theta}\right)_\xi = -\frac{r_s p_0'}{B_p}\tilde{B}_x^{(1)}. \tag{4.14}$$

In the large-aspect-ratio approximation, we obtain from Maxwell's equation (3.27) the equation

$$\frac{\partial \tilde{B}_x^{(1)}}{\partial x} = -\left(\frac{\partial \hat{B}^{2(1)}}{\partial \theta}\right)_\xi. \tag{4.15}$$

This equation, together with Eq. (4.14), gives

$$\frac{\partial \hat{p}^{(1)}}{\partial x} = \frac{r_s p_0'}{B_p}\hat{B}^{2(1)}. \tag{4.16}$$

Using relationship (4.13) and Eq. (4.16), we convert Eq. (4.11) into the form

$$k_\parallel\left(\frac{\partial J_{\mathrm{mw}}}{\partial \xi}\right)_\psi = \frac{cm}{R}\left(\frac{B_0}{p_0'}W^{(0)}\left(\frac{\partial \hat{p}^{(0)}}{\partial \xi}\right)_x - \frac{1}{8\pi^2 B_0 r^2}\frac{\partial}{\partial \xi}[(\hat{B}^2\sqrt{g}Q)^{(0)}]_x\right). \tag{4.17}$$

We now turn to the θ-independent component of Eq. (3.25). Using expression (3.8), we reduce this component to the equation (cf. Eq. (4.11))

$$\left[\frac{\partial \hat{p}^{(0)}(x,\xi)}{\partial \xi}\right]_\psi = 0, \tag{4.18}$$

which gives

$$\hat{p}^{(0)}(x,\xi) = \hat{p}^{(0)}(\psi), \tag{4.19}$$

where $\hat{p}^{(0)}(\psi)$ is an arbitrary function of the magnetic flux function of the magnetic islands, ψ, defined by relationship (3.1). It is supposed that this arbitrary function can be determined with the help of the transport equation averaged over the magnetic surfaces of an island (see Subsection 4.3 for details).

4.2. Magnetic Field of the Islands and Its Contribution to the Magnetic-Well-Related Current

4.2.1. Calculation of the magnetic field of the islands. Applying the approach developed in [26], we arrive at the following solution to Eq. (4.9):

$$\sqrt{g}\hat{B}^2 = \frac{1}{N}\left\{\frac{(\sqrt{g}\hat{B}^2)^{(0)}}{(1/N)^{(0)}} + \frac{4\pi\hat{p}^{(0)}}{RB_p}\left[\frac{(\sqrt{g}/N)^{(0)}}{(1/N)^{(0)}} - \sqrt{g}\right]\right\}, \tag{4.20}$$

where the quantity $(\sqrt{g}\hat{B}^2)^{(0)}$ is given by formula (3.20) and is thus the θ-independent component of the magnetic field of the islands. According to solution (4.20), the θ-dependent component of the magnetic field of the islands is related to the geodesic curvature.

4.2.2. Magnetic-well-related current in terms of the θ-independent plasma pressure component. Using solution (4.20) and the first of relationships (3.20) and averaging the right-hand side of Eq. (4.17) over θ, we obtain

$$(\hat{B}^2\sqrt{g}Q)^{(0)} = \left(\frac{\partial \psi}{\partial x}\right)_\xi \frac{(Q/N)^{(0)}}{(1/N)^{(0)}} + \frac{4\pi\hat{p}^{(0)}}{RB_p}\left[\frac{(Q/N)^{(0)}(\sqrt{g}/N)^{(0)}}{(1/N)^{(0)}} - \left(\frac{Q\sqrt{g}}{N}\right)^{(0)}\right]. \tag{4.21}$$

According to the second of relationships (3.20) expressed in terms of the variables (x, ξ), the first term on the right-hand side of relationship (4.21) is independent of ξ and, consequently, does not contribute to Eq. (4.17).

Using formula (4.2), we represent the determinant of the metric tensor as

$$\sqrt{g} = \sqrt{g}^{(0)} - \frac{RB_p}{8\pi^2 p_0'}Q. \tag{4.22}$$

The expression in the square brackets of relationship (4.21) then reduces to

$$\frac{(Q/N)^{(0)}(\sqrt{g}/N)^{(0)}}{(1/N)^{(0)}} - \left(\frac{Q\sqrt{g}}{N}\right)^{(0)} = \frac{RB_p}{8\pi^2 p_0'}\left\{\left(\frac{Q^2}{N}\right)^{(0)} - \frac{[(Q/N)^{(0)}]^2}{(1/N)^{(0)}}\right\}. \tag{4.23}$$

With the help of Eqs. (2.47) in [8], we express the terms on the right-hand side of relationship (4.23) through the parameters A_0, A_1, and A_2 introduced in relationship (A.1) (it is these parameters that were discussed in Subsection 2.1; see, e.g., relationship (2.4)):

$$(1/N)^{(0)} = A_0, \tag{4.24}$$

$$(Q/N)^{(0)} = 2\pi r B_0 A_1, \tag{4.25}$$

$$(Q^2/N)^{(0)} = (2\pi r B_0)^2 A_2. \tag{4.26}$$

As a result, Eq. (4.17) takes the form (cf. relationship (2.4))

$$k_\parallel\left(\frac{\partial J_{\rm mw}}{\partial \xi}\right)_\psi = \frac{cmB_0}{Rp_0'}\left(\frac{\partial \hat{p}^{(0)}}{\partial \xi}\right)_x\left[W^{(0)} - \frac{1}{4\pi}\left(A_2 - \frac{A_1^2}{A_0}\right)\right]. \tag{4.27}$$

We now turn to formula (2.25). As in [7, 8] (and in many other papers on linear theory), the factor $1/4\pi$ in this formula is omitted for convenience. Consequently, in order to compare the right-hand sides of Eq. (4.27) and of formula (2.25), we must also omit this factor in the equation. We thus obtain

$$W^{(0)} - \left(A_2 - \frac{A_1^2}{A_0}\right) = \frac{q'^2}{q^4 A_0} U_{\rm MI}, \tag{4.28}$$

where the parameter $U_{\rm MI}$ is defined by expression (2.31). As a result, Eq. (4.27) becomes

$$k_\parallel\left(\frac{\partial J_{\rm mw}}{\partial \xi}\right)_\psi = \frac{cmB_0}{Rp_0'}\left(\frac{\partial \hat{p}^{(0)}}{\partial \xi}\right)_x \frac{q'^2}{q^4 A_0} U_{\rm MI}. \tag{4.29}$$

We can see that the magnetic-well-related current is proportional to the parameter $U_{\rm MI}$, which justifies the use of the term *magnetic well of the magnetic islands* for this parameter.

4.3. Contribution of the Magnetic Well Effect to the Generalized Rutherford Equation

According to relationships (3.10) and (3.1), the longitudinal wavenumber in terms of the (ψ, ξ) variables has the form

$$k_\parallel = -\frac{\sigma_x k_y w}{\sqrt{2} L_s}(\Omega + \cos\xi)^{1/2}. \tag{4.30}$$

Then, for a circular tokamak or for a slightly noncircular tokamak such that $A_0 = R/r$ (see Eq. (8.1) in [8]), Eq. (4.29) reduces to

$$\left(\frac{\partial J_{\rm mw}}{\partial \xi}\right)_\Omega = -\frac{\sigma_x csB_0 U_{\rm MI}}{2^{3/2}\pi p_0' qRw(\Omega + \cos\xi)^{1/2}}\left(\frac{\partial \hat{p}^{(0)}}{\partial \xi}\right)_x. \tag{4.31}$$

Taking into account the relationship

$$\left(\frac{\partial \hat{p}^{(0)}}{\partial \xi}\right)_x = \sin\xi \frac{\partial \hat{p}^{(0)}(\Omega)}{\partial \Omega}, \tag{4.32}$$

which follows from solution (4.20) and relationship (3.1), we obtain from Eq. (4.31) the equation

$$\left(\frac{\partial J_{\rm mw}}{\partial \xi}\right)_\Omega = -\frac{\sigma_x csB_0 U_{\rm MI}}{2^{3/2}\pi p_0' qRw}\frac{\partial \hat{p}^{(0)}(\Omega)}{\partial \Omega}\frac{\sin\xi}{(\Omega + \cos\xi)^{1/2}}. \tag{4.33}$$

We integrate Eq. (4.33) over ξ at constant ψ to obtain the following equation, which is analogous to Eq. (17) in [13]:

$$J_{\rm mw} = \frac{\sigma_x csB_0 U_{\rm MI}}{\sqrt{2}\pi p_0' qRw} \times [(\Omega + \cos\xi)^{1/2} - \langle(\Omega + \cos\xi)^{1/2}\rangle]\frac{\partial \hat{p}^{(0)}(\Omega)}{\partial \Omega}, \tag{4.34}$$

where the angle brackets stand for averaging over the magnetic surface of an island (see [27, 28] for details).

Substituting Eq. (4.34) into expression (3.5) gives

$$\Delta_{\rm mw} = \frac{2U_{\rm MI}}{\pi p_0' w^2}\sum_{\sigma_x}\sigma_x \int_{-1}^{\infty} d\Omega \frac{\partial \hat{p}^{(0)}}{\partial \Omega} \times \langle(\Omega + \cos\xi)^{1/2}\rangle \int \frac{\cos\xi d\xi}{(\Omega + \cos\xi)^{1/2}}. \tag{4.35}$$

For the Rutherford profile function [25], we have

$$\frac{\partial \hat{p}^{(0)}}{\partial \Omega} = \begin{cases} (\pi/8)\sigma_x w(dp_0/dr)\kappa/E(\kappa), & \Omega > 1, \\ 0, & -1 < \Omega < 1, \end{cases} \tag{4.36}$$

where $E(\kappa)$ is a complete elliptic integral of the second kind and $\kappa = [2/(\Omega + 1)]^{1/2}$. In this case, we integrate Eq. (4.35) over ξ and Ω and obtain

$$\Delta_{\rm mw} = -\frac{2c_{\rm bs}}{w}U_{\rm MI} \equiv -\frac{1.58}{w}U_{\rm MI}, \tag{4.37}$$

where $c_{\rm bs} = 0.79$ is the factor that enters the expression for the contribution of the bootstrap current to Eq. (3.4) and is defined by the relationship [27]

$$c_{\rm bs} = -\frac{1}{4}\int_1^{\infty} d\Omega \frac{\kappa}{E(\kappa)}\langle(\Omega + \cos\xi)^{1/2}\rangle \times \int \frac{\cos\xi d\xi}{(\Omega + \cos\xi)^{1/2}}. \tag{4.38}$$

Equation (4.37) generalizes Eqs. (22) and (23) in [13] to include finite beta effects and magnetic-shear-related effects.

5. ANALYSIS OF THE MAGNETIC WELL OF THE MAGNETIC ISLANDS

5.1. General Properties of the Magnetic Well of the Magnetic Islands

In the case of a circular tokamak or a slightly noncircular tokamak, the second of Eqs. (8.1) in [8] implies that

$$A_1 = 2p_0'\xi_0'/(B_pB_T), \tag{5.1}$$

where ξ_0 is the Shafranov shift, the prime denotes the radial derivative, and $B_T \simeq B_0^{(0)}$ is the mean equilibrium toroidal magnetic field. It is known (see, e.g., Eq. (2.29) in [8]) that the quantity ξ_0' is positive, $\xi_0' > 0$. Therefore, the parameter A_1 is negative, $A_1 < 0$, because $p_0' < 0$. Thus, for standard situations with a positive magnetic shear ($s > 0$), i.e., for $q' > 0$, relationship (5.1) implies that

$$U_{\rm MI} > U_0. \tag{5.2}$$

Hence, in the presence of an ideal magnetic well, i.e., when $U_0 > 0$, the magnetic well has a stabilizing effect on the magnetic islands (cf. Subsection 2.5).

At the same time, according to [7], condition (2.28), which is condition (5.2) with $U_{\rm MI}$ replaced by $U_{\rm R}$, holds only for moderate plasma pressures, whereas, for sufficiently high pressures, condition (2.29), which is opposite to condition (2.28), is satisfied.

5.2. Circular Tokamak at a Low (but Finite) Plasma Pressure

Using formulas (2.4), (2.27), and (2.31) and taking into account the results of [7] and of Subsection 8.1 in [8], we arrive at the following relationships, which are valid for a circular tokamak and for moderate values of the parameter β_p (the ratio of the plasma pressure to the pressure of the poloidal magnetic field), $\beta_p \ll \epsilon^{-2/3}$:

$$U_0 = -\frac{2rp_0'q^2}{s^2B_T^2}\left(1-\frac{1}{q^2}\right), \tag{5.3}$$

$$U_{\rm MI} = U_{\rm R} = -D_{\rm R}$$

$$= -\frac{2rp_0'q^2}{s^2B_T^2}\left(1-\frac{1}{q^2}+\frac{qq'}{r^3}\int_0^r\frac{dr_1r_1^3}{q^2(r_1)}\left[1-\frac{2r_1p'(r_1)}{B_p^2(r_1)}\right]\right). \tag{5.4}$$

In this case, the magnetic well of the magnetic islands coincides with the resistive magnetic well and exceeds the ideal magnetic well, because it takes into account the contribution of magnetic shear (cf. the discussion in Section 2).

The difference between U_0, on the one hand, and $U_{\rm MI}$ and $U_{\rm R}$, on the other, arises from the presence of the parameter $H_{\rm I}$ on the right-hand sides of relationships (2.10) and (2.32) (see also formulas (2.14), (5.1), (A.5)). That $U_{\rm MI}$ and $U_{\rm R}$ coincide follows from the fact that, on the right-hand side of relationship (2.34), the term H^2 (which is small for low plasma pressures) and the term $H_{\rm R}$ (which is small because the problem under consideration contains an "implicit" small parameter) are both ignored.

The expression for $D_{\rm R}$ that is contained in relationships (5.4) was first derived by Glasser *et al.* [12], who pointed out that an equivalent expression was derived in [7]. Let us show that relationships (5.4) can be obtained with the help of Eqs. (5.10) and (5.11) in [7].

5.3. Slightly Noncircular Tokamak at a Moderate Plasma Pressure

As in Subsection 5.2, we use the approximation in which $\beta_p \ll \epsilon^{-2/3}$ but, at the same time, $\beta_p \gg 1$. We assume that the plasma pressure profile is parabolic and that the ellipticity and triangularity of the magnetic surfaces are both small. We characterize the ellipticity and triangularity by the parameters e and τ that were defined in Subsection 2.5 of [8]. Then, using Eq. (8.17) from [8], we obtain

$$U_0 = -\frac{4\beta_pr^2}{s^2R^2}\left(1-\frac{1}{q^2}-\frac{e^2\beta_p}{2}+6e\tau R\right). \tag{5.5}$$

We also arrive at the following relationships, which are analogous to relationships (5.4):

$$U_{\rm MI} = U_{\rm R} = -D_{\rm R} = U_0 + 4\epsilon^2\beta_p^2/s. \tag{5.6}$$

The last term on the right-hand side of relationships (5.6) is quadratic in β_p. This quadratic dependence stems from the fact that, on the one hand, the parameter A_1, which is defined by relationship (5.1), is directly proportional to β_p and, on the other hand, the Shafranov shift at $\beta_p \gg 1$, by virtue of Eq. (A.6), is also directly proportional to β_p (cf. relationships (5.4)).

We can see that, in accordance with general condition (5.2), the magnetic well certainly has a stabilizing effect on the magnetic islands when $U_0 > 0$. At the same time, according to relationship (5.5), the condition $U_0 > 0$ is satisfied only when the effect of the squared ellipticity is more important than the combined effect of the ellipticity and triangularity (see Subsection 8.2 in [8] for details).

Relationships (5.5) and (5.6) may be of interest for analyzing tokamak discharges with optimized magnetic shear. In [13], such an analysis was carried out in the approximation $U_{\rm MI} = U_0$, which, in particular, implies that the squared ellipticity is ignored.

5.4. Second Stability Region of the Ballooning Modes

Although the parameter U_0 in the problem of Mercier modes plays an important role in the plasma stability theory, it characterizes their stability only partially, because the Mercier stability criterion is given by condition (2.24). At the same time, the general theory of ideal MHD modes implies that, in order to achieve good plasma confinement, it is necessary to stabilize not only Mercier modes but also ideal ballooning modes. It is well known (see, e.g., Subsection 8.5 in [8]) that there are two stability regions of the ballooning modes, called the first and second stability regions. The second stability regime seems to be more attractive for fusion reactors because it corresponds to high plasma pressures. That is why it is important to find out whether the magnetic well has a stabilizing or a destabilizing effect on the magnetic islands in the second stability region.

It is well known that the stability boundary of ideal ballooning modes is determined by the equation (see Eq. (8.50) in [8])

$$\left(\frac{\hat{\alpha}}{s}\right)^{1/2}\left(1-\frac{3}{32}\frac{\hat{\alpha}^2}{s}\right)^{1/2} = \frac{1}{2}+\left[\frac{\hat{\alpha}\epsilon}{s^2}\left(1-\frac{1}{q^2}\right)+\frac{1}{4}\left(1+\frac{3}{32}\frac{\hat{\alpha}^4}{s^2}\right)\right]^{1/2}, \quad (5.7)$$

where the parameter $\hat{\alpha}$ is defined by the relationship $\hat{\alpha} \equiv 4\epsilon\beta_p$. (In the literature on ballooning modes, this parameter is, as a rule, denoted by α.) We can see that, in terms of the parameter $\hat{\alpha}$, the quantities U_{MI} and U_{R} are expressed as (cf. Eq. (11.52) in [8])

$$U_{\mathrm{MI}} = \frac{\epsilon\hat{\alpha}}{s^2}\left[1-\frac{1}{q^2}+\frac{\hat{\alpha}}{4\epsilon}\left(s+\frac{3}{32}\hat{\alpha}^2\right)\right], \quad (5.8)$$

$$U_{\mathrm{R}} = \frac{\epsilon\hat{\alpha}}{s^2}\left[1-\frac{1}{q^2}+\frac{\hat{\alpha}}{4\epsilon}\left(s-\frac{5}{32}\hat{\alpha}^2\right)\right], \quad (5.9)$$

while the ideal magnetic well has the form (see Eq. (8.33) in [8])

$$U_0 = \frac{\epsilon\hat{\alpha}}{s^2}\left(1-\frac{1}{q^2}+\frac{3}{128}\frac{\hat{\alpha}^3}{\epsilon}\right). \quad (5.10)$$

In contrast to relationships (5.4) and (5.6), which indicate that the parameters U_{MI} and U_{R} coincide, relationships (5.8) and (5.9) imply that these parameters are different. This difference, which arises because the right-hand side of relationship (2.34) contains the term with H^2, manifests itself in the terms that are on the order of β_p^4, because, according to the aforesaid, we have $H \sim \beta_p^2$ for $\beta_p \gg 1$. Hence, in order for the terms proportional to β_p^4 in relationships (5.8)–(5.10) to be calculated correctly, it is necessary to use the quantity ξ_0' given by an expression in the form of (A.7).

From Eq. (5.7), it is clear that, in the "lower part" of the second stability region, i.e., for

$$\hat{\alpha} \simeq \epsilon^{1/3} \quad (\beta_p \simeq \epsilon^{-2/3}), \quad (5.11)$$

$$s \simeq \epsilon^{2/3}, \quad (5.12)$$

the terms with $\hat{\alpha}^2$ in the square brackets on the right-hand sides of relationships (5.8) and (5.9) should be regarded as being of the same order as s. In this case, we can see that, in the second stability region of the ballooning modes, the magnetic well has a stabilizing effect on magnetic islands, whereas the linear resistive interchange modes in this region are unstable.

6. DISCUSSION OF THE DISTINCTIVE FEATURES OF DIFFERENT MAGNETIC WELLS

6.1. Why Does the Magnetic Well of the Magnetic Islands Differ from the Ideal Magnetic Well?

According to linear theory, Mercier modes are described by the equation (see, e.g., Eq. (7.59) in [8])

$$x\frac{\partial^2}{\partial x^2}(x\Xi) - U_0\Xi = 0, \quad (6.1)$$

where the function $\Xi = \Xi(x)$ is related to the θ-averaged component of the perturbed plasma displacement $\tilde{X}^{(0)}(x, \xi)$ by the relationship

$$\tilde{X}^{(0)}(x, \xi) = \Xi(x)\cos\xi. \quad (6.2)$$

On the one hand, using expression (2.31), we find that the right-hand side of Eq. (4.29) contains the difference $U_0 - q^2A_1/q'$. This raises the question of why the term with A_1 "disappears" when switching from nonlinear to linear theory.

To answer this question, we turn to solution (4.20). We can see that, in a linear problem, the analogue to this solution has the form

$$\sqrt{g}\tilde{B}^2 = \frac{1}{N}\left\{\frac{(\sqrt{g}\tilde{B}^2)^{(0)}}{A_0}+\frac{4\pi\tilde{p}^{(0)}}{RB_p}\left[\frac{(\sqrt{g}/N)^{(0)}}{A_0}-\sqrt{g}\right]\right\}. \quad (6.3)$$

The perturbed plasma pressure $\tilde{p}^{(0)}$ is given by the familiar relationship $\tilde{p}^{(0)} = -p_0'\tilde{X}^{(0)}$ (see, e.g., Eq. (7.6) in [8]), which, by virtue of relationship (6.2), takes the form

$$\tilde{p} = -\Xi p_0'\cos\xi. \quad (6.4)$$

In this case, Eq. (4.17) yields the following linear analogue of Eq. (4.29):

$$k_\parallel \tilde{J}_{\rm mw} = \frac{mB_0}{A_0 R}\left[\tilde{p}^{(0)}\frac{U_{\rm MI}}{p_0'} - \frac{q^4 A_1}{q'^2 B_0}(\sqrt{g}\tilde{B}^2)^{(0)}\right]. \quad (6.5)$$

From Eq. (3.26) we obtain the equation

$$m\frac{\partial}{\partial\xi}(\sqrt{g}\tilde{B}^2)^{(0)} = -\frac{\partial}{\partial x}(\sqrt{g}\tilde{B}^1)^{(0)}. \quad (6.6)$$

Using Eq. (7.16) from [8] and relationship (6.2) for $\tilde{X}^{(0)}$, we arrive at the relationship

$$(\sqrt{g}\tilde{B}^1)^{(0)} = mB_0\frac{q'}{q^2}x\Xi\sin\xi. \quad (6.7)$$

Equation (6.6) then reduces to

$$(\sqrt{g}\tilde{B}^2)^{(0)} = \frac{q'}{q^2}B_0\frac{\partial}{\partial x}(x\Xi)\cos\xi. \quad (6.8)$$

Substituting relationship (6.4) and Eq. (6.8) into Eq. (6.5) gives

$$k_\parallel \tilde{J}_\parallel^{(0)} = -\frac{mB_0}{A_0 R}\left[U_{\rm MI}\Xi + \frac{q^2 A_1}{q'}\frac{\partial}{\partial x}(x\Xi)\right]. \quad (6.9)$$

Here, we have redesignated $J_{\rm mw}$ as $\tilde{J}_\parallel^{(0)}$. For linear modes, the current $\tilde{J}_\parallel^{(0)}$ should be calculated with the help of Eqs. (84) and (88) from [26]:

$$k_\parallel \tilde{J}_\parallel^{(0)} = -\frac{mB_0 x\cos\xi}{A_0 R}\left[\frac{\partial^2}{\partial x^2}(x\Xi) + \frac{q^2 A_1}{q'}\frac{\partial\Xi}{\partial x}\right]. \quad (6.10)$$

Inserting relationship (6.10) into relationship (6.9), we arrive at Eq. (6.1).

Hence, the fact that the magnetic well of the magnetic islands passes over to the ideal magnetic well, $U_{\rm MI} \longrightarrow U_0$, when switching from nonlinear equation (4.29) to linear equation (6.1) is explained by the following: the incorporation of the derivative $(\partial\psi/\partial x)_\xi$ on the right-hand side of relationship (4.21) and the presence of the term proportional to $\partial\Xi/\partial x$ in relationship (6.10) for the θ-averaged longitudinal current $\tilde{J}_\parallel^{(0)}$.

On the other hand, in investigations on the linear theory of ideal modes, the question naturally arises: why does the transition from linear to nonlinear theory require the replacement $U_0 \longrightarrow U_{\rm MI}$? The answer is as follows: According to relationships (3.20), in linear theory, the θ-averaged part of the perturbed function $\sqrt{g}\tilde{B}^2$ (i.e., of the *perturbed poloidal magnetic field*) is zero,

$$(\sqrt{g}\tilde{B}^2)^{(0)} = 0, \quad (6.11)$$

while in nonlinear theory, this is not the case, $(\sqrt{g}\tilde{B}^2)^{(0)} \neq 0$.

6.2. Procedure for Passing to Zero Resistivity in the Glasser–Greene–Johnson Approach

Formulas (2.13), (2.15), (2.18), and (2.20) imply that, in order to pass to the ideal limit in the GGJ approach, it is necessary to calculate two parameters that depend essentially on resistivity, namely, the parameters H and E. This is a consequence of the resistive ordering approach adopted in [4]. Hence, the resistive ordering approach necessitates the use of a set of equations for the perturbed functions that are strongly dependent on resistivity (see Eqs. (9)–(12) in [4]). In terms of these equations, the ideal limit cannot be taken simply by omitting certain terms in them. Instead, it is necessary to take into account the products of the factors that formally tend to zero and those that formally tend to infinity; in Subsection 2.2, this was characterized as the procedure for resolving singularities of the 0/0 type. We now describe this procedure in more detail.

We restrict ourselves to the "infinite-$G_{\rm GGJ}$" approximation, $G_{\rm GGJ} \longrightarrow \infty$, where $G_{\rm GGJ}$ is the GGJ parameter defined by Eq. (13) from [4] (in that paper, the parameter $G_{\rm GGJ}$ is denoted by G). This approximation is valid if the adiabatic index in the parameter in question is equal to zero (which corresponds to the incompressible plasma approximation) or if the plasma pressure is assumed to be low in comparison to the magnetic field pressure. For $G_{\rm GGJ} \longrightarrow \infty$, Eq. (11) from [4] gives

$$\Upsilon = \Xi, \quad (6.12)$$

where Υ and Ξ are the parameters used in [4].

In this case, Eqs. (9), (10), and (12) from [4] reduce to

$$\Psi_{XX} - H\Xi = Q_{\rm GGJ}(\Psi - X\Xi), \quad (6.13)$$

$$Q_{\rm GGJ}^2\Xi_{XX} - Q_{\rm GGJ}X^2\Xi + E\Xi + Q_{\rm GGJ}X\Psi + \Gamma = 0, \quad (6.14)$$

$$\Gamma_X = H\Psi_{XX} + F\Xi X. \quad (6.15)$$

Here, Ψ and Γ are the variables used in [4] and the quantities $Q_{\rm GGJ}$ and X, which characterize the growth rate γ and the deviation $\hat{V} = V - V_0$ from the singular magnetic surface V_0, are defined by the relationships

$$Q_{\rm GGJ} = \gamma/Q_0, \quad (6.16)$$

$$X = \hat{V}/X_0, \quad (6.17)$$

where the expressions for Q_0 and X_0 are given by Eqs. (14) in [4]. An important point for our analysis is that, as the resistivity tends to zero, the parameters Q_0 and X_0 both tend to zero, so that the quantities $Q_{\rm GGJ}$ and X both tend to infinity. Note that the variable Ψ is also normalized to a resistivity-depended factor. Conse-

quently, to within a resistivity-independent factor, we can write

$$\Psi \sim \tilde{B}^{1(0)}/X_0, \tag{6.18}$$

where $\tilde{B}^1 \equiv \tilde{\mathbf{B}} \cdot \nabla V$ is the contravariant "radial" component of the perturbed magnetic field $\tilde{\mathbf{B}}$. We add the subscript GGJ to the quantity Q in order to distinguish it from the function Q, which was introduced through relationship (4.2). Recall that, in [4], the parameter Q_{GGJ} is denoted by Q.

To begin the procedure for passing to zero resistivity, we simplify Eq. (6.13) to

$$\frac{\tilde{B}^{1(0)}}{i\alpha\Lambda} - \hat{V}\Xi = \frac{\beta\langle\mathbf{B}^2\rangle}{\gamma\langle\langle\mathbf{B}^2\rangle/|\nabla V|^2\rangle}\left[\frac{d^2}{d\hat{V}^2}(\hat{V}\Xi) - H\frac{d\Xi}{d\hat{V}}\right], \tag{6.19}$$

where α and Λ are the quantities introduced in [4]. Simultaneously, Eqs. (6.14) and (6.15) transform into the equations

$$E\Xi + \Gamma + \hat{V}\frac{\gamma\langle\langle\mathbf{B}^2\rangle/|\nabla V|^2\rangle}{\eta\langle\mathbf{B}^2\rangle}\left(\frac{\tilde{B}^{1(0)}}{i\alpha\Lambda} - \hat{V}\Xi\right) = 0, \tag{6.20}$$

$$\Gamma = F\Xi + \frac{H}{i\alpha\Lambda}\frac{d\tilde{B}^{1(0)}}{d\hat{V}}. \tag{6.21}$$

According to relationship (6.18), it is in Eq. (6.19) that we deal with a singularity of the 0/0 type.

Using relationship (6.18) and Eq. (6.20), we convert Eq. (6.19) into the form

$$\hat{V}\frac{d^2}{d\hat{V}^2}(\hat{V}\Xi) - (E + F + H)\Xi = 0. \tag{6.22}$$

A comparison of Eq. (6.22) with Eq. (6.1) shows that they are identical provided that U_0 is given by relationship (2.3). It is precisely relationship (2.3) that follows from the first of Eqs. (16) from [4].

On the other hand, the parameter U_0 is determined by relationship (2.22), whose right-hand side does not contain the resistive parts of the parameters E and H. This indicates that, generally, it would be inconvenient to use the approach developed in [4] to take the zero resistivity limit. Thus, special care is needed in describing ideal phenomena in terms of the GGJ parameters E and H.

6.3. Derivation of the Expression for the Parameter D_R

The sought expression for the parameter D_{R} can be derived based on the analysis carried out in [7]. In doing so, it is necessary to ignore the polarization current effect, i.e., to ignore the terms with the square of the growth rate γ, multiplied by the θ-independent component of the perturbed radial plasma displacement. As a result, we arrive at the following reduced version of Eq. (4.11) from [7]:

$$\frac{\partial}{\partial k_x}\left[\frac{k_x^2}{1 + k_x^2 C_0/(k_{\mathrm{R}}^2 A_0)}\frac{\partial\Xi_k}{\partial k_x}\right] - U_1\Xi_k - \Delta = 0. \tag{6.23}$$

Here, the functions U_1 and Δ are defined by the relationships

$$U_1 = \frac{q^4}{q'^2}A_0\left\{W^{(0)} + k_x^2(Q_x^*\alpha_0^{1(2)})^{(0)} + k_x^2\frac{[(Q_x^*\alpha_0^{(1)})^{(0)}]^2}{Q_x^{*(0)}} + \frac{q'}{q^2}\frac{\partial}{\partial k_x}\left[k_x\frac{(Q_x^*\alpha_0^{(1)})^{(0)}}{Q_x^{*(0)}}\right]\right\}, \tag{6.24}$$

$$\Delta = \frac{q^3}{q'^2}\frac{k_x A_0}{m p_0'}\left(\alpha_0^{(1)}\frac{\partial\delta\tilde{p}_k^{(1)}}{\partial\theta}\right)^{(0)}, \tag{6.25}$$

where the function Q_x^* is defined by

$$Q_x^* = \left(\frac{2\pi}{\Phi'}\right)^2\frac{\sqrt{2}\mathbf{B}_0^2}{g^{11}}\left(\frac{1}{k_x^2} + \frac{g^{11}}{k_{\mathrm{R}}^2}\right), \tag{6.26}$$

with $g^{11} = |\nabla x^1|^2$. We see that the function Q_x^* can be represented in the form (cf. Eq. (4.7) in [7] and Eq. (11.4) in [8])

$$Q_x^* = DQ_x, \tag{6.27}$$

where

$$D = 1 + g^{11}k_x^2/k_{\mathrm{R}}^2, \tag{6.28}$$

$$Q_x = \left(\frac{2\pi}{\Phi'}\right)^2\frac{\sqrt{g}\mathbf{B}_0^2}{k_x^2 g^{11}}. \tag{6.29}$$

Equation (6.23) is written in terms of Fourier representation in the x coordinate, so that the variable k_x is the same as that in relationship (2.5). The quantity k_{R} is defined by relationship (2.6). The subscript k on the perturbed quantities indicates the harmonic in the Fourier representation of the corresponding function in the x coordinate. It is assumed that each perturbed function depends on the variable ξ introduced by expression (3.2) with the replacement $\omega \longrightarrow i\gamma$, so that the dependence has the form $\exp(i\xi)$. The function $\alpha^{(0)}$ is the equilibrium part of the function α introduced by Eq. (3.4) from [7].

The function $\delta\tilde{p}_k^{(1)}$ is the Fourier harmonic of the θ-dependent component of the perturbed plasma pressure. The meaning of this function will be clarified

below. At this point, we note only that, for the one-fluid equation of motion (3.23), it is identically zero,

$$\delta\tilde{p}_k^{(1)} \equiv 0. \tag{6.30}$$

In this case, instead of relationship (2.5) for the function U, we arrive at the relationship

$$U = U_1. \tag{6.31}$$

On the other hand, according to Subsection 2.1, relationship (2.5) in the limit of high resistivity, $k_R/k_x \longrightarrow 0$, leads to expression (2.9). In other words, in this limit, we have $U = -D_R$, in accordance with relationship (2.11). However, we can be assured that relationship (6.31) does not lead to expression (2.9).

In [3], as well as in [11], the one-fluid equation of motion (3.23) was used. However, as was pointed out in Subsection 2.3, a correct procedure based on this equation cannot lead to the conclusion that the magnetic curvature effect is characterized by the parameter D_R. This result of our analysis by no means lessens the value of [3], because that paper does not yield the above conclusion, which is, however, the main result of [11]; the latter paper therefore appears to be erroneous.

The quantity D_R is calculated in Appendix B. The calculations yield

$$\Delta = U_2\Xi_k, \tag{6.32}$$

where

$$U_2 = \frac{q^4A_0}{q'^2}k_x^2\left\{[\alpha_0^{(1)2}(Q_x^* - Q_x)]^{(0)}\right.$$
$$-\frac{(\alpha_0^{(1)}Q_x^*)^{(0)}}{Q_x^{*(0)}}[\alpha_0^{(1)}(Q_x^* - Q_x)]^{(0)} \tag{6.33}$$
$$\left.+\frac{(\alpha_0^{(1)}\mathbf{B}_0^2\sqrt{g})^{(0)}}{(\mathbf{B}_0^2\sqrt{g})^{(0)}}\left[(\alpha_0^{(1)}Q_x)^{(0)} - \frac{Q_x^{(0)}}{Q_x^{*(0)}}(\alpha_0^{(1)}Q_x^*)^{(0)}\right]\right\}.$$

Using relationships (6.24) and (6.33), we find

$$U = U_1 + U_2, \tag{6.34}$$

where the parameter U is given by relationship (2.5). According to relationships (2.9) and (2.11), the resistive limit of the function U is nothing more than $-D_R$. We thus have shown that the resistive curvature effect can be described in terms of the parameter D_R provided that plasma compressibility is taken into account.

7. CONCLUSIONS

We have analyzed the status of the existing theory of the effect of the magnetic curvature on magnetic islands. The primary objective of such a theory is to construct a criterion for determining whether the magnetic curvature has a stabilizing or a destabilizing effect. The criterion is formulated in terms of the sign of the GGJ parameter D_R, and the conclusion is drawn that, at $D_R < 0$, the magnetic curvature has a stabilizing effect, while, at $D_R > 0$, the effect is destabilizing. Since the existing theory uses the parameter D_R as a reference point for determining the stabilization conditions, we have called it *the D_R trend in the theory of magnetic islands*.

We have demonstrated that the D_R trend is erroneous and have developed a correct theory of the effect of the magnetic curvature on magnetic islands. We have pointed out that, although the results obtained in the D_R trend can be valid under certain particular conditions, there may be equilibrium conditions for which this trend yields wrong results. An example of such erroneous results obtained with the D_R trend is given in Subsection 5.4, in which the magnetic curvature effect has been analyzed in the second stability region of the ideal ballooning modes. In particular, we have shown that, according to the correct theory developed here, the magnetic curvature exerts a stabilizing effect on magnetic islands, whereas the D_R trend predicts a destabilizing effect.

ACKNOWLEDGMENTS

This work was supported in part by the Russian Foundation for Basic Research (project no. 03-02-16294), the Russian Federal Program for State Support of Leading Scientific Schools (project no. 2024.2003.2), the Department of Atomic Science and Technology of the RF Ministry of Atomic Industry, the U.S. Civilian Research and Development Foundation for the Independent States of the Former Soviet Union (CRDF) (grant no. BRHE REC-011), the National Program of Support for Excellence Groups (PRONEX) of the National Council for Scientific and Technological Development (CNPq), and the State of São Paulo Foundation for the Support of Research (FAPESP) (Brazil).

APPENDIX A

Summary of the Results on the Equilibrium Parameters Used in [5–8]

In [5–8], investigations were carried out in terms of the toroidal and poloidal magnetic flux functions, Φ and χ, respectively, and the radial coordinate $x^1 \equiv a$ in a coordinate system with straightened magnetic field lines. The equilibrium longitudinal electric current density $\mathbf{j}_{0\|} \equiv \mathbf{B}_0(\mathbf{j}_0 \cdot \mathbf{B}_0)/\mathbf{B}_0^2$ was represented as $\mathbf{j}_0 = \alpha_0\mathbf{B}_0/\mathbf{B}_0^2$. The equilibrium plasma states were described in terms of the metric tensor g_{ik} ($i = 1, 2, 3$) with the determinant g in the coordinates ($x^2 = \theta$, $x^3 = \zeta$), where θ and ζ are the poloidal and toroidal 2π-periodic angular variables. Along with the metric tensor g_{ik}, the inverse metric tensor g^{ik} was also used.

The parameters A_n ($n = 0, 1, 2$) and C_n ($n = 0, 1$) were determined by the relationships

$$A_n = \left(\frac{2\pi}{\Phi'}\right)^2\left(\alpha_0^{(1)n}\frac{\sqrt{g}\mathbf{B}_0^2}{g^{11}}\right)^{(0)}, \quad (A.1)$$

$$C_n = \left(\frac{2\pi}{\Phi'}\right)^2(\alpha_0^{(1)n}\sqrt{g}\mathbf{B}_0^2)^{(0)}. \quad (A.2)$$

Here, the prime denotes the derivative with respect to x^1, α_0^1 is the θ-dependent part of the function α_0 (i.e., the part of α_0 that oscillates in θ) given by the relationship

$$\alpha_0^{(1)} = \alpha_0 - \alpha_0^{(0)}, \quad (A.3)$$

and the superscript (0) indicates averaging over θ. The function $W^{(0)}$ used in [5–8] was defined by the relationship

$$W^{(0)} = \frac{1}{\Phi'^2}(p_0'V'' + J'\chi'' - I'\Phi'') + \frac{q'}{q^2}\alpha_0^{(0)} - \left(\frac{2\pi p_0'}{\Phi'}\right)^2\left(\frac{\sqrt{g}}{\mathbf{B}_0^2}\right)^{(0)}, \quad (A.4)$$

where J and I are the toroidal and poloidal current flux functions, respectively, and V is the volume of a torus with the minor radius x^1.

Equations (A.1) are identical to those in the first rows of Eqs. (4.20) in [7] and of Eqs. (7.61) in [8]. Equations (A.2) reproduce the equations in the second row of the set of equations in [7] and Eqs. (11.24) in [8]. Equation (A.4) is Eq. (3.2) from [5], or Eq. (3.7) from [7], or Eq. (7.41) from [8]. Note that Eq. (7.41) from [8] contains two misprints: the plus sign in front of the last term on the right-hand side of the equality should be replaced by the minus sign and the prime should be added to μ.

Turning to relationship (2.32) or (2.34), we can see that the main difference among the parameters U_{MI}, U_0, and U_{R} is their relationship to the parameter H_{I}. For a circular tokamak or for a slightly noncircular tokamak, this parameter is determined by the parameter A_1 given in relationship (5.1). The characteristic feature of the parameter A_1 is that it is proportional to the radial derivative of the Shafranov shift, ξ_0'. For moderate β_p values such that $\beta_p \ll \epsilon^{-2/3}$, Eq. (2.9) in [8] gives the following expression for ξ_0':

$$\xi_0' = \frac{q^2}{Rr^3}\int_0^r \frac{r_1^3}{q^2(r_1)}\left[1 - \frac{2r_1 p_0'(r_1)}{B_p^2(r_1)}\right]dr_1. \quad (A.5)$$

For a low magnetic shear and for a parabolic plasma pressure profile, Eq. (A.5) passes over to Eq. (2.52) in [8], namely,

$$\xi_0' = \epsilon\left(\beta_p + \frac{1}{4}\right). \quad (A.6)$$

Since some terms in the expression for the magnetic well mutually cancel out, corrections on the order of $\epsilon^2\beta_p^2$ on the right-hand side of Eq. (A.6) may be important. Consequently, instead of Eq. (A.6), one must use an equation of the form

$$\xi_0' = \epsilon\left[\beta_p + \frac{1}{4} + O(1)\epsilon^2\beta_p^3\right], \quad (A.7)$$

where $O(1)$ is a factor on the order of unity. The corrections in question can be calculated with the help of Eq. (2.104) in [8]. (Note that the right-hand side of this equation contains a misprint: the quantity α' in front of the second square brackets should be replaced with ξ'.)

APPENDIX B

Contribution of the Plasma Compressibility to the Equation for Linear Resistive Modes

According to the adiabatic equation, we have

$$\tilde{p}_k^{(1)} = -\gamma_0 p_0(\nabla\cdot\boldsymbol{\xi})_k^{(1)}, \quad (B.1)$$

where $\boldsymbol{\xi}$ is the perturbed plasma displacement vector, γ_0 is the adiabatic index, and the subscript k indicates (as in Subsection 6.3) a harmonic in the Fourier representation of a function in the variable x.

The right-hand side of relationship (B.1) contains the perturbed longitudinal plasma displacement, which can be expressed in terms of the function Z given by Eq. (10.7) in [8]:

$$Z = \boldsymbol{\xi}\cdot\mathbf{B}_0/\mathbf{B}_0^2. \quad (B.2)$$

In order to describe this function, it is necessary to generalize the longitudinal component of the one-fluid equation of motion (3.23) to include the *longitudinal inertia*. In this way, instead of Eq. (3.23), we arrive at Eq. (4.12) from [7]:

$$\frac{\partial\delta\tilde{p}^{(1)}}{\partial\theta} = -\frac{2\pi q\sqrt{g}}{\Phi'}[\gamma^2\mathbf{B}_0^2\rho_0 Z - p_0'(\hat{D}-1)\tilde{b}]. \quad (B.3)$$

Here, ρ_0 is the plasma mass density, $\tilde{b} \equiv \tilde{B}^1$, and $\hat{D}$ is the resistivity-depended operator defined by

$$\hat{D} = 1 - \frac{g^{11}}{k_{\mathrm{R}}^2}\frac{\partial^2}{(\partial x^1)^2}, \quad (B.4)$$

where x^1 is the radial coordinate. The Fourier representations of the operator $\hat{D}$ reduces to the function D defined by relationship (6.28).

In analogy with Eq. (4.14) in [7], we obtain from Eq. (B.3) the equation

$$\gamma^2 Z^{(0)} = \frac{p_0'}{\rho_0}\frac{[\sqrt{g}(\hat{D}-1)\tilde{b}]^{(0)}}{(\sqrt{g}\mathbf{B}_0^2)^{(0)}}, \qquad \text{(B.5)}$$

which differs from Eq. (4.14) in [7] in that its right-hand side does not contain the term with γ^2. This term is omitted because the polarization current effect is ignored.

Using Eq. (B.5), we convert Eq. (B.3) into the form

$$\frac{\partial \delta\tilde{p}^{(1)}}{\partial\theta} = -\frac{2\pi q p_0'\sqrt{g}}{\Phi'}\left[\mathbf{B}_0^2\frac{[\sqrt{g}(\hat{D}-1)\tilde{b}]^{(0)}}{(\sqrt{g}\mathbf{B}_0^2)^{(0)}} - (\hat{D}-1)\tilde{b}\right]. \qquad \text{(B.6)}$$

Here, the function $\tilde{b}$ is expressed in terms of the function Ξ in the standard way described in [7, 8]. As a result, Eq. (B.6) gives

$$\frac{\partial \delta\tilde{p}_k^{(1)}}{\partial\theta} = \left(\frac{2\pi}{\Phi'}\right)^2 q p_0'\frac{m k_x \Xi_k}{k_R^2}\frac{\sqrt{g}\mathbf{B}_0^2}{(\sqrt{g}\mathbf{B}_0^2)^{(0)}}$$

$$\times\left\{\left[(\sqrt{g}\mathbf{B}_0^2\alpha_0^{(1)})^{(0)} - (\sqrt{g}\mathbf{B}_0^2\alpha_0^{(1)})^{(0)}\frac{(\alpha_0^{(1)}Q_x^*)^{(0)}}{Q_x^{*(0)}}\right]\right. \qquad \text{(B.7)}$$

$$\left. - (\sqrt{g}\mathbf{B}_0^2)^{(0)}\left[\alpha_0^{(1)} - \frac{(\alpha_0^{(1)}Q_x^*)^{(0)}}{Q_x^{*(0)}}\right]\right\}.$$

Substituting this expression into relationship (6.25), we arrive at formula (6.32).

REFERENCES

1. ITER Physics Expert Group on Disruptions, Plasma Control, and MHD and ITER Physics Basis Editors, Nucl. Fusion **39**, 2251 (1999).
2. O. Sauter, R. J. La Haye, Z. Chang, *et al.*, Phys. Plasmas **4**, 1654 (1997).
3. M. Kotschenreuther, R. D. Hazeltine, and P. J. Morrison, Phys. Fluids **28**, 294 (1985).
4. A. H. Glasser, J. M. Greene, and J. L. Johnson, Phys. Fluids **18**, 875 (1975).
5. A. B. Mikhailovskii, Zh. Éksp. Teor. Fiz. **64**, 536 (1973) [Sov. Phys. JETP **37**, 274 (1973)].
6. A. B. Mikhailovskii, Nucl. Fusion **14**, 483 (1974).
7. A. B. Mikhailovskii, Nucl. Fusion **15**, 95 (1975).
8. A. B. Mikhailovskii, *Instabilities in a Confined Plasma* (Inst. Phys., Bristol, 1998).
9. A. B. Mikhailovskii and A. A. Skovoroda, Plasma Phys. Controlled Fusion **44**, 2033 (2002).
10. J. L. Johnson and J. M. Greene, Plasma Phys. **9**, 611 (1967).
11. C. C. Hegna, Phys. Plasmas **6**, 3980 (1999).
12. A. H. Glasser, J. M. Greene, and J. L. Johnson, Phys. Fluids **19**, 567 (1976).
13. A. B. Mikhailovskii, B. N. Kuvshinov, V. D. Pustovitov, and S. E. Sharapov, Fiz. Plazmy **26**, 403 (2000) [Plasma Phys. Rep. **26**, 375 (2000)].
14. W. X. Qu and J. D. Callen, Report No. UWPR855 (Wisconsin University, 1985).
15. R. Carrera, R. D. Hazeltine, and M. Kotschenreuther, Phys. Fluids **29**, 899 (1986).
16. The JET Team, Plasma Phys. Controlled Fusion B **39**, 353 (1997).
17. A. C. C. Sips, Y. Baranov, C. D. Challis, *et al.*, Plasma Phys. Controlled Fusion **40**, 1171 (1998).
18. R. Fitzpatrick, Phys. Plasmas **2**, 825 (1995).
19. N. N. Gorelenkov, R. V. Budny, Z. Chang, *et al.*, Phys. Plasmas **3**, 3379 (1996).
20. S. V. Konovalov, A. B. Mikhailovskii, M. S. Shirokov, and V. S. Tsypin, Plasma Phys. Controlled Fusion **44**, 579 (2002).
21. A. B. Mikhailovskii, private communication, 2001.
22. H. Lutjens, J. F. Luciani, and X. Garbet, Phys. Plasmas **8**, 4267 (2001).
23. C. M. Bishop, J. W. Connor, R. J. Hastie, and S. C. Conley, Plasma Phys. Controlled Fusion **33**, 389 (1991).
24. H. P. Furth, J. Killeen, and M. N. Rosenbluth, Phys. Fluids **6**, 459 (1963).
25. P. H. Rutherford, Phys. Fluids **16**, 1903 (1973).
26. A. B. Mikhailovskii and V. P. Lakhin, Fiz. Plazmy **21**, 291 (1995) [Plasma Phys. Rep. **21**, 271 (1995)].
27. B. N. Kuvshinov and A. B. Mikhailovskii, Fiz. Plazmy **24**, 275 (1998) [Plasma Phys. Rep. **24**, 245 (1998)].
28. A. B. Mikhailovskii, Contrib. Plasma Phys. **43**, 125 (2003).

Translated by I.A. Kalabalyk

Plasma Physics Reports, Vol. 30, No. 7, 2004, pp. 568–581. Translated from Fizika Plazmy, Vol. 30, No. 7, 2004, pp. 615–629.

PLASMA DYNAMICS

Relation between the Electric Parameters of a Z-Pinch Discharge and Plasma Production in the Load during the Implosion of a Cylindrical Wire Array

V. V. Aleksandrov*, E. V. Grabovskiĭ*, K. N. Mitrofanov*, G. M. Oleĭnik*, V. P. Smirnov*, P. V. Sasorov, and I. N. Frolov***

**Institute for Innovation and Fusion Research, Troitsk, Moscow oblast, 142190 Russia*

***Institute of Theoretical and Experimental Physics, Bol'shaya Cheremushkinskaya ul. 25, Moscow, 117259 Russia*

Received May 19, 2003; in final form, December 1, 2003

Abstract—A study of the process of implosion of a cylindrical tungsten wire array by electrical and optical methods shows that it involves two phases. In the first phase, the plasma is produced from the dense wire cores under the action of the heat flux from the current-carrying plasma. This plasma then fills the internal space of the liner array. The measured inductance of the liner and its visible diameter vary only slightly in this phase. During the second phase, the total material of the liner is compressed toward the axis and the inductance of the discharge gap increases. The process of the implosion of wire arrays is studied by analyzing the electric parameters (current and voltage) of the load in the Angara-5-1 facility. The time behavior of the load inductance, the average current radius, and the start time of the liner compression are determined. The compression start time determined from the visible size of the liner is found to coincide with that determined from electric measurements. The compression ratio of the liner in terms of the average current radius turns out to be lower than that measured by optical and X-ray diagnostics. The reason is that, by the instant of maximum compression, only a portion of the current flows at the periphery of the initial wire array. © *2004 MAIK "Nauka/Interperiodica".*

1. INTRODUCTION

In recent years, the implosion of liners under the action of the magnetic field produced by the current flowing through the liner has been extensively studied. Experiments on the implosion of cascade liners [1, 2] performed in the early 1990s in the Angara-5-1 facility showed that he duration of the soft X-ray (SXR) pulse generated during the collision of liners can be reduced to 3–5 ns. This line of research has attracted much attention since significant progress was made in the Sandia National Laboratory (United States), where the implosion of wire arrays was accompanied by an SXR pulse with an intensity of higher than 180 TW and a total radiation energy of about 2 MJ [3].

Some features of the implosion of hollow cylindrical wire arrays in the Angara-5-1 facility were described in [4, 5]. It was shown that the determining factor that should be taken into account in studying the physics of fast Z-pinches is that the plasma is produced from the dense wire material throughout the entire current pulse [6–8]. A theoretical model of prolonged plasma production is presented in [9]. The process of the implosion of a wire array is conventionally divided into two phases.

The first phase is the prolonged production of a plasma that fills the internal space of the liner array. In this phase, the liner inductance increases only slightly. The second phase is the liner compression. After most of the initial wire material is converted into a hot plasma, the rate of plasma production decreases and the portion of the current that was previously confined within the initial liner radius begins to flow through a plasma region whose radius decreases at a progressively increasing rate. A similar picture of the implosion of multiwire arrays was observed later in the MAGPIE facility [10, 11]. The transition from the first phase to the second is accompanied by a rapid decrease in the liner radius, whereas the system inductance begins to increase, resulting in a decrease in the discharge current and an increase in the voltage across the load. This transition is easy to observe because of a rather sharp change in the measured parameters.

As was noted in [12], the process of implosion is axially nonuniform. In the present paper, we do not consider axial and azimuthal nonuniformities arising during the implosion. Instead, based on measurements of the electric parameters (current and voltage) of the load, we study the space-integrated characteristics of implosion, such as the load inductance, the average current radius, and the start time of compression. It is shown that, within the experimental errors, the compression start times determined from optical and electrical measurements are found to coincide with one another. The time dependence of the average current radius agrees well with that of the liner radius determined from the optical streak image of the transverse cross section of the imploding plasma.

1063-780X/04/3007-0568$26.00 © 2004 MAIK "Nauka/Interperiodica"

In Section 2, a model of the wire array implosion is presented that will be used in Section 3 to validate the method for measuring the load inductance. In the subsequent sections, the experimental setup, the methods for testing the electric measurements of the load inductance, and the results of experiments on the implosion of wire arrays are described. The testing methods are based on experiments with an incompressible metal cylinder mimicking a cylindrical wire array and on the analysis of how the currents flowing outside the liner influence the measured inductance.

2. MODEL OF IMPLOSION

A few nanoseconds after the current starts to flow through the load, the plasma is produced on the wire surfaces and the current switches from the wires to the plasma corona [13]. Hence, the plasma of an imploding multiwire array consists of two phases: a hot plasma (with a temperature of 20–30 eV [14]), through which the main current flows, and relatively cold dense cores inside the plasma, which are the residues of the exploded wires. The plasma is then produced from the wire material by the heat transferred from the hot current-carrying plasma to the dense cores. Below, by the term "plasma production," we mean the production of a high-conductivity plasma, rather than merely the ionization process. This plasma conducts most of the generator current, and its ohmic resistance is lower than (or comparable to) the effective resistance determined by the varying inductance of the liner. The dense cores are plasma sources that remain in their initial position for a fairly long time, almost until their material is totally converted into the hot plasma. The outer size of the wire array does not change until this process is complete.

The current flowing through the plasma results in its acceleration by the Ampére force toward the array axis. When a portion of the plasma is shifted far enough toward the array axis, a fresh plasma produced by the heating and ionization of the core material comes to take its place. As a result, a steady-state regime of the continuous production of a fresh hot plasma and its motion toward the system axis is established. In this case, the plasma takes away the magnetic field frozen in it. Thus, the radial flow of a hot plasma with the frozen-in magnetic field is formed. Inside this flow, the electric current flows parallel to the discharge axis. As was noted in [9], more than half of the current can flow through the plasma inside the array under similar conditions. Due to the continuous production of a fresh plasma, the remainder of the current flows along the boundary layer located near the initial liner radius. Such a quasi-steady character of plasma production, the plasma acceleration toward the discharge axis, and the confinement of one-half of the discharge current near the initial radius of the array are observed as long as the plasma-producing material can provide the required production rate of the fresh hot plasma at the initial radius of the array.

The rate of plasma production is a crucial parameter for the implosion of a heterogeneous liner. This rate is determined by the combined action of Joule heating and the heat transfer and plasma diffusion across the magnetic field in the boundary layer. The internal structure of the boundary layer was considered in [9]. Its thickness is governed by the plasma resistance and thermal conductivity and determines the self-consistent value of the plasma production rate $\dot{m}$. In [9], the following formula was derived for the production rate $\dot{m}$ of a tungsten plasma from the unit surface of a cylindrical liner with radius R when the current I flows through the array:

$$\dot{m} = 0.2\left(\frac{I\ [\mathrm{MA}]}{R\ [\mathrm{cm}]}\right)^{\mu}\ \mu\mathrm{g/(cm^2\ ns)}. \qquad (1)$$

The exponent μ by the current lies in the range 1.7–2. The uncertainty in determining this exponent corresponds to a factor on the order of 2–3. This is a consequence of both the simplicity of the adopted formulas for describing the plasma properties and the ignoring of the initial azimuthal structure. A comparison of this formula with experimental data is performed in [15].

It follows from formula (1) that the plasma production rate increases nearly in proportion to the square of the current. When the entire wire material is transformed into a hot plasma, plasma production terminates, so that nothing confines the current at the periphery of the initial wire array and the second phase (liner compression) begins. This scenario of the implosion of a wire array is, of course, only a rough approximation. One of the discrepancies between this model and an actual situation lies in the fact that, as the dense cores are depleted, they cannot provide the plasma production rate required to contain almost half of the current at the initial radius of the array. Thus, the outer liner boundary begins to move toward the axis when the proportionality between the plasma production rate and the current squared breaks. Since this proportionality breaks down gradually, the transition from the first to the second phase occurs over a certain (quite long) time interval, rather than instantaneously [15, 16]. The duration of this interval depends on many factors. In particular, the inhomogeneity of the local rate of plasma production [14] or the nonuniformity of the mass distribution along the wires can lead to a situation in which, in the places where the plasma production has finished, the outer liner boundary begins to move toward the axis, while in the places where the plasma production still continues, the outer liner boundary stays at the initial liner radius.

After the start of compression, some portion of the plasma-producing material in the form of drops and small localized wire residues can remain at the periphery of the initial wire array. We recall again that these residues most probably consist of a dense, cold, low-conductivity plasma. These residues of the plasma-pro-

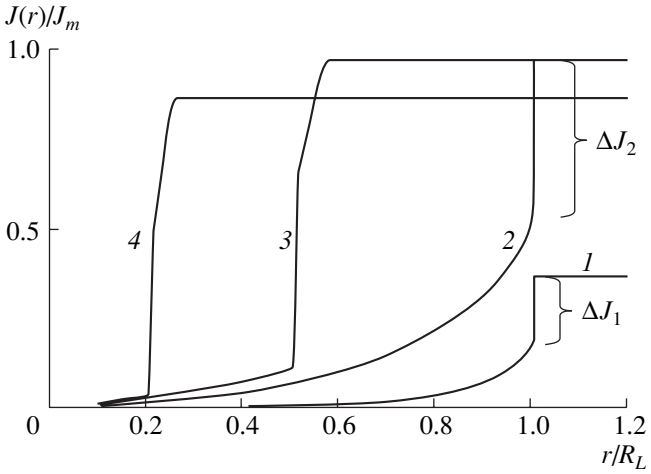

Fig. 1. Profiles of the total current $J(r)$ inside a cylinder of radius r, normalized to the maximum current J_m through a liner at the instants (*1*) $0.4t_J$, (*2*) $0.9t_J$, (*3*) $1.1t_J$, and (*4*) $1.2t_J$, where t_J is the time at which the current reaches its maximum. The plasma production was terminated abruptly at the instant $0.9t_J$. Here, ΔJ is the current in the boundary layer and R_L is the initial liner radius.

ducing material at the periphery of the initial wire array do not prevent the implosion of the hot plasma and the penetration of the current into the axial region of the discharge.

2.1. Current Distribution inside a Liner in the Model of Implosion

To determine the profile of the current distribution inside a liner, we performed 1D MHD simulations of the implosion of a wire liner using the model concept of prolonged plasma production.

The model used in these calculations is similar to that described previously in [9] (see also [12, 14]). It is based on the assumption that the azimuthal structure of the plasma source, the plasma diffusion across the magnetic field, the Joule heating, and the heat transfer are of minor importance in the narrow region adjacent to the cylinder on which the cold products of the initial wire explosion are situated. Hence, in the main body of the radial plasma flow, we can average all the parameters over the azimuthal angle and consider that the magnetic field is frozen in the plasma and the plasma moves under the action of the Ampére force only. The azimuthal structure of the flow would introduce only small corrections because the ratio of the interwire distance to the liner radius is small. The main difference between the results of our calculations and those presented in [9] is that we used current waveforms close to the experimental ones and, for the rate of plasma production, we employed formulas derived from magnetic probe measurements inside an imploding liner [12, 14][1] (see formula (1) and the explanations and refinements presented below). In such a situation, the complicated, azimuthally nonuniform process of plasma production near the plasma source, which is excluded from consideration in this model, is effectively taken into account by using the plasma production rate obtained from the experimental data. Another important feature of this model is the boundary condition for the velocity of the plasma leaving the source region in the case where the velocity of the bulk of the plasma flow is higher than the Alfvén velocity (see formula (35) in [9]). In the case at hand, this velocity should be higher than or equal to the local Alfvén velocity. In this paper, as in [9, 12, 14], the coefficient in this boundary condition was assumed to be equal to unity. This version of the boundary condition, which is usually called the Jouguet condition, was derived for the case of a 1D flow in the plasma source region [9]. In a more general case, the coefficient can be slightly larger than unity. Special calculations performed to check the effect of this assumption showed that the value of this coefficient has no qualitative effect on the final results of this section.

Let us consider simulation results for the case $\mu = 2$ in formula (1). Figure 1 shows the radial distribution of the total current inside a cylinder of radius r (which is equal to R_L at the initial liner radius) at the instants $0.4t_J$, $0.9t_J$, $1.1t_J$, and $1.2t_J$, where t_J is the time at which the current reaches its maximum value. The plasma production was terminated abruptly at $0.9t_J$. The mass of the wire liner was chosen such that the collapse in the zero-dimensional model occurred at $1.2t_J$. It can be seen that the time interval during which the plasma is produced ($0.9t_J$) is chosen to be comparable to the duration of the implosion process ($1.2t_J$). Such a relation between the plasma production and liner implosion times agrees with the experimental data. Note that a significant portion of the current (42%) flows at the initial liner radius until the end of plasma production. The reminder of the current (58%) is distributed inside the initial liner radius.

Let us estimate how the internal liner inductance varies during the first phase. This inductance is caused by the magnetic flux concentrated inside the cylinder of radius R_L (the initial liner radius). By the end of plasma production, the radial distribution of the total current inside the cylinder of radius r (shown in Fig. 1) can be roughly approximated as $\sim(r/R_L)^\alpha$, where $\alpha \cong 3.5$. For early times, α is greater. It can be shown that the inductance per unit length caused by the magnetic flux inside the cylinder is equal to $2/\alpha$ nH/cm. For $\alpha = 3.5$, it is equal to 0.57 nH/cm. Taking into consideration that only 58% of the current flows inside a cylinder of radius R_L, the contribution of this current to the inductance per unit length is ~0.33 nH/cm. A comparison of this value to the increase in the inductance per unit length in the second phase of implosion in the case of tenfold compression (4.6 nH/cm) shows that, during the first phase, the liner inductance increases only slightly (by 7%). In

[1] This problem will be considered in detail in a separate paper that is being prepared for publication.

what follows, we will assume that the liner inductance is constant. In our opinion, the fact that the load inductance increases only slightly (by no more than ~10%) during the first phase is not related to the assumptions made in the model used.

3. VALIDATION OF THE METHOD FOR MEASURING THE INDUCTANCE

In physics and engineering, resistance and perveance are used as load characteristics when examining the operation of electron and ion diodes connected to a generator. Their values can be calculated from the experimentally measured waveforms of the current and voltage. In the case of a wire array implosion, such a characteristic is the liner inductance, which can be used to describe the implosion dynamics and the efficiency of energy transfer. The value and time dependence of the liner inductance can also be calculated from the experimentally measured waveforms of the current and voltage under certain assumptions. The results from studies of the interaction of a single generator module in the Angara-5-1 facility under a load and the determination of the load inductance from the measured current and voltage were presented in [17].

Let us consider the procedure for measuring the load inductance $L(t)$ in more detail.

The voltage $U(t)$ in a circuit with a variable inductance $L(t)$ is equal to the sum of the inductive and reactive components of the voltage:

$$U = d(LJ)/dt + RJ, \quad (2)$$

where $J(t)$ and $R(t)$ are the time-dependent load current and load resistance, respectively.

It is evident that, $L(t)$ and $R(t)$ cannot be found simultaneously from this equation by using the measured values of the current and voltage without additional assumptions.

From independent measurements of the electric field strength on the liner axis, it is known that, in both hollow gas puffs [18] and wire liners [13, 14], 10–15 ns after the start of the current, the resistive component of the voltage measured directly between the anode and cathode on the axis of a hollow cylinder becomes smaller (by a factor of less than 0.1) than the inductive component. Assuming that the contribution of the resistive component is small, we can find the inductance as a function of time:

$$L(t) = \frac{\int_{t_0}^{t} U(\tau)d\tau + C}{J(t)}, \quad (3)$$

where C is the constant of integration. Henceforth, in contrast to the inductance calculated from the load dimensions, the inductance found from formula (3) will be referred to as the measured inductance.

Note that the integration constant cannot be set at zero (even though at the instant t_0, at which the current starts, we have $J(t_0) = 0$ and $U(t_0) = 0$), because, over the first 10–15 ns after the current begins to flow through the liner, the resistive component of the voltage cannot be ignored and equation (3) does not apply for this time interval.

For times close to t_0, when the current and voltage are still low and the relative measurement errors are large, the error in measuring the inductance is large. Taking into consideration the above factors, we believe that, under our experimental conditions, the inductance can be reliably determined 15–20 ns after the beginning of the current pulse.

The ratio $U/(dJ/dt)$ is not equal to the inductance but is also measured in H. This quantity is suitable for considering the electric aspects of implosion because, as will be shown below, the ratio $U/(dJ/dt)$ is more sensitive to variations in the electric parameters in comparison to $L(t)$.

When it is known a priori that, within a certain time interval, $L(t) = \text{const}$ (or changes slightly), this fact can be used to find the integration constant. If $dL(t)/dt = 0$ at some instant, then the measured inductance at this instant is equal to $U/(dJ/dt)$. From here we can find the integration constant. The obtained value of the integration constant will be true throughout the entire time interval under study, including the intervals in which the inductance $L(t)$ varies rapidly (provided that the resistive component of the voltage can be ignored).

Note that, when a heavy incompressible metal cylinder is used as a load, the measured inductance should not change while the generator current is flowing through this cylinder and should be equal to the calculated inductance.

In the above formulas, the inductance L corresponds to the magnetic flux LJ contained between the radius at which the voltage is measured and the liner axis. Let us divide the measured inductance L into two inductances L_{const} and L_{var} that correspond to two fluxes, the first of which is contained between the radius at which the voltage is measured and the initial liner radius R_L, while the latter is contained between the initial liner radius and the liner axis. Before the current-carrying plasma begins to expand inward, we have $L_{\text{var}} = 0$. During the liner implosion, the inductance L_{const} remains unchanged (if we ignore the motion of the electrode plasma and the low-probability ejection of the liner plasma beyond R_L), while the inductance L_{var} should increase. Knowing the inductance L_{var}, we can find the average current radius r from the formula

$$L_{\text{var}} = 2h\ln(R_L/r)\ \text{nH},$$

where h [cm] is the liner height. This formula is, in essence, the definition of the average current radius r. The average current radius is a convenient parameter describing the localization of the current and its pene-

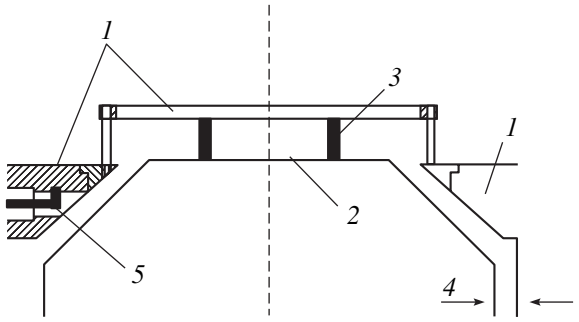

Fig. 2. Schematic of the output unit of the Angara-5-1 facility: (*1*) anode, (*2*) cathode, (*3*) load (an incompressible cylinder or a wire liner), (*4*) point at which the voltage is measured, and (*5*) current detector.

tration into the volume of the initial wire array. During the liner implosion, this parameter should decrease. By analogy with an ordinary contracting cylinder, we can introduce a compression factor in terms of the average current radius: $\exp[L_{var}/(2h)]$. A comparison of the time evolution of the average current radius r (which was derived from the measured values of the current and voltage) to the optical streak images of the transverse cross section of the liner is presented in the following sections.

4. EXPERIMENT

The experiments were performed in the Angara-5-1 facility, which consists of eight modules connected in parallel to the load [19]. Figure 2 shows a schematic of the experiment.

As a load, we used cylindrical tungsten wire arrays with a height of 1 cm and diameters of 20, 12, and 8 mm. In some cases, we used nested cylindrical arrays, the diameters of the outer and inner arrays being 12 and 6 mm, respectively. The wire diameter varied from 5 to 10 μm, and the total number of wires in a cylindrical array varied from 16 to 120, the interwire spacing being 0.1–1 mm. Sometimes, we placed a 1.5-mm-diameter agar-agar cylinder on the array axis.

In some experiments, when testing the method, a model load was connected to the generator output instead of a wire array. This load was a heavy metal cylinder with known dimensions.

The time derivative of the current flowing through the liner dJ/dt was measured with eight loops (Fig. 2, item *5*) placed on the side of each module at a radius of 55 mm from the array axis. The loop signals were averaged over eight modules. The total current J inside the radius 55 mm was calculated by numerically integrating the averaged current derivative. The time resolution of the method was no worse than 1 ns.

The voltage U between the anode and cathode of the generator was measured with an inductive divider [20] at a radius of 60 mm, at the point where the currents of the individual modules merged (Fig. 2, item *4*). The point at which the voltage was measured by the inductive divider coincides with the separatrix surface, which separates the family of magnetic field lines that envelop the axis of the cylindrical load from the eight families of magnetic field lines enveloping each of the eight cathodes of the modules' transmission lines. Consequently, in the above formulas, the voltage U is the voltage on the separatrix and the magnetic flux LJ is the magnetic flux contained between the separatrix and the liner axis. The time resolution of the inductive divider is 2 ns.

In the experiments, the waveforms of the X-ray emission generated during the implosion of a multiwire array were recorded with the help of vacuum X-ray diodes with different filters. To monitor variations in the outer liner radius during implosion, we recorded an optical image of the liner cross section perpendicular to the liner axis.

The above pulsed electric signals characterizing the process of liner implosion were recorded with the help of TLS216, SRG5, and SRG7 oscilloscopes with upper frequencies of 500 MHz, 1500 MHz, and 7 GHz, respectively. The length of the cable connecting the detector and recorder was 10–15 m. RK-75-9-35, RK-75-9-12, RK-75-17-31, and RK-50-17-51 commercial cables were used. The testing of the cable lines showed that the transmission coefficient of a 15-m-long RK-75-9-35 cable at a frequency of 1400 MHz was no worse than 0.9. For RK-50-17-51 cables of length 10 m, the attenuation at a frequency of 3 GHz was 1.8 dB.

5. EXPERIMENTAL RESULTS

5.1. Testing the Method

The voltage detector was sensitive enough to study the implosion dynamics and to measure an increase in the voltage during the liner implosion (although the voltage was measured far from the liner, at a radius of 60 mm). Figure 3 compares the signals of the current time derivative dJ/dt and voltage U at the separatrix for two different loads: (a) a heavy incompressible metal cylinder with an inductance at the separatrix of 4 nH and (b) a wire array (sixteen 6-μm tungsten wires) with a diameter of 20 mm and an initial inductance of 4.9 nH. It can be seen that, in the case of an incompressible cylinder, these signals are almost proportional to one another throughout the voltage pulse, as is expected for current flowing in a circuit of fixed geometry. For an imploding wire liner, the signals are also almost proportional to one another in the initial stage; the character and rate of their variations then differ radically. The current through the liner decreases, which is seen from the change of the sign of the current derivative dJ/dt, while the voltage U increases substantially. This effect is related to the fact that the load impedance increases substantially because the shape and dimensions of the

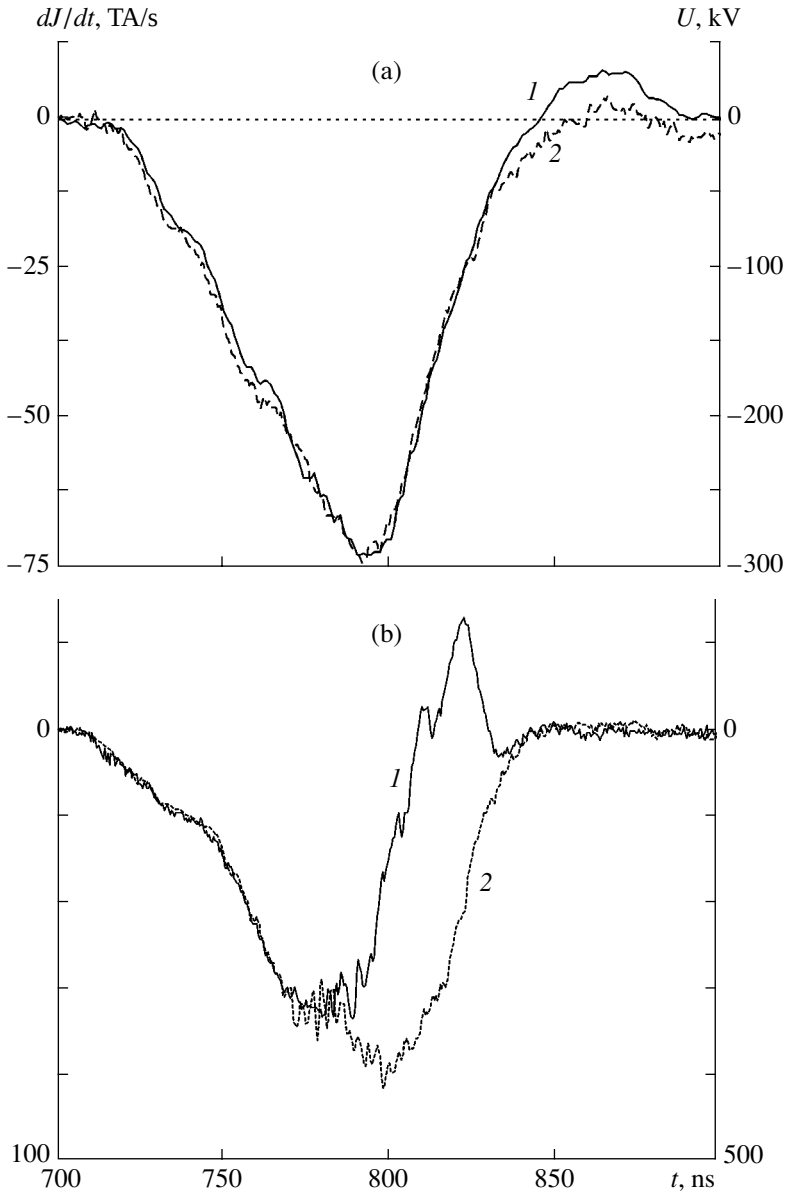

Fig. 3. Comparison of the signals of (*1*) the current time derivative dJ/dt and (*2*) the voltage at the separatrix for two different loads: (a) a heavy incompressible metal cylinder (the inductance at the separatrix is 4 nH) and (b) a multiwire liner (the inductance at the separatrix is 4.9 nH).

liner are strongly modified at the instant of maximum compression.

A suitable model load for testing the method is a heavy incompressible metal cylinder, because its inductance can easily be calculated. From the U and dJ/dt signals, we calculated the inductance $L(t)$. Figure 4 shows time dependences of the current and inductance for three experiments with a calculated inductance of 3.8 nH.

A common feature of the experiments with heavy metal cylinders is that the measured inductance somewhat decreases during the current pulse. This effect could be related to the plasma production on the electrode surface and its subsequent expansion. From the rate at which the measured inductance decreases, we can estimate the velocity with which the current layer moves from the electrodes. This velocity turns out to be ~10^6 cm/s.

5.2. Implosion of Wire Liners

In the experiments on the implosion of wire arrays, we measured the voltage $U(t)$ at the separatrix, the current time derivative dJ/dt, and the SXR power P_{SXR}, and

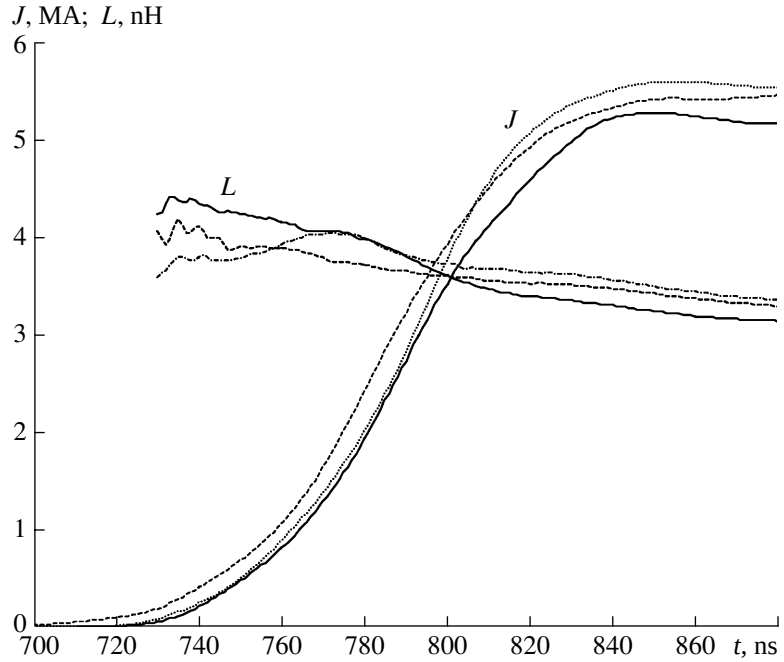

Fig. 4. Waveforms of the current J and measured inductance L for three shots with a calculated inductance of 3.8 nH.

recorded the optical streak images of the transverse cross section of an imploding liner. From the $U(t)$ and dJ/dt signals, we calculated the time dependences of the liner inductance $L(t)$ and the ratio $U/(dJ/dt)$. Figure 5 shows typical waveforms of the voltage U, current J, the current time derivative dJ/dt, the SXR power P_{SXR}, the liner load inductance L, and the ratio $U/(dJ/dt)$. The optical streak image (synchronized with the above curves) of the transverse cross section of a 12-mm-diameter imploding wire array consisting of sixty 6-μm tungsten wires is also shown; the initial liner inductance at the separatrix is 5.9 nH.

In the time dependences of $U/(dJ/dt)$ and L, we can distinguish two phases: a quasi-steady phase and a fast increase 25–35 ns before the instant of maximum compression. The transition from the first phase to the second is clearly seen in the time behavior of the ratio $U/(dJ/dt)$ (marked with a circle). In the waveform of the inductance L, the transition is somewhat smoother, due to the integral character of the inductance. In Fig. 5, there are two vertical lines: the left line indicates the transition from the first to the second phase, while the right line indicates the instant at which the SXR power is maximum.

During the first phase, in which $U/(dJ/dt)$ and $L(t)$ change only slightly, the current-carrying plasma that is produced from the wire material under the action of the increasing current fills the internal volume of the wire array.

The second phase is characterized by the efficient compression of the plasma under the action of the discharge current. As the liner radius decreases, the load inductance increases.

A comparison of the time behavior of the ratio $U/(dJ/dt)$ with the dynamics of the outer liner boundary seen on the streak image shows that the instant at which $U/(dJ/dt)$ begins to grow coincides with the instant at which the visible radius of the liner begins to decrease. The time after which the plasma glow disappears in the vicinity of the initial radius of the wire array will hereafter be referred to as the experimentally measured (by two independent methods) start time of the compression.

5.2.1. Geometric parameters of the liner. The measured inductance $L(t)$, which remains almost constant during the first phase, agrees with the calculated inductance of the initial wire array. Figure 6 compares the measured and calculated inductances. The calculated inductance is plotted on the abscissa, and the corresponding measured average value of $U/(dJ/dt)$ during the first phase is plotted on the ordinate. It can be seen that this average value coincides well with the calculated inductance. There are some factors that can disturb this coincidence:

(i) the expansion of the current channel at the beginning of the current pulse, when the plasma produced on the wire surface begins to expand;

(ii) the filling of the liner cavity with a current-carrying plasma during the implosion;

(iii) the current leakage near the separatrix;

(iv) the nonuniform distribution of the current in the liner unit; and

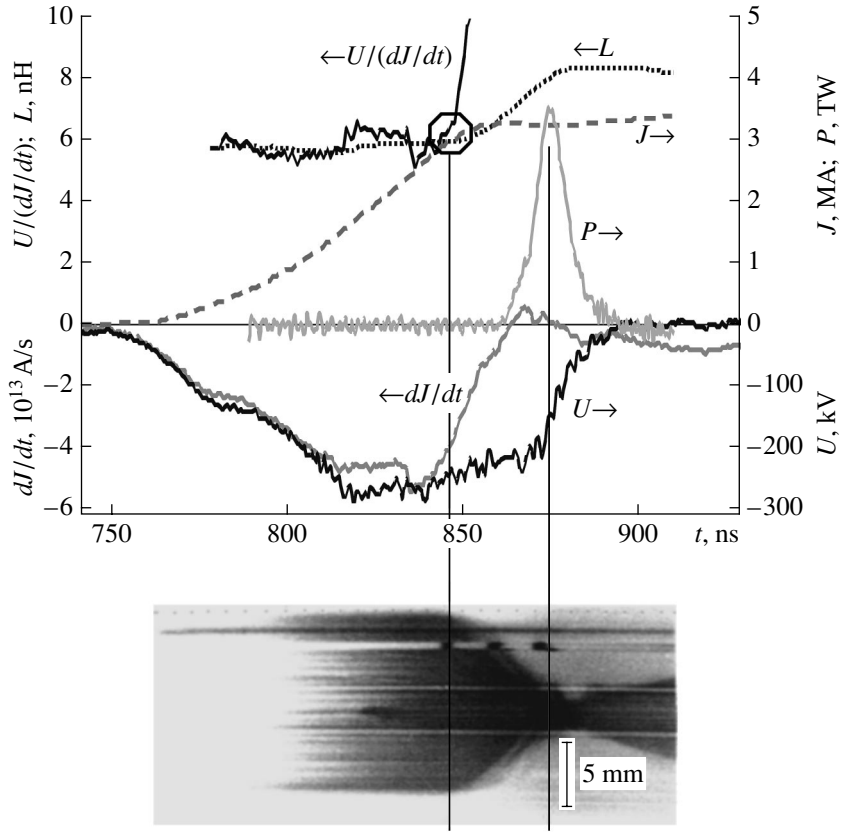

Fig. 5. Waveforms of the voltage U, current J, current time derivative dJ/dt, SXR power P, inductance L, and ratio $U/(dJ/dt)$ and the synchronized optical streak image of the transverse cross section of an imploding wire array (sixty 6-μm tungsten wires) with a diameter of 12 mm and an initial inductance at the separatrix of 5.9 nH.

(v) the expansion of the plasma layers produced at the current-carrying electrodes.

Let us consider these factors in more detail:

(i) It should be noted that the inductance of a multiwire array depends weakly on the number of wires and their diameter and is approximately equal to the inductance of a hollow cylinder with an outer radius equal to the array radius. Under our experimental conditions, as the current channel expands from 6 μm up to 100 μm, the inductance decreases by less than 0.2 nH/cm (by less than 5% of the inductance of the initial wire array). This fact allows us to ignore the expansion of the current channel.

(ii) At first glance, the gradual filling of the liner cavity with a current-carrying plasma during the first phase should lead to an increase in $U/(dJ/dt)$ and $L(t)$. However, as was noted in Section 2, this increase (~0.33 nH/cm) is rather small (~7% of the initial inductance of the array).

(iii) A more detailed analysis (see Fig. 6) shows that, as the load inductance increases, the measured inductance becomes smaller than the calculated one. This is probably due to the fact that, as the load inductance increases, the voltage at the separatrix increases too, which leads to an increase in the electron-current leakage near the load. The minimum value of the magnetic self-insulation current [21] (526 kA at a voltage of 2 MV and diameters of the coaxial vacuum transport line of 132 and 120 mm) required to suppress the electron-current leakage at a radius of 60 mm is much smaller than the measured current (2–5 MA); therefore the leakage should be suppressed. However, there are always regions on the separatrix surface where the magnetic field is zero and the self-insulation condition fails to hold. The difference between the calculated and measured inductances at large values of the latter is associated with an increase in the current leakage due to an increase in the voltage at the separatrix at large load inductances.

(iv) A substantial current loss resulting in the difference between the measured and calculated inductances can also be related to the asynchronous operation of the eight modules of the Angara-5-1 facility. Figure 7 shows the effect of the asynchronous operation of the modules on the time behavior of the ratio $U/(dJ/dt)$ for an incompressible cylindrical load with a calculated inductance of 3.4 nH. The shape, start time, and duration of the current pulse are the same as in Figs. 3, 4,

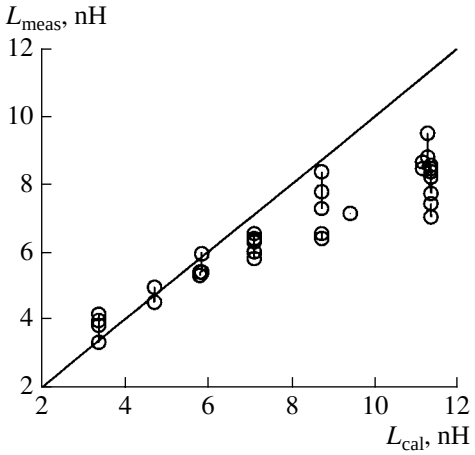

Fig. 6. Comparison of the measured inductance L_{meas} during the first phase to the calculated inductance of the initial wire array L_{cal}.

and 5. In the case of the simultaneous operation of the modules (the scatter in the switching times is smaller than 10 ns; see Fig. 7a), the current loss is small and the ratio $U/(dJ/dt)$ is almost constant and coincides with the calculated inductance. When the scatter in the switching times is larger than 50 ns, the current loss is large and the ratio $U/(dJ/dt)$ varies substantially over time (Fig. 7b). Since the ratio $U/(dJ/dt)$ depends only on the current distribution inside the separatrix, significant variations in this ratio may be an indication that the current distribution varies substantially inside the separatrix. In this case, the shape of the separatrix changes in an uncontrolled way, though it is localized, as before, near the point where the currents of the individual modules merge. The experimental results allow us to conclude that only the current losses at the separatrix and inside it have any effect on the ratio $U/(dJ/dt)$.

(v) A decrease in the inductance may be caused by the drift of the current-carrying plasma layer away from the electrodes. As is seen from Fig. 4, this decrease can be as large as 1 nH.

It should be noted that Fig. 6 shows the results of the shots in which both the scatter in the parameters and the current loss were small. For these shots, the ratio $U/(dJ/dt)$ during the first phase of implosion changes only slightly. In some shots, we observed a small increase (see Fig. 5) or decrease in this ratio during the first phase. The increase could be caused by the penetration of the current into the liner cavity during the implosion (see item (ii)). The decrease could be related to the displacement of the current-carrying plasma layer away from the electrodes (as was described in Section 5.1) and to the expansion of the current channel at the beginning of the current pulse (see item (i)). The resulting effect depends on which effect is predominant.

Thus, the calculated and measured inductances coincide well in the first phase of the implosion. This fact, first, testifies to the validity of the proposed method for measuring the inductance during the liner implosion. Second, it was confirmed experimentally that, during the first phase, the load inductance changes only slightly, which agrees with the concept of the prolonged plasma production during the implosion of a wire array.

5.2.2. Second phase. As was noted above, the second phase is characterized by efficient plasma compression. The measured inductance increases, which indicates that the average current radius decreases. From the measured value of the inductance, we can calculate the average current radius r, as was discussed above. Figure 8 illustrates the time dependence of the average

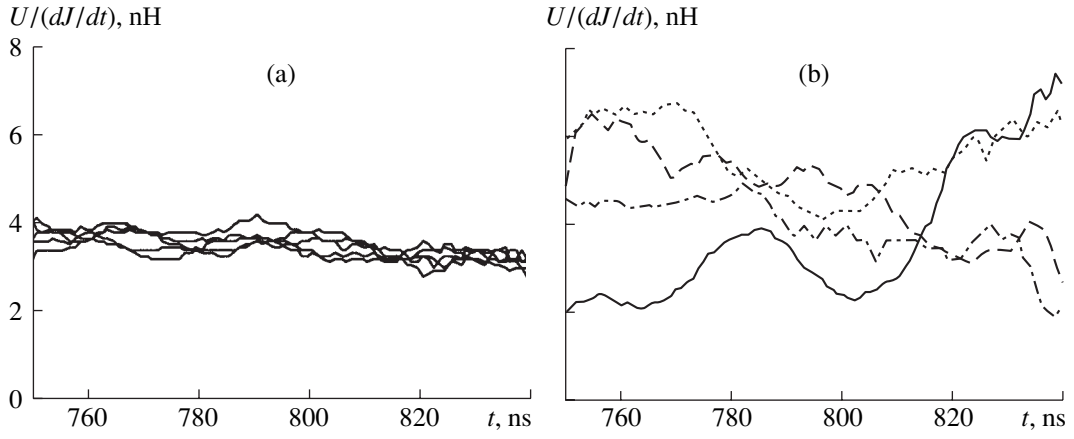

Fig. 7. Effect of the scatter in the operating times of the modules on the ratio of the voltage to the current time derivative $U/(dJ/dt)$ for (a) five shots with small current losses (the scatter in the operating times is smaller than 10 ns) and (b) four shots with large current losses (the scatter in the operating time is larger than 50 ns). The load is an incompressible cylinder with a calculated inductance of 3.4 nH.

current radius r superimposed on the optical streak image of the transverse cross section of the liner. The average radius is calculated from the dependence $L(t)$ deduced from the simultaneous measurements of the voltage and the current time derivative. It can be seen that the average current radius is close to the outer visible boundary of the liner. However, the compression ratio in terms of the average current radius is somewhat lower than that determined from the streak image. The reasons for this difference will be analyzed below.

5.2.3. Nested array. In this experiment, we used nested cylindrical arrays. The diameters of the outer and inner arrays, each of which consisted of 40 tungsten wires, were 12 and 6 mm, respectively. The wire diameter was 5 μm for the outer array, while it was 8 μm for the inner array. A 1.5-mm-diameter agar-agar cylinder was placed on the array axis.

As in the experiments with ordinary wire arrays, we calculated the inductance and the ratio $U/(dJ/dt)$ from the measured waveforms of the current time derivative dJ/dt and voltage $U(t)$ at the separatrix. In the time dependences of $U/(dJ/dt)$ and L, as with ordinary arrays, two phases can be distinguished: the initial quasi-steady phase and the subsequent rapid increase. The time behavior of the $U/(dJ/dt)$ and L in the quasi-steady phase is almost the same as in the case of ordinary wire arrays, which were discussed above. This is natural because, during the first phase, the plasma is produced at the outer radius of the array, most of the current is localized at the outer radius and near it, and the inductance varies only slightly.

As the plasma production rate in the outer array decreases, the implosion of its material begins. In this case, the average current radius decreases too. The implosion process is clearly seen in the optical streak image of the transverse cross section of the liner (on the bottom of Fig. 9). When the bulk of the material of the outer array reaches the inner array, the implosion rate of the outer-array plasma sharply decreases.

After this, the process of plasma production in the inner array rapidly terminates. This is because, from the very beginning of the process, a small portion of the current (~5–10% [22]) penetrates into the outer array. This current and the SXR emission from the outer array ionize and heat the material of the inner array over a relatively long time (~100 ns). For the given shot, the simultaneous compression of the plasma of the outer and inner arrays begins ~20 ns after the beginning of the compression of the outer array.

From the measured inductance, we calculated the average current radius and, thus, the rate at which this radius varies. Figure 9 shows typical time dependences of the rate of change of the average current radius, the signal from the SXR detector, and the synchronized optical streak image of the transverse cross section of an imploding liner. The left vertical line indicates the start time of the compression of the outer array. The middle line indicates the instant at which the visible

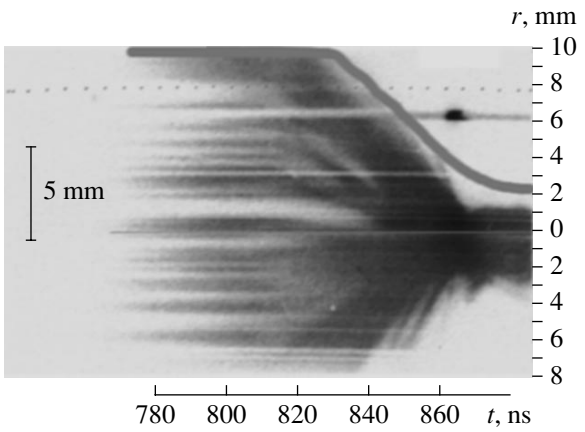

Fig. 8. Time dependence of the average current radius (derived from the measured current and voltage) superimposed on the optical streak image of the transverse cross section of the liner. The start time of the current is 730 ns.

radii of the outer and inner arrays coincide; this instant corresponds to a local maximum in the rate of change of the average current radius. The right line indicates the instant at which the SXR power is maximum; this instant coincides with the instant at which the rate of change of the average current radius reaches its maximum value.

It is clearly seen that, after the instant at which the visible radii of the outer and inner arrays coincide, the rate of change of the average current radius decreases by nearly a factor of 2 over a time of 10 ns. The energy released during the interaction of the plasmas of the outer and inner arrays is radiated in the form of SXR emission. This follows from an increase in the signal from the SXR detector at this instant.

As the implosion progresses, the leading front of the SXR pulse is delayed by nearly 7 ns with respect to the waveform of the rate of change of the average current radius. On the other hand, the instant at which the rate of change of the average current radius reaches its maximum coincides with the peak of the SXR pulse. This indicates that the plasma kinetic energy accumulated during the implosion is radiated in the form of SXR emission. After the instant of maximum compression, the plasma expansion is clearly seen both in the streak image and in the waveform of the rate of change of the average current radius.

All this shows that the method for determining the load inductance, the average current radius, and the rate of change of this radius can be used to study fine details of the implosion. The absolute values of the rate of change of the average current radius and the compression ratio in terms of this radius are lower than those derived from streak images, as is the case of ordinary wire arrays. Reasons for this discrepancy are analyzed in the following section.

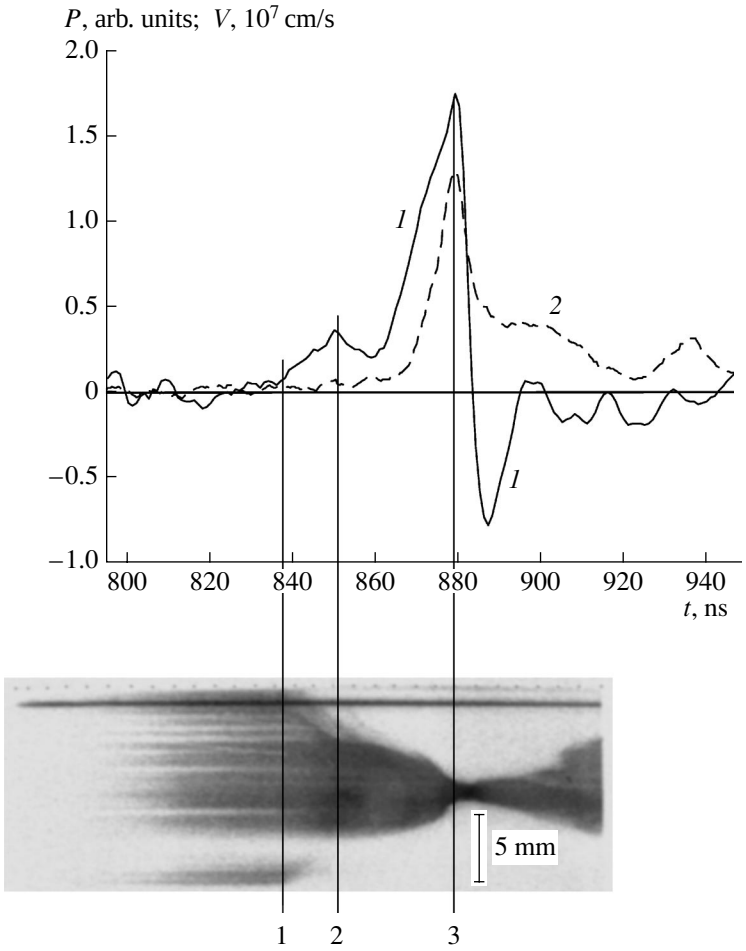

Fig. 9. Implosion of a nested wire array: (*1*) time dependence of the rate of change of the average current radius *V*, (*2*) SXR power *P*, and the synchronized optical streak image of the transverse cross section of an imploding liner. Vertical lines 1, 2, and 3 mark the beginning of the implosion of the outer array, the instant at which the visible radii of the outer and inner arrays coincide, and the instant corresponding to the maximum SXR power (which coincides with the instant at which the rate of change of the average current radius reaches its maximum), respectively.

5.2.4. Implosion dynamics and the compression ratio in terms of the average radius of the current distribution. An analysis of the time behavior of the measured inductance reveals two unexpected features. First, the measured inductance continues to increase after the instant at which the SXR power reaches its maximum (see Fig. 5). Second, the increase in the measured inductance is as small as 3–3.5 nH, which corresponds to a compression ratio in terms of the average current radius of 5–6 and to the relatively low rate at which this radius decreases. Note that the typical compression ratio derived from pinhole-camera images in the Angara-5-1 facility is as high as 10–30 [23].

The reason for these features is that the plasma production at the periphery of the initial wire array still continues by the instant of maximum compression. By this instant, most of the plasma-producing material has already transformed into plasma and has been shifted toward the axis together with the magnetic field frozen in it. However, some amount of the plasma-producing material can remain at the periphery of the initial wire array. A high-conductivity plasma still continues to be produced from these small localized remainders of the plasma-producing material. An estimate of the plasma mass located at the periphery at the instant of maximum compression is given in [24]. A fraction of the generator current continues to flow through a fresh plasma produced at a large radius; this leads to the acceleration of plasma toward the axis. Note that this process results in the generation of additional SXR bursts after the instant of maximum SXR power; this is related to the repeated implosions of the plasma located at a large radius. The implosion of this current-carrying plasma leads to a further increase in the inductance.

Thus, an increase in the inductance after the instant of maximum SXR power is explained by the continuing implosion of the plasma remaining at the periphery of the initial wire array. This also explains the low value of the compression ratio in terms the average current radius. Since some fraction of the current continues to

flow at the periphery of the initial wire array, the average current radius cannot be very small; hence, the compression ratio in terms of the average current radius cannot be high.

6. COMPARISON WITH THE RESULTS OF NUMERICAL SIMULATIONS

We performed 1D MHD simulations of the liner implosion with allowance for prolonged plasma production. The current waveform used in simulations corresponded to that measured in one of the shots. The plasma production rate was calculated by formula (1) up to a certain instant, after which this rate decreased exponentially. The simulations were performed for two cases: the fast switching-off of plasma production (with a fall time constant of 4 ns) and the slow switching-off of plasma production (with a fall time constant of 16 ns).

Figure 10 compares the results of these two simulations and the experiment. The figure shows time dependences of the calculated and measured inductances and the ratio $U/(dJ/dt)$. The waveforms of the current through the liner (which are the same for the simulations and the experiment), the calculated plasma production rate dm/dt, and the measured signal from the SXR detector are also shown. Figures 10a and 10b show the simulation results for the fast and slow switching-off of plasma production, respectively (see the time dependence of dm/dt), while Fig. 10c shows the experimental results.

It can be seen from Fig. 10a that a sharp increase in $U/(dJ/dt)$ appears when the plasma production rate is no longer proportional to the current squared. In this case, the remaining plasma-producing material at the initial radius of the wire array is insufficient to produce hot plasma in large amounts.

A comparison of the simulation results for the cases of the fast and slow switching-off of plasma production shows that the increase in the inductance is smaller for the latter case. As was noted above, this is explained by the fact that some fraction of the current continues to flow at the periphery of the initial wire array over a relatively long time. This means that the average current radius cannot be very small and, accordingly, the increase in the inductance cannot be large; therefore, the compression ratio in terms of the average current radius cannot be high.

Figure 11 shows the results of the same simulations in the form of a contour plot of the plasma density on the (r, t) plane. One can clearly see a sharp break in the outer liner boundary (marked by the arrow). This break can also be seen in the streak image of the transverse cross section of the liner (see Figs. 5, 8). A similar effect was also observed in experiments on the implosion of wire liners in the MAGPIE facility [25]. The presence of such breaks in both the measured time dependences and the results of MHD simulations indicates that the motion of the outer plasma boundary begins immediately after the plasma production rate starts to decrease at the periphery of the initial wire array.

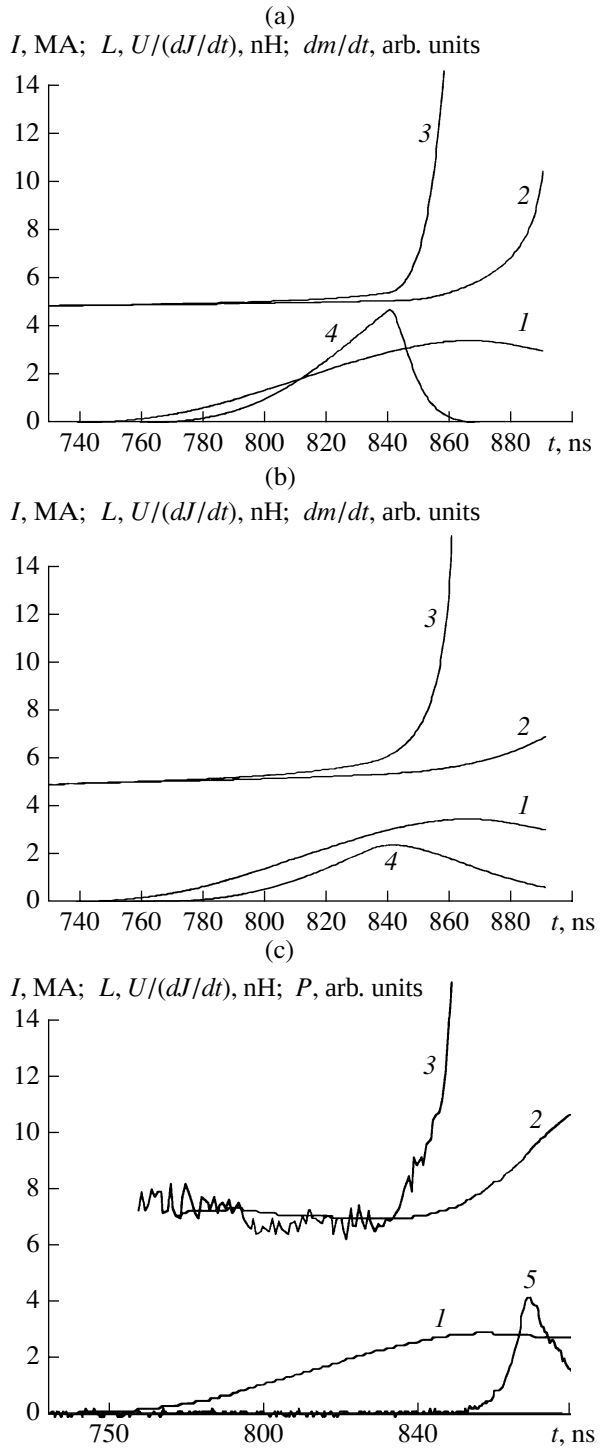

Fig. 10. Comparison of the experimental results (c) with the results of 1D MHD simulations with allowance for prolonged plasma production for the cases of the (a) fast and (b) slow switching-off of plasma production: (*1*) current J, (*2*) inductance L, (*3*) ratio $U/(dJ/dt)$, (*4*) plasma production rate dm/dt, and (*5*) SXR signal P.

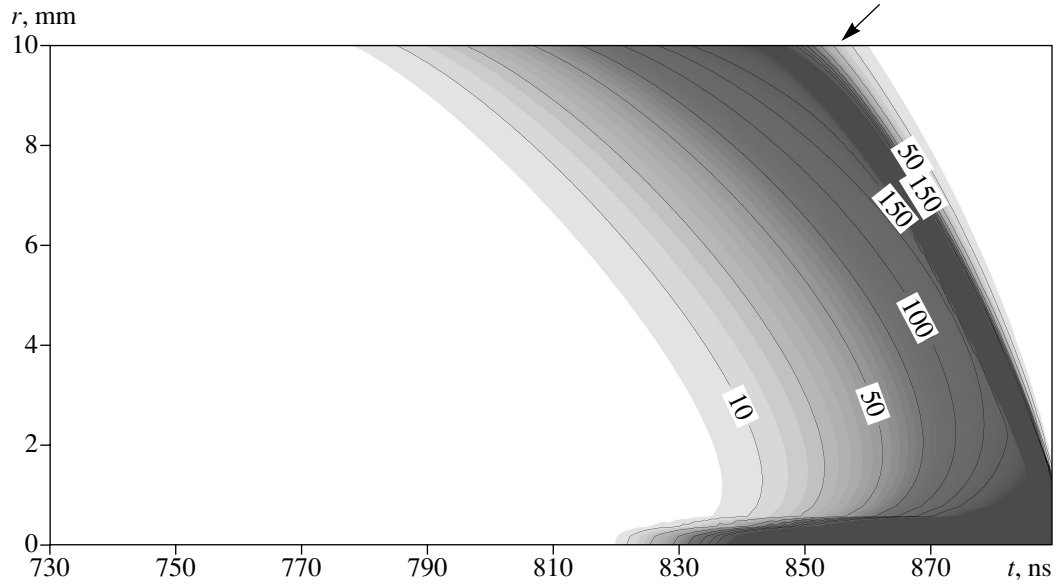

Fig. 11. Result of 1D MHD simulations of the implosion of a tungsten liner with allowance for prolonged plasma production: the contour plot of the plasma density on the (r, t) plane (numerals by the contour lines show the plasma density in units of $\mu g/cm^3$). The point of the sharp break in the outer liner boundary is indicated by the arrow.

Obviously, 1D simulations fail to provide an adequate description of all the processes occurring in an imploding liner. Thus, the model does not take into account the effects related to the onset of instabilities and the difference in the rates of plasma production in the neighboring wires, as well as the axial nonuniformity of plasma production [8]. Nevertheless, some important features of the implosion dynamics can be described in a 1D model. The simulations demonstrate that the same break in the time dependence of the outer boundary of the liner is present in the optical streak images of the transverse cross section of the liner. The simulations also reproduce exactly the behavior of the measured time dependences of $U/(dJ/dt)$ and $L(t)$, namely,

(i) these curves have flat segments corresponding to the first phase of a discharge, and

(ii) after the plasma production rate begins to decrease, a sharp increase in $U/(dJ/dt)$ and a smooth increase in $L(t)$ are observed, which corresponds to the second phase of a discharge.

7. CONCLUSIONS

The experiments performed have demonstrated that the proposed method for determining the load inductance during the implosion of a wire array can be implemented in practice. The method, which is based on measurements of the current and voltage during the implosion of a wire liner, makes it possible to determine the time behavior of the liner inductance. The time dependences of both $U/(dJ/dt)$ and L include two phases: an initial quasi-steady phase and a fast increase (over 20–35 s) before the instant of maximum compression. The same phases can be distinguished in analyzing the optical streak images of the transverse cross section of the liner. The transition between these phases corresponds to the instant at which the rate of plasma production begins to decrease.

The measured inductance in the quasi-steady phase corresponds to the inductance of a cylinder having the same diameter as the liner. This testifies to the validity of the method. Certain differences observed at large inductances can be explained by an increase in the electron-current leakage in this regime.

The compression start time determined from the visible liner size was found to coincide with that determined from electric measurements.

The average current radius, the rate of its change, and the compression ratio in terms of this radius were determined from the measured load inductance. The rate of change of the average current radius and the compression ratio turned out to be lower than those determined by other methods. This discrepancy is explained by the fact that a fraction of the current flows at the periphery of the initial wire array at the instant of maximum compression. As a result, the average current radius is larger than the visible radius in the optical or X-ray spectral region. The radiation yield can probably be increased by decreasing the current flowing at the liner periphery at the instant of maximum compression.

ACKNOWLEDGMENTS

We thank S.L. Nedoseev for fruitful discussions. This work was supported in part by the Russian Foun-

dation for Basic Research, project nos. 01-02-17319 and 01-02-17526.

REFERENCES

1. A. V. Branitsky, V. D. Vikharev, E. V. Grabovsky, *et al.*, in *Proceedings of the 8th International Conference on High-Power Particle Beams, Novosibirsk, 1990*, Vol. 1, p. 437.
2. A. V. Branitskiĭ, V. D. Vikharev, S. V. Zakharov, *et al.*, Fiz. Plazmy **17**, 531 (1991) [Sov. J. Plasma Phys. **17**, 311 (1991)].
3. R. B. Spielman, C. Deeney, G. A. Chandler, *et al.*, Phys. Plasmas **5**, 2105 (1998).
4. M. B. Bekhtev, V. D. Vikharev, S. V. Zakharov, *et al.*, Zh. Éksp. Teor. Fiz. **95**, 1653 (1989) [Sov. Phys. JETP **68**, 955 (1989)].
5. I. K. Aĭvazov, M. B. Bekhtev, V. V. Bulan, *et al.*, Fiz. Plazmy **16**, 645 (1990) [Sov. J. Plasma Phys. **16**, 373 (1990)].
6. A. Alexandrov, A. Branitskii, E. V. Grabovskii, *et al.*, in *Inertial Fusion Sciences and Application 99*, Ed. by C. Labaune, W. J. Hogan, and K. A. Tanaka (Elsevier, St. Louis, 1999), p. 591.
7. V. V. Alexandrov, E. A. Azizov, A. V. Branitsky, *et al.*, in *Proceedings of the 13th International Conference on High-Power Particle Beams, Nagaoka, 2000*, p. 147.
8. V. V. Alexandrov, M. V. Fedulov, I. N. Frolov, *et al.*, in *Proceedings of the 5th International Conference on Dense Z-Pinches, Albuquerque, 2002* (AIP, New York, 2002), Vol. 651, p. 91.
9. V. V. Aleksandrov, A. V. Branitskiĭ, G. S. Volkov, *et al.*, Fiz. Plazmy **27**, 99 (2001) [Plasma Phys. Rep. **27**, 89 (2001)].
10. S. V. Lebedev, F. N. Beg, S. N. Bland, *et al.*, Phys. Plasmas **8**, 3734 (2001).
11. M. G. Haines, S. V. Lebedev, J. P. Chittenden, *et al.*, in *Proceedings of the 5th International Conference on Dense Z-Pinches, Albuquerque, 2002*; AIP Conf. Proc. **651**, 345 (2002).
12. V. V. Aleksandrov, E. V. Grabovskiĭ, G. G. Zukakishvili, *et al.*, Zh. Éksp. Teor. Fiz. **124**, 829 (2003) [JETP **97**, 745 (2003)].
13. A. V. Branitskii, E. V. Grabovskii, M. V. Frolov, *et al.*, in *Proceedings of the 12th International Conference on High-Power Particle Beams, Haifa, 1998*, Vol. 2, p. 599.
14. V. V. Aleksandrov, A. G. Alekseev, V. N. Amosov, *et al.*, Fiz. Plazmy **29**, 1114 (2003) [Plasma Phys. Rep. **29**, 1034 (2003)].
15. V. V. Alexandrov, I. N. Frolov, M. V. Fedulov, *et al.*, in *Proceedings of the 5th International Conference on Dense Z-Pinches, Albuquerque, 2002*; AIP Conf. Proc. **651**, 87 (2002).
16. V. V. Alexandrov, I. N. Frolov, E. V. Grabovsky, *et al.*, IEEE Trans. Plasma Sci. **30**, 559 (2002).
17. E. V. Grabovskiĭ, V. I. Zaĭtsev, G. M. Oleĭnik, *et al.*, Prib. Tekh. Éksp., No. 5, 116 (1992).
18. A. V. Branitskii, E. V. Grabovskii, M. V. Fedulov, *et al.*, in *Proceedings of the 11th International Conference on High-Power Particle Beams, Prague, 1996*, p. 542.
19. Z. A. Al'bikov, E. P. Velikhov, A. I. Veretennikov, *et al.*, At. Énerg. **68**, 26 (1990).
20. G. M. Oleĭnik, Prib. Tekh. Éksp., No. 3, 49 (2000).
21. E. I. Baranchikov, A. V. Gordeev, V. D. Korolev, and V. P. Smirnov, Zh. Éksp. Teor. Fiz. **75**, 2102 (1978) [Sov. Phys. JETP **48**, 1058 (1978)].
22. I. Frolov, E. Grabovsky, K. Mitrofanov, *et al.*, in *Advanced Diagnostics for Magnetic and Inertial Fusion*, Ed. by P. E. Stott, A. Wootton, G. Gorini, *et al.* (Kluwer, New York, 2001), p. 419.
23. E. V. Grabovskiĭ, G. G. Zukakishvili, S. L. Nedoseev, *et al.*, Fiz. Plazmy **30**, 33 (2004) [Plasma Phys. Rep. **30**, 30 (2004)].
24. V. V. Aleksandrov, G. S. Volkov, E. V. Grabovskiĭ, *et al.*, Fiz. Plazmy **30**, 245 (2004) [Plasma Phys. Rep. **30**, 218 (2004)].
25. F. N. Beg, S. V. Lebedev, S. N. Bland, *et al.*, IEEE Trans. Plasma Sci. **30**, 552 (2002).

Translated by E.L. Satunina

Plasma Physics Reports, Vol. 30, No. 7, 2004, pp. 582–586. Translated from Fizika Plazmy, Vol. 30, No. 7, 2004, pp. 630–634.

BEAMS IN PLASMA

Spatial and Temporal Characteristics of Electron and Ion Beams Generated by High-Voltage Nanosecond Discharges in Dense Molecular Gases

L. P. Babich, R. I. Il'kaev, T. V. Loĭko, N. G. Pavlovskaya, and V. T. Punin

Russian Federal Nuclear Center, All-Russia Research Institute of Experimental Physics, Sarov, Nizhni Novgorod oblast, 607188 Russia

Received July 1, 2003

Abstract—Observations of ordered-structure electron beams generated by high-voltage nanosecond discharges in relatively dense (0.04–1 torr) molecular gases at high overvoltages are reported. The beams of accelerated ions generated by high-voltage nanosecond discharges are found to exhibit the same ordered structure. The observed structure of ion beams casts doubt on the mechanisms for the formation of a striped electron-beam structure that assume a regular ecton distribution. Parameters characterizing the temporal behavior of the accelerated electron and ion beams are measured. © *2004 MAIK "Nauka/Interperiodica".*

1. INTRODUCTION

High-voltage nanosecond discharges in dense gases at high overvoltages are accompanied by the generation of intense beams of runaway electrons [1]. High-voltage nanosecond discharges in deuterium at pressures of 0.01–5 torr generate nanosecond neutron pulses in a tritium-containing target placed at the cathode [2, 3]. The maximum neutron yield of 10^6 neutrons per pulse was measured at a deuterium pressure of $P = 0.3$ torr [3]. The generation of neutrons testifies that the D^+ and D_2^+ deuterium ions are accelerated to energies that ensure a rather high efficiency of nuclear fusion reactions in the target. For example, the maximum cross section for the reaction ${}_1H^3$ (${}_1d^2$, ${}_0n^1$) ${}_2He^4$ is reached at a neutron energy of 109 keV. Since the dependence of the neutron yield on the deuterium pressure has a pronounced maximum, one can conclude that the generation of accelerated ion beams is a gas-discharge effect [2]. Nuclear fusion reaction is a process of the second order of smallness relative to the generation of a gaseous plasma and the acceleration of ions. Hence, ion acceleration to much lower energies at which fusion is inefficient should take place at much higher pressures [2].

In [4, 5], a complicated spatial structure of electron beams generated by high-voltage nanosecond discharges at high vacuum was observed. The beam patterns produced by high-energy electrons behind the anode formed a system of ordered stripes. This indicates that self-organization processes play an important role in beam formation. The regular structure of beams was attributed either to the formation of an ordered distribution of the explosive centers of electron emission (ectons [6]) at the cathode as a result of the Rayleigh–Taylor instability of the explosive plasma layer on the cathode surface [4] or to the suppression of emission in the vicinity of an existing ecton [5].

In the present study, the same ordered structure was observed for electron beams generated by high-voltage nanosecond discharges in relatively dense gases at high overvoltages. The accelerated ion beams generated by high-voltage nanosecond discharges in dense gases were directly observed for the first time. The patterns of these beams exhibit the same characteristic ordered structure. Studies of the transverse structure of ion beams in a discharge provide information about the distribution of their density on the tritium target. This information is needed to efficiently use the target; it also allows one to identify the mechanism for the formation of ion beams. The parameters characterizing the time behavior of discharges are measured.

2. MEASUREMENT RESULTS AND DISCUSSION

We studied discharges in deuterium and air. The discharges were excited in a diode in which the high-voltage electrode was a 7-mm-diameter cylinder made of 50-μm tantalum foil. The cylinder was perpendicular to a plane grounded electrode. The interelectrode distance d was varied from 2 to 9 mm. Voltage pulses with an amplitude of about 800 kV, a rise time of 1 ns, and a full duration of 30 ns were applied to the diode. The high-voltage source was the high-voltage unit of the MIN-1 accelerator with a sharpening switch [3]. The stored energy was 10 J. At pressures $P = 0.05$–0.5 torr, the amplitude of the voltage pulses at the diode attained 800–400 kV; this corresponded to high overvoltages, because in the range of the gas-discharge parameter Pd under study, the static breakdown voltage was no higher than 20 kV. In the high-voltage phase of the gas dis-

1063-780X/04/3007-0582$26.00 © 2004 MAIK "Nauka/Interperiodica"

charge, current pulses with an amplitude of 2–4 kA, a rise time of ~1.0 ns, and a full duration of 15–20 ns passed through the diode. As the gas pressure increased, the current amplitude increased, whereas the duration of the current and voltage pulses decreased. At pressures above 0.5 torr, we observed an oscillatory mode with damping current oscillations. This indicates the development of breakdown, i.e., the formation of a high-conductivity plasma channel. In this mode, the neutron yield of discharges in deuterium with a tritium-containing cathode sharply decreased.

Gas discharges operating at high overvoltages are characterized by a high ionization rate. To measure the delay time of the gas-discharge current pulse relative to the voltage pulse, the current and voltage signals were fed to the input of an oscilloscope through cables of different length. The time delay was measured using the same reference signal for both cables. As a reference signal, we used the voltage pulse at the diode. When the deuterium pressure was 0.3 torr, the delay time of the current maximum with respect to the voltage maximum in the neutron-generation mode was ~1.0 ns. The current rise time was ~1.0 ns. Thus, as early as 2 ns after the beginning of the voltage pulse, the kiloampere current flowed through the diode. According to these data, the velocity of the ionization wave in the discharge gap can be estimated from below as 10^8 cm/s.

The generation of neutrons by a high-voltage nanosecond discharge in deuterium is accompanied by an intense X-ray burst generated in the anode due to the deceleration of runaway electrons accelerated in the discharge gap. To determine the time delay of neutron generation relative to the onset of the X-ray burst, both the neutron and X-ray pulses were recorded using the same detector—a CNFT-3 photomultiplier. The use of a POPOP scintillator 170 mm in diameter and 60 mm in height allowed us to enhance the detector sensitivity and perform measurements with the use of an SRG-6 oscilloscope at path lengths of 112 and 227 cm. Signals from X-ray (γ) and neutron (n) pulses were separated in time because of the different velocities of X-ray photons ($v_\gamma = c = 3 \times 10^{10}$ cm/s) and neutrons ($v_n = 5.2 \times 10^9$ cm/s) arriving at the detector. Figure 1 shows oscilloscope traces of the X-ray and neutron pulses recorded at two path lengths. The processing of 20 oscilloscope traces shows that there is a time delay between the onsets of the X-ray and DT neutron pulses; it turned out that the time interval between the γ and n signals did not agree with the transit time calculated under the assumption that neutrons and photons were generated simultaneously. The beginning of the neutron pulse was delayed from the X-ray pulse by 2–3 ns. Such a delay may be related to the time required for deuterium ions to pass through the interelectrode gap.

The electron and ion beams were recorded using a TsVID-0.1-1 dosimetric film with a mass thickness of 10 mg/cm^2.

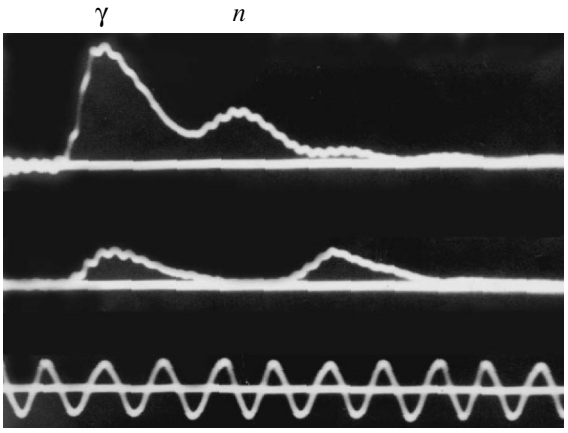

Fig. 1. Oscilloscope traces of X-ray (γ) and neutron (n) pulses at path lengths of 112 (on the top) and 227 cm. Discharges are excited in deuterium at $P = 0.3$ torr. The period of the reference sinusoid is 10 ns.

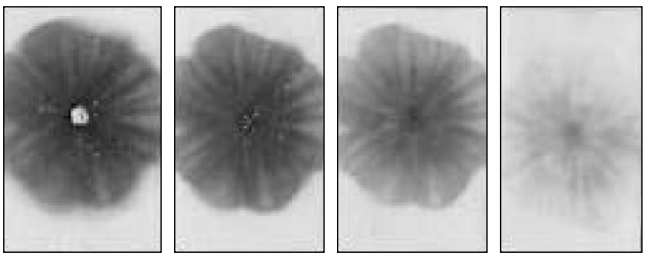

Fig. 2. Single-shot patterns of an electron beam in a package of four TsVID-0.1-1 films. The discharge is excited in deuterium at $P = 0.3$ torr and $d = 2.5$ mm. The cathode is a foil cylinder.

To study the structure of electron beams, the film was placed behind a plane grounded anode made of a 15-μm aluminum foil. A high-voltage pulse was applied to the cylindrical foil cathode. Figure 2 shows one-shot patterns of the electron beam generated by a discharge at a deuterium pressure of $P = 0.3$ torr and an interelectrode distance of $d = 2.5$ mm. A package of four films was placed behind the anode. As the beam propagated through the films, it was partially absorbed, so that each subsequent film recorded beam electrons of higher energies. The filtering by the films revealed a fine space–energy beam structure that was sharply nonuniform. We observed stripes perpendicular to the edge of the cylindrical cathode and converging to its center, where the beam density was so high that the film was locally fused. With weak filtering, the pattern diameter was nearly twice as large as the cathode diameter. The beam structure was most clearly seen in the fourth film after the low-energy electrons had been filtered by the previous films. The low-energy electrons were subject

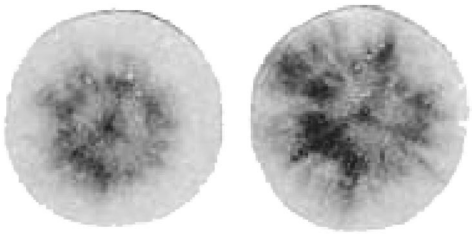

d = 2.5 mm d = 5 mm

Fig. 3. Patterns of ion beams on a TsVID-0.1-1 film. The discharge is excited in deuterium at P = 0.3 torr and two values of the interelectrode distance: d = 2.5 mm (20 shots) and d = 5 mm (35 shots). The anode is a foil cylinder.

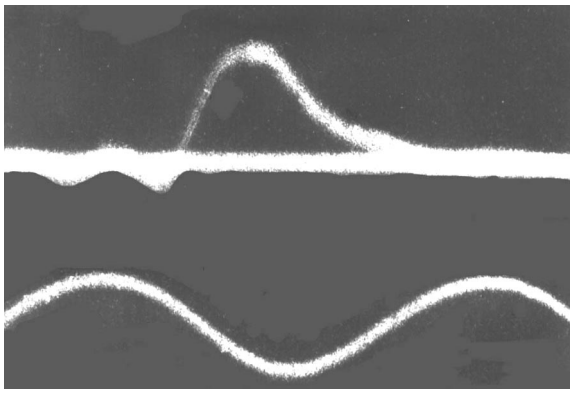

Fig. 4. Oscilloscope trace of the ion current pulse generated by a discharge in deuterium at P = 0.3 torr and d = 2.5 mm. The period of the reference sinusoid is 10 ns.

to scattering in the film material and to the action of the space-charge field, so that the initial beam structure in the low-energy range was smeared out. The beam electrons with energies above 150 keV [7] reached the fourth film. The size of the pattern produced by these electrons was somewhat larger than the cathode diameter.

The structure of ion beams was studied in a diode in which the high-voltage electrode (anode) was a foil cylinder. In the case of a cathode made of a 10-μm aluminum foil, no pattern of ion beams appeared on film placed behind the cathode even after one hundred shots. The reason was the strong absorption of deuterium ions in the foil. With a cathode made of a nickel grid with a thickness of 4 μm and a cell size of 18 μm, patterns appeared after a few dozens of shots. Figure 3 shows ion beam patterns produced at a deuterium pressure of 0.3 torr after 20 shots when the interelectrode distance was d = 2.5 mm and after 35 shots when the interelectrode distance was d = 5 mm. The patterns of the ion beams generated in deuterium discharges also exhibit stripes perpendicular to the sharp edge of the cylindrical anode. In the case of strong filtering, the ion beam structure is similar to the structure of the electron beams. This is quite natural because the ions are produced along the ionization trace of electrons in a gas. At P = 0.3 torr and d = 2.5 mm, the ion energy was determined with the help of a wedge composed of micrometer-thick Mylar films. This energy turned out to be about 300 keV.

Using the data of [8] on the neutron yield from a tritium target at different energies of the accelerated deuterons and assuming the neutron yield per one discharge to be 10^6 [3] and the duration of the neutron pulse to be 2.5 ns (for P = 0.3 torr and d = 2.5 mm), we can estimate the current of the accelerated deuterium ions in a discharge to be about 10 A, which is much lower than the total gas-discharge current (equal to 2.5 kA).

Direct measurements of the current pulse of the accelerated deuterium ions were performed using the same configuration: a positive high-voltage pulse was applied to the cylindrical foil anode, and the plane cathode was made of a nickel grid. The ions that passed through the cathode arrived at the collector, and the current signal was recorded by the oscilloscope. The collector was located at a distance of 1.7 cm from the cathode. When the deuterium pressure in the collector chamber was equal to that in the diode (0.3 torr), the recorded positive pulse was superimposed by a high-frequency electromagnetic disturbance with a frequency of about 2 GHz, which hampered the measurements of the ion current pulse. The disturbance was eliminated by evacuating the collector chamber and insulating it from the diode by a 3-μm Mylar film, which attenuated the ion beam by a factor of about 5. The beam was fully absorbed in 10-μm film. Figure 4 shows the waveform of the ion current pulse at deuterium pressures of 0.3 torr in the diode and 10^{-3} torr in the collector chamber. The pulse amplitude was ≈1.5 A, and the full width at half-maximum was $\tau_{0.5} \approx 3$ ns. Taking into account the ion absorption in the Mylar film and in the cathode, we can assume that the current of accelerated ions was no higher than 10 A. The measured time delay of the deuterium ions arriving at the collector relative to the voltage pulse was 6–7 ns. This time was related to both the delay of the discharge onset relative to the beginning of the voltage pulse and the propagation of ions through the diode discharge gap and the gap between the cathode and the collector. The measured time delay agrees with that between the hard X-ray and neutron pulses with allowance for the propagation of deuterium ions through the interelectrode gap. This time delay is also consistent with the estimate of the deuterium ion energy. Since the velocity of the deuterium ions with an energy of 300 keV is $\sim 5 \times 10^8$ cm/s, they cover a distance of 1.7 cm for nearly 3.4 ns.

Thus, along with beams of runaway electrons, beams of accelerated ions with a current much lower

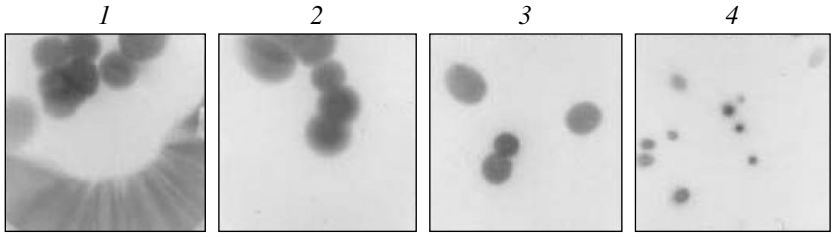

Fig. 5. Patterns of electron beams in the case of a cathode with a developed emitting surface (a 28-mm-diameter hemisphere) at different working-gas pressures P and different values of the aluminum anode thicknesses Δ: (*1*) P = 0.04 torr, Δ = 15 μm; (*2*) P = 0.04 torr, Δ = 30 μm; (*3*) P = 0.3 torr, Δ = 30 μm; and (*4*) P = 1 torr, Δ = 15 μm. Discharges are excited in air at d = 5 mm.

than the electron current are generated by high-voltage nanosecond discharges at reduced pressures.

Similar experiments were performed with discharges in air. The structures of electron and ion beams and the time behavior of ion beams generated by discharges in air turned out to be similar to those for discharges in deuterium. The patterns of the electron beams generated by discharges in air in the pressure range of P = 0.04–1 torr were obtained in one shot, except for the case of d = 5 mm and P = 1 torr, when ten shots were required, because the voltage drop at the diode (and, hence, the electron energy) decreased with increasing Pd. The typical transverse size (diameter) of electron beam patterns significantly exceeded the cathode diameter (equal to 7 mm), increased with increasing interelectrode distance d, and decreased with increasing air pressure P. Thus, at P = 0.04 torr and d = 5 mm, the pattern diameter was 25 mm, whereas at d = 9 mm, it increased to 45 mm. The clearly pronounced striped structure of an electron beam was observed up to pressures of 0.3 torr. At pressures above 1 torr, the structure was smeared out because of the electron beam collapse due to the scattering of electrons by the gas molecules. A characteristic feature of the high-voltage electrodes used in our experiments and in [1, 2] was the sharp emitting edge. The presence of a great number of ectons on the sharp edge of the foil cathode did not allow us to distinguish the effect of a single ecton. To find out whether the striped structure of charged particle beams was due to a specific electrode configuration, we performed experiments with a diode in which a smooth, massive, 28-mm-diameter steel hemisphere with a rounded edge (the rounding radius being 3 mm) was used as the high-voltage electrode (cathode). Figure 5 shows patterns of the electron beams generated in discharges in air at different pressures for two values of the aluminum foil anode thickness Δ, which places a lower limit on the energy of the beam electrons: at Δ = 15 μm, the electrons with energies above 50 keV reach the film, whereas at Δ = 30 μm, the pattern is produced by electrons with energies above 80 keV. On the spherical part of the cathode, only a few ectons were formed; the distance between the ectons was so great that the interaction between them could be ignored. At a pressure of P = 0.04 torr, the diameter of the pattern produced behind the anode by the electron beam emitted by an individual ecton was 5–6 mm, which corresponded to a beam angular divergence of 60°. As the pressure increased, the diameter decreased because of gas focusing and became equal to 1–2 mm at P = 1 torr. The pattern of the electron beam emitted by the rounded cathode edge had a pronounced striped structure. The electron energy in this beam did not exceed 80 keV, because the beam was absent behind the 30-μm-thick anode. This pattern probably reflects the distribution of ectons along the cathode edge. A similar ecton distribution was observed in vacuum discharges in an external magnetic field [6].

When the magnetic pressure of the explosive emission current is equal to the gas-dynamic pressure of the metal vapor plasma, the characteristic plasma size r can be estimated as $r^5 \approx \dfrac{6M_1 t_{\text{del}} kT}{\pi \mu_0 m_n AC}$. Here, $M_1 \approx 10^{-11}$ g is the mass of the metal evaporated from a single microscopic protrusion during a discharge (~10 ns) [6], $t_{\text{del}} \approx$ 1–10 ns is the explosion delay time, k is the Boltzmann constant, $T \approx 10^4$ K is the plasma temperature, μ_0 is the magnetic permeability of free space, m_n is the nucleon mass, A = 181 is the atomic weight of tantalum, and $C \approx 4 \times 10^{17}$ A^4 s/m^4 [6]. For the observed values of M_1, t_{del}, and T, the size r is close to the typical size of a single microscopic protrusion (~1 μm). This means that the explosive plasma cannot merge into a single layer on the cathode edge during a discharge.

3. CONCLUSIONS

High-voltage nanosecond gas discharges at high overvoltages generate beams of accelerated electrons and ions with the same complicated ordered space–energy distribution that was earlier observed in electron beams generated at high vacuum. The spatial structure of the electron beams probably reflects the regular distribution of ectons along the emitting edge of the cathode (see [4, 5]). In fact, the electron beams are formed

and accelerated near the sharp edge of the cathode, where the electric field is maximal. This is confirmed by fact that the fine structure of the electron and ion beams is preserved when the interelectrode distance is varied. However, according to the above estimates, the mechanism that implies the confluence of the plumes of explosive plasma into a unified layer which is then torn [4] seems to be nonphysical. In general, the detection of structured ion beams casts doubt on the mechanisms for the electron beam formation that assume a regular ecton distribution [4, 5]. Since the ion source is a gas ionized by electrons, the structure of ion beams is a consequence of the electron beam structure. However, the formation of an ordered distribution of ectons on a grid cathode with a large geometrical transparency seems to be improbable. The regular structure of charged particle beams is most probably a result of the filamentation of electron beams themselves with the subsequent transformation of the filaments into plane layers because of electrostatic expansion.

REFERENCES

1. L. P. Babich, T. V. Loĭko, and V. A. Tsukerman, Usp. Fiz. Nauk **160** (7), 49 (1990) [Sov. Phys. Usp. **33**, 521 (1990)].
2. L. P. Babich and T. V. Loĭko, Dokl. Akad. Nauk SSSR **313**, 846 (1990) [Sov. Phys. Dokl. **35**, 750 (1990)].
3. V. Ya. Averchenkov, L. P. Babich, T. V. Loĭko, *et al.*, Zh. Tekh. Fiz. **65** (5), 156 (1995) [Tech. Phys. **40**, 493 (1995)].
4. A. J. Toepfer and L. P. Bradley, J. Appl. Phys. **43**, 3033 (1972).
5. L. P. Babich, N. G. Pavlovskaya, and S. L. Él'yash, Izv. Vyssh. Uchebn. Zaved. Radiofiz. **18**, 769 (1975).
6. G. A. Mesyats, *Ectons in Vacuum Discharge: Breakdown, Spark, Arc* (Nauka, Moscow, 2000).
7. A. A. Vorob'ev, *Electron Propagation through Substance* (Tomsk. Gos. Univ., Tomsk, 1966).
8. G. I. Kir'yanov and S. V. Syromukov, Vopr. At. Nauki Tekh., Ser. Radiats. Tekh., No. 2, 53 (1982).

Translated by E.L. Satunina

Plasma Physics Reports, Vol. 30, No. 7, 2004, pp. 587–594. Translated from Fizika Plazmy, Vol. 30, No. 7, 2004, pp. 635–643.

PLASMA ELECTRONICS

Interaction of a High-Current Electron Beam with Hybrid Waveguide and Plasma Modes in a Dielectric Cherenkov Maser with a Plasma Layer

A. S. Shlapakovski* and E. Schamiloglu**

**Nuclear Physics Institute, Tomsk Polytechnic University, ul. Lenina 2a, Tomsk, 634050 Russia*

***Department of Electrical and Computer Engineering, University of New Mexico, Albuquerque NM, 87131 USA*

Received October 14, 2003; in final form, December 4, 2003

Abstract—The characteristics of a high-current electron beam-driven microwave amplifier—a dielectric Cherenkov maser—are investigated in the framework of linear theory for the case of a plasma layer present at the surface of the maser slow-wave structure. The dispersion relation for axisymmetric perturbations is obtained for the conventional configuration (a circular dielectric-lined waveguide and a thin annular beam propagating within the vacuum region inside the annular plasma) in the model of a fully magnetized plasma and beam. The results of numerically solving the dispersion relation for different beam and plasma parameters are presented, and an analysis based on these results is given with regard to the features of the beam interaction with the hybrid waves of the system (both hybrid waveguide and hybrid plasma modes). For the hybrid waveguide mode, the dependences of the spatial growth rate on the frequency demonstrate an improvement in the gain at moderate plasma densities, along with narrowing the amplification band and shifting it toward higher frequencies. For the hybrid plasma mode, the interaction with a mildly relativistic (200–250 keV) beam, when the wave phase velocity is close to the speed of light in the dielectric medium, is most interesting and, therefore, has been studied in detail. It is shown that, depending on the beam and plasma parameters, different regimes of the hybrid plasma mode coupling to the hybrid waveguide mode or a usual, higher order plasma mode take place; in particular, a flat gain vs. frequency dependence is possible over a very broad band. The parameters at which the –3-dB bandwidth calculated for the 30-dB peak gain exceeds an octave are found. © *2004 MAIK "Nauka/Interperiodica".*

1. INTRODUCTION

Wide-bandwidth microwave amplifiers driven by high-current electron beams represent an unexplored class of high-power pulsed microwave sources. In contrast, numerous studies of oscillators and narrow-bandwidth amplifiers have already resulted in successful developments and practical applications. Meanwhile, devices capable of frequency tuning over an octave range at 1–100 MW output power levels could be used in many interesting areas, so that their development would represent considerable progress in the field of high-power microwave electronics.

A feature necessary to achieve a large amplifier bandwidth is weak dispersion of the operating slow-wave structure mode, as is the case in the classical broadband microwave amplifier—the helix traveling wave tube (TWT). However, increasing operating voltages make a helix-type structure inappropriate to maintain the beam–wave synchronism. In classical high-power TWTs at 10–100 kV voltages, periodic slow-wave structures are used that provide a bandwidth, as a rule, of no larger than 20% due to the stronger dispersion and the presence of stopbands. In relativistic TWTs, where corrugated waveguides are employed, the bandwidth is a few percent.

At relativistic phase velocities of the microwave drive signal, relatively weak dispersion can take place in a waveguide lined with dielectric material with a small dielectric constant ε. It follows from the linear theory of a dielectric Cherenkov maser (DCM) that, under certain conditions (namely, the use of a fairly thick dielectric liner and the proper choice of the optimum beam current for a given electron energy), a DCM bandwidth of 40–50% can be achieved [1]. The first experimental investigations of the wide-bandwidth DCM amplifier prototype demonstrated the effect of strong enhancement of the output power by switching on the external microwave source operating at two well-spaced X-band frequencies, but, at the same time, showed that the above-mentioned conditions contributed to more intensive plasma production at the dielectric surface [2]. The density of the near-surface plasma layer that was formed turned out to be so high that the pulse-to-pulse instability of its parameters strongly affected the electrodynamic properties of the DCM slow-wave structure.

Meanwhile, a dense plasma in a waveguide itself supports the propagation of slow electromagnetic waves with relativistic phase velocities—the plasma modes that can have weak dispersion. Plasma relativistic microwave electronics has long been developing as an independent branch of physical electronics [3], and

1063-780X/04/3007-0587$26.00 © 2004 MAIK "Nauka/Interperiodica"

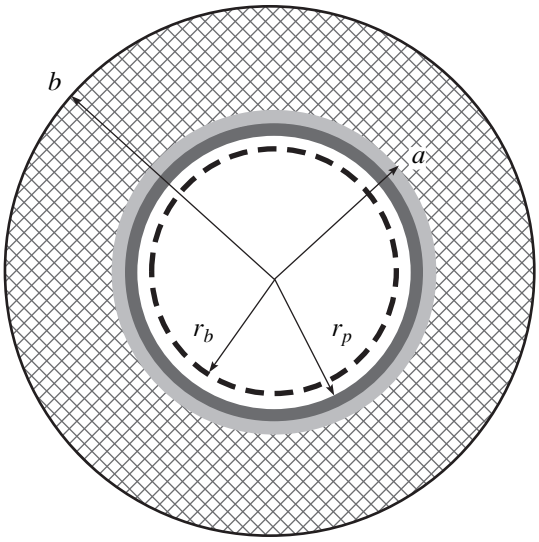

Fig. 1. Cross section of the interaction space for a DCM with a plasma layer.

the operation of plasma masers-oscillators with a very wide band of frequency tuning by means of plasma density variation was successfully demonstrated in experiments. The experiments on the plasma maser-amplifier in [3] also demonstrated the possibility of amplifying the drive signal at two well-spaced X-band frequencies at a fixed plasma density. The calculations of the gain, as was noted in [4], show that a bandwidth of ~40% is achievable. The conventional configuration of a plasma maser comprises a circular metallic waveguide, an annular plasma column, and an annular electron beam propagating within the plasma column. If one fills the space between the plasma and the smooth conducting wall of this configuration with a uniform isotropic dielectric, then a DCM configuration with a plasma layer results.

On the other hand, a DCM with a plasma layer can be considered to be a kind of plasma-filled TWT. Numerous investigations (see, e.g., [5, 6] and references therein) have shown that the presence of a controlled amount of plasma inside a slow-wave structure can improve the characteristics of Cherenkov microwave oscillators and amplifiers in comparison to their vacuum operation. In this way, in relativistic backward-wave oscillators, a multifold [7, 8] or modest [6] increase in the output power was achieved, but, in any case, at certain optimal plasma densities. In the devices known as PASOTRONs [9], neutralizing the beam space charge by means of the plasma makes possible the operation of a Cherenkov microwave oscillator without an external magnetic field; in addition, a specific mechanism of efficiency enhancement appears [10]. In a nonrelativistic plasma-filled coupled-cavity TWT amplifier [11], the power and gain-bandwidth were more than doubled as compared to the vacuum case. Here, the combination of the output power and bandwidth levels (>20 kW and ~30% in the continuous operation mode) remains inaccessible for vacuum amplifiers. In this case, the physical mechanism for such an achievement is the formation of hybrid waves in the system that have properties of both plasma and waveguide modes.

The hybrid modes existing in slow-wave structures with partial plasma filling [11, 12] are strongly coupled to the electron beam, which is typical of plasma modes.[1] At the same time, the microwave energy transmitted by these waves is concentrated mainly outside the plasma, so that it can be extracted with minimal losses. The hybrid modes are formed as a result of the deep transformation of usual waveguide and plasma modes: the waveguide mode, the microwave field profile of which is changed due to the presence of plasma, and the plasma mode, which is transformed by surrounding the plasma column with some slowing medium (artificial or natural), represent two different types of hybrid modes. The existence of two types of hybrid modes is especially important in view of the problem of the development of high-power wide-bandwidth amplifiers. The hybrid waveguide mode is characterized by an increased coupling impedance, whereas the hybrid plasma mode can have a weaker dispersion compared to the usual plasma mode. In addition, an important fact is that the hybrid plasma and waveguide modes having the same phase velocity at different eigenfrequencies can be coupled through the electron beam of sufficiently large current; this also leads to the expansion of the amplification band. Therefore, the plasma loading of a smooth slow-wave structure seems promising for obtaining an octave amplification bandwidth.

In this work, a linear theory has been developed for a DCM with a thin annular electron beam and a plasma layer adjoining the dielectric liner surface (Fig.1). The electrodynamics of the cold system (no beam case) was investigated in detail in [2]. The consideration of a system with a plasma layer has two aims: on the one hand, it allows one to determine the degree of plasma influence on the characteristics of a vacuum DCM and to analyze, on this basis, particular results of the first experiments [2]. The analysis of the beam interaction with the hybrid waveguide mode leads to this goal. On the other hand, in a system with a plasma layer, the dispersion of the hybrid plasma mode can be very weak. The phase velocity here corresponds to a relatively low kinetic energy (200–250 keV), the coupling impedance is sufficiently high, and the portion of the microwave power contained in the dielectric region approaches

[1] In [3], hybrid microwave devices are defined as usual vacuum microwave tubes with plasma filling in which the mechanism for wave excitation is the same as in the vacuum case. Cherenkov devices operating in the hybrid modes, however, do not come under this definition, unlike the devices of [7–10], because their operating frequency is lower than the plasma frequency, as it is in plasma masers, and, therefore, the presence of plasma is of fundamental importance for their operation.

80% [2]. The analysis of the beam interaction with the hybrid plasma mode allows one to answer whether a superwide (octave) bandwidth is achievable in this case.

It should be noted that earlier theoretical investigations of the Cherenkov interaction with a beam in the case of annular plasma geometry (beginning from the work [13] until now) were only carried out for the plasma maser configuration [3]. For a dielectric-lined waveguide loaded with plasma, the models of solid (pencil) plasma were considered for the cases of the total [14, 15] or partial [16, 17] filling of the beam transport channel of the waveguide and the analysis was usually limited to the hybrid waveguide mode.

2. DISPERSION RELATION

The geometric parameters of the system under consideration are depicted in Fig. 1. The dielectric liner has the inner radius a and the outer radius b (equal to the radius of the circular metallic waveguide). The plasma layer of inner radius r_p adjoins the dielectric surface. The electron beam of radius r_b is assumed to be infinitesimally thin. As in [2], the plasma is assumed to be fully magnetized, uniform, cold, and collisionless; ion motion is ignored. The validity of the conditions for this model was discussed in [2]. Accordingly, the beam is assumed to be fully magnetized and monoenergetic as well.

We consider axisymmetric TM waves, i.e., perturbations proportional to $\exp\{i(kz - \omega t)\}$, where ω and k stand for the circular frequency and axial wavenumber, respectively. The wave equations for the E_z component of the microwave field in the vacuum, plasma (in the linear approximation), and dielectric regions are reduced to the following equations describing its dependence on the radial coordinate:

$$\begin{aligned}
&\frac{1}{r}\frac{d}{dr}\left(r\frac{dE_z}{dr}\right) - q^2 E_z = 0, \quad 0 < r_p, \\
&\frac{1}{r}\frac{d}{dr}\left(r\frac{dE_z}{dr}\right) - \kappa^2 E_z = 0, \quad r_p < r < a, \\
&\frac{1}{r}\frac{d}{dr}\left(r\frac{dE_z}{dr}\right) + p^2 E_z = 0, \quad a < r < b,
\end{aligned} \tag{1}$$

where q, κ, and p are the corresponding transverse wavenumbers,

$$-q^2 = \frac{\omega^2}{c^2} - k^2, \quad \kappa^2 = q^2\left(1 - \frac{\omega_p^2}{\omega^2}\right), \quad p^2 = \varepsilon\frac{\omega^2}{c^2} - k^2,$$

ω_p is the electron plasma frequency; and c is the speed of light in vacuum.

For a relativistic electron beam, integration of the linearized equation for E_z over an infinitesimally small interval results in the condition for the jump in the derivative at $r = r_b$:

$$\left\{\frac{dE_z}{dr}\right\}_{r = r_b} = -\frac{2I_b}{\beta\gamma^3 I_A}\frac{q^2c^2}{(\omega - ku)^2}\frac{E_z(r_b)}{r_b}. \tag{2}$$

Here, I_b is the beam current; $I_A = mc^3/e$; m and e are the electron rest mass and charge, respectively; $u = \beta c$ is the beam velocity; and γ is the Lorentz factor. The corresponding conditions at the plasma–vacuum and plasma–dielectric boundaries (the continuity of the H_φ component) are

$$\left\{\frac{dE_z}{dr}\right\}_{r = r_p} = 0, \quad \frac{1}{q^2}\frac{dE_z}{dr}\bigg|_{r = a - 0} = -\frac{\varepsilon}{p^2}\frac{dE_z}{dr}\bigg|_{r = a + 0}. \tag{3}$$

Matching the solutions of Eqs. (1) with the use of conditions (2) and (3) and the continuity conditions for E_z at all the boundaries and accounting for the condition $E_z = 0$ at the conducting waveguide wall, one can finally obtain (after simple but tedious formula manipulations) the following dispersion relation:

$$\begin{aligned}
D(\omega, k)&\left[(\omega - ku)^2 - \frac{2q^2c^2I_b}{\beta\gamma^3 I_A}\Phi(qr_p, qr_b)\frac{I_0(qr_b)}{I_0(qr_p)}\right] \\
&= \frac{2q^2c^2I_b}{\beta\gamma^3 I_A}\frac{I_0^2(qr_b)}{I_0^2(qr_p)} \\
&\times \frac{\Phi'(\kappa a, \kappa r_p) - \dfrac{\varepsilon q^2}{\kappa p}\dfrac{F'(pa, pb)}{F(pa, pb)}\Phi(\kappa r_p, \kappa a)}{\kappa r_p\Phi'(\kappa r_p, \kappa a) - qr_p\dfrac{I_0'(qr_p)}{I_0(qr_p)}\Phi(\kappa r_p, \kappa a)}.
\end{aligned} \tag{4}$$

Here,

$$\begin{aligned}
D(\omega, k) &= \frac{\varepsilon q^2}{\kappa p}\frac{F'(pa, pb)}{F(pa, pb)} \\
&+ \frac{\Phi''(\kappa r_p, \kappa a) + \dfrac{q}{\kappa}\dfrac{I_0'(qr_p)}{I_0(qr_p)}\Phi'(\kappa a, \kappa r_p)}{\Phi'(\kappa r_p, \kappa a) - \dfrac{q}{\kappa}\dfrac{I_0'(qr_p)}{I_0(qr_p)}\Phi(\kappa r_p, \kappa a)},
\end{aligned}$$

and the functions entering Eq. (4) are defined as

$$\begin{aligned}
F(x, y) &= J_0(x)Y_0(y) - J_0(y)Y_0(x), \\
F'(x, y) &= J_0'(x)Y_0(y) - J_0(y)Y_0'(x), \\
\Phi(x, y) &= I_0(x)K_0(y) - I_0(y)K_0(x), \\
\Phi'(x, y) &= I_0'(x)K_0(y) - I_0(y)K_0'(x), \\
\Phi''(x, y) &= I_0'(x)K_0'(y) - I_0'(y)K_0'(x),
\end{aligned}$$

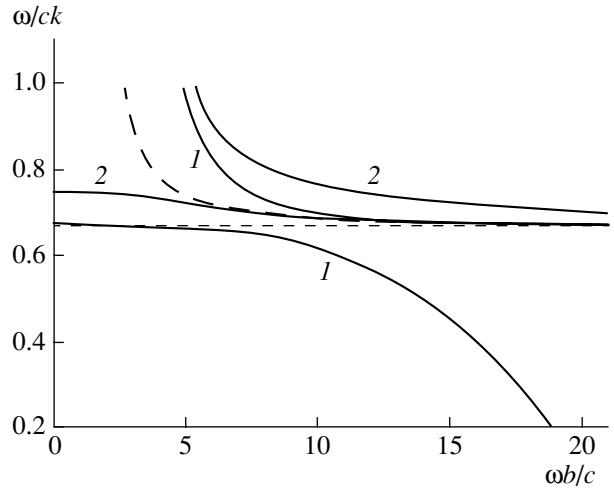

Fig. 2. Dispersion of the waveguide and plasma modes for a circular dielectric-lined waveguide with a plasma layer for $\varepsilon = 2.25$, $a/b = 0.5$, and $r_p/b = 0.42$ at different values of the plasma frequency: $\omega_p b/c$ = (*1*) 20 and (*2*) 40. The dashed curve corresponds to the waveguide mode dispersion in the absence of plasma. The horizontal dashed line corresponds to the speed of light in the dielectric.

where J_0 and Y_0 are Bessel functions and I_0 and K_0 are modified Bessel functions.

The equation $D(\omega, k) = 0$ represents the dispersion relation for a cold system (see [2]). In the absence of plasma, one can show that, upon taking the limits $\omega_p \longrightarrow 0$ or $r_p \longrightarrow a$, Eq. (4) reduces to the dispersion relation for a DCM with a thin annular beam (see, e.g., [1]).

Equation (4) was solved numerically using an iterative algorithm that employed the analytical solution (found at the frequency of velocity synchronism with the beam for a given cold system mode) as an initial approximation. Such an approach allows one to unambiguously identify the regimes of beam interaction with hybrid waveguide or hybrid plasma modes, as well as regimes of coupling the modes to one another through the electron beam. Before analyzing the numerical results, let us characterize the properties of the hybrid modes in greater detail.

In Fig. 2, the phase velocity vs. frequency dependences obtained by solving the equation $D(\omega, k) = 0$ at two values of the plasma frequency are shown for the fundamental (with the lowest radial index) waveguide and plasma modes. As usual, the waveguide mode is characterized by the appearance of a cut-off frequency and its phase velocity approaches the speed of light (in the medium) with increasing frequency, whereas the plasma mode has no cut-off frequency and its phase velocity varies from a maximum at $\omega \longrightarrow 0$ to zero at $\omega \longrightarrow \omega_p$. The "hybridity" of the waveguide and plasma modes occurs at certain portions of their dispersion curves. For the hybrid waveguide mode, this is the portion where the phase velocity is less than c and the frequency is lower than ω_p. Within the frequency ranges for which the dispersion curves are presented in Fig. 2, the waveguide mode is hybrid for both curves *1* and *2*. For the hybrid plasma mode, this is the portion where the phase velocity exceeds the speed of light in the dielectric. The plasma mode represented by curve *2* in Fig. 2 is hybrid within all the range shown, whereas for curve *1*, the portion to the right of the crossing with the dashed straight line corresponds to the usual plasma mode: the hybrid wave here corresponds to the low-frequency portion. The hybrid waveguide mode differs from the usual one in that its field has the volume profile in the region of the plasma layer, rather than is evanescent from the dielectric surface to the axis. As was shown in [2], the field profile in the dielectric region becomes similar to that of the higher order mode of a coaxial waveguide; this transformation is the main cause of the increase in the coupling impedance in the system with a plasma layer, in contrast to the solid plasma case. The hybrid plasma mode differs from the usual one in that its field has the volume profile in the dielectric region, rather than being evanescent from the plasma surface to the waveguide wall. Here, if the phase velocity is close to $c/\sqrt{\varepsilon}$, then the field in the dielectric becomes nearly transverse, like that of the TEM mode of a coaxial waveguide.

Finally, we note that synchronism with the beam is impossible for the plasma mode if the beam velocity exceeds the maximum phase velocity of the plasma mode. Nevertheless, if the beam current exceeds a certain value, amplification occurs in the regime of collective (Raman) interaction. The algorithm of the solution of dispersion relation (4) allows one to identify this regime, which, as will be shown below, plays an important role in providing a superwide amplification band.

3. NUMERICAL RESULTS

3.1. Hybrid Waveguide Mode: the Influence of Plasma Density

The beam interaction with the hybrid waveguide mode was investigated for the parameters of the electron beam and dielectric waveguide corresponding to the experimental conditions in [2]. The thickness of the plasma layer was taken such that the plasma filled 80% of the gap between the beam and the liner surface. In Fig. 3, the influence of the magnitude of the plasma density in the layer on the DCM gain and bandwidth is shown. One can see that, at $\omega_p b/c = 3$ (curve *1*), the dependence of the instability spatial growth rate on the frequency is practically identical to that in the absence of plasma (dashed curve). It should be noted that, in the absence of plasma, the frequency of the waveguide mode synchronous with the beam at the given parameters corresponds to $\omega b/c \approx 3.45$. Hence, at the peak gain of curve *1*, the interaction with the usual waveguide mode takes place. Although the plasma frequency here is not much less than ω, one can say that the presence

of plasma does not affect the amplifier characteristics. The situation is changed when the plasma density increases to such values that the interaction occurs with the hybrid waveguide mode at any frequency over the entire amplification band. It is seen from Fig. 3 that, in this case, the gain increases significantly and reaches its maximum with increasing plasma density (curve *3*). In addition, the amplification band shifts toward higher frequencies as the plasma frequency increases (as is seen from Fig. 2, this is caused by shifting the synchronous frequency), so that the relative bandwidth decreases considerably.

Shifting the amplification band in the case of interaction with the hybrid waveguide mode greatly affects the dependence of the gain on the plasma density at a given frequency; this can easily be observed in experiments. The dependence of the output power of the plasma-filled coupled-cavity TWT [11] on the gas pressure in the slow-wave structure is well known: the power first remains constant with increasing pressure (which corresponds to the interaction with the usual structure mode), and a rapid growth is then observed, followed by a rapid decrease after the optimal plasma density is exceeded. For a DCM with a plasma layer, an analysis of the dependence of the hybrid waveguide mode coupling impedance on the plasma density at a fixed frequency [2] allows one to draw the conclusion about the disruption of amplification at high densities. The growth rate vs. plasma frequency dependence for a given frequency, which is important from the standpoint of comparison with the experiment, is presented in Fig. 4.

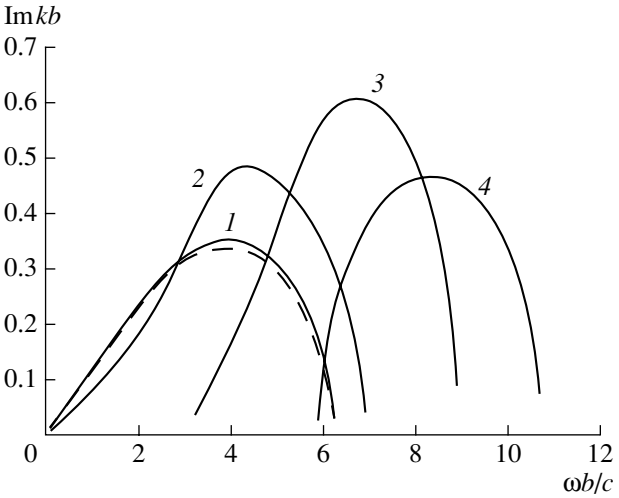

Fig. 3. Spatial growth rate vs. frequency at different values of the plasma frequency: $\omega_p b/c$ = (*1*) 3, (*2*) 10, (*3*) 20, and (*4*) 30. The dashed curve corresponds to the case of $\omega_p = 0$. The parameters of the electron beam are $\gamma = 1.8$, $I_b/I_A = 0.2$, and $r_b/b = 0.4$. The parameters of the dielectric liner and plasma layer are the same as in Fig. 2.

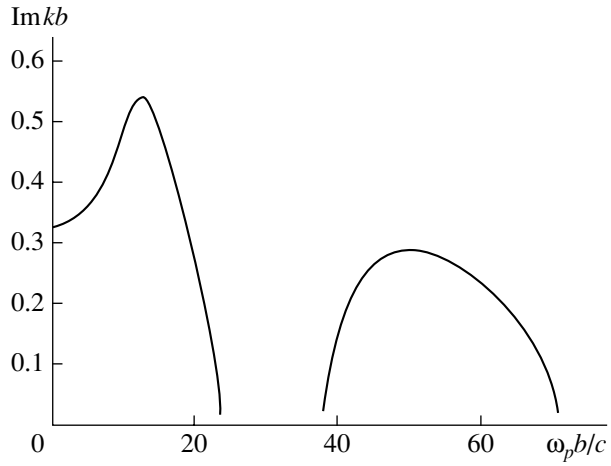

Fig. 4. Spatial growth rate vs. plasma frequency at the fixed frequency $\omega b/c = 4.5$. The other parameters are the same as in Fig. 3.

3.2. Effect of "Substitution"

The calculations were performed for the normalized frequency $\omega b/c = 4.5$, corresponding to one of the drive signal frequencies of the experiment on the wide-bandwidth DCM prototype [2]. Figure 4 gives a manifest explanation of the observed poor reproducibility of output microwave pulses. It is seen how strongly the gain at the given frequency depends on the density of the plasma layer. Therefore, the unstable character of plasma formation, as well as the possible dependence of the plasma density on the drive signal power, leads to very large variations of the output power from pulse to pulse. At the same time, it turns out that, after the amplification fails in the hybrid waveguide mode, the gain at the given frequency appears anew as the plasma frequency increases further. This is now due to the beam interaction with the hybrid plasma mode. The values of Imk in the peak portion of the right curve in Fig. 4 are only 10% smaller than for the interaction with the usual waveguide mode. The possibility of such "substitution" was also noticed in [2]. Note that in the range of plasma frequencies corresponding to the gain in the hybrid plasma mode, the interaction occurs first in the Raman regime (see the dispersion curve for $\omega_p b/c = 40$ in Fig. 2), and then, with increasing plasma frequency, the phase velocity of the hybrid plasma mode reaches the value synchronous with the beam and finally exceeds the beam velocity so much that the gain disappears once again.

Comparison of Fig. 4 with the experimental data shows that, in the wide-bandwidth DCM prototype, the amplification of the hybrid plasma mode might occur. The peak corresponding to the plasma mode is broader compared to the hybrid waveguide mode; therefore, an amplifier operating in the hybrid plasma mode can be less sensitive to variations in the plasma layer parameters. Nevertheless, at these parameters, the regime of interaction with the hybrid waveguide mode is much

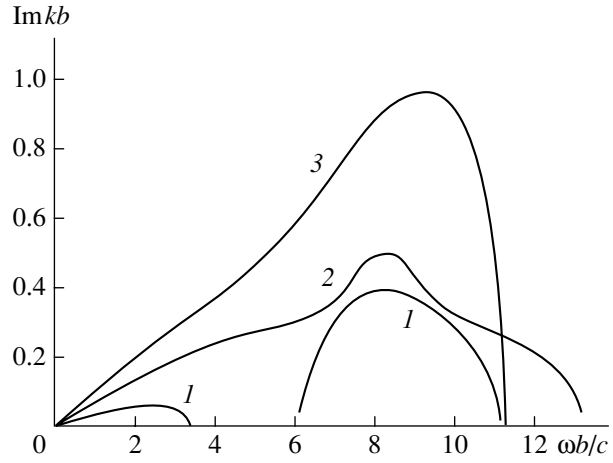

Fig. 5. Spatial growth rate vs. frequency at different beam currents for $\gamma = 1.5$, $\omega_p b/c = 20$, and different values of the beam current: I_b/I_A = (*1*) 0.03, (*2*) 0.065, and (*3*) 0.12. The other parameters are the same as in Figs. 2–4.

more attractive. First, in this case, the gain at the optimal plasma density is almost twice as high, whereas the bandwidth, as follows from the calculations, is not narrower than for the hybrid plasma mode. Second, for the hybrid plasma mode, the calculations of the Poynting flux (without a beam) show that more than 70% of the transmitted microwave power is concentrated in the region of the plasma layer; hence, the microwave extraction losses would be large. The interaction with the hybrid plasma mode is of interest in the case of lower electron energy, when the beam velocity just slightly exceeds the Cherenkov threshold and the main portion of the transmitted power is concentrated in the dielectric region.

3.3. Hybrid Plasma Mode

In Fig. 5, the results of the solution of dispersion relation (4) are presented for $\gamma = 1.5$ and different beam currents at a normalized plasma frequency of $\omega_p b/c = 20$. The liner parameters and the geometric parameters of the beam and plasma layer are taken to be the same as those for calculations presented above in Figs. 2–4. The value of the Lorentz factor corresponding to the maximum phase velocity of the hybrid plasma mode (see Fig. 2) is ≈1.35; i.e., this velocity is lower than the beam velocity. Thus, amplification here results from the synchronism between the plasma mode and the slow beam space charge mode (Raman regime), whose phase velocity is less than the beam velocity by a value depending on the current magnitude I_b. Amplification only occurs at sufficiently high currents; however, it is the large I_b values corresponding to megawatt levels of the output microwave power that are of interest to us.

It is seen from Fig. 5, that for $I_b \approx 510$ A (curve *1*), the amplification bands corresponding to the hybrid plasma and hybrid waveguide modes are well separated on the frequency axis. For the hybrid plasma mode, the gain vs. frequency dependence is much flatter; it is predetermined by its very weak dispersion in this frequency range (see Fig. 2). Nevertheless, the –3-dB bandwidth calculated for a peak gain of 30 dB is ≈43%, which is quite far from an octave. This value is on the same order as for a conventional DCM [1]. In addition, the gain in the hybrid waveguide mode is much higher, though its bandwidth is twice as narrow. As the beam current increases, the phase velocity of the slow space charge mode decreases and its interaction with the plasma mode occurs over a significantly wider frequency range. The spatial growth rate increases, and the hybrid plasma and waveguide modes are coupled through the electron beam, so that their amplification bands merge into one. However, in spite of such overlapping, the –3-dB bandwidth does not become larger. It is seen from Fig. 5 that, for $I_b \approx 1.1$ kA (curve *2*), the gain vs. frequency dependence has a typical "hat," so that, at the –3-dB level from the 30-dB peak gain, the bandwidth is only ≈16%.

It should be noted that similar curves with a "hat" were also obtained in [17], where the case of a solid beam in a plasma-loaded helix-type slow-wave structure was considered. One can interpret the presence of such a hat as the increase in the instability growth rate over a relatively narrow frequency range, where the coupling between the hybrid plasma and waveguide modes occurs. A further increase in the current (curve *3*) leads to a sharp increase in the gain due to strong coupling, as in [17]; the bandwidth also increases, but insignificantly.

A superwide bandwidth in the hybrid plasma mode can be achieved at higher plasma densities. This possibility is illustrated in Fig. 6 for $\omega_p b/c = 40$. In this case, as one can see by comparing curves *1* and *2*, the increase in the beam current does not lead to a coupling to the hybrid waveguide mode since, for the latter, the interaction regime also becomes Raman and the amplification band shifts significantly. At the same time, curve *3*, corresponding to a current of $I_b \approx 3.1$ kA, has a very extended plateau. For the parameters of curve *3*, the –3-dB bandwidth is ≈74% (at the 30-dB peak gain); i.e., it exceeds an octave. At the given energy of the beam electrons (~250 keV), the output power of such a microwave amplifier could be a few tens of megawatts.

3.4. Superwide Bandwidth as a Result of the Hybrid Plasma Mode Coupling to the Usual Higher Order Plasma Mode

A comparison of the dispersion curves of the hybrid plasma mode for the two values of the normalized plasma frequency under consideration (see Fig. 2) allows one to suppose that, for $\omega_p b/c = 40$, the bandwidth can be superwide because of the weaker dispersion. Meanwhile, the possibility of obtaining an octave

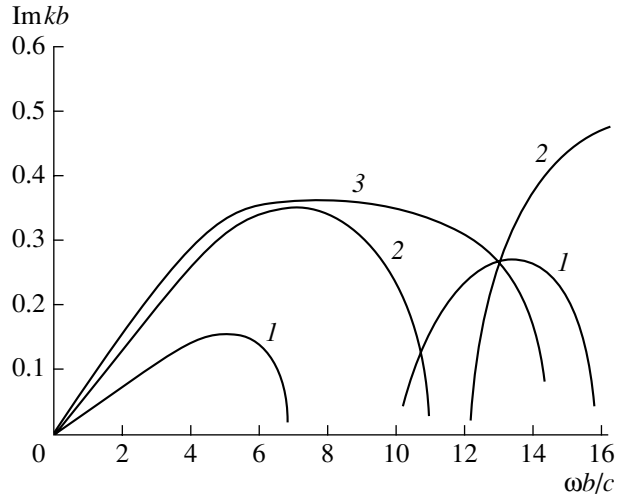

Fig. 6. The same as in Fig. 5 except for $\omega_p b/c = 40$ and I_b/I_A = (*1*) 0.01, (*2*) 0.09, and (*3*) 0.18.

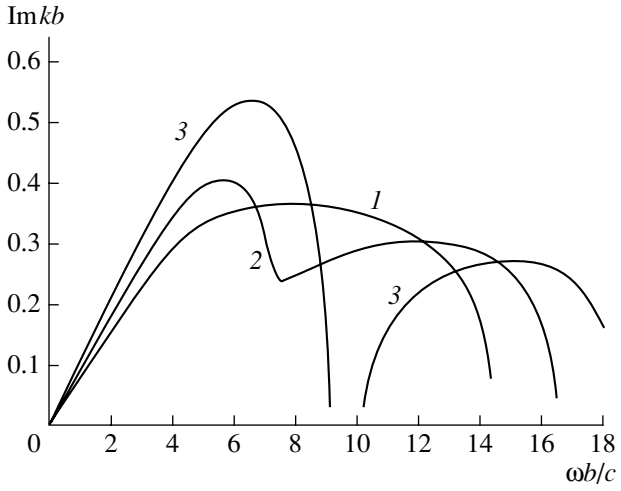

Fig. 7. The same as in Fig. 6 except for I_b/I_A = (*1*) 0.18, (*2*) 0.23, and (*3*) 0.27.

bandwidth is related not only (and not so much) to the weak dispersion, but also to the coupling of the hybrid plasma mode to the usual higher order plasma mode. This becomes evident under more detailed analysis of the growth rate vs. frequency dependences in the parameter range yielding such a wide bandwidth.

In Fig. 7, the dependences obtained by further increasing the beam current from the value $I_b \approx 3.1$ kA are depicted (curve *1* replicates the dependence with an extended plateau presented above in Fig. 6). It is seen how the character of the dependence changes: a local minimum appears, the low-frequency maximum increases, the high-frequency maximum decreases (curve *2*), and the amplification band is finally split into two parts (curve *3*). Such behavior means that interaction with two different modes takes place in this case. The modes are coupled at the beam current within a certain range, and the mode corresponding to the low-frequency band is the usual higher order plasma mode.

Indeed, it is well known that the spectrum of plasma modes becomes denser as the plasma density increases. In Fig. 8, the dispersion curve is shown that was calculated for the plasma mode next (in the radial index) to the lowest hybrid plasma mode at the given parameters. The phase velocity of this mode is everywhere lower than the speed of light in the liner material; i.e., this is the usual plasma mode. Nevertheless, the relative difference in phase velocities with respect to the lowest, hybrid plasma mode is quite small. The beam velocity in our case slightly exceeds the Cherenkov threshold for the given dielectric. At a relatively low beam current (as is the case, e.g., for curve *1* in Fig. 6), the phase velocity of the slow space charge mode remains superluminal and the interaction at low frequencies occurs with the hybrid plasma mode alone. As the current increases, the velocity of the space charge wave possesses values intermediate between the phase velocities of the hybrid and next mode. This makes possible beam interaction with both modes, and the coupling of the two modes appears. At a sufficiently high current (Fig. 7, curve *3*), the phase velocity of the space charge wave becomes such that its synchronism is only possible with the usual higher order plasma mode at low frequencies and with the hybrid mode at high frequencies. This results in the splitting of the amplification band.

One can observe the same band splitting at a fixed beam current if other parameters affecting the phase velocities of the slow beam space charge mode and the lowest and next plasma modes are varied. This is illustrated in Fig. 9, where the gain vs. frequency dependences are presented for different values of the electron energy. It should be noted that the relative energy variation resulting in the band splitting is very small; hence,

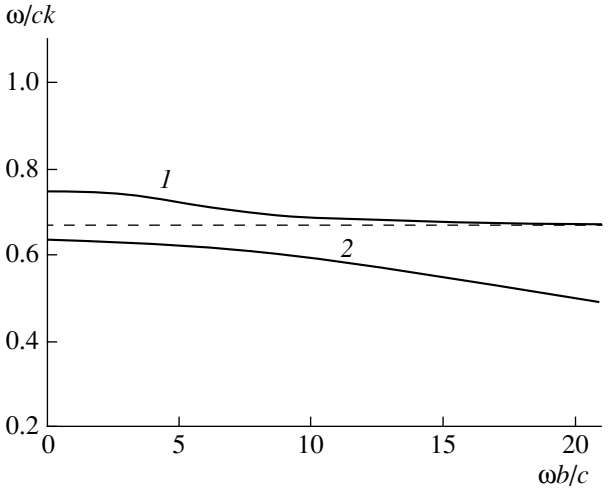

Fig. 8. Dispersion of (*1*) the lowest (in the radial index) and (*2*) second plasma modes at $\omega_p b/c = 40$. The other parameters are the same as in Fig. 2. The dashed line corresponds to the speed of light in the dielectric.

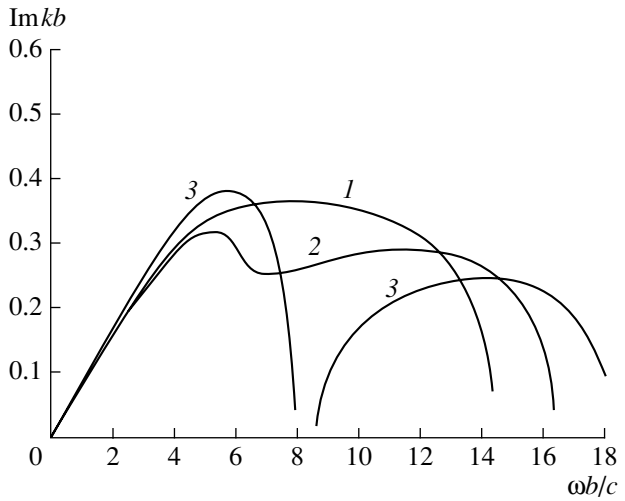

Fig. 9. Spatial growth rate vs. frequency at different values of the electron energy for $\omega_p b/c = 40$, $I_b/I_A = 0.18$, and different values of the Lorentz factor: $\gamma = (1)$ 1.5, (*2*) 1.485, and (*3*) 1.475. The other parameters are the same as in Figs. 2–8.

the regime with a superwide bandwidth can be very sensitive to the poor stability of the beam and plasma parameters.

4. CONCLUSIONS

We have derived a dispersion relation using the linear theory for a DCM with a plasma layer and analyzed the results of its numerical solution. Different regimes of the Cherenkov interaction of a high-current electron beam with hybrid waves in the smooth slow-wave structure with a near-surface plasma have been investigated. For the interaction with the hybrid waveguide mode, the character of plasma influence on the amplifier operation has been determined, in particular, for the conditions of the experiment with the wide-bandwidth DCM prototype [2]. It has been shown that, as the plasma density increases, the hybrid waveguide mode is "substituted" with the hybrid plasma mode in the interaction with the beam at a fixed frequency. Such a substitution is, on the whole, undesirable for the case of a relativistic beam whose velocity significantly exceeds the Cherenkov threshold for the dielectric liner material. Meanwhile, for a mildly relativistic beam whose velocity just slightly exceeds the speed of light in the dielectric, it has been shown that superwide bandwidth operation is possible in the regime of collective (Raman) interaction with the hybrid plasma mode. The parameters at which the –3-dB bandwidth calculated for a peak gain of 30 dB exceeds an octave have been found. At these parameters, the beam energy and current are such that the corresponding microwave amplifier could have an output power at a level of a few tens of megawatts and the gain estimations give quite reasonable values on the order of 0.8–1.0 dB/cm for X-band frequencies. At the same time, the regime of interaction with the hybrid plasma mode providing a superwide bandwidth can be rather sensitive to the poor stability of the beam and plasma parameters. Therefore, further investigations of this regime are necessary to be performed in more adequate models compared to the one considered in this work, in particular, for a beam of finite thickness and at a finite guiding magnetic field.

ACKNOWLEDGMENTS

This work was supported in part by the Russian Foundation for Basic Research (grant no. 00-02-17720) and the NATO–Russia Collaborative Linkage Grant (no. 978693).

REFERENCES

1. A. Shlapakovski and K. Chirko, IEEE Trans. Plasma Sci. **22**, 544 (1994).
2. G. V. Mel'nikov, A. V. Petrov, and A. S. Shlapakovskii, Fiz. Plazmy **26**, 1085 (2000) [Plasma Phys. Rep. **26**, 1015 (2000)].
3. M. V. Kuzelev, O. T. Loza, A. A. Rukhadze, *et al.*, Fiz. Plazmy **27**, 710 (2001) [Plasma Phys. Rep. **27**, 669 (2001)].
4. A. V. Ponomarev, P. S. Strelkov, and A. G. Shkvarunets, in *Proceedings of the 12th Symposium on High Current Electronics, Tomsk, 2000*, p. 437.
5. G. S. Nusinovich, Y. Carmel, T. M. Antonsen, Jr., *et al.*, IEEE Trans. Plasma Sci. **26**, 628 (1998).
6. C. Grabowski, J. M. Gahl, and E. Schamiloglu, IEEE Trans. Plasma Sci. **26**, 653 (1998).
7. Y. Carmel, K. Minami, W. R. Lou, *et al.*, IEEE Trans. Plasma Sci. **18**, 497 (1990).
8. X. Zhai, E. Garate, R. Prohaska, and G. Benford, Appl. Phys. Lett. **60**, 2332 (1992).
9. D. M. Goebel, J. M. Butler, R. W. Schumacher, *et al.*, IEEE Trans. Plasma Sci. **22**, 547 (1994).
10. T. M. Abu-elfadl, G. S. Nusinovich, A. G. Shkvarunets, *et al.*, IEEE Trans. Plasma Sci. **30**, 1126 (2002).
11. M. A. Zavyalov, L. A. Mitin, V. I. Perevodchicov, *et al.*, IEEE Trans. Plasma Sci. **22**, 600 (1994).
12. V. I. Kanavets, N. I. Karbushev, E. I. Ostrenskiĭ, and A. I. Slepkov, Radiotekh. Élektron. (Moscow) **35**, 2574 (1990).
13. M. V. Kuzelev, F. Kh. Mukhametzyanov, and A. G. Shkvarunets, Fiz. Plazmy **9**, 1137 (1983) [Sov. J. Plasma Phys. **9**, 655 (1983)].
14. H. Kosai, E. Garate, and A. Fisher, IEEE Trans. Plasma Sci. **18**, 1002 (1990).
15. A. K. Berezin, N. M. Zemlyanskiĭ, V. I. Mirnyi, *et al.*, Ukr. Fiz. Zh. **37**, 999 (1992).
16. A. G. Shkvarunets, S. Kobayashi, J. Weaver, *et al.*, IEEE Trans. Plasma Sci. **24**, 905 (1996).
17. S. Kobayashi, T. M. Antonsen, Jr., and G. S. Nusinovich, IEEE Trans. Plasma Sci. **26**, 669 (1998).

Translated by the authors

Plasma Physics Reports, Vol. 30, No. 7, 2004, pp. 595–604. Translated from Fizika Plazmy, Vol. 30, No. 7, 2004, pp. 644–653.

NONLINEAR PHENOMENA

Lasing without Inversion and Electromagnetically Induced Transparency under Electron Cyclotron Resonance Conditions

M. D. Tokman, A. G. Litvak, M. A. Erukhimova, and A. Yu. Kryachko

Institute of Applied Physics, Russian Academy of Sciences, ul. Ul'yanova 46, Nizhni Novgorod, 603950 Russia

Received May 28, 2003; in final form, October 14, 2003

Abstract—Parametric effects of lasing without inversion and electromagnetically induced transparency in classical systems are considered. The characteristic features of the effect of lasing without inversion in ensembles of classical electrons are analyzed using an "inversionless" cyclotron maser as an example. A theory of the effect of electromagnetically induced transparency is developed for electron cyclotron waves in a high-temperature plasma. Possible applications of these two effects in plasma physics and microwave electronics are discussed. *© 2004 MAIK "Nauka/Interperiodica".*

1. INTRODUCTION

In recent years, the interaction of electromagnetic waves with multilevel quantum systems in the so-called coherent states has been the subject of active investigation. The best-known examples of such interaction processes are lasing without inversion (LWI) [1] and electromagnetically induced transparency (EIT) [2], as well as the "slowing down" [3] and "stopping" [4, 5] of light—phenomena that are closely related to the EIT. Interest in these effects stems not only from their possible applications (for more specific information on this matter, see [1, 2, 6]) but also from their relation to the fundamental questions of the physics of the interaction of radiation with matter. These effects can radically change the active and reactive properties of a resonant medium in its interaction with radiation whose intensity is relatively low and cannot substantially alter the population distributions over the levels. Hence, the occurrence of LWI and EIT effects is associated with the fact that the interaction of nonmonochromatic radiation with resonance quantum transitions is not always determined completely by the population distribution. The well-known analogy between radiative processes in ensembles of quantum and classical oscillators [7–9] naturally raises the hope that a system of classical particles with a decreasing energy spectrum in the resonance region may exist in states in which the stimulated emission of radiation is possible or electromagnetic waves can propagate without attenuation. Nevertheless, in classical systems, the LWI and EIT effects possess a number of peculiar features. It is this aspect of the electrodynamics of plasmas and electron flows that is the main subject of our study.

Although the nature of the LWI and EIT effects in quantum systems might seem to be paradoxical, they can in principle be thought of as parametric radiative processes, which have been investigated quite thoroughly for many decades. These investigations were originally based on a theoretical model involving the so-called three-level Λ scheme (see Fig. 1). In the Λ scheme, the usual practice is to consider two high-frequency (HF) electromagnetic waves with frequencies close to the resonant frequencies of the transitions $|3\rangle$–$|1\rangle$ and $|3\rangle$–$|2\rangle$, which are coupled parametrically to one another through oscillations (quantum coherence) at a low-frequency (LF) transition $|2\rangle$–$|1\rangle$. The state of the LF transition can be determined by the action of external sources and by the HF fields themselves; in the latter case, a process like resonant scattering is usually considered (see [1] for details]), in which one of the HF waves is a control (pump) wave and the other is a test (signal) wave. Bichromatic radiation in the LWI regime or an HF test wave in the resonant scattering regime can be amplified in the absence of inversion at any of the transitions of the Λ scheme; in this case, the electrons

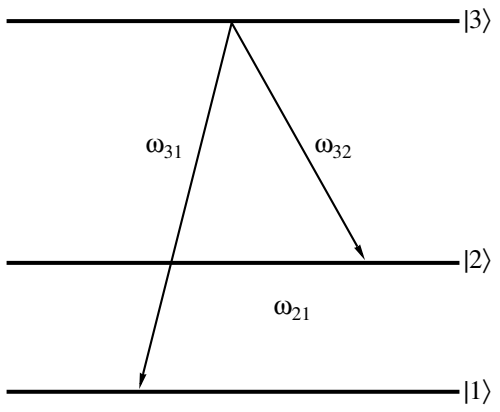

Fig. 1. Three-level Λ scheme.

1063-780X/04/3007-0595$26.00 © 2004 MAIK "Nauka/Interperiodica"

transfer their energy to the electromagnetic field. Strictly speaking, the EIT effect is simply the "threshold" for the LWI effect. However, for the EIT effect in the resonant scattering regime, the features of the propagation of a test wave are so peculiar that this case is of particular interest by itself (see [2–6]).

The parametric interaction of waves in an ensemble of electrons executing cyclotron oscillations in a magnetic field was found to be a direct classical analogue of the parametric wave interaction in an original quantum system, so that, from the standpoint of the behavior of the electromagnetic field, the quantum system and electron ensemble can be considered to be essentially equivalent. The parametric cyclotron instability at two harmonics of the cyclotron frequency that are coupled to one another by premodulating the electron distribution function in the phases of cyclotron gyration at the difference frequency (the difference in frequency between the two harmonics) was found to be a classical analogue of the LWI in its simplest form (in a Λ scheme with the initially created LF coherence) [10]. The features of propagation of the waves that correspond to the features of the EIT effect were discovered theoretically in [11, 12] for an electron cyclotron wave in a cold plasma that is coupled parametrically to an electrostatic mode by an electromagnetic pump wave.

Hence, it does seem certain that the LWI and EIT effects are of a general physical nature, as is conventional stimulated emission of radiation, which is equally characteristic of quantum and classical systems (see, e.g., [9]). In Section 2, we consider the features of the LWI effect in a classical system using an inversionless cyclotron maser as an example. In Section 3, we construct a theory of the EIT effect for electron cyclotron waves in a high-temperature plasma.

2. INVERSIONLESS GENERATION OF CYCLOTRON RADIATION

2.1. Phenomenological Interpretation of the LWI Effect

In simplest quantum systems with LWI (i.e., in systems based on the principles of a Λ scheme with the initially created LF coherence) and in their classical analogues, the inversionless amplification effect is in essence the process of parametric interaction that occurs between two coherent HF modes in an ensemble of electrons whose distribution is modulated at the difference frequency and in the course of which, under certain conditions, both of the modes are amplified, rather than the energy being transferred from one mode to another. In this case, the electron ensemble is inversionless in the sense that it is stable against the generation of each of the HF modes (when, e.g., the propagation of one of the modes is forbidden by external electrodynamic conditions).

In the simplest case, the interaction of two HF modes in a medium with modulated electromagnetic parameters is usually described by the reduced equations [13]

$$\beta_1\dot{E}_1 + \gamma_1 E_1 = \delta\varepsilon E_2, \quad \beta_2\dot{E}_2 + \gamma_2 E_2 = -\delta\varepsilon^* E_1. \quad (1)$$

Here, $E_{1,2}$ are the complex amplitudes of the modes with frequencies $\omega_{1,2}$ and wave vectors $k_{1,2}$, $\delta\varepsilon$ is the complex amplitude of the perturbation (with the frequency $\Omega = \omega_1 - \omega_2$ and wave vector $\kappa = k_1 - k_2$) of an electrodynamic parameter of the medium, the constants $\beta_{1,2}$ are determined by the linear mode dispersion, and the quantities $\gamma_{1,2}$ account for linear dissipation. Equations (1) describe the known processes of three-wave interaction involving a fixed-amplitude pump wave and also the process of stimulated scattering of electromagnetic waves by elementary perturbations of the medium. In the first case, the modulation of the parameters of the medium, which ensures the parametric interaction between the HF waves in question, is produced by a third wave, the evolution of which is excluded from consideration. In the second case, the nonlinear response of the medium at the difference frequency is governed consistently by the action of the fields involved in the scattering process and is not affected by the third wave. In terms of Eqs. (1), the two HF modes can be amplified simultaneously only when the coefficients β_1 and β_2 have opposite signs. This well-known case corresponds to waves with energies of opposite sign. Otherwise, the simultaneous amplification of two HF waves is forbidden by the Manley–Rowe relation, which expresses the conservation law for the number of quanta of HF radiation and is valid for a system with an arbitrary reactive nonlinearity. In a generalized sense, the LWI effect in both quantum and classical systems is akin to the known three-wave interactions but, at the same time, it differs radically from the above processes. The main difference is in the violation of the Manley–Rowe relation. It is meaningful to consider the LWI effect for two waves, neither of which possesses the main property of waves with negative energy [14], namely, their capability for amplification in a system with linear dissipation in the absence of parametric coupling. For waves with positive energy, the possible simultaneous amplification of two parametrically coupled HF modes is described by formally changing the sign of the right-hand side of one of Eqs. (1) or by multiplying the right-hand sides of Eqs. (1) by the imaginary unit (that these ways are equivalent is evidenced by the replacement $\delta\varepsilon \longrightarrow i\delta\varepsilon$). Gaponov-Grekhov and Tokman [10] noted that, in the quantum Λ scheme, the LWI mechanism is the parametric interaction between the modes in a medium with modulated conductivity (it is just this interaction that is described by the equations in question). In this case, the averaged (unmodulated) conductivity component can be positive, which ensures the absorption of the modes in the absence of parametric coupling; it is in this sense that the system is inversionless.

To pursue the analogy between the quantum Λ scheme and an ensemble of classical electrons, it is convenient to consider the interaction of radiation with particles under electron cyclotron resonance (ECR) conditions. In this way, in the system of Landau levels, which characterize the motion of an electron in a direction transverse to the magnetic field in the quantum limit, the three-level "Λ-block" is singled out (Fig. 2) and thereafter a limiting transition to the continuum is made (see [10] for details). The frequencies of electromagnetic waves propagating transverse to the magnetic field direction should be close to the electron cyclotron harmonic frequencies $N_1\omega_B/\gamma$ and $N_2\omega_B/\gamma$, where ω_B is the nonrelativistic electron gyrofrequency; γ is the relativistic factor; and $N_{1,2} = 1, 2, 3, \ldots$. For a classical system, an analogue to the LF quantum coherence is the modulation of the distribution function of the resonant particles at the cyclotron-harmonic difference frequency $(N_1 - N_2)\omega_B/\gamma$, in which case the Doppler resonance condition [8] is satisfied for both HF waves ($\omega_{1,2} = N_{1,2}\omega_B/\gamma$) and the beat wave ($\omega_1 - \omega_2 = (N_1 - N_2)\omega_B/\gamma$). The presence in the system of resonant particles, which produce the active response of the medium to an HF action, ensures that two HF fields can be amplified simultaneously, which contradicts the customary Manley–Rowe relations. That the averaged (unmodulated) conductivity component is positive results from the fact that the energy spectrum averaged over the period of modulation at the difference frequency is decreasing in the energy range corresponding to resonant particles.

An important difference from the Λ scheme was found in the case in which the waves propagate obliquely to the magnetic field, when the resonant interaction is governed to a large extent by the Doppler effect associated with electron motion along the magnetic field.

Investigations of the LWI effect in different versions of an inversionless cyclotron maser [15, 16] showed that, in classical systems (unlike in the known quantum systems), inversionless amplification is possible even when there are no particles that are in resonance with the partial waves. In this case, the nature of the parametric mode coupling that would be adequate for amplification is ensured by the "antiphase" modulation of the responses of the electron ensemble to two different individual modes (rather than by the modulation of the conductivity of the medium). Note that, in this case, an unmodulated electron ensemble constitutes a truly reactive (i.e., dissipationless) medium; however, in a medium with spatial or temporal dispersion, the modulation of a certain parameter ultimately leads to a complex response to a monochromatic action [17]. Consequently, the situation in which the energy can be exchanged between radiation and a reactive medium is not in fact paradoxical. The principal reason why, in such a system (in which, it seems, the Manley–Rowe relations ought to be satisfied), two HF waves can be amplified simultaneously is that the energy exchange effect occurs within a finite time. In particular, this effect can manifest itself in the initial stage of the relaxation of the induced scattering process to a steady state.

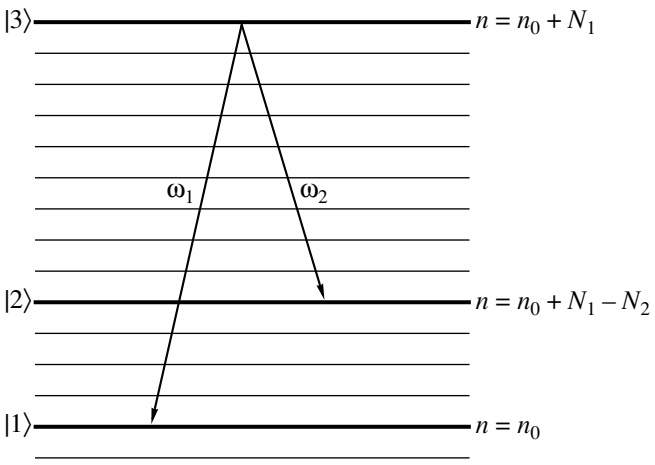

Fig. 2. Λ scheme in the system of Landau levels, in which $p_\perp^2/2m = (n + 1/2)\hbar\omega_B$, with $p_\perp$ the absolute value of the particle momentum component transverse to the magnetic field. The frequencies of the waves propagating transverse to the magnetic field are equal to $\omega_{1,2} = N_{1,2}/\gamma$.

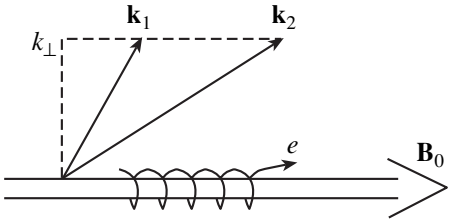

Fig. 3. Inversionless cyclotron maser operating at the first harmonic of the gyrofrequency.

In this section, we consider one of the schemes for inversionless generation of the cyclotron radiation. Using this scheme, we illustrate all the main features of the inversionless amplification regimes in a classical system. We again emphasize that, although the consideration of relevant processes often involves nonequilibrium systems (such as beams of charged particles), the systems themselves are stable in their interactions with monochromatic radiation. It is in this sense that they are referred to as inversionless. Recall that, in comparison with the traditional process of three-wave interaction, the processes in the systems in which we are interested here possess some specific features.

2.2. Basic Equations

We consider two plane waves propagating at an angle to a constant magnetic field $\mathbf{B} = B\mathbf{z}_0$ (see Fig. 3)

and having the same transverse wavenumber but different frequencies and different longitudinal wavenumbers:

$$\mathbf{E} = \mathbf{y}_0 \sum_{j=1}^{2} \mathrm{Re}\, E_j \exp(ik_\perp x + ik_{\|j} z - i\omega_j t).$$

Let the conditions of Doppler resonance at the first harmonic of the gyrofrequency be satisfied for both of the waves and for electrons having the momentum components $p_{\|R} = mc\rho_{\|R}$ and $p_{\perp R} = mc\rho_{\perp R}$:

$$\omega_j = \omega_B/\gamma_R + ck_{\|j}\beta_{\|R},$$

where $\omega_B = eB/mc$, m is the rest mass of an electron, c is the speed of light, $\gamma_R = (1 + \rho_{\|R}^2 + \rho_{\perp R}^2)^{1/2}$ is the relativistic factor, and $\beta_{\|R}$ is the longitudinal velocity of the resonant electrons in units of the speed of light. We consider the interaction of the waves with an ensemble of electrons whose longitudinal and transverse momentum components, $p_\| = mc\rho_\|$ and $p_\perp = mc\rho_\perp$, are close to their resonant values. This electron ensemble is described by the distribution function over "slow" variables, $f(r, \chi, \theta, z, X, t)$, where $r = \rho_\| - \rho_{\|R}$, $\chi = \rho_\perp^2/2 - \rho_{\perp R}^2/2$, θ is the phase of the electron cyclotron gyration, and X is the transverse coordinate of the center of the Larmor circle. We describe the distribution function by the following reduced form of the Liouville equation [10, 15]:

$$\left(\frac{\partial}{\partial t} + \omega_H \frac{\partial}{\partial \theta} + c\beta_\| \frac{\partial}{\partial z}\right) f + \sum_{j=1}^{2} F_j \left(\frac{\omega_B}{\omega_j}\frac{\partial}{\partial \chi} + n_{\|j}\frac{\partial}{\partial r}\right) f = 0. \quad (2)$$

Here,

$$\omega_H = \omega_B(1 - \chi/\gamma_R^2 - \beta_{\|R} r/\gamma_R)/\gamma_R,$$

$$\beta_\| = \beta_{\|R} + r(1 - \beta_{\|R}^2)/\gamma_R - \beta_{\|R} r/\gamma_R^2,$$

$$F_j = G\,\mathrm{Re}\{\alpha_j \exp(i\theta + ik_\perp X + ik_{\|j} z - i\omega_j t)\};$$

$$G = (\rho_{\perp R}/\gamma_R) J_1'(k_\perp r_H),$$

$n_{\|j} = ck_{\|j}/\omega_j$, $r_H = c\rho_{\perp R}/\omega_B$, J_1' is the derivative of the Bessel function, and $\alpha_j = eE_j/mc$ are the normalized wave amplitudes. The wave amplitudes are also described by reduced equations:

$$\partial\alpha_j/\partial t = -(2\pi e/mc) I_j, \quad (3)$$

in which it is assumed that the wave vectors and wave frequencies are related by the "vacuum" dispersion relation. For simplicity, we consider the initial-value problem (the corresponding boundary-value problem was discussed in [15]). In Eqs. (3), the amplitudes of the resonant harmonics of the current are expressed in terms of the distribution function as follows [10, 15, 18]:

$$I_j = ecG\langle \int d\chi dr d\theta f(\chi, r, \theta, z, X, t) \times \exp(-i\theta - ik_\perp X - ik_{\|j} z + i\omega_j t)\rangle\big|_{X,z,t}. \quad (4)$$

The parametric coupling of the two waves in question is ensured by premodulating the electron distribution function in the longitudinal coordinate. The initial modulation is specified to be

$$f_{\mathrm{in}}(t = 0) = f_0(\chi, r) + f_M(\chi, r)\cos(\kappa z + \varphi_M), \quad (5)$$

where $\kappa = k_{\|1} - k_{\|2}$. At later times, the unperturbed distribution function differs from function (5) in the phase of the modulated component, which has the form $\varphi_M + \kappa z - c\kappa\beta_\| t = \varphi_M + \kappa z - \Omega t + \Delta_M t$, where $\Omega = \omega_1 - \omega_2$ and

$$\Delta_M = \Omega - c\kappa\beta_\| = \Omega\chi/\gamma_R^2 - c\kappa r(1 - \beta_{\|R}^2)/\gamma_R \quad (6)$$

is the deviation from the phase synchronization of an electron with the beat wave. The deviations from phase synchronization with the individual HF waves are given by the expressions

$$\Delta_j = \omega_j - \omega_H - ck_{\|j}\beta_\| = (\omega_j/\gamma_R)[\chi/\gamma_R + r(\beta_{\|R} - n_{\|j})] = \Delta_{\chi j} + \Delta_{rj}. \quad (7)$$

Let us solve kinetic equation (2) to first order in the wave amplitudes. We consider an asymptotic solution that corresponds to Landau's circumvention rule and is valid under the condition

$$\langle \delta\Delta_j\rangle t \gg 1, \quad (8)$$

where the characteristic spread in deviations from phase synchronization of the beam electrons with the waves, $\langle\delta\Delta_j\rangle$, is determined by the distribution function. We restrict ourselves to considering the time scales for which the "ballistic relaxation" of the modulated component of the distribution function can be ignored,

$$\Delta_M t \ll 1. \quad (9)$$

In order to satisfy conditions (8) and (9) simultaneously, it is necessary that, first, the modes be spectrally close to one another ($\omega_1 \approx \omega_2 \approx \omega$) and, second, the condition $r|\beta_{\|R} - n_{\|j}| \ll \langle\delta\chi\rangle/\gamma_R$ hold, which indicates that the spread in deviations from phase synchronization of the beam electrons with the waves is determined primarily by the spread in relativistic deviations because of the dependence of these relativistic deviations on the transverse momentum. As a result, taking into account Eqs. (3) and expressions (4), we arrive at

the following equations describing the parametric mode coupling:

$$\begin{cases} \dot{\alpha}_1 + (\Gamma^0 + iD^0)\alpha_1 \\ = -\exp(i\varphi_M)[(\Gamma^s + iD^s) + (\Gamma^a + iD^a)]\alpha_2, \\ \dot{\alpha}_2 + (\Gamma^0 + iD^0)\alpha_2 \\ = -\exp(-i\varphi_M)[(\Gamma^s + iD^s) - (\Gamma^a + iD^a)]\alpha_1. \end{cases} \quad (10)$$

The left-hand sides of these equations contain the standard coefficients determining the linear response of the electron ensemble:

$$\Gamma^0 = \frac{2\pi^2 e^2 G^2 \omega}{m\gamma_R}(1 - n_\parallel^2)\int d\chi dr\, f_0(\chi, r)\frac{\partial\delta(\Delta_\chi)}{\partial\Delta_\chi},$$

$$D^0 = \frac{2\pi e^2 G^2 \omega}{m\gamma_R}(1 - n_\parallel^2)\int d\chi dr(f_0(\chi, r) - f_0(0, r))\frac{P}{\Delta_\chi^2},$$

where the symbol P denotes the principal value of the integral.

The right-hand sides of these equations describe the parametric mode coupling due to the modulation of the distribution function. The presence of the term $f_0(0, r)$ in the integrand (as well as similar terms in the subsequent expression for the parametric coefficients) is related to the method of finding the principal value of the integral (by taking the integral by parts). The coefficients with superscripts s are determined by the symmetric part of the distribution function, $f_M(r) = f_M^s(r) + f_M^a(r)$, i.e., by the part satisfying the condition $f_M^s(\chi, r) = f_M^s(\chi, -r)$:

$$\Gamma^s = \frac{\pi^2 e^2 G^2 \omega}{m\gamma_R}(1 - n_{\parallel 1} n_{\parallel 2})\int d\chi dr\, f_M^s(\chi, r)\frac{\partial\delta(\Delta_\chi)}{\partial\Delta_\chi},$$

$$D^s =$$

$$= \frac{\pi e^2 G^2 \omega}{m\gamma_R}(1 - n_{\parallel 1} n_{\parallel 2})\int d\chi dr(f_M^s(\chi, r) - f_M^s(0, r))\frac{P}{\Delta_\chi^2}.$$

The coefficients with superscripts a are determined by the antisymmetric part of the distribution function, i.e., by the part satisfying the condition $f_M^a(\chi, r) = -f_M^a(\chi, -r)$:

$$\Gamma^a =$$

$$= \frac{\pi e^2 G^2 \omega}{m\gamma_R^2}(1 - n_{\parallel 1} n_{\parallel 2})\int d\chi dr(f_M^a(\chi, r) - f_M^a(0, r))r$$

$$\times\left\{-c\kappa(1 - \beta_{\parallel R}^2)t\frac{P}{\Delta_\chi^2} + \pi\frac{\partial^2\delta(\Delta_\chi)}{\partial\Delta_\chi^2}\omega(n_{\parallel 1} - \beta_{\parallel R})\right\},$$

$$D^a = \frac{\pi e^2 G^2 \omega}{m\gamma_R^2}(1 - n_{\parallel 1} n_{\parallel 2})\int d\chi dr\left\{-f_M^a(\chi, r)rc\kappa\right.$$

$$\times(1 - \beta_{\parallel R}^2)t\pi\frac{\partial\delta(\Delta_\chi)}{\partial\Delta_\chi}$$

$$\left. + \left(f_M^a(\chi, r) - \frac{\partial}{\partial\chi}f_M^a(\chi, r)\Big|_{\chi = 0}\right)r\frac{2P}{\Delta_\chi^3}\omega(n_{\parallel 1} - \beta_{\parallel R})\right\}.$$

2.3. Different Regimes of Inversionless Parametric Generation

According to Eqs. (10), the nature of the parametric coupling and, accordingly, the amplification condition and amplification mechanism for the HF modes under consideration depend very strongly on the character of the modulation of the distribution function. We can distinguish between the following two typical situations:

(a) The distribution function is modulated *in the transverse momenta*, in which case it is assumed that $f_M^a(r) = 0$, whereas the symmetric part of the distribution function $f_M(\chi)$ is nonzero. An important point is that the deviations from synchronization Δ_1 and Δ_2, given by formulas (7), oscillate in phase, thereby producing similar responses to both of the HF fields. The result is that, in the system, the bichromatic mode is amplified and its amplitude grows exponentially according to the law $\alpha_j \propto \exp(\mu t)$. The amplification condition has the form

$$|\Gamma^s| > \Gamma^0.$$

This is just the regime of inversionless amplification via the modulation of the distribution function of the resonant particles. In this regime, the unmodulated component of the distribution function is "uninverted," so that we have $\Gamma^0 > 0$. The amplification of the two modes is achieved by optimally modulating the conductivity to stay in phase with the beatings of the HF modes. This amplification is a direct classical analogue of the LWI in the Λ scheme. In [10], such a generation regime was illustrated by considering a somewhat different interaction scheme as an example—one in which, first, HF modes with frequencies close to the cyclotron harmonic frequencies propagate across a constant magnetic field and, second, an electron ensemble with an energy spread is modulated at the difference frequency.

(b) The distribution function is modulated *in the longitudinal momenta*, in which case it is assumed that $f_M^s(r) = 0$. In this situation, the deviations Δ_1 and Δ_2 in formulas (7) oscillate in antiphase, because, for the waveguide modes, the parameters $\beta_{\parallel R} - n_{\parallel j}$ have opposite signs. The responses of an electron ensemble to both of the HF fields are also modulated in antiphase. As a result, the corresponding bichromatic mode can be

amplified in the system in such a way that its amplitude grows exponentially according to the law $\alpha_j \propto \exp(\mu t)$. The amplification condition has the form

$$|D^a| > \Gamma^0.$$

This condition can be satisfied, in particular, in a system in which there are no particles that are in resonance with HF waves (when $\Gamma^0 = 0$). This is in fact the regime of amplification in a reactive medium. Such amplification is possible because deviations from phase synchronization depend in a special manner on the momentum components of the electrons: they are determined by both the relativistic shift of the electron gyrofrequency and the Doppler shift.

Note that a modulated ensemble whose electrons are capable of interacting with waves in this amplification regime can be formed according to the following scheme. Let there be an initially monoenergetic beam with a large pitch-angle scattering—a beam like those produced by widely used magnetron injectors (for waves propagating obliquely to the magnetic field, the pitch-angle scattering plays the same role as the large energy spread does for waves propagating perpendicular to the field). The electron distribution function is modulated in longitudinal momentum in the short-term interaction of the beam with the longitudinal pump field $\mathbf{E} = \mathrm{Re}[\mathbf{z}_0 E_0 \exp(i\kappa z - i\Omega t)]$ within the preliminary section, in which case the electron beam modulation required for the onset of instability is already produced in the linear stage of the interaction of the beam with the pump field (see [15]).

The mechanism for energy exchange between a bichromatic HF field and a modulated ensemble of nonresonant particles was analyzed by two of us in [19]. In order to ensure the take-up of energy from an electron ensemble, it is necessary to correlate the motion of the electrons with the spatial structure of the beat wave; it is this correlation that is established between the electron ensemble premodulated in longitudinal velocity and the bichromatic field in the above unstable regime. An important point here is that such an amplification regime can only occur in the presence of a magnetic field. In the absence of a magnetic field, the only possible effect is conventional scattering because, in the frame of reference of the modulation wave, the sum of the mean energy of the oscillatory motion of a beam electron and the energy of the slow motion of the guiding center of its Larmor orbit is conserved [20].

Investigations of the mechanisms for the saturation of LWI in a classical system, including estimates of the generation efficiency (see [21, 22]), were made only for the first of the above two instability mechanisms, which is associated with the modulation of the distribution function of the resonant particles. The most important result of these studies is the conclusion that the "electron ensemble + electromagnetic field" system relaxes to a steady state in which the energy spectrum does not have a "standard" plateau shape [14] but instead is declining. It should be noted that, during the generation process, the energy of the electron ensemble decreases; in the energy range corresponding to resonant particles, the formed electron energy spectrum decreases more rapidly with increasing energy than does the initial spectrum. As for the ratio between the energy transferred from electrons to the HF field during its amplification and the energy expended in premodulating the beam, it is governed by the initial electron distribution function. In [15], it was shown that, for quasi-monoenergetic beams with a large pitch-angle scattering (like those typically produced by conventional magnetron injectors), the LWI effect can take place in the "linear" LF modulation regime, when the energy of the electron ensemble increases in proportion to the second power of the amplitude of the modulating field. An analogous situation can in principle occur in beams with an electron energy spectrum of finite width [10]. In such a situation, the electron energy converted into the field energy can exceed the energy expended in premodulating the beam. The situation with beams with a monotonically decreasing electron energy spectrum is radically different. In this case, the threshold for LWI can only be achieved with LF modulation in the nonlinear electron trapping regime, in which the averaged component of the electron distribution function is inevitably subject to considerable distortions (see [10]). The results of the quasilinear theory developed in [22] lead to the conclusion that, in such a generation regime, the energy lost by the LF field in the modulating section is several times higher than the energy transferred from electrons to the HF field.

3. ELECTROMAGNETICALLY INDUCED TRANSPARENCY FOR ELECTRON CYCLOTRON WAVES IN A PLASMA

As was shown in [11, 12], the EIT effect in a classical system is a kind of so-called "dynamic damping." By this is meant the suppression of resonantly growing oscillations of a harmonic oscillator at the expense of its coupling to another oscillator (see, e.g., [23]). However, the dynamic damping is ordinarily ensured by a linear coupling between two harmonic oscillators, which leads to the growth of oscillations of the damping system at the frequency of the generalized driving force. In the case at hand, the oscillators are coupled parametrically by a pump wave; this results in the growth of oscillations of the damping system at the beat frequency. This is the main feature of the effect under consideration.

In a distributed system, the role of such a "dynamic damper" is played by a certain wave mode. It is clear that the conditions for efficient parametric excitation of this mode are governed by its dispersion properties.

Under ECR conditions in a plasma, resonant wave–particle interaction can be suppressed by the parametric excitation of, e.g., Langmuir waves. Let us consider the EIT effect under ECR conditions in a magnetized

plasma by means of hydrodynamic theory. Despite the conditional character of the hydrodynamic model, it provides insight into the main features of the EIT effect that are associated with the wave nature of the damping subsystem.

We consider two circularly polarized waves propagating along a constant external magnetic field $\mathbf{B} = B\mathbf{z}_0$ in a magnetized plasma. Let the electric field of the waves rotate in the same direction that the electrons gyrate around the magnetic field (in which case we are dealing with extraordinary waves):

$$\begin{aligned}\mathbf{E}_\perp(z,t) = \mathrm{Re}\{\mathbf{e}_+[&E_1\exp(-i\omega_1 t + ik_1 z)\\ &+ E_2\exp(-i\omega_2 t + ik_2 z)]\},\end{aligned} \tag{11}$$

where $\mathbf{e}_+ = 2^{-1/2}(\mathbf{x}_0 + i\mathbf{y}_0)$ is the polarization vector of the waves and $(\mathbf{x}_0, \mathbf{y}_0, \mathbf{z}_0)$ are unit vectors along the axes of a Cartesian coordinate system.

The oscillations of the transverse and longitudinal (with respect to the constant magnetic field) components of the electron velocity are described by the Euler equations with allowance for the Lorentz force exerted by the wave fields on the electrons:

$$\begin{cases}\dfrac{\partial \mathbf{V}_\perp}{\partial t} + \omega_B[\mathbf{V}_\perp, \mathbf{z}_0] + \gamma\mathbf{V}_\perp + V_\parallel\dfrac{\partial \mathbf{V}_\perp}{\partial z}\\ \quad = -\dfrac{e}{m}\left(\mathbf{E}_\perp + V_\parallel\dfrac{\partial}{\partial z}\displaystyle\int_{-\infty}^{t}\mathbf{E}_\perp dt\right),\\ \dfrac{\partial V_\parallel}{\partial t} + \gamma V_\parallel + V_\parallel\dfrac{\partial V_\parallel}{\partial z}\\ \quad = -\dfrac{1}{mN_e}\dfrac{\partial p}{\partial z} - \dfrac{e}{m}E_p + \dfrac{e}{m}\mathbf{V}_\perp\dfrac{\partial}{\partial z}\displaystyle\int_{-\infty}^{t}\mathbf{E}_\perp dt.\end{cases} \tag{12}$$

Here, γ is the effective collision frequency, E_p is the electric field in the plasma wave, p is the gas-kinetic pressure, and N_e is the electron density. Equations (12) should be supplemented with the continuity equation

$$\partial N_e/\partial t + \partial(N_e V_\parallel)/\partial z = 0 \tag{13}$$

and with the equation describing the excitation of the electric field in the plasma wave,

$$\partial E_p/\partial t = -4\pi j_z = 4\pi e N_e V_\parallel, \tag{14}$$

where j_z is the longitudinal component of the electron current. Assuming that the ion density N_i is constant and that the plasma is quasineutral,

$$N_i = N_0 = \mathrm{const}, \quad |N_e - N_i| \ll N_e, N_i, \tag{15}$$

we can reduce Eqs. (12)–(14) to the following set of equations, which describes the excitation of longitudinal collective oscillations by the ponderomotive force of the HF fields (assuming that the process under consideration is adiabatic):

$$\begin{cases}\dfrac{\partial^2 n}{\partial t^2} + \gamma\dfrac{\partial n}{\partial t} + \omega_p^2 n - 3V_T^2\dfrac{\partial^2 n}{\partial z^2} = -\dfrac{eN_0}{m}\dfrac{\partial}{\partial z}\mathbf{V}_\perp\dfrac{\partial}{\partial z}\displaystyle\int_{-\infty}^{t}\mathbf{E}_\perp dt,\\ V_\parallel = -N_0^{-1}\displaystyle\int_{-\infty}^{z}(\partial n/\partial t)dz.\end{cases} \tag{16}$$

Here, $n = N_e - N_0$ is the perturbed electron density, $\omega_p = (4\pi e^2 N_0/m)^{1/2}$ is the electron plasma frequency, and $V_T = (T/m)^{1/2}$ and T are the electron thermal velocity and electron temperature.

We assume that the following synchronization conditions are satisfied:

$$\begin{aligned}&\text{(a)}\ \ |\omega_1 - \omega_B|, \quad \gamma \ll \omega_1, \omega_B,\\ &\text{(b)}\ \ |\omega_L - \omega_p|, \quad \gamma \ll \omega_L, \omega_p,\\ &\text{(c)}\ \ k_{1,2,L}V_T \ll \omega_{1,2,L},\end{aligned} \tag{17}$$

where $\omega_L = \omega_1 - \omega_2$ and $k_L = k_1 - k_2$ are the frequency and wave vector of the beat wave generated by a signal wave and pump wave. The first of inequalities (17) indicates that, for the signal wave, ECR conditions are satisfied, so that its cyclotron absorption is possible in the absence of a pump wave. The second inequality is the condition for the excitation of plasma waves at the beat frequency ω_L. Finally, the third inequality is the condition that the spatial dispersion be weak.

Synchronization conditions (17a) and (17b) allow us to apply the method of reduced equations, i.e., to simplify Eqs. (12)–(14) by keeping only the terms with resonant frequencies. It is important to note that, in deriving the desired reduced set of equations, it is necessary to account for the nonlinear component of the transverse electron velocity that rotates in the same direction that the polarization vector of an ordinary wave advances (the direction of rotation of the electric field in an ordinary wave is opposite to that of the Larmor electron gyration). The reason is that, because of the energy transfer to the collective degrees of freedom, the resonant components of the electron velocity turn out to be suppressed, so that taking into account this nonlinear velocity component leads to significant corrections, which, however, are not of fundamental importance for our analysis. Having derived the reduced set of equations, we can find the expression for the effective refractive index of the plasma for a signal wave [24]:

$$N^2 = 1 - \frac{\omega_p^2}{\omega_1}\frac{Z_p + \xi_{EC}\omega_L\omega_2(2k_1/k_2 - 1 - \omega_1/2\omega_2)}{(\omega_1 - \omega_B + i\gamma)Z_p - \omega_L^2\omega_1\xi_{EC}}. \tag{18}$$

Here, $\xi_{EC} = |eE_2/2m(\omega_2 - \omega_B + i\gamma)|^2(k_2/\omega_2)^2 = |V_2|^2/(2V_{\mathrm{ph}})^2$ is the dimensionless nonlinearity parame-

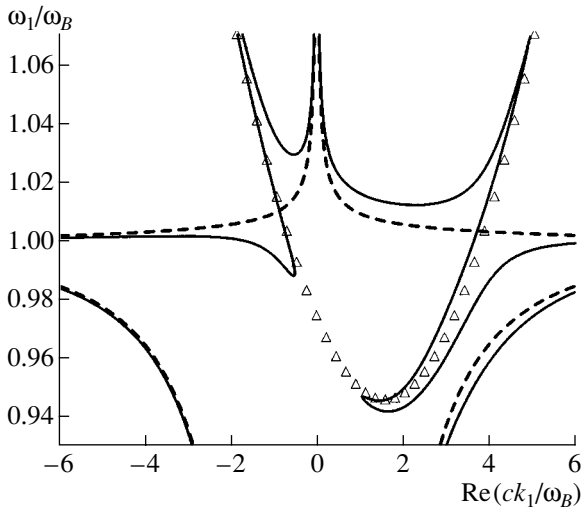

Fig. 4. Dispersion relation of an electron cyclotron wave under EIT conditions. The solid curves and dashed curves are for $\xi_{EC} = 10^{-3}$ and 0, respectively, and the triangles are for $Z_p = 0$ (△). The parameter values are as follows: $\omega_p/\omega_B = 0.75$, $\omega_2/\omega_B = 0.2$, $\gamma/\omega_B = 2.5 \times 10^{-3}$, and $V_T/c = 7.5 \times 10^{-2}$.

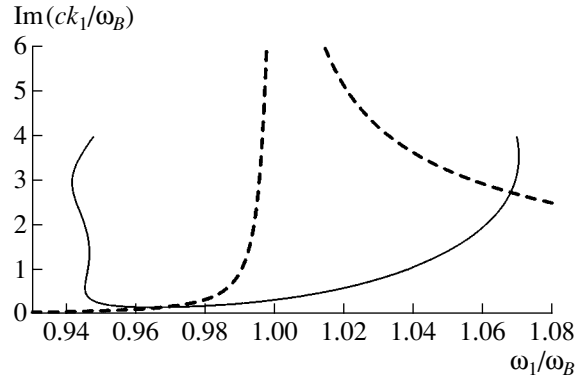

Fig. 5. Formation of the transparency window, $\mathrm{Re}(k_1) > 0$. The parameters are the same as in Fig. 4.

ter, which is equal to the ratio of the squares of the oscillatory and phase velocities of the pump field, and $Z_p = \omega_L^2 - \omega_p^2 - 3k_L^2 V_T^2 + i\gamma\omega_L$. The equality $Z_p = 0$ is the standard dispersion relation for plasma waves in a hydrodynamic approach. Expression (18) differs from the corresponding expression obtained in [11, 12, 25] for a cold plasma in that it contains corrections from electron thermal motion.

We now discuss the features of the dispersion relation for a signal wave under EIT conditions in a "warm" plasma. To do this, we represent expression (18) in the form

$$Z_p(N^2 - N_0^2) = -\xi_{EC}\frac{\omega_2\omega_L^2}{\omega_1 - \omega_B + i\gamma}\left[1 - N^2 + \frac{\omega_p^2}{\omega_1\omega_L}\left(\frac{2k_1}{k_2} - 1 - \frac{\omega_1}{2\omega_2}\right)\right], \quad (19)$$

where $N_0^2 = 1 - \omega_p^2/[\omega_1(\omega_1 - \omega_B + i\gamma)]$ is the "linear" refractive index of a cold magnetized plasma for a signal wave (see, e.g., [7]). The quantity ξ_{EC} is the small parameter of the problem; for reasonable pump field intensities (about 10–100 kW/cm^2), the values of ξ_{EC} are about 10^{-6}–10^{-5}. As a consequence, the dispersion curves of the signal wave that are given by expression (19) are close either to the linear dispersion curve of the signal wave, $N^2 = N_0^2$, or to the dispersion curve of the plasma waves, $Z_p = 0$ (which is, of course, displaced along the corresponding axes by amounts equal to the frequency ω_2 of the pump wave and to its wave vector k_2). It is only in the vicinities of the points of intersection of the curves $N^2 = N_0^2$ and $Z_p = 0$ that the dispersion curves of the signal wave exhibit a different behavior: they pass from one curve to another. These results are confirmed by Fig. 4, which illustrates the results of numerical calculations carried out using expression (18). From this figure, we can see that the behavior of the dispersion curves in the EIT region is in fact determined by the dispersion relation of the plasma waves. In particular, some portions of the dispersion curves correspond to a substantial slowing down of a signal wave propagating with the group velocity (which is also peculiar to a three-level quantum system) and even to the vanishing of the group velocity (which is impossible in a three-level quantum system).

The curves shown in Fig. 5 illustrate the absorption of a signal wave under EIT conditions. It can be seen that there exists a frequency range in which the resonant absorption of the wave is suppressed; the frequency at which the absorption is weakest corresponds approximately to the point of the dispersion curve where the group velocity is zero. Note that the threshold pump wave amplitude ξ_{EC}^* for the EIT effect is governed by dissipative processes (see also [11, 12]): $\xi_{EC}^* = \gamma^2/(\omega_p\omega_B)$.

According to the hydrodynamic theory of a warm plasma, expression (18) implies that, under EIT conditions, the width of the transparency region, $\Delta\omega$, is determined by the relationship $|(\omega_1 - \omega_B)\mathrm{Re}Z_p| \approx \omega_p^2\omega_B\xi_{EC}$, which leads to the following expression for $\Delta\omega$:

$$\Delta\omega \sim \max\{(\omega_p\omega_B\xi_{EC})^{1/2}, k_L^2V_T^2/\omega_p\}. \quad (20)$$

This expression shows, in particular, that the transparency region in a warm plasma can be significantly wider than that in a cold plasma, provided that the plasma temperature is sufficiently high:

$$T/mc^2 > [\omega_p/(ck_L)]^2(\omega_B\xi_{EC}/\omega_p)^{1/2}. \quad (21)$$

It is important to note that, under some conditions, the width of the transparency region can be independent of ξ_{EC}. Thus, for a pump field with an intensity of

100 kW/cm^2, this is the case when the plasma temperature is higher than 150 eV.

The above estimates of the main parameters of the EIT "window" enable us to formulate at least the strictest (most pessimistic) requirements for achieving this effect in a plasma. The restrictions on the maximum allowable nonuniformities of the magnetic field B and the density N_0 follow from expression (20):

$$\delta B,\ \delta N_0 \sim \max\{(\omega_B \xi_{EC}/\omega_p)^{1/2},\ k_L^2 V_T^2/\omega_p^2\}, \qquad (22)$$

where δB and δN_0 are the relative perturbations of B and N_0. For a pump field with an intensity on the order of 10 kW/cm^2, and for plasma temperatures on the order of 1 and 10 keV, the values of δB and δN_0 should not exceed 1 and 5%, respectively, in which case the characteristic dimension of the working region should be about one meter (see [24]). It may be, however, that a more detailed theory of EIT for an inhomogeneous plasma slab will lead to less stringent restrictions.

Hence, the characteristic features of the EIT effect in a plasma are governed by the dispersion properties of the plasma waves. The behavior of the dispersion curves in the EIT window is determined mainly by the dispersion relation for the damping system (plasma waves) and is essentially independent of the pump wave intensity (which, however, should be higher than a certain threshold intensity). In other words, the EIT effect occurs within a constant range of frequencies and wave vectors of the signal wave and, at the same time, within a fairly arbitrary interval of pump wave intensities; in contrast, in the cold plasma approximation (as well as in a three-level quantum system), the corresponding range becomes narrower as the pump wave intensity decreases. It should be noted that the most important of the above features of the dispersion curves and of the curve characterizing the absorption of a signal wave are also provided by more thorough investigations of the EIT effect by means of kinetic theory [24], which, in addition, confirm the above estimates for the width of the transparency region and for the maximum allowable plasma inhomogeneity.

4. CONCLUSIONS

In conclusion, we discuss possible applications of the systems considered above. The LWI effect in ensembles of classical electrons can in principle be used to convert LF monochromatic radiation into HF nonmonochromatic cyclotron or undulator radiation. In this case, depending on the properties of an electron flow, the energy that is transferred from the electron ensemble to the HF radiation can be both higher and lower than the energy transferred from the LF wave to the electrons. In any case, however, this method of energy conversion is expected to be relatively insensitive to the quality of the electron beam because of the inversionless nature of the stimulated radiation under consideration.

As regards possible applications of the EIT effect in plasma physics and in electronics, it may be used, first of all, for the purposes of spectroscopy. However, in order to develop particular schemes for its implementation, it is necessary to construct an appropriate theory of this effect with allowance for the inhomogeneity of typical plasma objects.

Shvets and Wurtele [25] proposed utilizing the EIT regime in compact plasma accelerators, in which case a substantial slowing down of the propagation of the signal wave with the group velocity (a feature peculiar to the EIT effect) may serve to compress electromagnetic pulses. Instead of an HF pump wave, they proposed using a magnetic undulator. Such a scheme provides the possibility of increasing the efficiency of energy transfer from the signal wave to the electrostatic oscillations, but it is disadvantageous in that it significantly reduces the range of the allowable values of the plasma parameters (because it is necessary to ensure that the plasma frequency and the cyclotron frequency be close to one another).

A report on this study was presented at the 30th Conference on Plasma Physics and Controlled Nuclear Fusion, Zvenigorod, 2003.

ACKNOWLEDGMENTS

This work was supported in part by the Russian Foundation for Basic Research, project nos. 03-02-17234, 03-02-06383, and 03-02-06384.

REFERENCES

1. O. Kocharovskaya, Phys. Rep. **219**, 175 (1992).
2. S. E. Harris, Phys. Today **50**, 36 (1997).
3. J. Marangos, Nature **397**, 559 (1999).
4. C. Liu, Z. Dutton, C. H. Behroozl, and L. V. Hau, Nature **409**, 490 (2001).
5. D. F. Phillips, A. Fleischhauer, A. Mair, *et al.*, Phys. Rev. Lett. **86**, 783 (2001).
6. S. E. Harris, Phys. Rev. Lett. **82**, 4611 (1999).
7. V. L. Ginzburg, *The Propagation of Electromagnetic Waves in Plasmas* (Nauka, Moscow, 1967; Pergamon, Oxford, 1970).
8. V. V. Zheleznyakov, *Radiation in Astrophysical Plasma* (Nauka, Moscow, 1997; Kluwer Academic, London, 1996).
9. A. V. Gaponov, M. I. Petelin, and V. K. Yulpatov, Izv. Vyssh. Uchebn. Zaved. Radiofiz. **10**, 1414 (1967) [Radiophys. Quantum Electron. **10**, 794 (1967)].
10. A. V. Gaponov-Grekhov and M. D. Tokman, Zh. Éksp. Teor. Fiz. **112**, 1176 (1997) [JETP **85**, 640 (1997)].
11. A. G. Litvak and M. D. Tokman, Phys. Rev. Lett. **88**, 095003 (2002).
12. A. G. Litvak and M. D. Tokman, Izv. Vyssh. Uchebn. Zaved. Radiofiz. **44**, 407 (2001) [Radiophys. Quantum Electron. **44**, 375 (2001)].
13. N. Bloembergen, *Nonlinear Optics* (Benjamin, New York, 1965; Mir, Moscow, 1966).

14. B. B. Kadomtsev, *Collective Phenomena in Plasma* (Nauka, Moscow, 1988).

15. M. A. Erukhimova and M. D. Tokman, Zh. Éksp. Teor. Fiz. **118**, 291 (2000) [JETP **91**, 255 (2000)].

16. M. A. Erukhimova and M. D. Tokman, in *Proceedings of the International Workshop "Strong Microwaves in Plasmas", Nizhni Novgorod, 2000*, Vol. 2, p. 827.

17. L. D. Landau and E. M. Lifshitz, *Electrodynamics of Continuous Media* (Nauka, Moscow, 1982; Pergamon, New York, 1984).

18. V. L. Bratman, N. S. Ginzburg, G. S. Nusinovich, *et al.*, in *Relativistic Microwave Electronics: Collection of Scientific Works*, Ed. by A. V. Gaponov-Grekhov (Inst. Prikl. Fiz. Akad. Nauk SSSR, Gorki, 1981).

19. M. A. Erukhimova and M. D. Tokman, in *Proceedings of the 29th EPS Conference on Plasma Physics and Controlled Fusion, Montreux, 2002*, ECA **26B**, 4.001 (2002).

20. A. G. Litvak, in *Reviews of Plasma Physics*, Ed. by M. A. Leontovich (Atomizdat, Moscow, 1980; Consultants Bureau, New York, 1986), Vol. 10, p. 164.

21. M. A. Erukhimova and M. D. Tokman, Izv. Vyssh. Uchebn. Zaved., Radiofiz. **44**, 190 (2001) [Radiophys. Quantum Electron. **44**, 176 (2001)].

22. M. A. Erukhimova and M. D. Tokman, Fiz. Plazmy **27**, 921 (2001) [Plasma Phys. Rep. **27**, 868 (2001)].

23. A. B. Pippard, *The Physics of Vibration* (Cambridge Univ. Press, Cambridge, 1989); M. I. Rabinovich and D. I. Trubetskov, *Introduction to the Theory of Oscillations and Waves* (Nauka, Moscow, 1984) [*Oscillations and Waves in Linear and Nonlinear Systems* (Kluwer, Dordrecht, 1989)].

24. A. Yu. Kryachko, A. G. Litvak, and M. D. Tokman, Zh. Éksp. Teor. Fiz. **122**, 805 (2002) [JETP **95**, 697 (2002)].

25. G. Shvets and J. S. Wurtele, Phys. Rev. Lett. **89**, 115003 (2002).

Translated by O.E. Khadin

Plasma Physics Reports, Vol. 30, No. 7, 2004, pp. 605–615. Translated from Fizika Plazmy, Vol. 30, No. 7, 2004, pp. 654–665.

IONOSPHERIC PLASMA

Numerical Integration of the Equations of Motion Describing the Acceleration of Plasma Particles in Syrovatskiĭ's Model of the Dynamic Current Sheet

A. V. Polyakov

Institute for Space Research, Russian Academy of Sciences, Profsoyuznaya ul. 84/32, Moscow, 117810 Russia

Received June 3, 2003; in final form, October 2, 2003

Abstract—The acceleration of solar-wind protons in a current sheet in the Earth's magnetotail, in which the geomagnetic field lines reconnect, is investigated numerically using the dynamic current sheet model proposed by S.I. Syrovatskiĭ. The dynamics of current sheets in the Earth's magnetotail is analyzed. In addition to the known solutions, the solution describing a contracting current sheet is derived. The time evolution of the magnetic field structure in Syrovatskiĭ's model is calculated numerically. The energy spectrum of the protons that are accelerated in the sheet by induction electric fields during rapid changes in the sheet topology is calculated and analyzed. A study is made of proton acceleration up to the time when the current sheet ruptures in the course of its evolution. © *2004 MAIK "Nauka/Interperiodica".*

1. INTRODUCTION

Interest in the study of thin current sheets in the Earth's magnetotail has grown considerably in connection with observations made in recent years by the *Interball-1*, *CLUSTER*, and *GEOTAIL* satellites [1–3]. The sheets occur on fairly long time scales and, presumably, evolve over time [4]. In the region of thin current sheets in the near-Earth magnetotail, solar wind protons that move around the Earth's magnetosphere can be accelerated from about 10 eV up to 1 MeV [5]. The formation of the current sheets is, as a rule, attributed to the reconnection of magnetic field lines [6]. In the Petschek model [7, 8], however, the reconnection process is explained without invoking the current sheet concept and is considered as occurring in the regime of anomalous plasma resistance. The formation of an infinitely thin current sheet and its evolution were described by S.I. Syrovatskiĭ [6], who developed the MHD reconnection model based on the theory of functions of a complex variable. It should be noted that, in the original Syrovatskiĭ model, the current sheet was treated in two-dimensional geometry. By now, however, comprehensive models of three-dimensional current sheet configurations have been developed by the theoreticians of Syrovatskiĭ's scientific school [9, 10]. Of course, in order to study the real effects occurring in a current sheet of finite thickness, it is more expedient to employ the kinetic theory of a current sheet [11, 12], which provides a more exact description of such a sheet than does the MHD model.

Syrovatskiĭ and his collaborators [10, 13] have thoroughly investigated the phenomena that accompany the rupture of a current sheet, in particular, the accompanying acceleration of plasma particles by the induction electric fields. The models constructed in Syrovatskiĭ's time [14] were based on fairly arbitrary assumptions about the possible ways of describing the "rupture" or "decay" of a current sheet (e.g., a ruptured current sheet was described in terms of its two halves running away from one another). In all the models, the problem was actually reduced to that of studying the particle dynamics in the vicinity of X lines (or, more precisely, hyperbolic null lines) under different assumptions regarding the dynamics of the fields by which the lines are formed. For a similar case, the energy spectrum of accelerated particles was calculated analytically by S.V. Bulanov and P.V. Sasorov [13]. In view of the importance of such physical phenomena as the thin current sheet, it is worthwhile to return to Syrovatskiĭ's model in order to investigate another phenomenon—the acceleration of particles over the entire course of sheet evolution. As will be shown below, the evolving current sheet may play a significant role in the acceleration process, although there is no doubt that protons are accelerated to the highest possible energies as the sheet ruptures. The point is that all the relevant effects are actually captured by the model itself and thus can be described without making any additional arbitrary assumptions. It should be noted that, as was shown by Ya.K. Khodataev and V.M. Fadeev [15], Syrovatskiĭ's model of a dynamic current sheet can be successfully applied to analytical and numerical analyses of the particle acceleration process in the solar atmosphere. In [15], a study was made of an oscillating current sheet without allowance for the magnetic drift of the particles. In contrast, the objective of the present paper is to consider an expanding current sheet and to describe the acceleration of particles with allowance for their magnetic drift.

1063-780X/04/3007-0605$26.00 © 2004 MAIK "Nauka/Interperiodica"

Hence, in the present paper, Syrovatskiĭ's model is applied to numerically calculate the spectrum of protons accelerated in an evolving current sheet up to the time when it ruptures. Calculations were carried out for about 2×10^5 particles. The following assumptions were used: The dissipation of the magnetic field energy was assumed to be negligibly small [16, 17]. The magnetic field was assumed to be frozen in the plasma everywhere except for the singular plane of the current sheet. The evolution of a thin current sheet was described in Syrovatskiĭ's MHD model (without the onset of instability); i.e., corrections for kinetic effects (including tearing instability) were ignored. (We note, however, that, in some specific situations, these effects should be taken into account in analyzing the dynamics of the current sheets [18].) The criterion for the rupture of a current sheet was derived analytically from the MHD equations of Syrovatskiĭ's model. Since the solar wind protons turn out to be accelerated to energies (~100 keV) substantially higher than their initial energy (~10 eV), the acceleration process was considered under the assumption that the initial kinetic energy of protons was zero. It was assumed that the magnetic field of the accelerated protons was much weaker than the characteristic magnetic field of the current sheet. It was also assumed that the topology of the magnetic field of an evolving current sheet was stable against small perturbations associated with the magnetic field of the accelerated protons.

In what follows, all dimensional formulas are written in cgs units.

2. ANALYTIC INVESTIGATION OF THE DISTINCTIVE FEATURES OF THE CURRENT SHEET DYNAMICS IN SYROVATSKIĬ'S MODEL

In Syrovatskiĭ's model [6], a current sheet is treated as an infinitely thin structure; mathematically, this is a cut in the complex plane. The magnetic field is assumed to be strong, which corresponds to the conditions

$$p \ll \rho v_A^2, \quad \frac{v^2}{v_A^2} \ll 1, \tag{1}$$

where p is the gas-kinetic plasma pressure (in fact, $p \approx 0$), ρ is the plasma density, v is the absolute value of the plasma flow velocity, v_A is the Alfvén velocity ($v_A = |\mathbf{H}|/\sqrt{4\pi\rho}$), and $\mathbf{H}$ is the magnetic field frozen in the plasma. We consider a two-dimensional planar plasma flow. Such a flow is described by the vector potential of the electromagnetic field that has only one nonzero component, namely, the z component, which is assumed to depend on time and on the coordinates x and y: $\mathbf{A} = \{0, 0, A(x, y, t)\}$. The plasma is assumed to be perfectly conducting. In the coordinate system adopted here, the sheet lies in the $y = 0$ plane and expands in both directions of the x axis, the current in the sheet being directed along the z coordinate. The complex coordinate is $w = x + iy$.

In order to calculate the acceleration of particles by the sheet, it is necessary to know how the components of the electric and magnetic fields depend on time and coordinates. In Syrovatskiĭ's model, these components are expressed in terms of the complex potential of the vortex-free potential field [19]:

$$F_{\text{pot}}(w, t) = A(x, y, t) + iB(x, y, t), \tag{2}$$

$$F_0(w, t) = \frac{\alpha}{2}w^2 - \beta(t), \tag{3}$$

$$\begin{aligned} F(w, t) &= \frac{\alpha}{2}w\sqrt{w^2 - b^2(t)} \\ &+ \frac{\Gamma(t)}{2\pi}\ln\frac{(w + \sqrt{w^2 - b^2(t)})}{b(t)} + A(t), \end{aligned} \tag{4}$$

$$\begin{aligned} F'(w, t) &= \frac{dF(w, t)}{dw} = -H_y(w, t) - iH_x(w, t) \\ &= \alpha\frac{w^2 - \frac{1}{2}b^2(t) + \frac{\Gamma(t)}{2\pi\alpha}}{\sqrt{w^2 - b^2(t)}}. \end{aligned} \tag{5}$$

Here, $F_{\text{pot}}(w, t)$ is the general complex potential describing a given magnetic and a given electric field, $F_0(w, t)$ is the complex potential of the initial magnetic field at a hyperbolic null point from which the current sheet originates, $F(w, t)$ is the complex potential describing the field of the current sheet, $A(x, y, t)$ is the z component of the vector potential, $B(x, y, t)$ is a function harmonically conjugate to $A(x, y, t)$ [19], $A(t)$ is a function determining the magnetic field that has annihilated in the current sheet, w is the complex coordinate, $b(t)$ is the half-width of the sheet in the x direction, α is the gradient of the initial hyperbolic magnetic field in the vicinity of the null point, and the quantity $\Gamma(t)$ determines the total current through the current sheet plane. Syrovatskiĭ's model assumes that there may be reverse currents at the ends of a current sheet, whereas the magnetic reconnection process in the Earth's magnetosphere is most likely to occur in current sheets with no reverse currents [20]. In the latter case, the quantity $\Gamma(t)$ has the form [6]

$$\Gamma(t) = -\pi\alpha b^2(t). \tag{6}$$

According to [16], the above assumption that the magnetic field does not dissipate its energy within the current sheet (see the Introduction) is equivalent to the condition

$$A(t) \equiv 0. \tag{7}$$

In the general case in which $A(t) \neq 0$, the half-width of the current sheet in Syrovatskiĭ's model is described by the equation [6]

$$\frac{\alpha}{4}b^2(t) + \frac{\Gamma(t)}{2\pi}\ln\frac{b(t)}{2b_*} - \beta(t) - \frac{\Gamma(t)}{4\pi}l_0 - A(t) = 0, \quad (8)$$

where b_* is a normalizing constant (below, it will be taken equal to the Earth's radius R_E) and l_0 is a constant determined by the geometry of the closing current circuit. The function $\beta(t)$ in Eq. (8) determines the electric field at the null line of the hyperbolic magnetic field. In the case in question, this electric field corresponds to the external electric field E_0 that initiates the development of a current sheet. In the Earth's magnetosphere, this is the so-called "morning–evening" electric field [21], which is driven by the solar wind flowing around the magnetosphere. In Syrovatskiĭ's model [6], we have

$$E_{\text{ext}}(t) = E(t)|_{w=0} = -\frac{1}{c}\text{Re}\left(\frac{\partial F_0(w,t)}{\partial t}\bigg|_{w=0}\right) = \frac{1}{c}\text{Re}\left(\frac{d\beta(t)}{dt}\right), \quad (9)$$

where $E_{\text{ext}}(t)$ is the external electric field, which depends generally on time. The constant l_0 in Eq. (8) can be approximately estimated by [16]

$$l_0 \approx \ln\frac{L_C}{R_E}, \quad (10)$$

where L_C is the characteristic spatial scale of the closing current circuit. In what follows, it will be more convenient to use the following representation for L_C:

$$L_C = lR_E, \quad (11)$$

where l is the characteristic spatial scale of the closing current circuit in units of the Earth's radius R_E.

The parameters α, $\beta(t)$, and $\dot{\beta}(t)$, normalized to their values characteristic of the Earth's magnetosphere, have the form

$$\alpha = \frac{H_0}{lR_E}, \quad (12)$$

$$\beta(t) = cE_0 f(t,\tau), \quad (13)$$

$$\dot{\beta}(t) \equiv \frac{d\beta(t)}{dt} = cE_0\dot{f}(t,\tau). \quad (14)$$

Here, a certain normalizing initial magnetic field strength H_0, characteristic of the system under consideration, is defined in the complex plane on the basis of formulas (3) and (11) as $H_0 = |\mathbf{H}_0(w,t)|_{|w|=L_C,\,t=0}$, and $f(t,\tau)$ is a function describing the onset and development of the external electric field E_0. The rise time of the electric field E_0 in the magnetosphere is determined by the induction effects (LR circuit) and, according to the estimates made in [22], does not exceed 15–20 min, which is far less than the characteristic lifetime of a current sheet (about 1–3 h). Hence, the fact that the rise time τ is much shorter than the lifetime $t_{\max}$ of the current sheet allows us to introduce the function describing the evolution of the external electric field. This function, which should be smooth in the closed time interval $[0, t_{\max}]$, and its first time derivative have the form [16]

$$f(t,\tau) = \frac{t^2}{t+\tau}, \quad \dot{f}(t,\tau) = \frac{t^2+2t\tau}{(\tau+t)^2}. \quad (15)$$

Function (15) can be chosen to have another form, which, however, will lead to essentially the same final results. With allowance for relationships (9) and (13), the evolution of the external electric field is described by the expression

$$E_{\text{ext}}(t) = E_0\dot{f}(t,\tau). \quad (16)$$

The resulting field of the current sheet is the sum of external electric field (16) and the induction electric field $E_i(t)$, whose evolution, according to Eqs. (2) and (4), is described by the equation

$$E_i(t) = -\frac{1}{c}\text{Re}\left(\frac{\partial F(w,t)}{\partial t}\right). \quad (17)$$

In what follows, for convenience in the numerical calculations, we will denote by $b(t)$ and $w = x + iy$ the dimensionless half-width of the current sheet and the complex and Cartesian coordinates expressed in units of R_E, because the Earth's radius R_E is the characteristic dimension of the problem: $b(t)/R_E \longrightarrow b(t)$, $w/R_E \longrightarrow w$, $x/R_E \longrightarrow x$, and $y/R_E \longrightarrow y$. In accordance with Eqs. (4), (5), and (17), the dynamics of the electric and magnetic fields is largely determined by the form of the functions $b(t)$ and $\dot{b}(t)$. Hence, taking into account relationships (6), (7), (10), and (11), we transform expression (8) to obtain the following equation for the half-width $b(t)$ of the current sheet:

$$\frac{R_E^2 b^2(t)}{4}\ln\left[\frac{4l^2e}{b^2(t)}\right] - \frac{\beta(t)}{\alpha} = 0, \quad (18)$$

where $e = 2.71828\ldots$. Equation (18) is a transcendental equation from which it is possible to numerically calculate the squared half-width of the current sheet $b^2(t)$. However, some properties of the function $b(t)$ can be determined analytically. Substituting representations (12), (13), and (15) for α, $\beta(t)$, and $f(t,\tau)$, respectively, into Eq. (18), we finally obtain

$$b^2(t)\ln\left[\frac{4l^2e}{b^2(t)}\right] - \frac{E_0}{H_0}\frac{4cl}{R_E}\left(\frac{t^2}{t+\tau}\right) = 0. \quad (19)$$

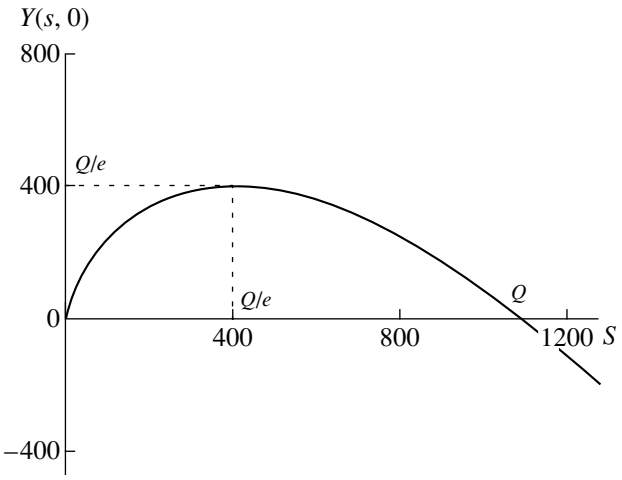

Fig. 1. Plot of the auxiliary function $Y(s, 0)$.

Equation (19) shows that the best way to work with the time t is to nondimensionalize it to a certain time T defined by the relationship

$$T = \frac{H_0}{E_0}\frac{R_E}{4cl}. \tag{20}$$

Setting $t/T \longrightarrow t$, $\tau/T \longrightarrow \tau$, and $t_{\max}/T \longrightarrow t_{\max}$, we then reduce Eq. (19) to the form

$$b^2(t)\ln\left[\frac{4l^2e}{b^2(t)}\right] - \frac{t^2}{t+\tau} = 0. \tag{21}$$

In what follows, by τ_0 and $t_{0\max}$ we will mean the dimensional equivalents of the corresponding dimensionless times.

In order to analyze the properties of Eq. (21), we consider the auxiliary function

$$Y(s, t) = s\ln\frac{Q}{s} + U(t), \tag{22}$$

which depends on the coordinate s and also on the parameter t corresponding to the time in Eq. (21). The notation in formula (22) is as follows:

$$s = b^2; \quad b > 0, \tag{23}$$

$$Q = 4l^2e, \tag{24}$$

$$U(t) = -\frac{t^2}{t+\tau}. \tag{25}$$

The set of points at which function (22) with different values of the parameter t intersects the abscissa gives a one-to-one correspondence between the coordinate s and the parameter t, consistent with the solutions to Eq. (21).

Let us consider the function $Y(s, 0)$,

$$Y(s, 0) = s\ln\frac{Q}{s}. \tag{26}$$

This function behaves asymptotically as

$$\lim_{s\to 0} s\ln\frac{Q}{s} = \lim_{s\to 0} s = 0, \tag{27}$$

$$\lim_{s\to\infty} s\ln\frac{Q}{s} = -\lim_{s\to\infty} s\ln\frac{s}{Q} = -\infty. \tag{28}$$

It is easy to see that the function $Y(s, 0)$ intersects the abscissa not only at the point $s = 0$ (see formula (27)) but also, in accordance with formula (26), at the point $s = Q$. This function then approaches minus infinity.

The extremes of the function $Y(s, 0)$ are found by equating its derivative with respect to s to zero:

$$\frac{dY(s, 0)}{ds} = \ln\frac{Q}{s} - 1. \tag{29}$$

Thus, from relationships (26) and (29) we readily see that the function $Y(s, 0)$ has only one extreme, namely, the maximum $Y(Q/e, 0) = Q/e$ at the point $s = Q/e$. In accordance with the aforesaid, Eq. (21) initially has two solutions, one of which corresponds to the intersection of the function $Y(s, 0)$ with the abscissa at the point $s = 0$ and the other corresponds to the intersection at the point $s = Q$.

We now consider how the function $Y(s, t)$ (22) evolves over time t. The nonzero values of the function $U(t)$ correspond to the shifts of the auxiliary function along the ordinate axis (Fig. 1). We can distinguish between the following four cases:

(i) $U(t) > 0$ (only the second solution exists),

(ii) $-\frac{Q}{e} < U(t) \le 0$ (both solutions exist),

(iii) $U(t) = -\frac{Q}{e}$ (the two solutions coincide, so that only one solution exists), and

(iv) $U(t) < -\frac{Q}{e}$ (there are no solutions).

Under actual physical conditions, the function $U(t)$ takes on values from zero to $-\infty$, which corresponds to cases (ii)–(iv). The case in which Eq. (21) has two solutions is of particular interest. The first solution is the standard one and corresponds to an expanding current sheet. It is this solution that was considered earlier in [16, 20]. The second solution describes a contracting current sheet and, of course, requires physical interpretation. Let there be a thin current sheet produced by some external action. If, at a certain instant, the surrounding conditions turn out to be consistent with Syrovatskiĭ's model, then, according to the second solution, the sheet should begin to contract. Such a specific dynamics of a current sheet is theoretically possible and requires a more detailed investigation. However, obser-

vations show that, in the Earth's magnetosphere, protons are accelerated by expanding current sheets. That is why, in the present paper, the energy spectrum is constructed based on the standard solution. In accordance with relationships (22) and (25), the dependence of the function $Y(s, t)$ on time t in Fig. 1 implies that, for the standard solution, the squared half-width of the current sheet cannot exceed the critical value Q/e, at which, in addition, both solutions coincide. This conclusion is confirmed by the numerical solution of Eq. (21) (see Fig. 2a).

Now, using formula (24), we switch from the auxiliary function to the half-width of the current sheet. So, the maximum value of $b(t)$ is equal to

$$l_{\max} = 2l, \tag{30}$$

and the initial value of the second solution, which corresponds to a contracting current sheet, is

$$l_2 = 2l\sqrt{e}. \tag{31}$$

Using the equality $U(t_{\max}) = -Q/e$, which holds for $b = 2l$, we can obtain an approximate estimate of the maximum lifetime of a current sheet from formulas (24) and (25). To do this, we take into account the inequality $t_{\max} \gg \tau$ and the approximate equality $f(t_{\max}, \tau) \approx t_{\max}$, which follows from the first of formulas (15). As a result, the maximum lifetime $t_{\max}$ turns out to be

$$t_{\max} \approx 4l^2. \tag{32}$$

To study the dynamics of the current sheet further, we must determine its expansion rate $\dot{b}(t)$. We differentiate Eq. (21) to obtain

$$\dot{b}(t) = \frac{\dot{f}(t, \tau)}{4b(t)\ln\dfrac{2l}{b(t)}}. \tag{33}$$

An analysis of the asymptotic behavior of the function $\dot{b}(t)$ (33) at $t \longrightarrow t_{\max}$,

$$\lim_{t \to t_{\max}} \dot{b}(t) = \lim_{b(t) \to 2l} \frac{1}{8l\ln 1} = \infty, \tag{34}$$

shows that, when the sheet expands to its maximum half-width $b(t_{\max}) = 2l$, the expansion rate becomes infinite, which corresponds to an explosive process: the sheet ruptures in an explosive manner. This is confirmed by the numerical solution of Eq. (33). The results of solving this equation numerically are illustrated in Fig. 2b, in which the dimensional expansion velocity $\dot{b}_0(t)$ of a current sheet is expressed in km/s. Of course, such a solution results from the assumptions made in the current sheet model adopted here. Before the rupture of the sheet, the characteristic value of $\dot{b}_0(t)$ is about 10 km/s (Fig. 2b). Hence, an analytic examination of the properties of Eqs. (21) and (23) shows that the maximum half-width of a current sheet cannot be greater than twice the characteristic spatial scale of the closing current circuit. The functions $b(t)$ and $\dot{b}_0(t)$ largely determine the dynamics of the electric and magnetic fields, whose components, according to Eqs. (2), (4)–(7), and (16), have the form

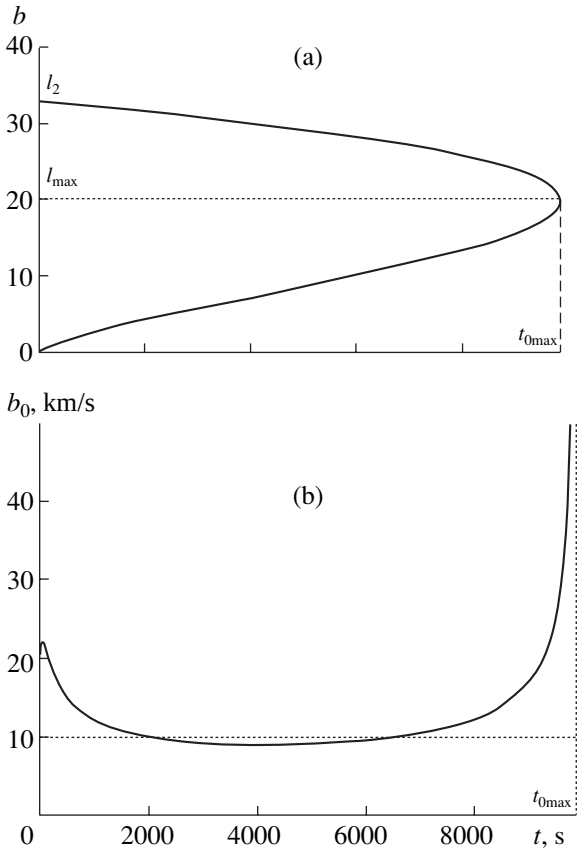

Fig. 2. Time evolution of (a) the dimensionless half-width of a current sheet b and (b) the dimensional expansion velocity of a current sheet $\dot{b}_0(t)$.

$$E_z(w, t) = -\frac{1}{c}\mathrm{Re}\left\{\frac{\partial F(w, t)}{\partial t}\right\} + E_{\mathrm{ext}}(t) \tag{35}$$

$$= \frac{R_E^2 \alpha b(t)\dot{b}(t)}{cT}\mathrm{Re}\left\{\ln\frac{w + \sqrt{w^2 - b^2(t)}}{b(t)}\right\} + E_0 \dot{f}(t, \tau),$$

$$H_x(w, t) = -\alpha R_E \mathrm{Im}\{\sqrt{w^2 - b^2(t)}\}, \tag{36}$$

$$H_y(w, t) = -\alpha R_E \mathrm{Re}\{\sqrt{w^2 - b^2(t)}\}, \tag{37}$$

$$E_x = E_y = H_z = 0. \tag{38}$$

3. NUMERICAL INTEGRATION OF THE EQUATIONS OF MOTION DESCRIBING THE ACCELERATION OF SOLAR WIND PROTONS IN A CURRENT SHEET IN THE EARTH'S MAGNETOTAIL

Recall that the acceleration process is considered here under the assumption that the initial kinetic energy of test particles in a collisionless plasma is zero. Consequently, there is no need to introduce the distribution function of the particles over initial energies and it is sufficient to consider the acceleration of freely moving particles in crossed electric and magnetic fields. Since the rest energy of a proton is approximately equal to 10^3 MeV, and since the maximum kinetic energy of protons accelerated in the region of magnetic reconnection in the Earth's magnetotail is about 1 MeV, the proton acceleration can be treated in the nonrelativistic approximation (here and below, all the formulas are written in dimensional form):

$$\dot{\mathbf{V}}(\mathbf{r}, t) = \frac{e_p}{m_p}\left(\mathbf{E}(w, t) + \frac{1}{c}[\mathbf{V}(\mathbf{r}, t)\mathbf{H}(w, t)]\right), \quad (39)$$

the initial velocity being

$$\mathbf{V}(\mathbf{r}, t = 0) = 0, \quad (40)$$

where $\mathbf{r}$ is the position vector in Cartesian coordinates, e_p and m_p are the charge and mass of a proton, $\mathbf{V}$ is the velocity vector of the accelerated protons, and $\mathbf{E}$ and $\mathbf{H}$ are the vectors of the electric and magnetic fields of the current sheet.

Thus, in order to construct the energy spectrum, it is necessary to analyze how the kinetic energy of test plasma particles (protons) increases from zero to a certain maximum value at which the particle leaves the sheet and gets out of the acceleration process. In accordance with the parameters of the problem, it is natural to choose the sizes of the system to be on the order of the characteristic spatial scale l of the closing current circuit. The computation region is chosen to have the form of a rectangular parallelepiped whose faces extend from $-l$ to l in the y and z directions and from $-2l$ to $2l$ in the x direction (in agreement with the fact that the current sheet expands to a maximum half-width equal to twice the characteristic spatial scale of the closing current circuit).

Let the test particles within the parallelepiped be initially at the mesh points of a three-dimensional uniform grid with the cell size $l_{st} = l/20$. It is necessary to take into account the fact that, because of the drift in crossed electric and magnetic fields [23], the plasma flows with the velocity $V_d = c|\mathbf{E}|/|\mathbf{H}|$ into the parallelepiped through the faces that are parallel to the xz plane of the current sheet. Thus, the particles on these faces of the parallelepiped are assigned the corresponding values of the initial velocity $V_d(x, t)$ (with account taken of the dependence of the plasma inflow velocity on time and on the coordinates on the faces). The plasma inflow is modeled as if the test particles above the faces of the parallelepiped were initially at the mesh points of a three-dimensional uniform grid identical to that within the parallelepiped. The spectrum is constructed by collecting the parameters of all the particles that escape from the parallelepiped (without allowance for the angle of escape). The effect of the magnetic field produced by accelerated protons on the current sheet is ignored. The total number of accelerated protons is on the order of 2×10^5.

The equations of motion were integrated numerically for the conditions of the Earth's magnetosphere. Accordingly, the parameters of the problem were chosen to be as follows [21]: $l = 10$, $l_{st} = 0.5$ [21], $E_0 = 2 \times 10^{-4}$ V/m [11], and $H_0 = 30$ nT [5]. For these parameter values, the characteristic time T (20) is about $T \approx 25$ s, so that we have $\tau \approx 12$ for $\tau_0 = 300$ s [5]. With these input values, parameters (30)–(32) are equal to $l_{max} = 20$, $l_2 \approx 33$, $t_{max} \approx 400$, and $t_{0max} \approx 10^4$ s.

The dynamics of the magnetic field topology in a current sheet is shown in Fig. 3, which illustrates the results of a numerical analysis carried out for the conditions of the Earth's magnetosphere in Syrovatskiĭ's model. The magnetic field lines are labeled by the numerical values of the vector potential of the electromagnetic field in units of T m. The typical trajectories of the particles accelerated by this evolving electromagnetic field are presented in Figs. 4 and 5.

The main result of the analysis of the energy spectrum of protons accelerated by a current sheet is the following: as is seen in Fig. 6, the spectrum consists of two parts separated by a minimum. The low-energy part of the spectrum corresponds to particles with energies lying in the range 10 eV $< E <$ 1 keV and obeys a power law, $E^{-(\kappa+1)}$, where $\kappa \approx 4.7$. The high-energy part of the spectrum corresponds to particles with energies in the range 1 keV $< E <$ 100 keV. The characteristic proton energy corresponding to the maximum concentration of protons in the high-energy part of the spectrum is about 5 keV (Fig. 6). The question naturally arises of how to explain the simultaneous presence of two very different populations of accelerated particles.

First, we can see from Fig. 4, which shows a representative trajectory of a low-energy particle an its projections onto the faces of the simulation box, that the low-energy particles escape predominantly through the side faces. That the plot has a striped structure stems from the specific features of numerical simulations: the initial positions of the particles are the mesh points of a three-dimensional uniform grid with the cell size $l_{st} = 0.5$, in which case the particles are only slightly displaced along the z coordinate. Second, we can see from Fig. 5, which shows a representative trajectory of a high-energy particle and its projections onto the faces of the simulation box, that the high-energy particles escape predominantly through the front face in the immediate vicinity of the ecliptic plane or, equivalently, the plane of the current sheet.

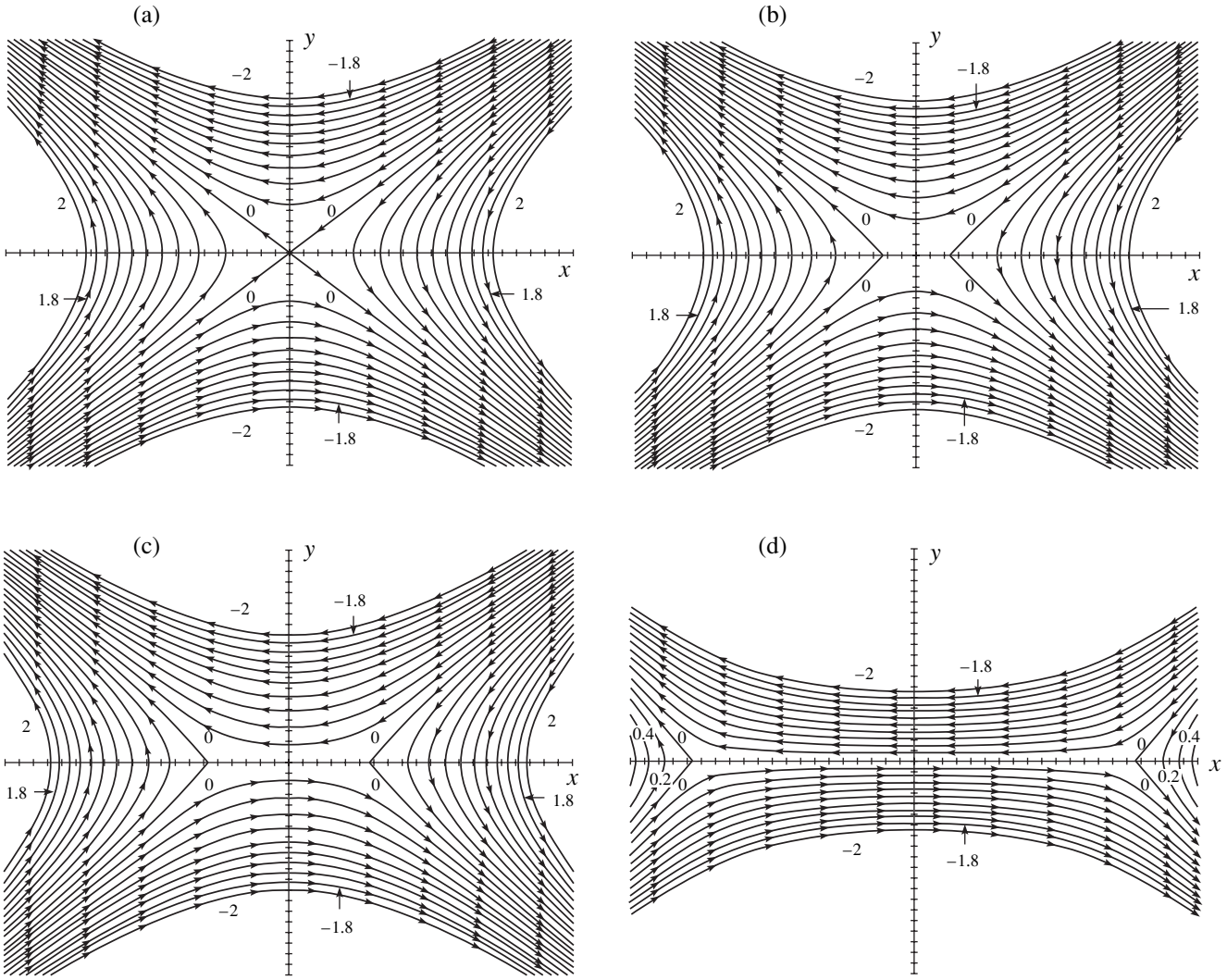

Fig. 3. Magnetic field topology at the times t = (a) 0, (b) 1000, (c), 3000, and (d) 9000 s. In this and other related figures, the magnetic field lines are labeled by values of the vector potential of the electromagnetic field in units of T m.

Hence, we see that the protons are accelerated by two different mechanisms. Low-energy protons are accelerated at the expense of drift in crossed electric and strong magnetic fields (the drift velocity being $V_d = c|\mathbf{E}|/|\mathbf{H}|$), while high-energy protons are accelerated by the electric field in the region of a weak magnetic field.

Let us examine the time dependence of the induction electric field in the plane of the current sheet. We choose a point x_1 on the x axis and consider how the electric field at this point will change over time. When the boundary of the current sheet approaches the chosen point, the electric field becomes maximum. Then, for $b(t \geq t_1) \geq x_1$, the field becomes equal to E_0; i.e., we have $E_i = 0$ (Fig. 7a). From Fig. 7a, which illustrates the dynamics of the magnetic field strength $|\mathbf{H}(w, t)|$, we can see that, as the boundary of the current sheet approaches the point x_1, the magnetic field decreases to zero at $b(t_1) = x_1$ and then, at $b(t > t_1) > x_1$, it increases. Hence, high-energy protons are accelerated predominantly at the ends of an expanding current sheet. Moreover, the closer the half-width of the sheet to its maximum possible value $b = 2l$, the higher the energy to which the protons are accelerated at the sheet ends (Fig. 7b). In fact, let us consider the asymptotic behavior of the electric and magnetic fields at $t \longrightarrow t_{\max}$ for the maximum possible value of the dimensionless coordinate on the x axis, $x_1 = 2l$, in the plane of the current sheet. Relationships (33)–(35) obviously yield

$$\lim_{t \to t_{\max}} E_z(x_1 = 2l, t) = \lim_{b(t) \to 2l} E_z(x_1 = 2l, t)$$
$$= \lim_{b(t) \to 2l} \frac{\ln \dfrac{2l + \sqrt{4l^2 - b^2(t)}}{b(t)}}{\ln \dfrac{2l}{b(t)}} = \infty, \qquad (41)$$

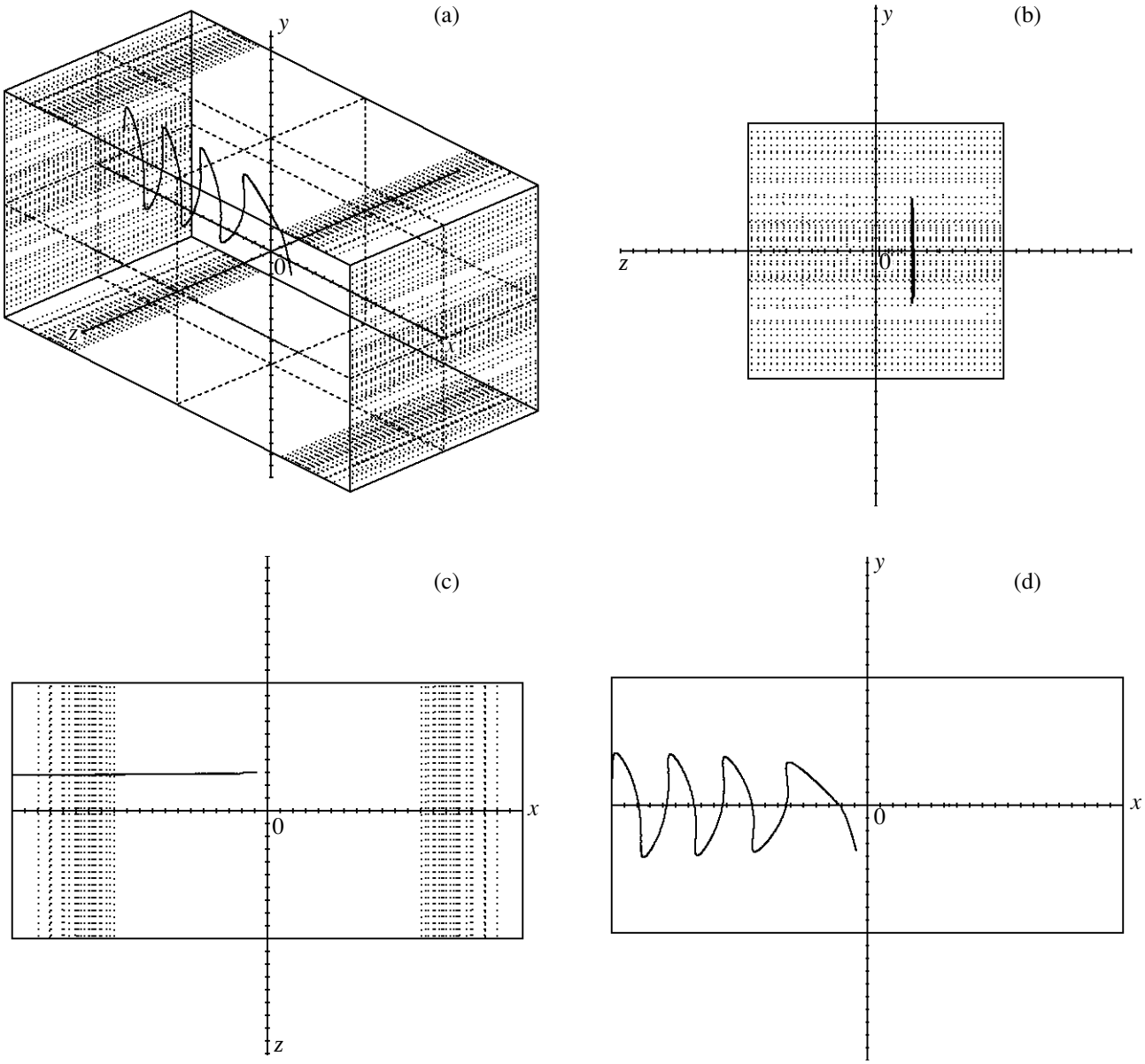

Fig. 4. (a) Representative trajectory of a proton slightly accelerated in the current sheet and the projections of this trajectory onto the (b) *yz*, (c) *xz*, and (d) *xy* planes. The dots show the points where low-energy protons escape from the acceleration region.

in which case the computations show that the following relationship is valid:

$$V_z \sim \int\limits_{0 < t < t_{\max}}^{t_{\max}} E_z(w, t)dt \neq \infty. \tag{42}$$

In turn, formulas (36) and (37) yield

$$\begin{aligned}\lim_{t \to t_{\max}} H_x(x_1 = 2l, t) &= \lim_{t \to t_{\max}} H_y(x_1 = 2l, t) \\ &= \lim_{b(t) \to 2l} |\mathbf{H}|(x_1 = 2l, t) = 0.\end{aligned} \tag{43}$$

Hence, formulas (41) the (43) show that, at the boundary $x_1 = 2l$ of the current sheet, the electric field approaches infinity as $t \longrightarrow t_{\max}$, while the magnetic field approaches zero (see Fig. 7c). This behavior of the electric field is explained by the fact that, for $b(t_{\max}) = 2l$, the current sheet ruptures in an explosive manner. Of course, in an actual sheet, the electric field cannot become infinite; however, by the time when the sheet ruptures, the electric field increases to a finite but fairly high value. Thus, it is because of the assumptions made in constructing the current sheet model that the electric field approaches infinity in accordance with

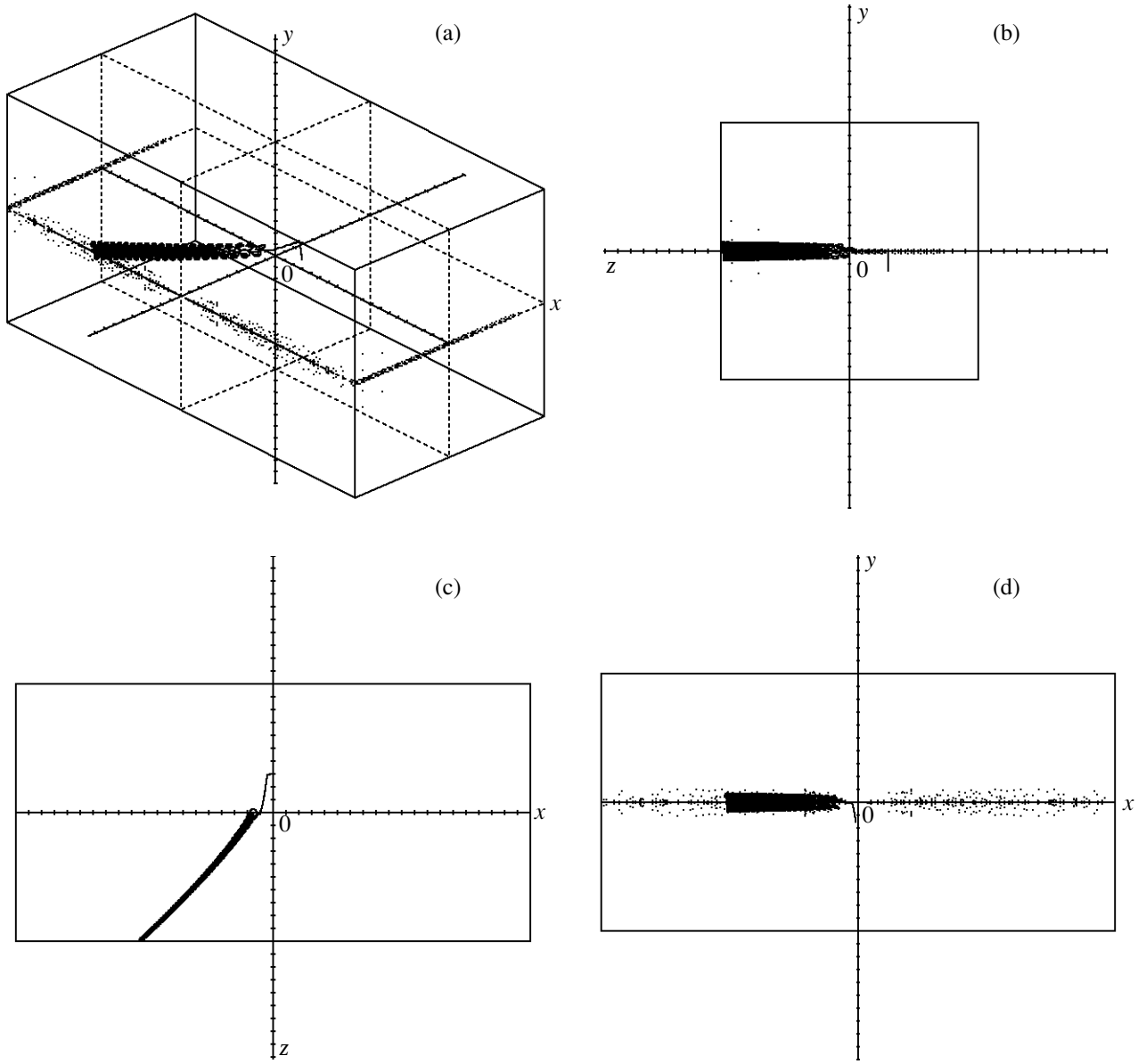

Fig. 5. (a) Representative trajectory of a proton accelerated in the current sheet to a high energy and the projections of this trajectory onto the (b) *yz*, (c) *xz*, and (d) *xy* planes. The dots show the points where high-energy protons escape from the acceleration region.

formula (41). Since integral (42) converges, these model assumptions are quite justified.

The maximum energy to which the protons can be accelerated by the current sheet under consideration is estimated to be about 280 keV. This numerical estimate was obtained in simulating the acceleration of particles in the plane of the current sheet in the electric field $E_z(x = 2l, t) = E_i(x = 2l, t) + E_{\text{ext}}(t)$, which is the sum of the induction field and the morning–evening external field and in which $E_i > E_{\text{ext}}$ (see expression (35)), the magnetic field being ignored ($|\mathbf{H}| \approx 0$).

It should be noted that spectra like that shown in Fig. 6 have not been observed experimentally in the Earth's magnetotail. The reason is that satellites measure the spectra of the entire flux of protons accelerated in the magnetotail rather than the spectra of protons accelerated by a particular individual current sheet. The entire proton flux consists of protons accelerated by a host of current sheets that have reached different stages of development and have originated at somewhat different conditions. In contrast, in the present paper, a study is made of the spectrum of particles accelerated by an infinitely thin individual current sheet that is assumed to

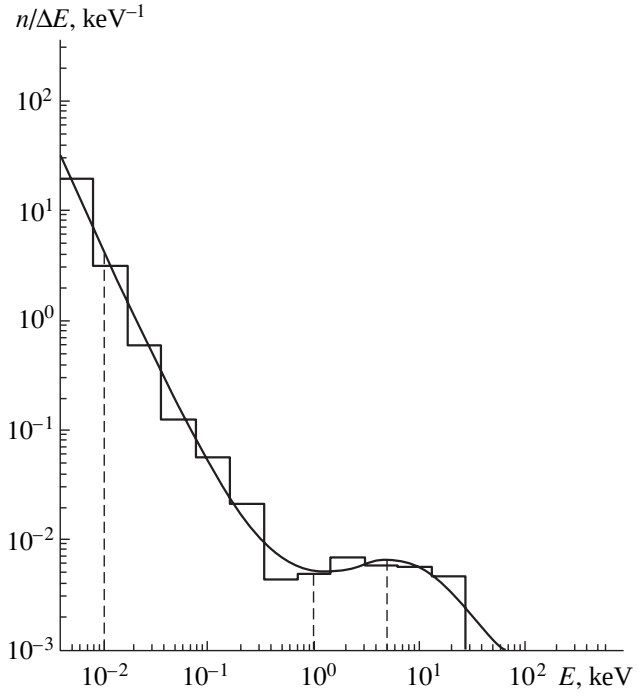

Fig. 6. Energy spectrum of the accelerated protons. Here, $n = \Delta N/N$, where ΔN in the number of protons with energies that lie in a given interval ΔE and N is the total number of accelerated protons. The energy interval ΔE is chosen so that, on a logarithmic scale, the lengths of the intervals are the same.

originate at certain average characteristic initial conditions and whose evolution is traced from a zero initial time at which it begins to expand, $b(t_0 = 0) = 0$. Moreover, not all of the actual current sheets can be approximately described as being infinitely thin. In addition, it is necessary to take into account the fact that the resulting proton energy spectra measured by satellites are contributed not only by the expanding current sheets but also by the current sheets that are already in the stage of rupture [13], during which protons are accelerated to higher energies than in the expansion stage. In [24–26], it was shown that an average statistical, experimentally observed energy spectrum consists of two parts: a Maxwellian part (in an energy range of 100 eV < E < 10 keV) and a power-law part (in an energy range of 10 keV < E < 1 MeV)—the so-called kappa distribution. Hence, the spectrum calculated here (see Fig. 6) determines the contribution that a sufficiently thin expanding current sheet described in Syrovatskiĭ's model makes up to the time when it ruptures to the average statistical energy spectrum of the accelerated protons. It can also be expected that spectra like that shown in Fig. 6 will be observed in experimental investigations of the acceleration of protons by individual current sheets modeled under laboratory conditions.

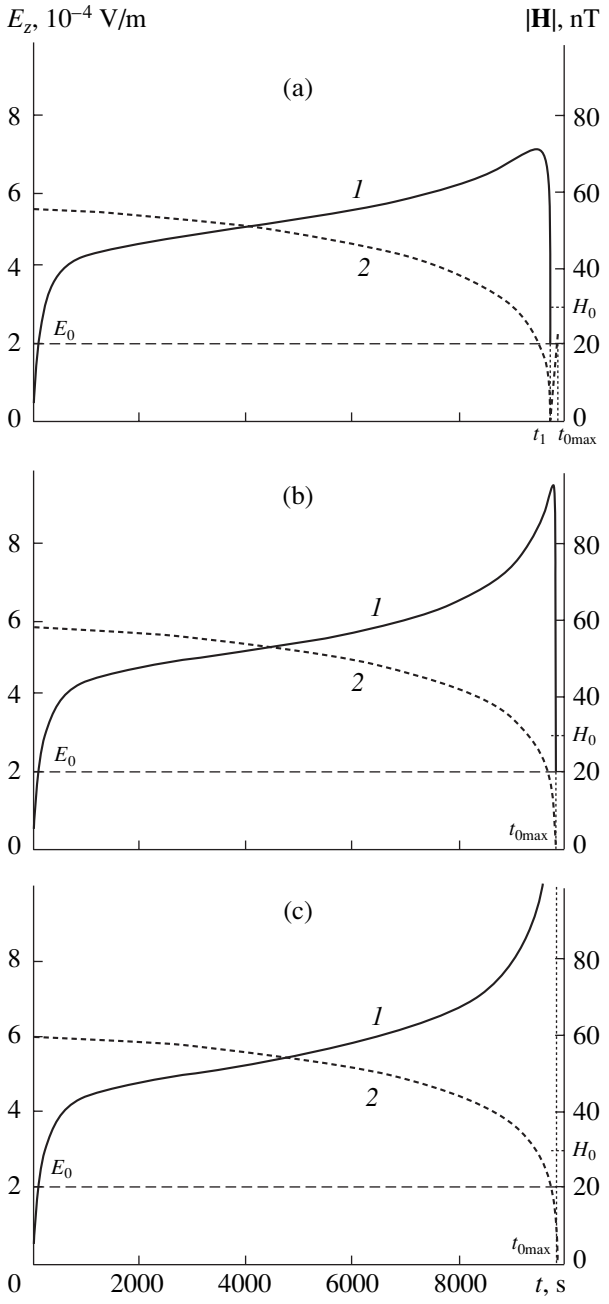

Fig. 7. Time evolution of the strengths of the (*1*) electric and (*2*) magnetic fields at the points with the following coordinates in the current sheet plane: (a) $x_1 = 18.5, y_1 = 0$; (b) $x_1 = 19.3, y_1 = 0$; and (c) $x_1 = 20, y_1 = 0$.

4. CONCLUSIONS

It has been shown that the numerical solution of transcendental equations (21) and (33) for the half-width $b(t)$ of the current sheet and for its expansion rate $\dot{b}(t)$ by using Syrovatskiĭ's model confirms the existence of two solutions corresponding to an expanding and a contracting current sheet.

The particle acceleration in a current sheet was simulated numerically for an expanding sheet, because it is such sheets that are observed experimentally in the Earth's magnetotail. The calculated energy spectrum of the accelerated protons consists of two parts, separated by a minimum. The first part is a power-law function and corresponds to low-energy protons, while the second corresponds to high-energy protons.

The fact that the spectrum consists of two parts indicates that protons are accelerated in two regimes: low-energy particles are accelerated at the expense of drift in the crossed electric and strong magnetic fields, while high-energy particles are accelerated by the electric field in the region of a weak magnetic field.

The numerical solution of Eqs. (21) and (33), which is required, in accordance with formulas (35)–(37), to analyze the dynamics of the electric and magnetic fields of a current sheet, shows that, in the plasma regions that form at both ends of an expanding sheet, the magnetic field is weak but the induction electric field is the strongest. This indicates that high-energy protons are accelerated predominantly at the ends of an expanding current sheet.

Although the energy spectrum of the accelerated protons that was calculated numerically in the present paper has not been observed directly in the Earth's magnetotail, it nevertheless determines the contribution that the expanding thin current sheet described in Syrovatskiĭ's model makes over the entire course of its evolution (up to its rupture) to the average statistical energy spectrum observed experimentally by satellites. Notably, it may be expected that the energy spectrum of protons accelerated in an individual thin current sheet in laboratory experiments will be similar to the spectrum calculated in the present paper.

ACKNOWLEDGMENTS

I am grateful to A.A. Galeev, L.M. Zelenyĭ, S.V. Bulanov, Kh.V. Malova, and V.Yu. Popov for discussing the results obtained and to I.A. Goryunova, T.M. Burinskaya, and V.V. Vovchenko for their help in preparing this paper. This work was supported in part by the Russian Foundation for Basic Research (project nos. 01-02-16367, 03-02-16967) and the Russian Federal Program for State Support of Leading Scientific Schools (project no. NSh-1739.2003.2).

REFERENCES

1. T. I. Pulkkinen, D. N. Baker, C. J. Owen, *et al.*, Geophys. Res. Lett. **20**, 2427 (1993).
2. V. A. Sergeev, V. Angelopoulos, C. Carlson, and P. Sutcliffe, J. Geophys. Res. **103**, 9177 (1998).
3. M. Hoshino, A. Nishida, T. Mukai, *et al.*, J. Geophys. Res. **101**, 24775 (1996).
4. L. M. Zelenyi, D. C. Delcourt, H. V. Malova, and A. S. Sharma, Geophys. Res. Lett. **29**, 49 (2002).
5. A. A. Galeev, in *Astrophysics and Space Physics Reviews*, Ed. by R. A. Syunyaev (Sov. Éntsiklopedia, Moscow, 1986; Gordon and Breach, London, 1981).
6. S. I. Syrovatskiĭ, Zh. Éksp. Teor. Fiz. **60**, 1727 (1971) [Sov. Phys. JETP **33**, 933 (1971)].
7. A. A. Galeev, in *Handbook of Plasma Physics: Basic Plasma Physics*, Ed. by A. A. Galeev and R. N. Sudan (Énergoatomizdat, Moscow, 1984; North-Holland, Amsterdam, 1984), Vol. 2.
8. D. Biskamp, *Nonlinear Magnetohydrodynamics* (Cambridge Univ. Press, Cambridge, 1997).
9. S. V. Bulanov, E. Yu. Echkina, I. N. Inovenkov, *et al.*, Tr. Fiz. Inst. Ross. Akad. Nauk **227**, 48 (2000).
10. A. G. Frank and G. M. Batanov, Tr. Fiz. Inst. Ross. Akad. Nauk **227**, 88 (2000).
11. L. M. Zelenyĭ, V. Perumyan, and M. Ashur-Abdalla, Tr. Fiz. Inst. Ross. Akad. Nauk **227**, 70 (2000).
12. L. M. Zelenyi and A. L. Taktakishvili, Astrophys. Space Sci. **134**, 185 (1987).
13. S. V. Bulanov and P. V. Sasorov, Astron. Zh. **52**, 763 (1975) [Sov. Astron. **19**, 464 (1975)].
14. L. M. Zelenyi, A. S. Lipatov, J. G. Lominadze, and A. L. Taktakishvili, Planet. Space Sci. **32**, 312 (1984).
15. Ya. K. Khodataev and V. M. Fadeev, Astron. Zh. **74**, 106 (1997) [Astron. Rep. **41**, 98 (1997)].
16. B. V. Somov and S. I. Syrovatskiĭ, Tr. Fiz. Inst. Ross. Akad. Nauk **74**, 14 (1974).
17. F. V. Coroniti, Space Sci. Rev. **42**, 399 (1985).
18. A. A. Galeev, Space Sci. Rev. **23**, 411 (1979).
19. M. A. Lavrent'ev and B. V. Shabat, *Methods of the Theory of Functions of a Complex Variable* (Nauka, Moscow, 1987).
20. S. I. Syrovatskiĭ, Tr. Fiz. Inst. Ross. Akad. Nauk **74**, 3 (1974).
21. L. Layons and D. Williams, *Quantitative Aspects of Magnitospheric Physics* (Dordrecht, Reidel, 1984; Mir, Moscow, 1987).
22. F. V. Coroniti and C. F. Kennel, J. Geophys. Res. **78**, 2837 (1973).
23. L. A. Artsimovich and R. Z. Sagdeev, *Physics of Plasma for Physicists* (Atomizdat, Moscow, 1979).
24. S. P. Christon, D. G. Mitchell, D. J. Williams, *et al.*, J. Geophys. Res. **93**, 2562 (1988).
25. S. P. Christon, D. J. Williams, D. G. Mitchell, *et al.*, J. Geophys. Res. **94**, 13409 (1989).
26. S. P. Christon, D. J. Williams, D. G. Mitchell, *et al.*, J. Geophys. Res. **96**, 1 (1991).

Translated by O.E. Khadin

Plasma Physics Reports, Vol. 30, No. 7, 2004, pp. 616–624. Translated from Fizika Plazmy, Vol. 30, No. 7, 2004, pp. 666–674.

PLASMA KINETICS

Fundamental Parameters of a Relativistic Runaway Electron Avalanche in Air

L. P. Babich*, E. N. Donskoy*, R. I. Il'kaev*, I. M. Kutsyk*, and R. A. Roussel-Dupre**

**All-Russia Research Institute of Experimental Physics, Russian Federal Nuclear Center, Sarov, Nizhni Novgorod oblast, 607188 Russia*

***Los Alamos National Laboratory, Los Alamos, New Mexico, 87545 USA*

Received July 1, 2003

Abstract—A relativistic runaway electron avalanche in air is simulated numerically by the Monte Carlo method with allowance for a large number of elementary processes involving electrons, positrons, and photons. The characteristic time scale of the avalanche amplification is calculated as a function of the overvoltage δ relative to the minimum value of the drag force between the electrons and the atomic particles of the medium. The dynamics of the formation of the electron energy distribution is investigated. The steady-state mean electron energy depends weakly on δ. Over a wide range of δ values, there exists a universal electron energy distribution, which is essentially independent of δ. The angular distributions of electrons integrated over energies, as well as the angular distributions for different energy groups, are calculated. Analytic approximations for the energy and angular distributions are obtained. © *2004 MAIK "Nauka/Interperiodica".*

1. INTRODUCTION

In order to explain the nature of penetrating radiation pulses recorded during thunderstorm activity in the Earth's atmosphere and the nature of optical phenomena observed above the thunderstorm clouds, Gurevich *et al.* [1] proposed a mechanism that governs the development of high-altitude atmospheric discharges and is based on the idea of a relativistic runaway-electron avalanche (RREA). The avalanche development is characterized by the time and spatial scales t_e and $l_e = t_e c$ (where c is the speed of light) of the e-fold avalanche enhancement. These scales play a fundamental role in the physics of gas breakdown by relativistic runaway electrons (REs), because the quantity $1/l_e$ is an analogue of the first Townsend ionization coefficient α_T in the relativistic energy range. At present, two approaches to calculating the time scale t_e have been developed. One of these is based on the numerical solution of the kinetic equation (KE) [2–8] that was first derived by Roussel-Dupre *et al.* [2] and contains an ionization integral that describes the kinetics of the production of high-energy secondary electrons. The other approach is based on direct statistical modeling by the Monte Carlo (MC) method [4, 6–10]. A comparison of the most recent results obtained by both of these approaches was carried out in [6–8]. Agreement between the results obtained by solving the KE and MC simulation results was achieved by refining the KE so that it could better describe the kinetics of two secondary electrons after an ionization event. When the accuracy of the approximation of the ionization integral in the azimuthal angle was improved, the results obtained by different scientific teams using independently generated numerical codes based on KE and MC methods were found to be in good agreement with each other. The only exception was the results obtained by the ELIZA MC code, developed at the All-Russian Research of Experimental Physics [11]. The code, into which the electric field was introduced to provide a calculation of the RREA kinetics [6–8], was found to yield far larger values of the time scale t_e. According to [7, 8], the reason for this disagreement is the following. The ELIZA code is intended for solving problems of the combined transport of electrons, positrons, and photons with allowance for all relevant elementary processes that are described in terms of the corresponding cross sections. In contrast, in the other approaches, including the simplified MC (SMC) method, account is taken exclusively of ionizing and elastic collisions of electrons with atomic particles and, moreover, the average effect of weak ionizing collisions is taken into account by the drag force. Gurevich *et al.* [12] believed that, for $\varepsilon \geq 5$ MeV, the bremsstrahlung drag is dominant and thus proposed to take into account the radiative component of the drag force. Note, however, that the bremsstrahlung process is incorporated into the ELIZA code; moreover, radiative losses in air become comparable to ionization losses only at electron energies close to 85 MeV [13], which, according to the MC calculations of RREA, are never achieved in practice. In this connection, it is worth noting that, for actual fields during thunderstorm activity in the Earth's atmosphere, the probability of an electron reaching an energy equal to the second root (in fact, the third root in the relativistic range [14]) of the equation [12]

$$eE = F(\varepsilon), \tag{1}$$

1063-780X/04/3007-0616$26.00 © 2004 MAIK "Nauka/Interperiodica"

is extremely low. In Eq. (1), $-eE$ is the electric force exerted on an electron and $F(\varepsilon)$ is the net drag force describing the average effect of ionizing and radiative interactions between electrons and atomic particles.

In the present paper, we point out the reason for the above disagreement (this is merely a Corrigenda mistake made in incorporating the electric field into the ELIZA code) and present the results of new calculations of the RREA rates carried out using the ELIZA code for air at a pressure of $P = 1$ atm and for the same three values as in [6–8] of the overvoltage $\delta = eE/F_{\min}$ relative to the relativistic minimum value of the drag force, equal to $F_{\min} = 2.18$ keV/cm for $P = 1$ atm [1, 2, 13]. We analyzed the dependence of the RE number on time and on the overvoltage δ. The RE energy and angular distributions were calculated. The process of relaxation of the RE energy distribution was investigated. We also calculated the enhancement time scale t_e as a function of the overvoltage δ over a wide range of the δ values that are of interest for the problem of the breakdown by relativistic REs.

2. DESCRIPTION OF THE CALCULATION METHOD (THE ELIZA CODE)

The calculation method implemented in the ELIZA code is intended to solve the following time-dependent linear Boltzmann equations by the MC technique:

$$\frac{\partial f^l(\mathbf{r}, \boldsymbol{\varepsilon}, t)}{\partial t} + \mathbf{v}^l(\varepsilon)\frac{\partial f^l(\mathbf{r}, \boldsymbol{\varepsilon}, t)}{\partial \mathbf{r}} + \sigma^l(\mathbf{r}, \boldsymbol{\varepsilon})v^l(\varepsilon) f^l(\mathbf{r}, \boldsymbol{\varepsilon}, t) = \int \sum_{l'} f^{l'}(\mathbf{r}, \boldsymbol{\varepsilon}', t) \times \sigma^{l'}(\mathbf{r}, \varepsilon')v^{l'}(\varepsilon')K^{l'l}(\mathbf{r}; \boldsymbol{\varepsilon}' \longrightarrow \boldsymbol{\varepsilon})d\boldsymbol{\varepsilon}' + g^l(\mathbf{r}, \boldsymbol{\varepsilon}, t), \quad (2)$$

where $f^l(\mathbf{r}, \boldsymbol{\varepsilon}, t)$ is the distribution function of the particles of species l over energies ε and directions $\boldsymbol{\omega}$ ($\boldsymbol{\varepsilon} = \varepsilon\boldsymbol{\omega}$; $\mathbf{v}^l = v^l\boldsymbol{\omega}$) at the time t and at the spatial point $\mathbf{r}$, v^l is the particle velocity, $\sigma^l(\mathbf{r}, \varepsilon)$ is the total interaction cross section, the kernel $K^{l'l}(\mathbf{r}; \boldsymbol{\varepsilon}' \longrightarrow \boldsymbol{\varepsilon})$ describes transitions due to interactions in which particles of species l are produced, and the term $g^l(\mathbf{r}, \boldsymbol{\varepsilon}, t)$ describes the source of particles of species l.

The recently developed second version of the ELIZA code (its first version is described in [11]) is based on new libraries of the cross sections for the interactions of photons, electrons, and positrons with matter, including new data on the relaxation of atomic shells. These libraries were compiled using the EPDL92 library [15], the EEDL92 library for electrons [16], and the EADL92 library for the relaxation of atomic shells [17], which are disseminated by the International Atomic Energy Agency (IAEA) [18], as well as using the literature data on the cross sections for interaction processes involving electrons and positrons.

In the second version of the ELIZA code, the following interaction processes are taken into account: the interactions of photons with matter include incoherent (Compton) scattering with allowance for the binding of electrons in the atom, coherent (Rayleigh) scattering, photoabsorption accompanied by the emission from the atom of fluorescent photons and Auger electrons, the production of electron–positron pairs and triplets. The interactions involving electrons are elastic scattering by nuclei, the ionization and excitation of atomic shells, and bremsstrahlung. Finally, for positrons, the processes included are elastic scattering by nuclei, scattering by free electrons, bremsstrahlung, and two-photon annihilation.

Since new cross-section libraries were used in the second version of the ELIZA code, the description was refined of the processes of Compton scattering, Rayleigh scattering, the production of electron–positron pairs and triplets, the elastic scattering of electrons and positrons by nuclei, and electron and positron bremsstrahlung and new numerical models of these physical processes were developed. The photoabsorption process was modeled separately for the following nine atomic subshells: K, $L1$, $L2$, $L3$, $M1$, $M2$, $M3$, $M4$, and $M5$. A new model of atomic shell relaxation was developed with allowance for all transitions to these subshells, accompanied by the emission of all the fluorescent photons and Auger electrons that are produced in these transitions. In the first version of the ELIZA code, the ionization of an atom by an electron was described as electron scattering by free electrons, the scattering cross section being calculated from the Meller formula (see [13]). In contrast, in the second version, the ionization of each of the above subshells is treated separately; moreover, these ionization processes, as well as the photoabsorption processes, are simulated with allowance for the relaxation of atomic shells. We also take into account the excitation of atomic shells by electrons—a process that was not included in the first version, in which the excitation of atoms was taken into account in calculating the mean electron energy losses.

In order to provide the possibility of computing the RREA development rate, we included in the second version of the ELIZA code the external electric field in the following way: For each section of the trajectory of a charged particle (an electron or a positron), the code solves the vector equation

$$\frac{d\mathbf{p}}{dt} = e\mathbf{E}, \quad (3)$$

where $\mathbf{p}$ is the relativistic momentum of the particle, e is the electric charge, $\mathbf{E} = \mathbf{E}(\mathbf{r})$ is the electric field vector, and $\mathbf{r}$ is the position vector of a point in space.

Some transformations in the spherical coordinate system

$$\begin{cases} p_x = p\sin\theta\cos\varphi, \\ p_y = p\sin\theta\sin\varphi, \\ p_z = p\cos\theta \end{cases}$$

reduce vector equation (3) to the set of equations

$$\begin{cases} \dfrac{dp}{dt} = eE_x\alpha\sqrt{1-\mu^2} + eE_y\sqrt{1-\mu^2}\sqrt{1-\alpha^2} + eE_z\mu, \\ \dfrac{d\mu}{dt} = \dfrac{-eE_x\alpha\mu\sqrt{1-\mu^2} - eE_y\mu\sqrt{1-\mu^2}\sqrt{1-\alpha^2} + eE_z(1-\mu^2)}{p}, \\ \dfrac{d\alpha}{dt} = \dfrac{eE_x(1-\alpha^2) - eE_y\alpha\sqrt{1-\alpha^2}}{p\sqrt{1-\mu^2}}, \end{cases} \tag{4}$$

where $\mu = \cos\theta$ is the cosine of the angle between the direction of the electric force exerted on an electron and the direction $\boldsymbol{\omega}$ of the electron motion, $\alpha = \cos\varphi$, and (E_x, E_y, E_z) are the components of the electric field vector **E**.

For a constant electric field directed along the *z* axis ($E = E_z$), Eqs. (4) take their simplest form:

$$\begin{cases} \dfrac{dp}{dt} = eE_z\mu, \\ \dfrac{d\mu}{dt} = \dfrac{eE_z(1-\mu^2)}{p}, \\ \alpha = \text{const}. \end{cases} \tag{5}$$

Replacing differentiation over time *t* with differentiation along the trajectories, $ds = c\beta dt$ (where β is the ratio of the velocity of an electron or a positron to the speed of light *c*), yields

$$\begin{cases} \dfrac{dp}{ds} = \dfrac{eE_z\mu}{c\beta}, \\ \dfrac{d\mu}{ds} = \dfrac{eE_z(1-\mu^2)}{pc\beta}, \\ \alpha = \text{const}. \end{cases} \tag{6}$$

The relationship between the increment in the kinetic energy of a particle and that in its momentum, $d\varepsilon = \beta c dp$, makes it possible to replace the momentum equation in set (6) by the energy equation

$$\frac{d\varepsilon}{ds} = eE_z\mu. \tag{7}$$

Setting $p = p_0$, $\beta = \beta_0$, and $\mu = \mu_0$ at the initial point of the trajectory section allows us to integrate the second of Eqs. (6) in quadratures:

$$\mu_t = \frac{A(1+\mu_0) - (1-\mu_0)}{A(1+\mu_0) + (1-\mu_0)}, \quad A = \exp\left\{\frac{2eE_z s}{p_0 c\beta_0}\right\}. \tag{8}$$

For an external electric field directed along the *z* axis, Eqs. (2) for electrons and positrons is reduced to

$$\begin{aligned} &\frac{\partial f^{\pm}(\mathbf{r}, \boldsymbol{\varepsilon}, t)}{\partial t} + \frac{\partial(\mathbf{v}^{\pm} f^{\pm}(\mathbf{r}, \boldsymbol{\varepsilon}, t))}{\partial \mathbf{r}} \\ &+ \frac{\partial}{\partial \varepsilon}(eE_z\mu\nu^{\pm}(\varepsilon) f^{\pm}(\mathbf{r}, \boldsymbol{\varepsilon}, t)) \\ &+ \frac{\partial}{\partial \mu}\left(eE_z\frac{1-\mu^2}{p} f^{\pm}(\mathbf{r}, \boldsymbol{\varepsilon}, t)\right) \\ &+ \sigma^{\pm}(\mathbf{r}, \varepsilon)\nu^{\pm}(\varepsilon) f^{\pm}(\mathbf{r}, \boldsymbol{\varepsilon}, t) \\ &= \int \sum_{l'} f^{\pm}(\mathbf{r}, \boldsymbol{\varepsilon}', t)\sigma^{l'}(\mathbf{r}, \varepsilon')\nu^{l'}(\varepsilon') \\ &\times K^{l'\pm}(\mathbf{r}; \boldsymbol{\varepsilon}' \longrightarrow \boldsymbol{\varepsilon}) d\boldsymbol{\varepsilon}' + g^{\pm}(\mathbf{r}, \boldsymbol{\varepsilon}, t), \end{aligned} \tag{9}$$

where the superscript plus and minus signs indicate positrons and electrons, respectively.

When including the external electric field in the second ELIZA version in order to perform the RREA simulations whose results were published in [6–8], a corrigendum was made, namely, the longitudinal electric field component in Eqs. (7) and (8) was set to be $E_z = E|\mu|$. Therefore, the electric force exerted on electrons and positrons turned out to be lower on the average by 15–20%. After this mistake was eliminated, a new series of simulations with the second version of the code was carried out, the results of which will be presented in the next section.

3. CALCULATED RESULTS

The simulations were performed for air at atmospheric pressure, the formulation of the problem being the same as that in [6–8]. It was assumed that, at the initial instant, a monoenergetic beam containing $N(0)$ electrons with the kinetic energy ε_0 is injected along the electric force. The computations were performed for two substantially different values of ε_0: 2 and 10 MeV. The number $N(0)$ of electron trajectories to be traced numerically was chosen in such a way that the statisti-

Table 1. Characteristic time scale t_e [ns] for avalanche amplification in air at P = 1 atm

Angular electron scattering			Ignored			Accounted for		
Overvoltage $\delta = E$ [kV/cm]/2.18			2	5	8	2	5	8
KE	Symbalisty *et al.* [4, 5]					161	34.4	18.9
	MigDesk code [6–8]		98	31	16.3	197	39.9	21.2
MC	Lehtinen *et al.* [10]					174.4	33.2	17.3
	SMC [6–8]		77.6	20.8	11.2	200	35.6	18.6
	ELIZA code	[6–8]	107	28	15.8	440	54	27.5
		New results	81	20.1	10.7	189.7	34.3	17.8

cal errors in calculations did not exceed 1–2%. The trajectories of the electrons were followed until their energies became as low as ε = 1 keV. Although the number of the generated electrons with energies below the runaway threshold ε_{th}, which is defined to be the second root of Eq. (1) [12, 14], is very large, they relax to thermal energies so rapidly that their contribution to the RREA can be ignored. The time dependences of the number $N(t)$ of REs for different values of the overvoltage δ are the results of simulations. The time scale of the RREA enhancement was calculated from the linear portion of the dependence $\ln[N(t)/N(0)]$ as follows:

$$t_e = t/\ln[N(t)/N(0)]. \quad (10)$$

Table 1 compares the results of the new calculations of t_e for three different δ values with the results published earlier in [6–8, 10]. It may be seen that the above considerable disagreement between the results obtained from the ELIZA code and those from other codes, based on the MC and KE methods, is eliminated. The substantial discrepancy that remains between the results calculated by the MC and KE methods without allowance for angular electron scattering is most likely attributed to differences in the methods themselves.

Figure 1 and Table 2 show the time scale $t_e(\delta)$ calculated by using the ELIZA code with and without allowance for angular electron scattering in the range of the overvoltage values of practical interest, $\delta \in [1.3, 14]$. Recall that the value $\delta \approx 14$ corresponds to conventional gas breakdown by electrons with energies close to the ionization energy threshold in air. The fact that t_e increases rapidly (up to 8905 ns) as the value δ = 1.3 is approached presumably indicates that the value δ = 1.3 is close to the critical overvoltage below which the REs are not generated; as a result, this value of the time scale t_e can be grossly erroneous.

Over broad ranges of δ values, the dependence $t_e(\delta)$ can be approximated with an accuracy of 5% by the following expressions:

$$t_e\ [\text{ns}] = \exp(7.11/\delta^{0.441}), \quad \delta \in [2, 10] \quad (11)$$

for a dependence calculated with allowance for angular electron scattering and

$$t_e\ [\text{ns}] = \exp(6.35/\delta^{0.475}), \quad \delta \in [3, 10] \quad (12)$$

for a dependence calculated without allowance for angular electron scattering.

Figure 2 shows the dependence $\ln[N(t)/N(0)]$ calculated for ε_0 = 2 MeV and for three different values $\delta \geq 2$ of the overvoltage. We can see that the time during which an RREA achieves the exponential mode in accordance with the relation $\frac{\partial}{\partial t}\ln[N(t)/N_0] \approx$ const is several times shorter than the corresponding characteristic time scale $t_e(\delta)$.

We also investigated how the RREA dynamics depends on the initial kinetic energy ε_0 of the electrons. The results of the relevant simulations carried out for

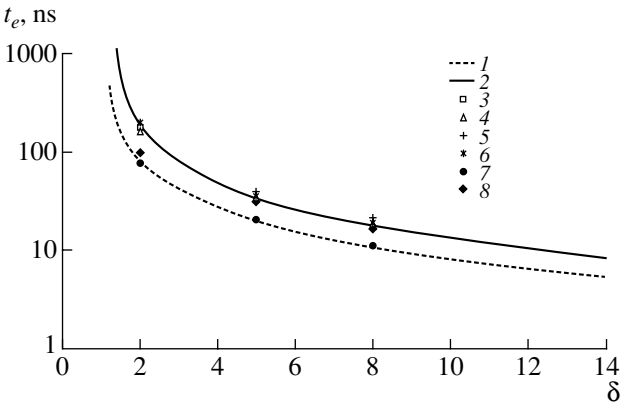

Fig. 1. Time scale of the *e*-fold avalanche enhancement in air at P = 1 atm versus overvoltage. Shown are the results calculated (*1*) without and (*2*) with allowance for electron scattering, the results obtained (*3*) by Lehtinen *et al.* [10] and (*4*) by Symbalisty *et al.* [4, 5], (*5*) the results from the MigDesk code [7], (*6*) the results calculated by the SMC method [7], (*7*) the results calculated by the SMC method [7] without allowance for electron scattering, and (*8*) the results calculated with the MigDesk code [7] without allowance for electron scattering.

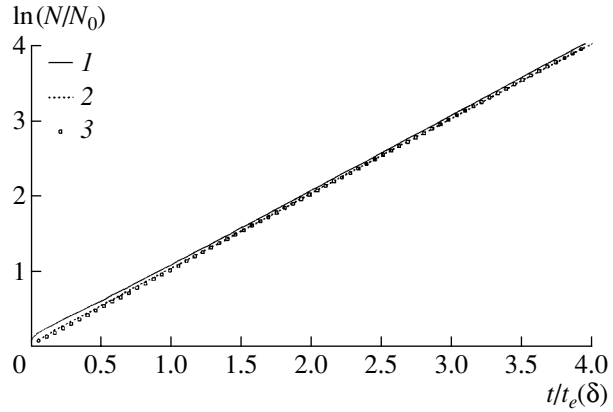

Fig. 2. Time dependence of the number of electrons for different values of the overvoltage δ: δ = (*1*) 2, (*2*) 8, and (*3*) 14. The calculations were carried for the initial electron energy ε_0 = 2 MeV and for air at P = 1 atm.

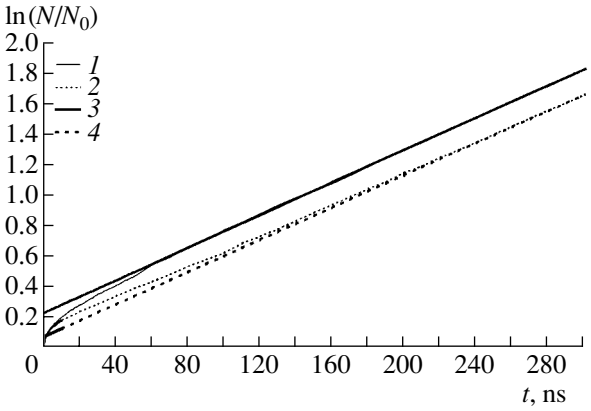

Fig. 3. Time dependence of the number of electrons for different values of their initial energy: ε_0 = (*1*) 10 MeV, (*2*) 2 MeV, (*3*) 10 MeV (linear approximation), and (*4*) 2 MeV (linear approximation). The calculations were carried for the overvoltage δ = 2 and for air at P = 1 atm.

the initial energies ε_0 = 2 and 10 MeV are illustrated in Figs. 3 and 4. For the considered energies, 2 and 10 MeV, the avalanches were found to exhibit different behavior at low overvoltage values δ ≤ 2; moreover, the higher the energy ε_0, the shorter the time after which the avalanche grows exponentially (see Fig. 3). For δ < 2, this time increases as δ decreases; moreover, the curves calculated for δ = 1.3 (see Fig. 4) imply that only electrons with sufficiently high initial kinetic energy can be involved in the runaway mode.

Table 2. Characteristic time scale t_e [ns] for avalanche amplification in air at P = 1 atm as a function of the overvoltage δ according to calculations with the ELIZA code

δ	Electron scattering	
	ignored	accounted for
1.2	–	491
1.3	8905	–
1.4	1236	201
1.5	696.4	–
1.6	447.2	133
1.8	270.1	99.3
2	189.7	81.0
2.5	109.8	–
3	77.6	41.4
4	47.5	27.1
5	34.3	20.1
6	26.4	15.7
7	21.3	12.8
8	17.8	10.7
10	13.3	8.0
12	10.45	6.36
14	8.56	5.48

The time during which an RREA relaxes to a steady-state energy distribution does not coincide with the time required for the avalanche to achieve the exponential mode. Indirect evidence of this is provided by Fig. 5, which illustrates the results of calculating the time dependence of the mean energy $\langle\varepsilon(t)\rangle$ of the electrons in RREA. The calculations carried out for ε_0 = 2 and 10 MeV show that the steady-state values of the mean energy $\langle\varepsilon\rangle$ differ insignificantly in the range δ = 2–14 of the overvoltage values (see Table 3) and that they are established on time scales of about ~(4–6)t_e. An analogous result was obtained by Symbalisty *et al.* [5]. It should be noted that the dependence of $\langle\varepsilon\rangle$ on δ is monotonic: the mean electron energy decreases slightly with increasing δ; this is because the electrons with increasingly lower energies become runaways.

The weak dependence of the established mean electron energy $\langle\varepsilon\rangle$ on δ over a wide range of values of the latter can be explained by referring to the following expression for $\langle\varepsilon\rangle$:

$$\langle\varepsilon\rangle_{\text{approx}} \approx c(\delta - 1)F_{\min}t_e(\delta). \qquad (13)$$

The physical meaning of this expression is quite obvious: the mean energy $\langle\varepsilon\rangle$ is estimated by the energy acquired by an electron of initial energy less than $\langle\varepsilon\rangle$ till it produces another RE. We can see from Table 3 that, for δ = 2–14, formula (13) gives nearly the same values of the mean electron energy, which differ little from the values calculated with the ELIZA code for the relaxation time scales t_e obtained without allowance for angular electron scattering (Table 1). The primary effect of the electron scattering in elastic collisions is a nearly threefold increase in the effective runaway generation threshold ε_{th} [8]. Since, for the overvoltage values under consideration, the runaway threshold ε_{th} is far

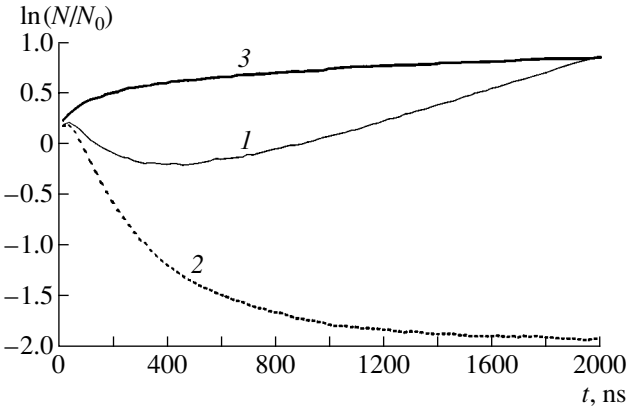

Fig. 4. Time dependence of the number of electrons for low values of the overvoltage δ: (*1*) δ = 1.4 and ε_0 = 2 MeV, (*2*) δ = 1.3 and ε_0 = 2 MeV, and (*3*) δ = 1.3 and ε_0 = 10 MeV. The calculations were performed for air at P = 1 atm.

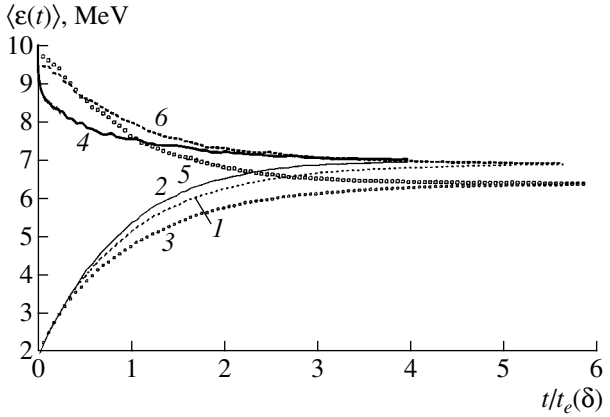

Fig. 5. Time dependence of the mean energy of the electrons for different values of their initial energy ε_0 and for different values of the overvoltage δ: (*1*) δ = 8 and ε_0 = 2 MeV, (*2*) δ = 2 and ε_0 = 2 MeV, (*3*) δ = 14 and ε_0 = 2 MeV, (*4*) δ = 2 and ε_0 = 10 MeV, (*5*) δ = 14 and ε_0 = 10 MeV, and (*6*) δ = 8 and ε_0 = 10 MeV. The calculations were performed for air at P = 1 atm.

lower than ⟨ε⟩, formula (13) with the corresponding t_e values can be used to obtain estimates with allowance for elastic collisions (Table 1). The formula produces qualitatively correct results: it yields approximately the same mean electron energies for different δ values except for δ = 2, but it does not take into account electron scattering in elastic collisions and thereby overestimates the values of ⟨ε⟩ in comparison to those calculated with the ELIZA code. The established mean electron energy is controlled by the competition between two processes: energization of the electrons by the field and the production of the secondary electrons, the vast majority of which have initial energies much lower than ⟨ε⟩. The first process, which is accounted for by the factor (δ – 1) in formula (13), acts to increase the mean electron energy, while the second process, which is accounted for by the factor $t_e(\delta)$, decreases ⟨ε⟩. The higher the overvoltage δ, the more efficiently the electrons will gain energy but, at the same time, the more intense will be the electron multiplication. Apparently, it is the "dynamic equilibrium" between these two processes that explains the weak dependence of ⟨ε⟩ on δ in the range δ = 2–8.

The weak dependence of ⟨ε⟩ on δ indicates that the steady-state electron energy distributions are close to one another, which is confirmed by numerical simulations. Figures 6 and 7 show the normalized electron energy distributions at different times. The time scale on which the steady-state distribution is established is approximately the same as that for the mean electron energy ⟨ε⟩. This time scale is defined as the time after which the electron distribution remains unchanged, except for a high-energy tail with an insignificant fraction of electrons (less than 10^{-4}–10^{-5}). In particular, this time scale can be determined by the time during which the mean electron energy becomes steady-state. The vertical lines in the figures indicate the maximum energies that can be attained by the primary electron by the time t calculated from the formula $\varepsilon_{max} \approx c(\delta - 1)F_{min}t + \varepsilon_0$. It can be seen that the electrons do indeed reach the maximum energies ε_{max}, which is evidence that the spectrum of primary electrons contains particles moving in the direction of the electric force. Gurevich *et al.* [12] estimated the maximum possible energy (the third root of Eq. (1) [14]) to which an electron can be accelerated in an external electric field. This energy is a nearly linear function of δ: it is equal to 430 MeV for δ = 5 and to 850 MeV at δ = 10 [12]. Unfortunately, in view of the inordinate amounts of computer time required for direct MC simulations of the steady-state distributions, it is impossible to reach these energies or to check the hypothesis that they can be reached by at least a few electrons.

In the range of the overvoltage values under investigation (δ = 2–8), the steady-state electron energy distributions in an RREA, normalized to unity, differ only

Table 3. Steady-state values of the mean electron energy calculated for different values of the overvoltage δ with and without allowance for angular electron scattering

δ	⟨ε⟩, MeV			
	with allowance for scattering		without allowance for scattering	
	ELIZA code	Formula (13)	ELIZA code	Formula (13)
2	6.96	12.41	4.20	5.30
5	6.92	8.97	4.56	5.26
8	6.87	8.15	4.32	4.90
14	6.35	7.28	4.17	4.66

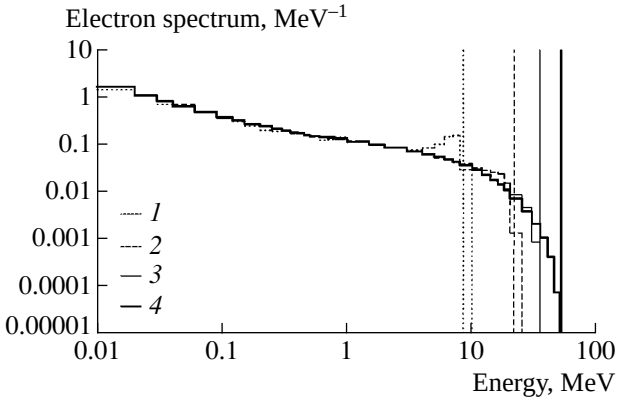

Fig. 6. Normalized electron energy distributions at different times: $t/t_e(\delta)$ = (*1*) 0.53, (*2*) 1.58, (*3*) 2.64, and (*4*) 3.95. The calculations were performed for $\delta = 2$ and for air at P = 1 atm.

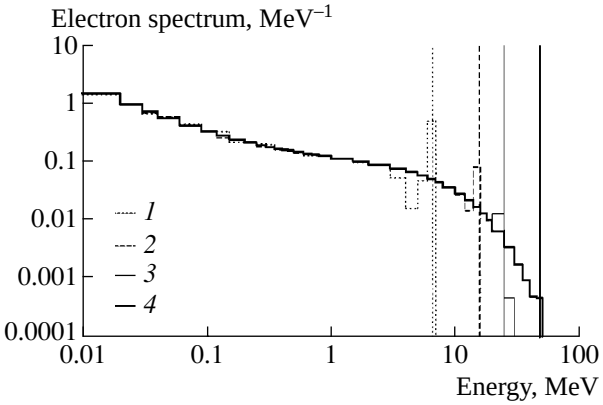

Fig. 7. Normalized electron energy distributions at different times: $t/t_e(\delta)$ = (*1*) 0.56, (*2*) 1.69, (*3*) 2.81, and (*4*) 5.62. The calculations were performed for $\delta = 8$ and for air at P = 1 atm.

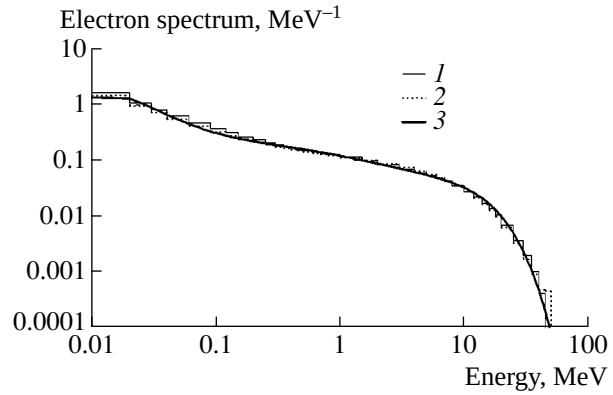

Fig. 8. Normalized steady-state electron energy distributions for δ = (*1*) 2 and (*2*) 8. Curve *3* is the analytic approximation for the distributions. The calculations were performed for air at P = 1 atm.

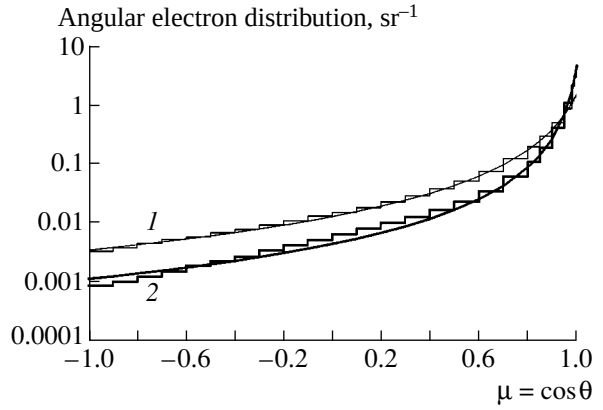

Fig. 9. Normalized angular distributions of the electrons for δ = (*1*) 2 and (*2*) 8. The histograms were calculated with the ELIZA code, and the curves were calculated from approximations (15). The calculations were performed for air at P = 1 atm.

slightly from each other. Figure 8 shows the electron distributions calculated for $\delta = 2$ and 8. In the energy range 0.01–40 MeV, the distributions differ by no more than 15%. We thus can speak of a universal distribution, which can be approximated by the function

$$\exp(-0.00108u^6 - 0.004235u^5 + 0.009757u^4 + 0.012652u^3 - 0.056372u^2 - 0.43325u - 2.1185), \quad (14)$$

where $u = \ln(\varepsilon\ [\text{MeV}])$.

Integrating over all energies yields the angular electron distributions. These distributions, normalized to unity, are illustrated in Fig. 9, which shows the results of calculations carried out for $\delta = 2$ and 8. In contrast to the energy distributions, the steady-state angular distributions are strongly dependent on δ: as δ increases, the distribution extends in the forward direction; i.e., the stronger the electric field, the larger the number of electrons accelerated by it. These distributions are approximated by the functions

$$g(\mu, b) = \frac{1 - b^2}{2\pi(1 - b\mu)^2}, \quad (15)$$

where $b = 0.91$ for $\delta = 2$ and $b = 0.97$ for $\delta = 8$. The maximum error of approximation (15) is inherent to μ values close to unity and is equal to 12% for $\delta = 2$ and to 34% for $\delta = 8$.

The normalized steady-state electron distribution over angles and energies (expressed in MeV) can be represented as

$$f(\varepsilon, \mu) = f_1(\varepsilon) f_2(\mu|\varepsilon). \quad (16)$$

Here, the normalized steady-state electron energy distribution $f_1(\varepsilon)$ is approximated by function (14), and the normalized steady-state angular distribution $f_2(\mu|\varepsilon)$ of

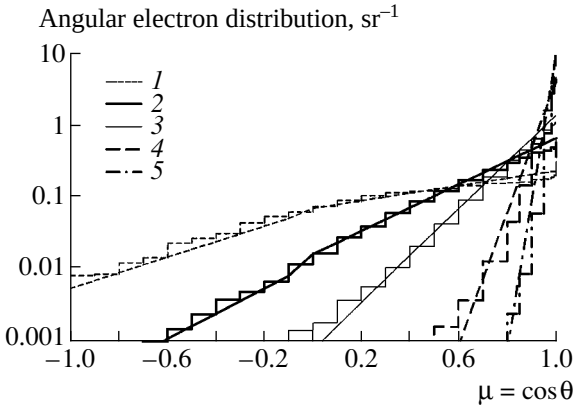

Fig. 10. Normalized angular distributions for different groups of electrons with energies lying in the following ranges $[\varepsilon_1, \varepsilon_2]$: (*1*) 40–60 keV, (*2*) 250–300 keV, (*3*) 0.8–1 MeV, (*4*) 5–6 MeV, and (*5*) 20–25 MeV. The histograms were calculated with the ELIZA code, and the curves were calculated from approximations (17)–(19). The calculations were performed for $\delta = 8$ and for air at $P = 1$ atm.

electrons with energy ε can be approximated as follows:

$$\ln f_2(\mu|\varepsilon) = \begin{cases} y_1(\varepsilon) - k_1(\varepsilon)(1-\mu), & \mu \geq 0 \\ y_2(\varepsilon) + k_2(\varepsilon)(\mu+1), & \mu < 0, \end{cases} \quad (17)$$

where

$$\begin{aligned} y_1(\varepsilon) &= 0.5756\ln(0.9\varepsilon) - 0.46, \\ k_1(\varepsilon) &= 1.24(14\varepsilon)^{0.5} - 0.92, \\ y_2(\varepsilon) &= -2.76(2.3\varepsilon)^{0.48} - 2.53, \\ k_2(\varepsilon) &= 0.557\ln\varepsilon + 2.91, \quad \text{for} \quad \delta = 2 \end{aligned} \quad (18)$$

and

$$\begin{aligned} y_1(\varepsilon) &= 0.6178\ln\varepsilon + 0.4145, \\ k_1(\varepsilon) &= 3.224(5\varepsilon - 0.07)^{0.57}, \\ y_2(\varepsilon) &= -7.6(4\varepsilon)^{0.31} - 0.6, \\ k_2(\varepsilon) &= 0.8858\ln\varepsilon + 5.142, \quad \text{for} \quad \delta = 8. \end{aligned} \quad (19)$$

Figure 10 illustrates the normalized angular distributions calculated with the ELIZA code for different groups of electrons whose energies lie in the ranges $\varepsilon_1 - \varepsilon_2$ = 40–60 keV, 250–300 keV, 0.8–1 MeV, 5–6 MeV, and 20–25 MeV. The fitting curves that were calculated by setting the corresponding electron energies equal to $\varepsilon = (\varepsilon_1 + \varepsilon_2)/2$ are also shown. It can be seen that, over a wide energy range, the numerical results are approximated satisfactorily by formulas (17)–(19).

For each of the electron groups, we calculated the average value of the cosine introduced above, $\langle\mu\rangle$, for which the following fitting formula was obtained:

$$\langle\mu(\varepsilon, \delta)\rangle = a(\delta)\varepsilon/[1 + a(\delta)\varepsilon]. \quad (20)$$

For $a(2) = 2.7$ MeV^{-1} and $a(8) = 12$ MeV^{-1}, the approximation error is ≤ 0.06. The runaway threshold can be estimated from the condition $eE\langle\mu(\varepsilon_{th}, \delta)\rangle = \langle F\rangle$, where $\langle F\rangle$ is the averaged drag force [13]. The values of $\varepsilon_{th}(\delta)$ calculated for $\delta = 2$ and 8 are equal to 470 and 67 keV, respectively, and are close to the values 650 and 65 keV, which were obtained earlier in a different way [9].

4. CONCLUSIONS

We have presented the results of MC simulations of the RREA kinetics in air at atmospheric pressure obtained with the ELIZA code. We have eliminated the earlier disagreement with the results of modeling by other codes based on the MK method and on solving the KE in finite differences. It turned out that the differences in approaches as well as in the sets of cross sections for elementary interactions had practically no effect on the final results. The most important result of our work is the calculated dependence of the characteristic time scale t_e of RREA enhancement on the electric field strength. This time scale determines the relativistic analogue of the first Townsend ionization coefficient, $1/(ct_e)$. The values of t_e for an arbitrary pressure P are recalculated from the value of t_e for atmospheric pressure by the formula

$$t_e(P) = \frac{t_e\ (1\ \text{atm})}{P\ (\text{atm})}. \quad (21)$$

We have investigated the dynamics of the formation of the electron energy distribution. In the range $\delta = 2$–8 of the overvoltage values, the electron distributions that are in equilibrium with the field essentially coincide. This indicates that there exists a universal electron distribution that is independent of δ. We have proposed an analytic approximation for this universal distribution. For $\delta = 2$ and 8, we have calculated the angular distributions of the electrons over all possible energies, as well as the angular distributions for electrons in different energy groups, and have derived approximating formulas for these distributions. As expected, the higher the overvoltage δ and the higher the electron energy, the larger the extent to which a beam of REs is stretched along the electric force. The results obtained can be used to model the high-altitude atmospheric discharges that occur above thunderstorm clouds due to the development of relativistic runaway-electron avalanches.

ACKNOWLEDGMENTS

We are grateful to Mrs. S. Voss and Dr. S. Gitomer for their vigorous efforts in encouraging collaboration between the All-Russia Research Institute of Experimental Physics, the Los Alamos National Laboratory, and the Lebedev Physical Institute on the physics of gigantic upward atmospheric discharges. We also thank Academician A.V. Gurevich for his long-term collaboration in this area of research. The work was supported

by the International Science and Technology Center, project no. 1480-2001.

REFERENCES

1. A. V. Gurevich, G. M. Milikh, and R. A. Roussel-Dupre, Phys. Lett. A **165**, 463 (1992).
2. R. A. Roussel-Dupre, A. V. Gurevich, T. Tunnel, and G. M. Milikh, *Kinetic Theory of Runaway Air Breakdown and the Implications for Lightning Initiation* (Los Alamos Nat. Lab., Los Alamos, 1993), Rep. LA-12601.
3. R. A. Roussel-Dupre, A. V. Gurevich, T. Tunnel, and G. M. Milikh, Phys. Rev. E **49**, 2257 (1994).
4. E. M. D. Symbalisty, R. A. Roussel-Dupre, L. P. Babich, *et al.*, EOS Trans. Am. Geophys. Union **78**, 4760 (1997).
5. E. M. D. Symbalisty, R. A. Roussel-Dupre, and V. Yukhimuk, IEEE Trans. Plasma Sci. **26**, 1575 (1998).
6. L. P. Babich, E. N. Donskoy, R. I. Il'kaev, *et al.*, Dokl. Akad. Nauk **379**, 606 (2001) [Dokl. Phys. **46**, 536 (2001)].
7. L. P. Babich, E. N. Donskoy, I. M. Kutsyk, *et al.*, IEEE Trans. Plasma Sci. **29**, 430 (2001).
8. L. P. Babich, E. N. Donskoy, A. Yu. Kudryavtsev, *et al.*, in *Book of Scientific Works of Russian Federal Nuclear Center–All-Russia Institute of Experimental Physics Nuclear Center* (RFYaTs-VNIIÉF, Sarov, 2001), Vol. 1, p. 432.
9. L. P. Babich, I. M. Kutsyk, E. N. Donskoy, and A. Yu. Kudryavtsev, Phys. Lett. A **24A**, 460 (1998).
10. N. G. Lehtinen, T. F. Bell, and U. S. Inan, J. Geophys. Res. **104**, 24699 (1999).
11. E. N. Donskoy, Vopr. At. Nauki Tekh., Ser.: Mat. Model. Fiz. Protsessov **1**, 3 (1993).
12. A. V. Gurevich, H. C. Carlson, Yu. V. Medvedev, and K. P. Zybin, Phys. Lett. A **275**, 101 (2000).
13. H. A. Bethe and J. Ashkin, in *Experimental Nuclear Physics*, Ed. by E. Segre (Wiley, New York, 1953; Inostrannaya Literatura, Moscow, 1955), p. 141.
14. L. P. Babich, Teplofiz. Vys. Temp. **33**, 659 (1995).
15. D. E. Cullen, M. H. Chen, J. H. Hubbell, *et al.*, *Tables and Graphs of Photon-Interaction Cross Sections from 10 eV to 100 GeV*, Report UCRL-50400 in *LLNL Evaluated Photon Data Library (EPDL)* (Lawrence Livermore National Laboratory, 1989), Vol. 6, Rev. 4.
16. D. E. Cullen, S. T. Perkins, and S. M. Seltzer, *Tables and Graphs of Electron Interaction Cross Sections Z = 1–100*, Report UCRL-50400 in *LLNL Evaluated Electron Data Library (EEDL)* (Lawrence Livermore National Laboratory, 1991), Vol. 31.
17. S. T. Perkins, *Tables and Graphs of Atomic Subshell and Relaxation*, Report UCRL-50 400 in *LLNL Evaluated Atomic Data Library (EADL)* (Lawrence Livermore National Laboratory, 1991), Vol. 30.
18. D. E. Cullen, M. H. Chen, and J. H. Hubbell, in *Evaluated Photon Data Library (EPDL) of the Lawrence Livermore National Laboratory*, Report IAEA-NDS-158, International Atomic Energy Agency, Nuclear Data Services, 1994.

Translated by O.E. Khadin

Plasma Physics Reports, Vol. 30, No. 7, 2004, pp. 625–631. Translated from Fizika Plazmy, Vol. 30, No. 7, 2004, pp. 675–682.

LOW-TEMPERATURE PLASMA

Physical Model of the Formation of a Low-Temperature Dense Plasma during the Irradiation of a Target by a Picosecond Laser Pulse

M. A. Yakovlev

Bauman State Technical University, Vtoraya Baumanskaya ul. 5, Moscow, 107005 Russia

Received July 11, 2003; in final form, October 22, 2003

Abstract—Results are presented from numerical simulations of the breakdown of a dense noble gas by the electrons of a boundary layer that forms during the irradiation of a metal target by a high-power picosecond laser pulse. It is shown that, when the electric field of the boundary layer is taken into account, the density of the seed electrons near the target surface increases substantially, so that the ionization process occurs much faster. The dependence of the time of the onset of breakdown on the electric field of the incident wave and on the concentration of gas atoms is calculated. © *2004 MAIK "Nauka/Interperiodica".*

1. INTRODUCTION

One of the most important effects of the emission electrons on the interaction of electromagnetic (EM) radiation with a condensed medium is seen in the rapid low-threshold ionization of a high-pressure ($p \approx$ 100 atm) gas. Experiments [1] showed that, in this case, the intensity of the incident EM radiation is several orders of magnitude lower than the threshold intensity required for gas breakdown far from the target.

The threshold intensities for gas breakdown by a nanosecond laser pulse were determined numerically by Mazhukin *et al.* [2, 3] and were found to be about $I_{em} \approx 9 \times 10^{12}$ W/m^2 for the pressure $P = 10^2$ atm and laser wavelength $\lambda = 1.06$ μm. The minimum laser energy density needed for such a breakdown is $F = I_{em}\tau_I \approx 3.9 \times 10^4$ J/m^2, where $\tau_I \approx 4.5$ ns is the time of the onset of breakdown (breakdown time).

In my earlier paper [4], it was shown that the ionizing effect of an electron boundary layer (EBL) that is formed when a target is irradiated by an ultrashort high-power laser pulse (with a duration of ≤1 ps and an intensity of $I_{em} \approx 10^{16}$ W/m^2) can help to significantly reduce the amount of laser energy expended in creating a dense plasma near the target surface without destroying the target: $F = 0.2 \times 10^4$ J/m^2 for $P = 10^2$ atm and $\lambda = 1.06$ μm.

Here, in contrast to [4], plasma production by laser pulses is investigated with allowance for both the high-frequency ponderomotive pressure of the laser radiation and the nature of the gas near the target surface.

In the present paper, a physical model is proposed that describes the formation of an EBL and the production of a low-temperature near-surface plasma when a target made of a condensed conducting material is irradiated by laser pulses. It is convenient to begin with a more detailed description of the mechanism for the formation of an EBL [5].

2. ELECTRON BOUNDARY LAYER

The main cause of the formation of an EBL during the irradiation of a metal target by ultrashort laser pulses is that the electron temperature starts to differ appreciably (by an amount of ≈1 eV) from the lattice temperature [6]. As a result, the thermoemission current rapidly increases and a fairly extended layer of negative space charge forms near the target surface.

It is well known that an electric double layer exists near a metal surface under the conditions of thermodynamic equilibrium between the electrons and the lattice. Under these conditions, the electron gas is degenerate and the electron density decreases abruptly away from the surface, $n_e \propto z^{-2}\exp(-\beta z)$, where the quantity β^{-1} is on the order of the mean interelectronic distance in the metal and z is the distance from the metal surface [7]. This makes it possible to treat the EBL as negligibly thin and to ignore its influence on the penetration of laser radiation into the metal. However, as the electron density decreases abruptly away from the surface, the degree of degeneration decreases, so that, when the Fermi energy $E_F(n_e)$ is on the order of the electron thermal energy kT_e, the electron distribution obeys classical statistics. At distances farther from the surface, the electron density decreases far more gradually [5]:

$$n_e(z) = n_0\left(1 + \frac{z}{\sqrt{2}L_d}\right)^{-2}, \qquad (1)$$

where $L_d = (\varepsilon_0 kT_e/e^2 n_0)^{1/2}$ is the Debye screening radius. The boundary electron density n_0 is determined from the degeneration condition $E_F(n_0) \approx kT_e$, which

1063-780X/04/3007-0625$26.00 © 2004 MAIK "Nauka/Interperiodica"

gives $n_0 \propto T_e^{3/2}$. Hence, as the electron temperature increases, the region in the EBL where the electron density decreases according to formula (1) becomes larger. Simultaneously, the boundary electron density n_0 increases; moreover, when the temperature of the electrons in the EBL increases to about E_F, they all obey classical statistics. In this case, they are distributed in accordance with formula (1) and their boundary density n_0 is on the order of the electron density within the metal. Consequently, intense nonequilibrium heating of the electrons within a metal target near its boundary can give rise to a fairly extended high-density electron layer.

An EBL whose electrophysical parameters allow it to profoundly affect the processes occurring near the surface can be produced only by an ultrashort laser pulse whose intensity I_{em} and duration τ_p lie within the limited ranges $I_{em}^{\min} \le I_{em} \le I_{em}^{\max}$ and $\tau_p^{\min} \le \tau_p \le \tau_p^{\max}$. The minimum laser intensity $I_{em}^{\min}$ is determined from the condition that, during the pulse, the electron temperature T_e becomes sufficiently different from the lattice temperature T_l: $\Delta T = T_e - T_l \approx T_F \approx 10^4$–$10^5$ K, where T_F is the degeneracy temperature of the electron subsystem. This condition yields $I_{em}^{\min} \approx \alpha l \Delta T$ [5], where $\alpha \approx 10^{16}$ W/(m^3 K) is the coefficient of heat exchange between the electron and lattice subsystems, l ($\approx \max[\delta, \sqrt{\chi\tau_p}]$) is the depth of the metal layer heated during the pulse, δ is the skin depth, and χ is the electron thermal diffusivity. For a picosecond laser pulse, we have $l \approx 10^{-7}$ m, so that $I_{em}^{\min} \approx 10^{13}$ W/m^2.

According to [6], when the surface of a typical metal is irradiated by a picosecond laser pulse with an intensity of $I_{em} \approx 3 \times 10^{13}$ W/m^2, the two competing emission processes—thermoemission and photoemission of the electrons from a metal surface—are comparable in influence. This indicates that, for such laser intensities, collective thermoemission can be expected to have the greatest effect on one-particle photoemission. As the laser intensity increases, thermoemission begins to predominate over photoemission; i.e., for the above laser intensities, an EBL is formed by thermoemission on the time scale $\tau_s \approx L_d/v_T \approx 10^{-15}$–$10^{-14}$ s (where v_T is the electron thermal velocity). It should also be noted that the thermoemission occurring in the case in question is very different from the thermoemission from an electrode in a closed circuit, because thermal electrons are emitted from an insulated metal surface. As a result, the emitted thermal electrons leave an unneutralized positive charge at the surface and, near the surface, they form a region of negative space charge, which, in turn, affects the thermoemission current. These factors considerably complicate the description of the formation of an EBL. Note, however, that the time scale τ_s on which the spatial electron distribution in the layer forms is much shorter than the duration τ_p of a picosecond laser pulse. Consequently, the distribution with the corresponding temperature can be considered to be steady-state during the entire course of the pulse.

The maximum laser intensity $I_{em}^{\max}$ corresponds to the near-threshold intensities for the melting and ablation of the target material. These processes can occur if the density of the energy stored in the electron subsystem during an ultrashort laser pulse exceeds a certain threshold: $I_{em}^{\max} \tau_p \le F_{\text{abl}}$, where the threshold energy density for laser ablation of the target material is about $F_{\text{abl}} = (0.2\text{–}0.5) \times 10^4$ J/m^2 [8, 9]. Therefore, for a laser pulse with a duration of $\tau_p \approx 1$ ps, we have $I_{em}^{\max} \approx 10^{16}$ W/m^2.

The limitations on the laser pulse duration τ_p are given by the conditions $\tau_p^{\min} \ge \tau_s$ (where $\tau_s \approx 10^{-13}$ s is the time scale for the formation of an EBL with a nondegenerate electron component) and $\tau_p^{\max} \le \tau_{\text{el}}$ (where τ_{el} is the characteristic time scale on which the energy is transferred from the electrons to the lattice). The latter condition guarantees that, in the course of the laser pulse, the lattice is not heated and the process of the evaporation of the target material, during which the EBL plays an insignificant role, has no time to develop.

Hence, the above results show that an EBL may have an appreciable influence on the near-surface processes in the following ranges of the laser-pulse intensities and durations: 10^{14} W/m$^2 \le I_{em} \le 10^{16}$ W/m^2 and 10^{-13} s $\le \tau_p \le 10^{-11}$ s. Although these ranges are limited, they are quite important for technological applications.

3. MATHEMATICAL MODEL

This section presents the results from numerical simulations of the breakdown of a dense gas by the electrons of a boundary layer formed during the irradiation of a metal target by a picosecond high-power laser pulse. The threshold values of the near-surface gas density and of the laser intensity are determined at which the gas near the surface can be ionized very rapidly (in a time as short as about $\tau_I \approx 10^{-12}$ s) and thereby can screen the target from the incident radiation. The breakdown time τ_I is much shorter than the characteristic electron–lattice relaxation time in a conducting material, $\tau_l \approx 10^{-10}$ s. In the case of very rapid gas ionization, this means that, by the time the screening becomes substantial, the lattice temperature remains of the same order of magnitude as at the beginning of the ionization process, so that the target material is not destroyed. The problem is treated in a one-dimensional formulation under the following two assumptions:

(i) The gas above the target is a noble gas, so that molecular compounds cannot be produced in the ion-

ization and recombination processes. The production of molecular ions A_2^+ is ignored because, under the conditions of the problem, the coefficient of dissociative recombination of these ions is substantially less than that of the electron-impact radiative recombination in three-body collisions [10].

(ii) From the numerical results presented below, it will be seen that, up to the time when the target has become screened, the degree of gas ionization is no higher than 10^{-2}. This indicates that only a few gas atoms are excited, so that, in simulations, account was taken of ionization from the ground state only.

The gas ionization kinetics is described by solving the set of equations that includes the heat-conduction equation for the electron temperature, the electron and ion continuity equations, and Maxwell's equations for the electric field of the EM wave and for the field of unneutralized space charge. The gas ionization mechanism governed by the multiphoton photoelectric effect is ignored because, under the conditions adopted here, the breakdown time is about 10^{-9}–10^{-10} s, which is much longer than the characteristic time of gas ionization by the electrons of the boundary layer [4].

Within the metal ($z < 0$), the heat-conduction equation has the form

$$C_m\frac{\partial T_e}{\partial t} = \frac{\partial}{\partial z}\left(\chi_m\frac{\partial T_e}{\partial z}\right) - \alpha(T_e - T_l) + \kappa_r\kappa_i k_0\varepsilon_0 c|E_0|^2\exp(2k_0\kappa_i z). \quad (2)$$

Here, T_e and T_l are the electron temperature and the crystal-lattice temperature in the metal, C_m and χ_m are the heat capacity of the electrons and their thermal conductivity, κ_r and κ_i are the real and imaginary parts of the complex index of refraction of the metal, E_0 is the wave field amplitude at $z = 0$, α is the coefficient of heat exchange between the electrons and the lattice, $k_0 = \omega/c$, and ε_0 is the dielectric constant. For typical metals with $n_m \approx 10^{28}$ m^{-3}, the heat-exchange coefficient is about $\alpha \approx 10^{16}$ W m^{-3} K^{-1} [11].

The heat-conduction equation for the gas ($z > 0$) has the form [12]

$$\frac{3}{2}k\frac{\partial T_e}{\partial t} = \frac{1}{n_e}\frac{\partial}{\partial z}\left(\chi_e\frac{\partial T_e}{\partial z}\right) - \frac{3m}{M}k(T_e - T_a)\nu_e - \left(I + \frac{3}{2}kT_e\right)\nu_I + \frac{e^2|E|^2\nu_e}{2m(\omega^2 + \nu_e^2)}. \quad (3)$$

Here, M is the mass of a gas atom, I is the ionization potential, the electron collision frequency ν_e in the gas is equal to the sum of the electron–ion and electron–atom collision frequencies, and the ionization frequency ν_I is calculated from the classical Thompson formula [10]. The electron–atom collision frequency is calculated using the known temperature dependence of the transport cross section for electron scattering by noble gas atoms [13].

Since, under the conditions of the problem, the duration of the processes under consideration is much less than the electron–lattice relaxation time in the metal ($\tau_l \approx 10^{-10}$ s), the lattice temperature and the temperature of the heavy gas component change very slightly over the course of a run. Thus, even if the mean electron temperature increases to $T_e \sim 10$ eV by the time $t \approx 10^{-13}$ s, the lattice temperature increases by an amount of about 10^2 K. This is why, in simulations, the temperatures of the lattice and of the gas were assumed to be unchanged. Also, the heat transport processes were calculated without allowance for radiative heat conduction because the rapid gas ionization results in the production of an optically transparent plasma (the mean free path of a photon is $I_{\rm ph} \approx (\omega/\omega_p)^2(\omega/\nu_e)\lambda \approx \lambda$, where ω_p is the electron plasma frequency and λ is the wavelength of the EM radiation).

The boundary conditions for Eqs. (2) and (3) have the form

$$\frac{\partial T_e}{\partial z} = 0, \quad z = -l_m, l_a, \qquad \left[\chi\frac{\partial T_e}{\partial z}\right] = 0, \quad z = 0, \quad (4)$$

where l_m and l_a determine the boundaries of the computation region in the metal and in the gas (formally, $l_m, l_a \longrightarrow \infty$) and the square brackets denote the jump in the corresponding quantity at the metal–gas interface.

The electron and ion continuity equations are written as

$$\frac{\partial n_{e,i}}{\partial t} = \frac{\partial}{\partial z}\left[D_{e,i}\frac{\partial n_{e,i}}{\partial z} \pm \mu_{e,i}\left(E_z + \frac{e}{4m_e\omega^2}\frac{\partial|E^2|}{\partial z}\right)n_{e,i}\right] + \nu_I n_e - \beta_1 n_e n_i - \beta_2 n_e^2 n_i. \quad (5)$$

Here, β_1 and β_2 are, respectively, the coefficients of the photorecombination and of the electron-impact radiative recombination and $D_{e,i}$ and $\mu_{e,i}$ are, respectively, the diffusion and mobility coefficients [12]. In Eq. (5), the divergence term $\nabla(n_{e,i}, \mathbf{u})$ is omitted because rapid ionization processes are governed primarily by the diffusive transport mechanism [2]. The electron density is represented as the sum

$$n_e = n_e^{\rm ion} + n_e^{\rm lay},$$

in which the density components $n_e^{\rm ion}$ and $n_e^{\rm lay}$ refer, respectively, to the ionization-produced electrons and

electrons escaping from the metal and satisfy the equations

$$\frac{\partial n_e^{\text{ion}}}{\partial t} = \frac{\partial}{\partial z}\left[D_e\frac{\partial n_e^{\text{ion}}}{\partial z} + \mu_e\left(E_z + \frac{e}{4m_e\omega^2}\frac{\partial|E^2|}{\partial z}\right)n_e^{\text{ion}}\right]$$
$$+ \nu_I n_e - \beta_1 n_e n_i - \beta_2 n_e^2 n_i, \quad (6)$$
$$\frac{\partial n_e^{\text{lay}}}{\partial t} = \frac{\partial}{\partial z}\left[D_e\frac{\partial n_e^{\text{lay}}}{\partial z} + \mu_e\left(E_z + \frac{e}{4m_e\omega^2}\frac{\partial|E^2|}{\partial z}\right)n_e^{\text{lay}}\right].$$

Equations (6) take into account the high-frequency ponderomotive force of the EM wave [14].

The electron density in the EBL near the metal surface, n_e^{lay}, is much higher than the density of the ionization-produced electrons, n_e^{ion}; consequently, according to formula (1), the electron density n_e at the boundary $z = 0$ is equal to n_0. This allows the boundary conditions for Eqs. (6) to be written as

$$z = 0: \quad \begin{aligned} &n_e^{\text{lay}} = n_0, \\ &D_e\frac{\partial n_e^{\text{ion}}}{\partial z} + \mu_e E_z n_e^{\text{ion}} = 0, \end{aligned} \quad (7)$$

$$z = l_a: \quad \begin{aligned} &D_e\frac{\partial n_e^{\text{lay}}}{\partial z} + \mu_e E_z n_e^{\text{lay}} = 0, \\ &D_e\frac{\partial n_e^{\text{ion}}}{\partial z} + \mu_e E_z n_e^{\text{ion}} = 0. \end{aligned} \quad (8)$$

The boundary conditions for the ion density n_i are analogous to those for the electron density component n_e^{ion}. The initial conditions for n_e^{ion} and n_i are as follows: $n_e^{\text{ion}}\big|_{t=0} = 0$ and $n_i|_{t=0}$. The initial condition for the electron density component n_e^{lay} corresponds to electron distribution (1) with the initial temperature T_0. Recall that distribution (1) is established on a time scale of about 10^{-15}–10^{-14} s; this indicates that the boundary density $n_0(T)$ manages to follow the changes of the temperature, which occur on far longer time scales.

The distribution of the longitudinal electric field E_z is calculated from the equation

$$\frac{\partial E_z}{\partial z} = -\frac{e}{\varepsilon_0}(n_e - n_i).$$

At every time step of the calculation, the boundary condition for this equation has the form

$$E_z\big|_{z=0} = \frac{e}{\varepsilon_0}\int_0^{l_a} n_e^{\text{lay}}\,dz,$$

where it is taken into account that the integral of $n_e^{\text{ion}} - n_i$ is equal to zero.

When account is taken of the charge of the ions in the metal, the electric field vanishes in the limit $l_a \longrightarrow \infty$.

The spatial distribution of the electric field of an EM wave is the solution to Maxwell's equations. However, since the time scale ν_I^{-1} on which the parameters of the problem (densities, temperature, etc.) vary is much longer than the time scale ω^{-1}, the field distribution can be determined by solving the following time-independent wave equation at each time step:

$$\frac{d^2E}{dz^2} + k_0^2\varepsilon' E = 0,$$
$$\varepsilon' = 1 - \frac{e^2 n_e}{m\varepsilon_0(\omega^2 + \nu_e^2)} - i\frac{e^2 n_e}{m\varepsilon_0(\omega^2 + \nu_e^2)}\frac{\nu_e}{\omega}, \quad (9)$$

where $k_0 = \omega/c$. This equation is written under the assumption that the parametric instabilities in the plasma produced (which are accompanied by the decay of EM waves into plasma waves and ion acoustic waves [15]) are considerably slower than the ionization. To satisfy this assumption, it is necessary that the decay rate γ_d of an EM wave, which is equal in order of magnitude to $\gamma_d \approx (eE/m\omega c)\omega_p$, be much slower than the ionization frequency ν_I. For a wave field of strength $E \le 5 \times 10^9$ V/m, a gas density of $n_a \ge 10^{27}$ m^{-3}, and an electron temperature of $T_e \approx I$ (the simulations were carried out precisely for these relationships between the parameters), we have $\gamma_d \le 10^{12}$ s^{-1} and $\nu_I \ge 10^{13}$ s^{-1}. Consequently, under the conditions at hand, EM energy is predominantly dissipated by collisions; this makes it possible to use the "traditional" dependence of the dielectric function ε' in Eq. (9).

Equation (9) is supplemented with the boundary conditions

$$z = 0, l_a: \quad [E] = 0, \quad \left[\frac{dE}{dz}\right] = 0, \quad (10)$$

where the wave field has the form

$$z < 0:$$
$$E = \frac{1}{2}\exp(k_0\kappa_i z)\{E_0\exp[i(\omega t + k_0\kappa_r z)] + \text{c.c.}\},$$
$$0 < z < l_a: \quad E = \frac{1}{2}[E_a(z,t)\exp(i\omega t) + \text{c.c.}], \quad (11)$$
$$z > l_a:$$
$$E = \frac{1}{2i}E_\infty\{\exp[i(\omega t - k_0 z)] - \exp[-i(\omega t - k_0 z)]\}$$
$$+ \frac{1}{2}\{R\exp[i(\omega t - k_0 z)] + \text{c.c.}\}.$$

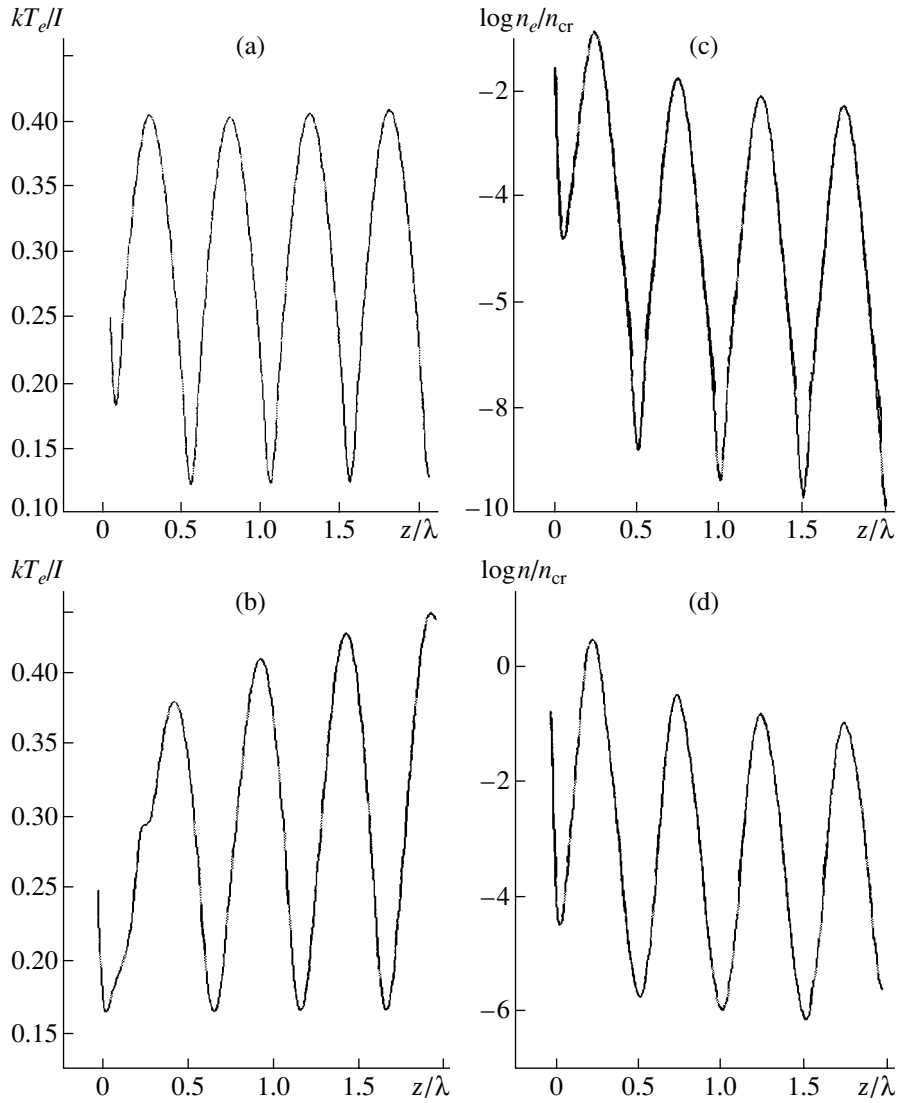

Fig. 1. Profiles of the ratio of the electron thermal energy to the ionization potential of a neutral gas (Ar) and profiles of the ratio of the electron density to the critical plasma density (on a logarithmic scale) along the dimensionless coordinate z/λ (where z is the distance from the target and λ is the laser wavelength) at different times (a, c) $t = 7.0 \times 10^{-13}$ s and (b, d) $t = 1.0 \times 10^{-12}$ s. The gas density is $n_a = 3 \times 10^{27}$ m^{-3} and the amplitude of the incident wave is $E_\infty = 2 \times 10^9$ V/m.

The wave amplitude and dielectric function are represented as $E_0 = E_{01} + iE_{02}$, $R = R_1 + iR_2$, $E_a = E_{a1} + iE_{a2}$, and $\varepsilon' = \varepsilon_1 + i\varepsilon_2$. These representations, together with boundary conditions (10), yield the following relationships at the boundaries of the computation region:

$$\begin{cases} \left.\dfrac{dE_{a1}}{dz}\right|_{z=0} - k_0\kappa_i E_{a1}(0) + k_0\kappa_r E_{a2}(0) = 0 \\ \left.\dfrac{dE_{a2}}{dz}\right|_{z=0} - k_0\kappa_r E_{a1}(0) - k_0\kappa_i E_{a2}(0) = 0 \\ \left.\dfrac{dE_{a1}}{dz}\right|_{z=l_a} - k_0 E_{a2}(l_a) = 2k_0 E_\infty \\ \left.\dfrac{dE_{a2}}{dz}\right|_{z=l_a} + k_0 E_{a1}(l_a) = 0, \end{cases} \tag{12}$$

in which case wave equation (9) splits into two equations,

$$\begin{cases} \dfrac{d^2E_{a1}}{dz^2} + k_0^2(\varepsilon_1 E_{a1} - \varepsilon_2 E_{a2}) = 0 \\ \dfrac{d^2E_{a2}}{dz^2} + k_0^2(\varepsilon_1 E_{a2} + \varepsilon_2 E_{a1}) = 0. \end{cases} \tag{13}$$

The above set of equations was solved by a finite-difference method. The finite-difference approximations to the heat conduction and continuity equations were constructed with the help of a conservative scheme of first-order accuracy in τ and h. The diffusion terms were expressed in implicit form, and the term

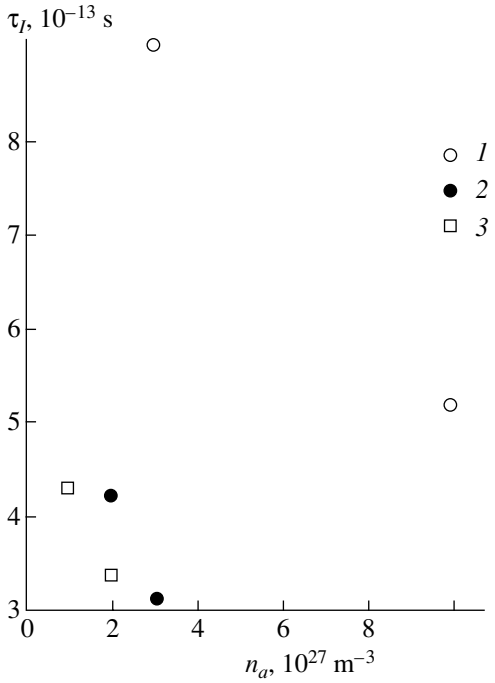

Fig. 2. Characteristic breakdown time $\tau_I = \tau_I(E_\infty, n_a)$ in argon at high laser frequencies ($\omega^2 \gg \nu_e^2$) for $E_\infty = (1)\ 2 \times 10^9$, $(2)\ 3 \times 10^9$, and $(3)\ 4 \times 10^9$ V/m.

μEn in the continuity equation was evaluated in explicit form.

4. NUMERICAL RESULTS AND DISCUSSION

The simulations were carried out for the following values of the parameters of the problem: the laser wavelength was $\lambda = 1.06$ μm, the laser intensity was $I_{em} \approx 3 \times 10^{15}$–$3 \times 10^{16}$ W/m^2, the refractive indices of the metal at the laser wavelength were $\kappa_r = 1.5$ and $\kappa_i = 10.1$ (in which case the density of conduction electrons in the metal is $n_m = 4 \times 10^{28}$ m^{-3}), the gas density was $n_a = 10^{27}$–10^{28} m^{-3}, the gas pressure was $p = 40$–400 atm, and the ionization potential (for argon) was $I = 15.8$ eV. The value of the initial temperature T_0 was varied from 300 to 3000 K and was found to have no significant effect on the final results. The dimensions of the computation region were $l_m = 10\kappa_i^{-1}k_0^{-1}$ and $l_a = 2\lambda$.

Figure 1 shows profiles of the electron temperature T_e (Figs. 1a, 1b) and electron density n_e (Figs. 1c, 1d) at two different times. The profiles correspond to the gas density $n_a = 3 \times 10^{27}$ m^{-3} and the incident wave field $E_\infty = 2 \times 10^9$ V/m. We can see that, for the quite high values of n_a and E_∞ that are under consideration here, the ambipolar diffusion mechanism does not qualitatively affect the spatial temperature and density profiles, which are quite close to the profile of $|E_a|^2$ for a standing EM wave with a period of $\lambda/2$ at the initial ionization stage, the profiles of n_e and n_i being virtually indistinguishable from one another. In this stage, the electron temperature rapidly increases until it reaches a value of several tenths of I, so that the ionization processes begin to proceed much faster. Then, the temperature remains essentially unchanged with time, while the electron density in the regions of maximum temperature T_e rapidly increases (this stage of ionization is well seen in Figs. 1a, 1b). After the maxima in n_e become higher than the critical value n_{cr}, the spatial distribution of the field E_a becomes nonperiodic and, as n_e increases further, the field amplitude begins to decrease, which results in a rapid drop in the electron temperature near the target surface. For the conditions of Fig. 1, the rate at which the temperature decreases at the beginning of this stage varies from 10^4 to 10^5 K/ps. The electron density reaches a critical value n_{cr} in the region of the first (closest to the target surface) maximum in intensity and, thereafter, the critical value is successively reached in the regions of other maxima (this tendency can be readily seen by comparing Fig. 1c and Fig. 1d). Simultaneously, the plasma layers of overcritical density increase in thickness and further merge into one layer, which completely screens the target under irradiation.

Figure 2 shows several calculated points that reflect the dependence of the characteristic breakdown time τ_I on n_a and E_∞. The breakdown time τ_I is defined by the instant when the electron–ion collision frequency ν_{ei} becomes higher than the electron–atom collision frequency ν_{ea}. This definition of the breakdown time, although fairly conditional, makes it possible to detect the beginning of the stage of strong ionization of a gas with an arbitrary density, i.e., to work with the degree of gas ionization rather than with the absolute electron density. By carrying out simulations for several values of E_∞ and of n_a, it is possible to obtain a family of curves $\tau_I = \tau_I(n_a, E_\infty)$. With these curves, it is easy to estimate any of the three parameters τ_I, n_a, and E_∞ by specifying the values of the remaining two.

If the field of the incident EM wave is below a certain threshold, then the target will not be screened. Thus, for $n_a = 10^{27}$ m^{-3} and $E_\infty = 2 \times 10^9$ V/m, the maxima in the temperature become as high as $0.4I$ in less than one picosecond, at which time the electron density does not exceed $(0.2$–$0.3)n_{cr}$; the temperature then continues to increase but at a far slower rate. Consequently, if the electron density ever reaches the critical density n_{cr}, this occurs on a time scale comparable to the electron–lattice relaxation time τ_l in the metal.

The results of numerical simulations of breakdown in an argon gas above the surface of a metal target show that the ponderomotive pressure acts to smooth the spatial profile of the electrostatic field along the normal to the surface.

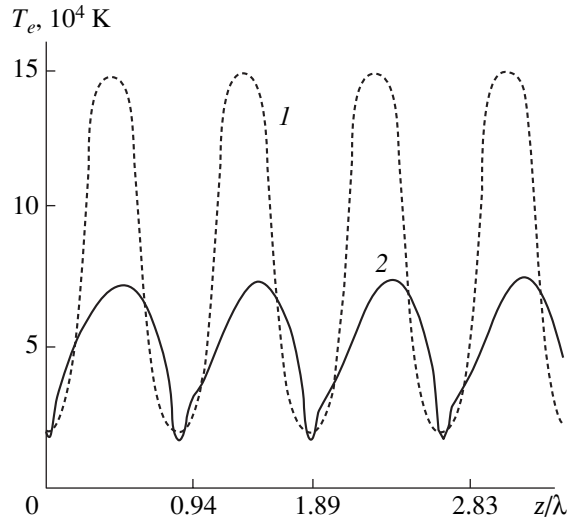

Fig. 3. Profiles of the electron temperature along the dimensionless coordinate z/λ 0.280 ps after the target begins to be irradiated by a laser pulse with an amplitude of $E_\infty = 2 \times 10^9$ V/m in (*1*) He and (*2*) Ar.

The results obtained also show that the main factor governing the nature of plasma production is the magnitude of the ionization potential. This is clearly implied by the above profiles of the temperature and density of the nascent plasma. Under the same conditions, gases with higher ionization potentials are heated to greater temperatures than those with lower ionization potentials because essentially no energy is lost to ionization. This is readily illustrated by Fig. 3, which compares the longitudinal profiles of the electron temperature in He, having the ionization potential $I = 24.59$ eV, and in Ar, having the ionization potential $I = 15.76$ eV.

5. CONCLUSIONS

Based on the results of the numerical calculations described above, the following conclusions can be formulated. During the irradiation of a metal target by EM pulses, nonequilibrium heating of the emission electrons gives rise to an electron boundary layer above the target surface. Under conditions of high gas pressure and high radiation intensity, the electrons of the boundary layer form highly ionized plasma regions, which screen the target from the incident radiation. For gas densities of $n_a \approx 10^{27}$–10^{28} m^{-3} and radiation intensities of $I_{em} \approx 3 \times 10^{15}$–$3 \times 10^{16}$ W/m^2 ($E_\infty = 3 \times 10^9$ V/m), this process lasts from several tenths of a picosecond to several picoseconds. Numerical calculations made it possible to obtain a relationship between the threshold values E_∞ and n_a for which the gas is ionized at a very fast rate ($\tau_I \ll \tau_l$).

ACKNOWLEDGMENTS

I am grateful to A.A. Rukhadze for his interest in this work and helpful support.

REFERENCES

1. A. A. Uglov, N. N. Rykalin, and M. M. Nizametdinov, Zh. Éksp. Teor. Fiz. **69**, 722 (1975) [Sov. Phys. JETP **42**, 367 (1975)].
2. V. I. Mazhukin, A. A. Uglov, and B. N. Chetverushkin, Dokl. Akad. Nauk SSSR **246**, 1338 (1979) [Sov. Phys. Dokl. **24**, 443 (1979)].
3. V. I. Mazhukin, A. A. Uglov, and B. N. Chetverushkin, Fiz. Khim. Obrab. Mater. **6**, 73 (1979).
4. M. A. Yakovlev, A. V. Ivlev, and A. N. Bordenyuk, Zh. Tekh. Fiz. **68** (8), 48 (1998) [Tech. Phys. **43**, 921 (1998)].
5. A. V. Ivlev, K. B. Pavlov, and M. A. Yakovlev, Zh. Tekh. Fiz. **64** (9), 51 (1994) [Tech. Phys. **39**, 888 (1994)].
6. S. I. Anisimov, B. L. Kapeliovich, and T. L. Perel'man, Zh. Éksp. Teor. Fiz. **66**, 776 (1974) [Sov. Phys. JETP **39**, 375 (1974)].
7. A. K. Gupta and K. S. Singwi, Phys. Rev. B **15**, 1801 (1977).
8. Yu. V. Afanas'ev, N. N. Demchenko, I. N. Zavestkovskaya, *et al.*, Izv. Akad. Nauk, Ser. Fiz. **63**, 667 (1999).
9. D. Riley, D. Langley, P. F. Taday, *et al.*, J. Phys. D **31**, 515 (1998).
10. Yu. P. Raizer, *Gas Discharge Physics* (Nauka, Moscow, 1987; Springer-Verlag, Berlin, 1991).
11. S. I. Anisimov, Ya. A. Imis, G. S. Romanov, and Yu. V. Khodyko, in *High Power Radiation Effect on Metals*, Ed. by A. M. Bonch-Bruevich and M. A. El'yashevich (Nauka, Moscow, 1970).
12. Ya. B. Zeldovich and Yu. P. Raizer, *Physics of Shock Waves and High-Temperature Hydrodynamic Phenomena* (Nauka, Moscow, 1966; Academic, New York, 1967).
13. L. J. Kieffer, At. Data **2**, 293 (1971).
14. L. A. Artsimovich and R. Z. Sagdeev, *Plasma Physics for Physicists* (Atomizdat, Moscow, 1979).
15. V. P. Silin, *Parametric Action of High-Power Radiation on Plasma* (Nauka, Moscow, 1973).

Translated by I.A. Kalabalyk

Plasma Physics Reports, Vol. 30, No. 7, 2004, pp. 632–637. Translated from Fizika Plazmy, Vol. 30, No. 7, 2004, pp. 683–688.

LOW-TEMPERATURE PLASMA

Prebreakdown Phase of an Interelectrode Discharge in Water

A. M. Anpilov, E. M. Barkhudarov, V. A. Kop'ev, I. A. Kossyĭ, V. P. Silakov, M. I. Taktakishvili, and S. M. Temchin

Prokhorov Institute of General Physics, Russian Academy of Sciences, ul. Vavilova 38, Moscow, 119991 Russia

Received August 29, 2003; in final form, November 26, 2003

Abstract—Results are presented from experimental studies of the prebreakdown phase of an electric discharge between point (anode) and plane (cathode) electrodes immersed in water with different initial conductivity. When a high-voltage pulse is applied, the induced conductivity is detected in the discharge gap. Its value is one order of magnitude higher than the initial conductivity. It is shown that the induced conductivity increases almost linearly with the initial conductivity. The induced conductivity correlates with the UV emission from the cathode surface. A qualitative analysis of the experimental results is performed. © *2004 MAIK "Nauka/Interperiodica".*

The physics of electrode breakdown in aqueous media is still poorly understood in spite of a great body of experimental and theoretical data [1–3] and various possible applications [4–7]. A self-consistent physical model adequately describing the evolution of the channel of an interelectrode discharge (especially in its early phase) is still lacking. This paper presents the results of experimental studies of the prebreakdown phase of a discharge in water and their qualitative analysis.

A schematic of the experimental setup is shown in Fig. 1. A cylindrical chamber (*1*) made of organic glass and having quartz windows was filled with water with different specific conductivities: $40 \le \eta_0 \le 2000$ μS/cm (distilled water with different concentrations of NaCl). The discharge was excited between two electrodes—point (needle) electrode (*6*) and plane electrode (*2*). The distance L between the electrodes was varied within the range $L \approx 0.2$–2.0 cm. The discharge was initiated by applying a high-voltage pulse ($U \ge 20$ kV, $\tau \le 10$ μs) to the electrodes.

We measured the voltage U across the discharge gap and the current I through the electrode circuit (the current was measured with Rogowski coil (*7*)).

The short-wavelength ($\lambda < 350$ nm) emission from different regions of the discharge gap was measured with an FEU-142 collimated photomultiplier (*4*), insensitive to visible light. An S2000 Ocean Optics spectrograph (*8*) recorded the total emission spectrum ($200 \text{ nm} \le \lambda \le 850$ nm) during the discharge and in the prebreakdown phase.

Figures 2 and 3 show typical signals from the divider measuring the voltage across the discharge gap and from the Rogowski coil measuring the discharge current (a needle serves as an anode). In Fig. 2, the discharge reaches the stage of the breakdown of the interelectrode gap, while in Fig. 3, the discharge is incomplete.

Figure 4 shows the waveforms of the discharge current and the signal from the collimated photomultiplier at different distances l from the point anode.

Figure 5 presents a typical time-integrated emission spectrum of the streamers that arise near the anode but have no time to cover the discharge gap during the voltage pulse.

An analysis of the waveforms presented in Figs. 2–5 allows us to distinguish the following features of the prebreakdown phase of a discharge in water:

(i) The breakdown process is characterized by several phases that differ, in particular, by the value and behavior of the conductivity σ of the interelectrode gap.

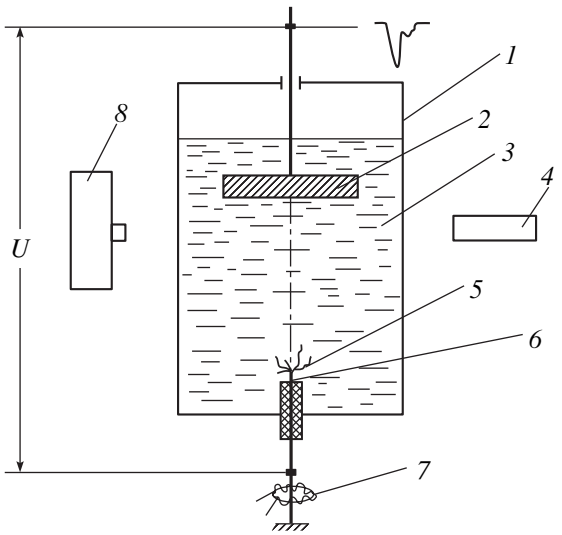

Fig. 1. Schematic of the experimental setup: (*1*) Plexiglass chamber, (*2*) plane cathode, (*3*) water, (*4*) photomultiplier, (*5*) anode streamers, (*6*) point anode, (*7*) Rogowski coil, and (*8*) S2000 spectrograph.

1063-780X/04/3007-0632$26.00 © 2004 MAIK "Nauka/Interperiodica"

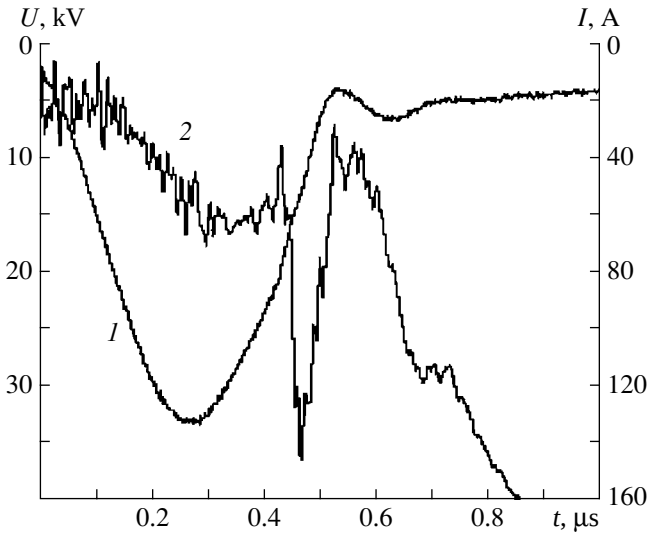

Fig. 2. Waveforms of the (*1*) electric voltage across the discharge gap and (*2*) current in the electrode circuit (η_0 = 400 μS/cm; the discharge is complete).

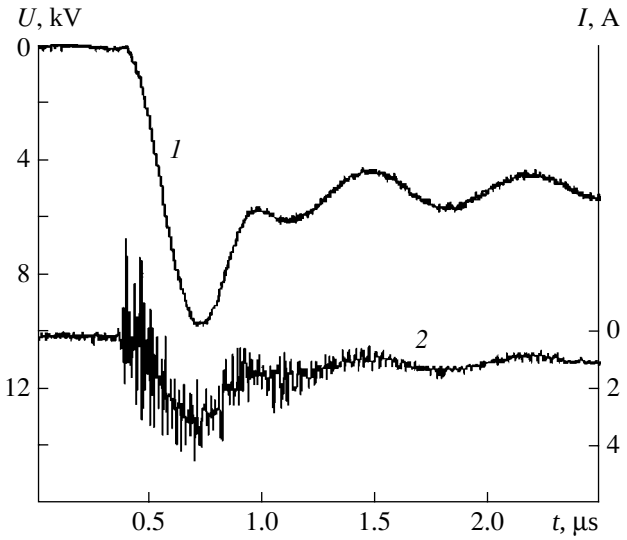

Fig. 3. Waveforms of the (*1*) electric voltage across the discharge gap and (*2*) current in the electrode circuit (η_0 = 550 μS/cm; the discharge is incomplete).

In the first (initial) phase, lasting for $\Delta t_1 \approx$ 100–200 ns ($0 \le t \le t_1$), the conductivity is constant and equal to its initial value $\sigma = \sigma_0$. The second phase, lasting for $\Delta t_2 \approx$ 200–250 ns ($t_1 \le t \le t_2$), is characterized by a substantial (by more than by one order of magnitude) increase in the conductivity of the interelectrode gap. By the end of this phase, a tendency of the conductivity to achieve a quasi-steady value is observed. In the third phase, lasting for $\Delta t_3 \approx 100$ ns ($t_2 \le t \le t_3$), the conductivity increases even more sharply than in the second phase; it reaches its peak value, which is nearly two orders of magnitude higher than the initial conductivity σ_0, and then rapidly decreases to the minimum value at the instant $t = t_3$. In the third phase, which corresponds to the transition from the prebreakdown phase to the breakdown itself, the interelectrode gap is bridged by the discharge channel. Finally, the fourth phase ($t \ge t_3$) is characterized by a relatively slow increase in σ in the formed discharge channel. The typical time behavior of σ derived from the current–voltage waveforms is shown in Fig. 6.

(ii) The higher the initial conductivity σ_0, the higher the induced conductivity σ of the interelectrode gap in the second phase ($\sigma/\sigma_0 \cong 10$).

(iii) In the second phase of a discharge, simultaneously with the increase in the conductivity, we observed the generation of UV emission from the region immediately adjacent to the point anode (see Fig. 4). It follows from photographs of the discharge gap that, early in this phase, both the surface of the point anode and the incomplete streamers contribute to this signal. The radiation from the discharge gap and from the region adjacent to the plane cathode is emitted in the form of a burst (a characteristic peak) only during the transition from the third phase to the phase in which the gap is bridged by the discharge channel. Note that, with the given resolution of time-delay measurements, no delay between the radiation bursts from the cathode and anode was observed. This means that, in this phase, the velocity at which the plasma glow propagates from the anode to the cathode is no lower than 10^8 cm/s. We observed a characteristic 40-ns delay of the UV peak with respect to the peak of the discharge current.

(iv) At an initial conductivity of $\eta_0 \ge 300$ μS/cm, the energy released in the interelectode gap in the prebreakdown phase turns out to be comparable to (or even higher than) the energy released in the fourth phase, in which the gap is closed by the discharge channel (see Fig. 7).

In the literature on electric breakdowns in liquid dielectrics, there are two fundamentally different points of view about the mechanisms initiating a discharge. It is suggested that breakdown is initiated by either a thermal or an ionization mechanism. Until recently, the prevailing concept was that, at pulsed voltages with a pulse duration of $\le 10^{-6}$ s, breakdown is initiated by the ionization mechanism [2, 3, 8]. This concept was based on the apparent similarity of electric discharges in liquids and gases; in this case, liquid was regarded as a very dense gas.

However, results obtained in recent years have made it necessary to revise the breakdown model adopted in [2, 3, 8] and based on the assumption of the decisive role of the electron conductivity of liquids. Thus, it was assumed in [9] that, even in strong electric fields, electrons are in a hydrated state [10, 11] and their mobility is close to ion mobility. Obviously, in this case, the mol-

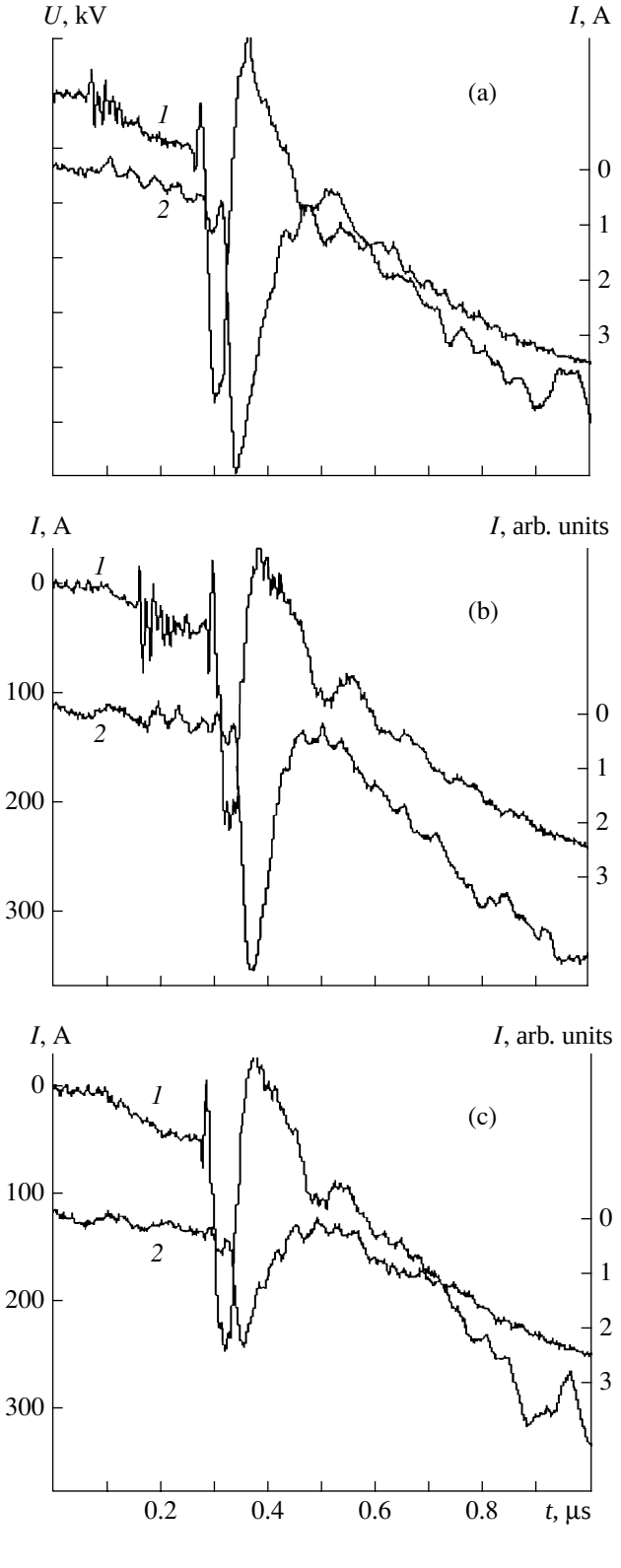

Fig. 4. Waveforms of the (*1*) electric voltage across the discharge gap and (*2*) photomultiplier signal for η_0 = 550 μS/cm and L = 1 cm: (a) radiation from the region adjacent to the anode ($l \cong 0$), (b) radiation from the middle of the discharge gap ($l \cong 0.5$ cm), and (c) radiation from the region adjacent to the cathode ($l \cong L$ = 1 cm).

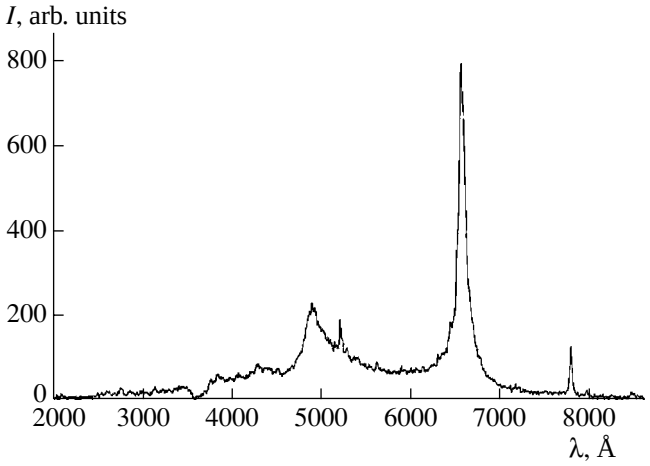

Fig. 5. Typical emission spectra from the discharge gap in the prebreakdown phase (radiation from the region located a distance of $l \cong 1$ mm from the anode).

ecules of a liquid cannot be ionized by electron impacts.

In many recent papers devoted to electric breakdowns of liquid dielectrics by high-voltage pulses with durations longer than 10^{-6} s, it is assumed that a pulsed voltage causes the phase inhomogeneity of liquid and the formation of bubbles, in which breakdown then occurs in a manner similar to gas breakdown [12–14].

An analysis of the experimental results presented above shows, first of all, that the conductivity σ of the interelectrode gap in the prebreakdown phase increases by nearly one order of magnitude as compared to its initial value (see Fig. 6). Such behavior of σ under the action of high-voltage pulses applied to electrodes in water was previously observed in [15]. However, an attempt of the authors to explain the observed increase in σ by an increase in the dissociation constant of water molecules in strong fields has not met with success. Simple estimates show that the effect observed in our study, namely, a substantial increase in the conductivity in the prebreakdown phase, cannot be explained on the basis of the assumption that the main carriers of negative charge are ions or hydrated electrons. On the other hand, taking into consideration the electron conductivity in place of the ion conductivity can explain the currents (50–100 A) observed in our experiment in the second and third phases of a discharge. The electron mobility is higher than the ion mobility by a factor of $(m_i/m_e)^{1/2}$; consequently, the current may increase by the same factor. If the main negative ion in the initial state is an OH^- ion, then we have $(m_i/m_e)^{1/2} \cong 170$.

Returning to the models adopted in [2, 3, 8], in which the electron conductivity (mobility) was assumed to be a governing factor, we come to the necessity (in order to explain our experiment) of searching for mechanisms for generating free (rather than hydrated) electrons with a nonincreased mass m_e

in the interelectrode medium. Taking into account the complexity of this problem, we only note here a number of effects that may promote the transformation of the originally ion conductivity to electron conductivity. First of all, we point out that, at times $t \geq t_1$, a UV source irradiating the interelectrode gap appears in the system under study (see Fig. 4). This radiation, in principle, can play a decisive role both in the formation of the free-electron component and in its maintenance during the high-voltage pulse applied to the point–plane gap. The source of radiation of this kind is the point anode, in which the formation of a hot spot similar to the spots arising in electrode microexplosions is observed as early as in the second phase [16].

The phenomenon of explosive emission was first observed in vacuum discharges [16] and then in high-pressure gas discharges (see [17, 18]). We note that microexplosions can also form on electrodes immersed in a liquid dielectric medium (the results of [19–21] can also be interpreted as the presence of microexplosions on the surface of electrodes immersed in water). Assuming that the size of a hot spot is ≈10–30 μm (as in vacuum and gas-filled diodes), it is easy to show that the current density in the spot during the prebreakdown phase is $j_s \approx 10^7$–10^8 A/cm^2 and the released energy density in the spot is $\varepsilon_s \approx 10^3$–$10^5$ J/cm^3. Such high values of j_s and ε_s are typical of microexplosive electrode processes.

The mechanism for the formation of microexplosions on an anode immersed in water is of particular interest and deserves special consideration. Here, we note only that the electric field near the micropoints on the anode is equal to [5]

$$E_p \approx 2U/(r_m \ln(4L/r_m)), \quad (1)$$

where r_m is the curvature radius of a micropoint and L is the length of the discharge gap. For $U \cong 30$ kV, $L \cong 1$ cm, and $r \cong 10$ μm, this field is as high as $E_p \cong 10^7$ V/cm. Taking into account that this field can be enhanced even more because the electrode surface is covered with a layer that contains air, adsorbed gases, and oxide films and whose dielectric constant is much less than that of water, we can see that the electric field near micropoints can be as high as (or even higher) than that required for microexplosions (see[16]).

It was shown in [22, 23] that explosive-emission centers are intense sources of UV radiation. This radiation may cause an increase in the conductivity of the interelectrode gap and a substantial increase in the current in the electrode circuit. In this case, there is a positive feedback between the intensity of UV emission I_{UV} from a hot spot and the conductivity of water σ,

$$I_{UV} \longrightarrow \sigma \longrightarrow I \longrightarrow \varepsilon_s \longrightarrow I_{UV}, \quad (2)$$

where I is the discharge current.

The presence of positive feedback (2) can cause instability resulting in a microexplosion on a point electrode. It is probable that instability of this kind, which is related to the photoprocesses initiated in gas by the UV emission from a hot spot, is also typical of discharges excited in high-pressure gases.

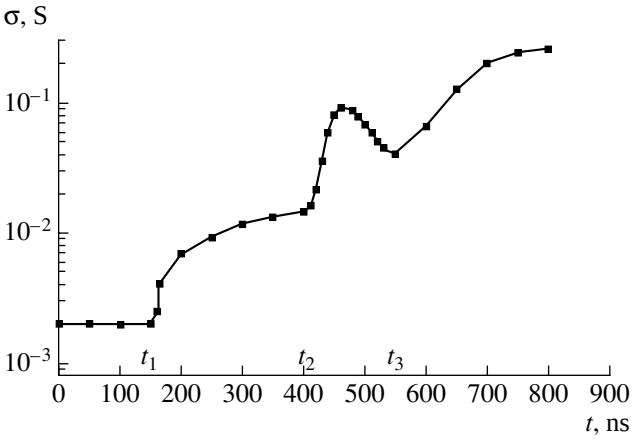

Fig. 6. Time dependence of the conductivity in the discharge gap for $\eta_0 = 400$ μS/cm.

Assuming that the induced conductivity is related to photoionization processes occurring under the action of UV radiation emitted from the anode (the photodetachment of electrons from negative ions), we can estimate the energy of this radiation as the fraction α of the total energy released in a microexplosion:

$$\alpha \geq \varepsilon_i L^2/(3\mu_e U^2 \Delta t), \quad (3)$$

where ε_i is the affinity energy of an electron to an atom (in eV), μ_e is the mobility of a free electron, and Δt is the lifetime of a hot spot. Assuming that $\mu_e \cong 1$ cm^2/(V s), $U \cong 30$ kV, $\Delta t \cong 100$ ns, $L \cong 0.5$ cm, and $\varepsilon_i \cong 3.62$ eV (the affinity energy of an electron to a chlorine atom), we obtain

$$\alpha \geq 0.003.$$

An analysis of the emission spectra of explosive-emission centers [22] shows that such a high conversion ratio of the energy liberated in microexplosions into UV radiation is quite possible.

If a liquid medium (water) is considered as a dense gas with a molecule density of $n_m \approx 3 \times 10^{22}$ cm^{-3}, then the reduced electric field $E_{eff} = E/n_m$ near a micropoint (and, probably, near the head of the discharge channel) can exceed the threshold field for the formation of an electron avalanche resulting in the development of a discharge (≈10^{-15} V cm^2) [24]. This can be considered an argument in favor of the gaseous model of electric discharge in water [2, 3, 8].

In the above analysis, we ignored the processes of electron hydration. The validity of ignoring this factor is not obvious and requires special consideration. The complexity of the analysis, however, consists in the absence of data on the elementary processes involving hydrated electrons (in particular, on the processes of their photoexcitation and photoionization). Since there

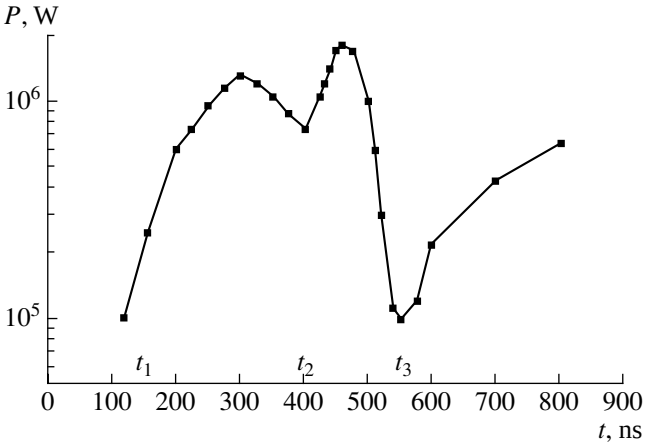

Fig. 7. Time dependence of the power released in water in the discharge gap for $\eta_0 = 400$ μS/cm.

are no theoretical grounds or experimental evidence that hydration cannot occur in strong electric and UV fields, it should be recognized (as in [9, 15, 25]) that the applicability of the free-electron model to liquids (especially, to polar liquids) is still disputable.

In this context, it is reasonable to search for conductivity mechanisms that can provide prebreakdown currents observed in our experiments. Among mechanisms of these kind, the quasi-hole transfer of positive charges can be of importance. The reason is that this process can take place in water [25]. The mobility of a hole (or a proton, in the terms adopted in [25]) is abnormally high and substantially exceeds the mobility of a hydrated electron. In this case, even a relatively low density of the holes can provide currents observed before the interelectrode gap is bridged by the discharge channel (in the second phase of a discharge). Radiation from hot spots on the anode (which can form due to positive feedback (2)) and the accompanying processes of photoionization can provide the presence of holes in the interelectrode gap.

Although the quasi-hole model [25] is quite attractive, its applicability to our experiment must be thoroughly examined; in particular, the question as to whether this model can explain the fact that the induced conductivity increases in proportion to the initial conductivity should be answered. However, the concept of hole conductivity in water in strong electric fields is certainly of interest in constructing a physical model of the electric discharge under study.

Figure 5 shows the emission spectrum of incomplete near-anode streamers. A characteristic feature of this spectrum is the presence of continuum and line components. In the line component, the most intense lines are $H_\alpha(\lambda \cong 6563$ Å) and $O(\lambda \cong 7774$ Å). Processing the continuous spectrum using the procedure adopted in [26], we can determine the streamer radiation temperature, $T_e \approx 2500$–3000 K. The high temperature of the bulk of the channel and the UV emission from it are typical of streamers in water, in contrast to those in high-pressure gases. This difference is probably due to the induced conductivity in water and, as a result, the possibility of high currents (up to 100 A) flowing through an incomplete discharge channel that has not yet bridged the interelectrode gap.

It should be noted that prebreakdown currents in the electrode circuit can determine a number of other specific features of electric discharges in water, e.g., the difference in the breakdown fields at positive and negative potentials at the point electrode (specifically, a decrease in the breakdown field at the point anode), as was observed both in [1–4] and in the experiment described in the present paper. At the same time, the induced conductivity and the related energy release in the prebreakdown phase (see Fig. 7) may be of significance for a number of applied problems, in particular, for the problem of electric-discharge disinfection of water (see [6, 7]), because the energy deposited in the discharge gap in the prebreakdown phase may be comparable to that deposited during the subsequent breakdown, and the character of the processes affecting the medium may be very different in these phases.

The results obtained can be summarized as follows: When a high-voltage pulse is applied to a point anode–plane cathode gap filled with water, the high induced conductivity (higher than the initial conductivity by almost a factor of 10) is observed in the prebreakdown phase of a discharge. It has been shown that the induced conductivity increases almost linearly with the initial conductivity. UV radiation correlating with the induced conductivity is detected in the prebreakdown phase. The source of this radiation is located on the cathode surface. It is suggested that, in a strong electric field, the presence of intense UV radiation can stimulate the appearance of the electron or hole conductivity, which results in the generation of fairly high (15–100 A) currents, which were measured experimentally in the phase preceding the bridging of the interelectrode gap by the discharge channel.

ACKNOWLEDGMENTS

This work was supported in part by the Russian Foundation for Basic Research, project no. 02-02-17209.

REFERENCES

1. *Pulsed Electrical Discharge in Dielectrics*, Ed. by G. A. Mesyats (Nauka, Novosibirsk, 1985).
2. I. Adamchevskiĭ, *Electric Conductivity of Liquid Dielectrics* (Énergiya, Leningrad, 1972).
3. V. Ya. Ushakov, *Pulsed Electric Breakdown in Liquids* (Tomsk. Gos. Univ., Tomsk, 1975).
4. L. A. Yutkin, *Electrohydraulic Effect and Its Industrial Applications* (Mashinostroenie, Leningrad, 1986).

5. K. A. Naugol'nykh and N. A. Roĭ, *Electric Discharge in Water* (Nauka, Moscow, 1971).
6. V. L. Goryachev, V. Yu. Korobochko, A. I. Kulishevich, *et al.*, Izv. Akad. Nauk, Ser. Fiz. **63**, 2294 (1999).
7. A. M. Anpilov, E. M. Barkhudarov, N. Christofi, *et al.*, Lett. Appl. Microbiol. **35**, 90 (2002).
8. G. I. Skanavi, *Physics of Dielectrics (Strong Field Range)* (Fizmatgiz, Moscow, 1958).
9. I. T. Ovchinnikov, K. V. Yanshin, and É. V. Yanshin, Zh. Tekh. Fiz. **48**, 2592 (1978) [Sov. Phys. Tech. Phys. **23**, 1487 (1978)].
10. A. K. Pikaev, *Pulsed Radiolysis of Water and Water Solutions* (Nauka, Moscow, 1965).
11. E. Hart and M. Anbar, *The Hydrated Electron* (Wiley, New York, 1970; Atomizdat, Moscow, 1973).
12. K. C. Kao, in *Proceedings of the AIEE Winter Meeting, New York, 1960*, p. 60.
13. Z. Krasucki, Report No. 5212 (Electrical Research Association, 1967).
14. J. S. Mirza, C. W. Smith, and J. H. Calderwood, J. Phys. D **3**, 580 (1970).
15. I. T. Ovchinnikov and É. V. Yashin, in *Pulsed Electric Discharge in Dielectrics*, Ed. by G. A. Mesyats (Nauka, Novosibirsk, 1985).
16. Yu. D. Korolev and G. A. Mesyats, *Cold-Emission and Explosion Processes in Gas Discharges* (Nauka, Novosibirsk, 1982).
17. A. V. Batrakov, N. I. Vogel, S. A. Popov, *et al.*, IEEE Trans. Plasma Sci. **30**, 106 (2002).
18. I. A. Kossyĭ, V. P. Silakov, N. M. Tarasova, *et al.*, Fiz. Plazmy **30**, 377 (2004) [Plasma Phys. Rep. **30**, 343 (2004)].
19. J. Sidney Clements, Sato Masayuki, and H. Robert Davis, IEEE Trans. Ind. Appl. **23**, 224 (1987).
20. V. G. Lopatin, V. Ya. Ushakov, and V. P. Chernenko, Izv. Vyssh. Uchebn. Zaved. Fiz., No. 3, 99 (1975).
21. V. F. Klimkin and A. G. Ponomarenko, *Problems of Gas Dynamics* (Inst. Teor. Prikl. Mekh. Sib. Otd. AN SSSR, Novosibirsk, 1975), p. 260.
22. N. K. Berezhetskaya, V. A. Kop'ev, I. A. Kossyĭ, *et al.*, Zh. Tekh. Fiz. **61** (2), 179 (1991) [Sov. Phys. Tech. Phys. **36**, 228 (1991)].
23. Yu. B. Bark, E. M. Barkhudarov, Yu. N. Kozlov, *et al.*, J. Phys. D **33**, 859 (2000).
24. Yu. P. Raizer, *Gas Discharge Physics* (Nauka, Moscow, 1992; Springer-Verlag, Berlin, 1991).
25. É. V. Yanshin, I. T. Ovchinnikov, and Yu. N. Vershinin, Dokl. Akad. Nauk SSSR **214**, 1303 (1974) [Sov. Phys. Dokl. **19**, 658 (1974)].
26. É. M. Barkhudarov, S. I. Gritsinin, G. V. Dreĭden, *et al.*, Fiz. Plazmy **30**, 575 (2004) [Plasma Phys. Rep. **30**, 531 (2004)].

Translated by N.F. Larionova